Lifetimes and Nuclear Structure around ^{132}Sn

Inaugural-Dissertation

zur Erlangung des Doktorgrades
der Mathematisch-Naturwissenschaftlichen Fakultät
der Universität zu Köln
in cotutelle mit der Universität Paris-Saclay

vorgelegt von

Guillaume Häfner
aus Mechernich

Als Dissertation im Jahr 2021 angenommen.

université PARIS-SACLAY

Lifetimes and nuclear structure around ^{132}Sn

Durées de vie et structure nucléaire autour de ^{132}Sn

Thèse de doctorat de l'université Paris-Saclay et de l'Université de Cologne

École doctorale n° 576, Particules, hadrons, énergie et noyau: instrumentation, imagerie, cosmos et simulation (PHENIICS)
Spécialité de doctorat: Structure et Réactions Nucléaires
Unité de recherche: Université Paris-Saclay, CNRS, IJCLab, 91405 Orsay, France
Graduate School: Physique. Référent: Faculté des sciences d'Orsay

Thèse présentée et soutenue à Orsay, le 29 Octobre 2021, par

Guillaume HÄFNER

Composition du jury

Marcella GRASSO Directrice de Recherche, Université Paris-Saclay, IJCLab	Présidente
Gilbert DÛCHENE Directeur de Recherche, IPHC et Université de Strasbourg	Examinateur et Rapporteur
Bo CEDERWALL Professeur, KTH Royal Institute of Technology	Examinateur et Rapporteur
Alison BRUCE Professeure, University of Brighton	Examinatrice

Direction de la thèse

Radomira LOZEVA Chargée de Recherche, Université Paris-Saclay, IJCLab	Directrice de thèse
Jan JOLIE Professeur, Universität zu Köln, Institut für Kernphysik	Codirecteur de thèse

Thèse de doctorat

NNT: 2021UPASP109

Acknowledgements

First of all, I would like to thank my supervisor Dr. Radomira Lozeva for giving me the chance for this PhD and her continuous help throughout the years. I am extremely grateful for her support (in- and outside of work) and for shaping me to become the scientist that I am today. None of the great experiences and travel opportunities would have been possible without your dedication. I am also indebted to my co-supervisor Prof. Jan Jolie for supporting me in every step of this co-tutelle and his guidance throughout all the years. To both my supervisors I wish to say thank you for always believing in me and helping me with all the administrative obstacles.

I would like to thank Dr. Gilbert Dûchene, Prof. Bo Cederwall, Prof. Alison Bruce and Dr. Marcella Grasso for accepting to be part of my jury and helping me to improve the manuscript.

Many thanks go out to all the people in the different collaborations with whom I had the pleasure to work with. It has been an interesting, challenging but also fun road to work in such international environments. I have met a great deal of amazing people in this journey, most notably, Rhiann and Tiia who have become great friends. It has been a pleasure to share the office with Min and Kuankuan, who have made my PhD time so much more enjoyable.

I thank all my colleagues around the groups in Cologne and Orsay who have helped me throughout my entire journey. In particular, I would like to thank Dr. Andrey Blazhev who supervised me from the beginning and has always been an inspiration.

I am grateful for my very good friends Arwin, Lukas, Miriam and Rosa, who have been by my side since my early days in the IKP in Cologne or before. You are very important to me and I would not have been where I am today if it were not for you. All the other friendships I have been blessed with during my time in Cologne will be forever remembered.

Nothing I have achieved would have been possible without the permanent support and love from my family. I cannot begin to explain how grateful I am. Let me keep it simple: I love you. Finally, I must thank Franziska, my best friend who has always been like a sister to me. I could not have survived the ups and downs of my PhD without sharing them with you. You are my rock and I am exceedingly grateful for our bond.

This list is incomplete and I apologize for not mentioning everyone. For everyone reading this: take a moment to appreciate the people in your life and tell them how grateful you are.

Contents

Chapter 1

Introduction

The atomic nucleus is a quantum many-body system comprised of protons and neutrons held together by the strong interaction. A successful description of properties of atomic nuclei and their constituent nucleons (protons and neutrons) is the goal of theoretical nuclear physics. This directly relates to an understanding of the strong force which is responsible for binding the nucleons together and forming a nucleus. Nuclei can be described in different ways, for example, microscopic approaches that treat nucleons individually or collective motions of protons and neutrons representing a macroscopic picture.

1.1 Nuclear models: independent particles vs. collective motions

In the 1930's, Gamow proposed the description of the atomic nucleus as a charged liquid drop [1]. The essential assumption of this approach is that the nuclear force saturates, i.e., the binding energy per nucleon reaches a constant value for (unrealistically) high masses. This energy describes the mass excess of a nucleus compared to its individual nucleons. The semi-empirical mass formula derived by Bethe and Weizsäcker describes the binding energy per nucleon B/A as a function of mass number A and charge number Z [2].

$$\frac{B}{A}(Z,A) = a_V - \frac{a_S}{A^{1/3}} - a_C\frac{Z^2}{A^{4/3}} - a_A\frac{(Z-A/2)^2}{A^2} + \frac{a_p}{A^{3/2}} \tag{1.1}$$

The coefficients $\{a_i\}$ in Eq. (1.1) are identified as volume (a_V), surface (a_S), Coulomb (a_C), asymmetry (a_A) and pairing terms (a_P), respectively. Packing nucleons of the same size together into the smallest possible volume, results in a nuclear energy proportional to the volume due to the short range of the nuclear potential.

Nucleons at the surface have fewer interaction counterparts leading to a smaller binding energy. The same result holds for the Coulomb repulsion that scales approximately with Z^2. The asymmetry term quantifies the proton or neutron excess reflecting empirical observations and vanishes when $N = Z$. The last term can either increase, decrease or have no effect on the binding energy depending on the number of protons and neutrons (see Eq. (1.2)).

$$a_p = \begin{cases} |a_p| & \text{for } A \text{ and } Z \text{ even} \\ 0 & \text{for } A \text{ odd} \\ -|a_p| & \text{for } A \text{ even and } Z \text{ odd} \end{cases} \tag{1.2}$$

Plotting the nuclear mass as a function of Z for a specific set of isobars yields a parabola with one minimum. Nuclei in such a minimum are stable with respect to β decay and form the line of stability. Nuclei far from this region are called exotic.

While being successful in describing the overall trend of the nuclear binding energy as a function of mass and charge, it turns out that the binding energy is particularly high for so-called magic nuclei, i.e., nuclei with N or $Z \in \{2, 8, 20, 28, 50, 82, 126\}$. Further experimental evidences for magicity such as high relative abundances, high excitation or nucleon separation energies are summarized in Ref. [3]. The reproduction of these magic numbers by Mayer and Jensen starts by assuming that the nucleons mainly move independently from each other in an average field generated by all the nucleons [4]. The corresponding Hamiltonian can consequently be written in terms of a mean field H_0 and a residual interaction V as described in Eq. (1.3).

$$H = H_0 + V = \sum_{i=0}^{A} t_i + \frac{1}{2} \sum_{i \neq j}^{A} V_{ij} \tag{1.3}$$

t_i is the kinetic energy of the i-th particle and V_{ij} describes the residual interaction between particles i and j.

Calculating the eigenvalues by solving the Schrödinger equation leads to degenerate states according to their respective quantum numbers, meaning that different wave functions carry the same energy. By choosing a Harmonic Oscillator or Woods-Saxon potential as residual interaction, magic numbers are only described up to 20. The addition of a spin-orbit force by Mayer and Jensen lead to the reproduction of all the magic numbers

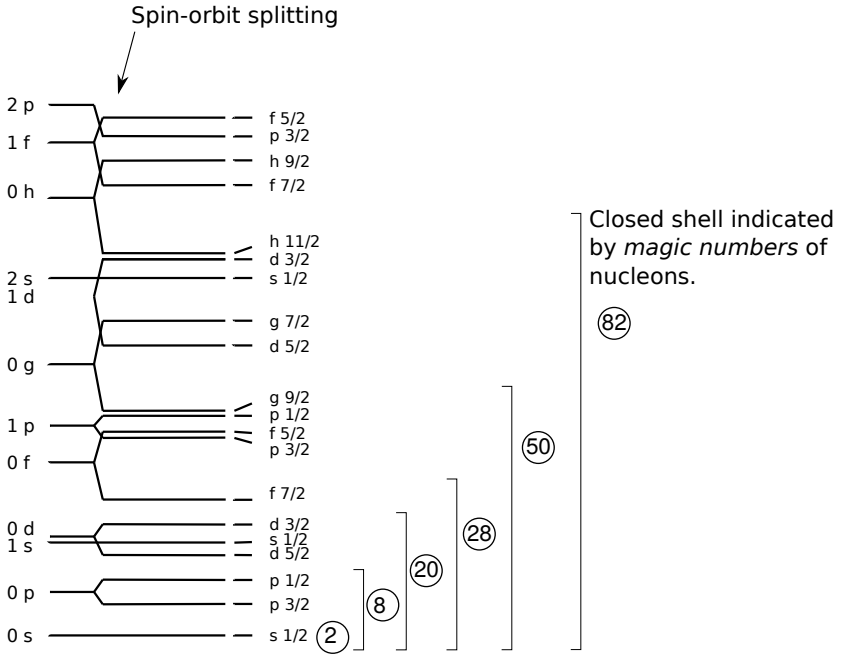

Figure 1.1: Energy spectrum of the shell model from a Harmonic Oscillator potential without (left) and with (right) spin-orbit coupling. The magic numbers are given to the right which correspond to the number of particles occupying the closed shells and the resulting energy levels are taken from Ref. [3].

[4, 5]. This spin-orbit force depends linearly on the scalar product of orbital angular momentum $\vec{l}$ and spin $\vec{s}$, i.e.,

$$V(r) = V(r) + V_{ls}(r) \cdot \left(\vec{l} \cdot \vec{s}\right) = V(r) + V_{ls}(r) \cdot \begin{cases} l & \text{for } j = l + 1/2 \\ -(l+1) & \text{for } j = l - 1/2 \end{cases}, \tag{1.4}$$

where $\vec{j} = \vec{l} + \vec{s}$ is the total angular momentum. The resulting energy spectrum is shown in Fig. 1.1 and shell closures are characterized by a relatively large energy spacing between two consecutive shells. The shell model as independent-particle model has been valuable in describing nuclei near magic numbers. For an increasing number of valence particles outside a closed shell, collective properties of atomic nuclei tend to be more important than the microscopic structure. Starting from the liquid-drop model, Bohr and Mottelson described the collective excitations either as a rotation of a non-spherical core or vibration of the surface around a spherical ground state [6].

The surface of a nucleus can be expanded in terms of spherical harmonics as [7]

$$R(\vartheta, \phi) = R_0 \left[1 + \sum_{\lambda=0}^{\infty} \sum_{\mu=-\lambda}^{\lambda} a_{\lambda\mu} Y_\lambda^\mu(\vartheta, \phi) \right], \tag{1.5}$$

R_0 describing the undistorted nuclear radius, $a_{\lambda\mu}$ specifying the dynamic surface coordinates and Y^{μ}_{λ} being the spherical harmonic functions. For a statically deformed nucleus, the coefficients $a_{\lambda\mu}$ are time independent. For a surface vibration around a spherical ground state, they periodically oscillate around zero. Depending on the summands in Eq. (1.5), nuclei can have different vibrational modes. Similar to the quantum theory of electromagnetism, the energy of nuclear vibrations is quantized in phonons with energies given as multiples of the energy of a single phonon $\hbar\omega$, i.e., $E_n = n\hbar\omega$. Vibrational spectra are thus characterized by equidistant spacing between energies of different multiplets, as can be seen in Fig. 1.2(a).

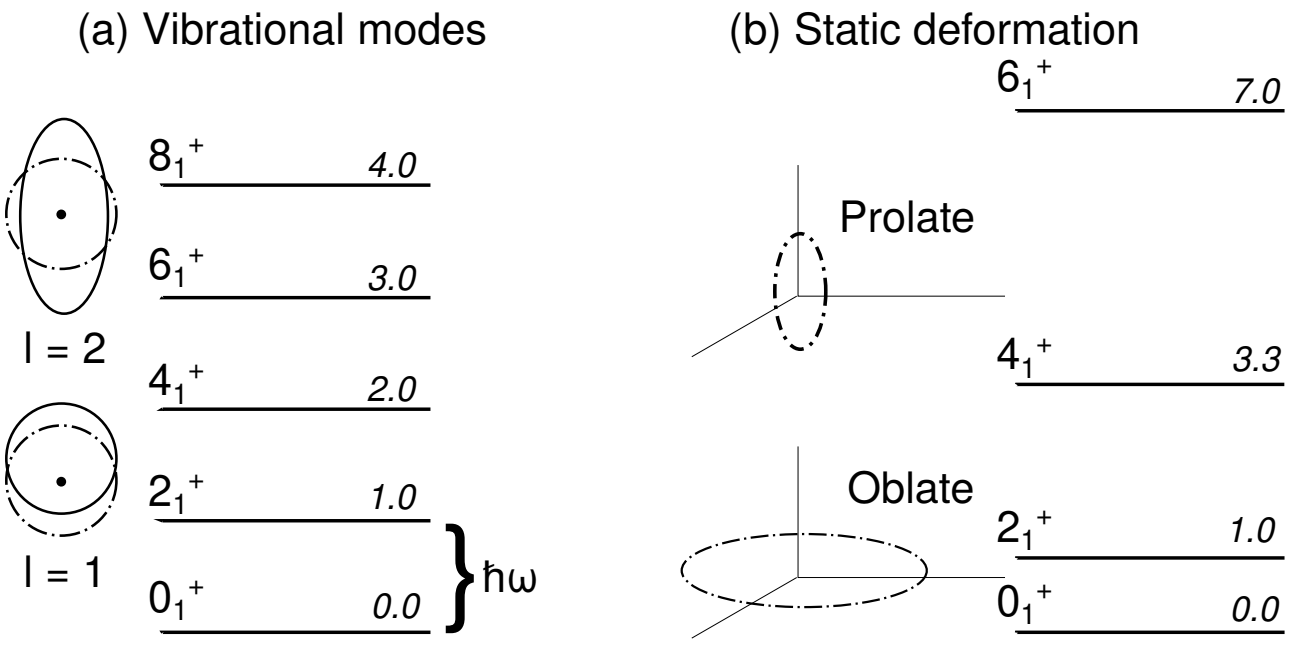

Figure 1.2: Schematic representation of collective motions in atomic nuclei. (a): Vibrational modes of dipole ($l = 1$) and quadrupole type ($l = 2$) around a spherical shape (dash-dotted line). The resulting energy spectrum is shown with equidistant spacing of the phonon energy $\hbar\omega$. (b): Rotational spectrum with two different types of deformation indicated as prolate and oblate. Idea taken from Refs. [3, 8].

For constant $a_{\lambda\mu}$ values, nuclei with deformed equilibrium shapes are represented by an ellipsoid with a surface described by [9]

$$R(\vartheta, \phi) = R_0 \left[1 + \beta Y_{20}\right], \tag{1.6}$$

where the quadrupole deformation parameter $\beta = a_{20}$ is defined as:

$$\beta = \frac{4}{3}\sqrt{\frac{\pi}{5}}\frac{\Delta R}{R_{av}}. \tag{1.7}$$

In Eq. (1.7), ΔR denotes the difference between semi-major and semi-minor axes of the ellipse and $R_{av} \approx R_0 A^{1/3}$ is the average radius of a nucleus with mass A. If $\beta > 0$, the nucleus has the form of a prolate ellipsoid and if $\beta < 0$ the nucleus appears in the flattened form of an oblate ellipsoid, see Fig. 1.2(b). The kinetic energy of a rotating deformed object is given by $\frac{1}{2}\Theta\omega^2$, Θ being the moment of inertia. In representation of total angular momentum J, this expression yields

$$E(J) = \frac{\hbar^2}{2\Theta} J(J+1). \tag{1.8}$$

From Eq. (1.8), an energy sequence with increasing spacing is obtained known as a rotational band, as shown in Fig. 1.2(b). The approximation in Eq. (1.8) is known as rigid rotor and deviations are expected due to the nucleus behaving more like a fluid rather than a rigid object with fixed moment of inertia.

1.2 Observables in γ-ray spectroscopy experiments

Nuclei in excited states may decay to lower-lying (excited) states via the emission of γ rays or conversion electrons [9]. The study of de-excitation via γ-ray spectroscopy allows for a detailed study of nuclear excited states and their properties. The following section describes observables relevant for this work that can be obtained in γ-ray spectroscopy experiments.

Transitions between different nuclear states can be described by changing the wave function from an initial state ψ_i to a final state ψ_f characterized by their respective quantum numbers. During γ decay, a photon is emitted with an energy equal to the difference between the initial (E_i) and final (E_f) state, minus the energy imparted to the recoiling nucleus of mass M [9].

$$E_\gamma = E_i - E_f - \frac{E_\gamma^2}{2Mc^2} \tag{1.9}$$

The energy of the recoiling nucleus $E_\gamma^2/2Mc^2$ is usually very small compared to the energy of the photon, E_γ. The emitted radiation field is specified by its type σ (electric or magnetic) and its multipole order L. The latter quantifies the angular momentum of the photon and can be determined via the triangle rule [9]:

$$|J_i - J_f| \leq L \leq J_i + J_f, \tag{1.10}$$

J_i and J_f being the angular momentum of initial and final states, respectively. Spins can be deduced experimentally by measuring the multipole order from an angular distribution of a given γ-ray transition $W(\vartheta, \varphi)$

[9]. The azimuth angle ϑ and polar angle φ specify the direction of radiation with respect to the orientation axis [9]. In addition to the energy and angular momentum conservation, the parity π is a conserved quantity and can be either $+1$ or -1. The radiation emitted by the photons can be of electric or magnetic character which is determined by the parity according to the following rules [9]:

$$\begin{aligned} \pi_f &= (-1)^L \pi_i \qquad \text{for electric radiation,} \\ \pi_f &= (-1)^{L+1} \pi_i \quad \text{for magnetic radiation.} \end{aligned} \tag{1.11}$$

The first excited state of most even-even nuclei is a 2^+ state. From the selection rules it is evident that its decay to the 0^+ ground state is of $E2$ character. It has to be noted that $E0$ transitions, i.e., from $0^+ \rightarrow 0^+$, are forbidden with respect to the γ decay. A photon carries an intrinsic angular momentum of $1\hbar$ and $L = 0$ would violate the conservation of angular momentum. On the other hand, a $0^+ \rightarrow 0^+$ transition is possible via the emission of conversion electrons.

Internal conversion

The de-excitation of an excited nuclear state via γ rays is in competition with the decay via internal conversion. Instead of directly emitting a photon, an electron (typically K or L electrons) is emitted with a probability related to the overlap of its wave function with the one from the atomic nucleus [9]. A typical conversion electron spectrum shows discrete peaks on a continuous background. Similar to the decay via γ rays, the conversion electrons carry the energy difference between initial and final state of the nucleus (minus the binding energy of the electron). The total conversion strength increases with rising multipolarity, increasing Z and decreasing energy. For example, low energy transitions have a strong decay via the emission of conversion electrons. To correct for such a decay, the total transition probability T_t has to be taken into account, i.e.,

$$T_t = T_\gamma + T_e, \tag{1.12}$$

where T_γ and T_e are the probabilities for γ-ray emission and internal conversion, respectively. The conversion coefficient α_T describes the probability for electron emission relative to the decay via γ rays [9]:

$$\alpha_T = \sum_i \alpha_i = \frac{T_e}{T_\gamma}, \tag{1.13}$$

where α_i has to be summed over all electron sub-shells (i.e., $i = \mathrm{K}, \mathrm{L}, \mathrm{M}, ..$). By measuring the γ-ray intensity I_γ, the total intensity of the transition is given by $I_t = I_\gamma(1 + \alpha_T)$.

1.2.1 Lifetimes and isomers

Another important property of nuclear states is the half-life $T_{1/2}$ which denotes the time period after which half the number of a given state have decayed. The mean lifetime $\tau = T_{1/2}/ln(2) = 1/\lambda$ is related to the decay constant λ and obeys the general decay law [9].

When the probability of transitions to occur is low, the lifetime of the state is large and the probability to de-excite is linked to metastability. These meta-stable states are called isomers and are generally referred to states with half-lives significantly longer than 1 ns [10]. Some of the reasons for the existence of isomers will be briefly mentioned in the following.

- **Spin traps**. When J_i and J_f differ by a comparably large number, a high amount of angular momentum transfer is required for the transition to occur, see Eq. (1.10). This results in a small transition probability which corresponds to a long half-life.

- **Shape isomerism.** A change in shape of a particular nucleus can result in a local energy minimum which leads to a lowered transition strength [10]. These minima can be analyzed using, for example, potential energy surfaces that map the energy according to the deformation parameters introduced in the previous section.

- **K isomers.** In deformed nuclei, K is the projection of the total angular momentum upon the nucleus' axis of symmetry [6]. If the difference in K quantum number $\Delta K = K_i - K_f$ is larger than the multipolarity of the transition L, the transition is called K-forbidden [10, 11].

A specific type of meta-stable states are called seniority isomers [12]. The seniority quantum number ν denotes the number of nucleons or holes that are not coupled to $J = 0$ [8, 13]. These isomers occur especially around (semi)magic nuclei where the low-lying states often have $\nu \approx 2$. The energy difference between two states decreases with increasing spin due to the residual interaction leading to long-lived states. This effect is strongest for high-j orbitals such as the $\nu(0h_{11/2})$ orbital around $^{132}\mathrm{Sn}$ [14] or the $\pi(0g_{9/2})$ orbital below $^{100}\mathrm{Sn}$ [15].

To gain insights into a configuration of such an isomer, the static magnetic moment can be used. Experi-

mentally, it is found that a nucleus in a state with non-zero spin J has a magnetic moment μ defined as [9]

$$\mu = gJ\mu_N, \tag{1.14}$$

where g is the gyromagnetic ratio, $\mu_N = e\hbar/m_p$ the nuclear magneton and m_p the proton mass. In the following, if not mentioned explicitly, the nuclear magnetic moments are given in units of μ_N. There are two sources of nuclear magnetism [9]: 1.) the orbital movement of charged particles and 2.) the intrinsic spin of the nucleons. The magnetic dipole operator $\vec{\mu}$ can be written as a summation over all A nucleons, i.e.,

$$\vec{\mu} = \mu_N \sum_{k=1}^{A} \left(g_l^k \vec{l}_k + g_s^k \vec{s}_k \right). \tag{1.15}$$

$\vec{l}_k$ and $\vec{s}_k$ denote the orbital and spin angular momentum for the k-th nucleon with their respective gyromagnetic ratios g_l^k and g_s^k. The gyromagnetic ratios, in short g factors, for free protons (π) and neutrons (ν) are experimentally deduced to be [9]:

$$\begin{aligned} g_l^\pi &= 1, & g_s^\pi &= 5.586 \\ g_l^\nu &= 0, & g_s^\nu &= -3.826. \end{aligned}$$

To calculate the magnetic moment of a nuclear state, the z component of the operator in Eq. (1.15) has to be applied onto a state with magnetic substate $M = J$. If the wave function of a nuclear state is denoted as $|J, M\rangle$, the magnetic moment is defined as

$$\mu = gJ = \langle J, M = J|\mu_z|J, M = J\rangle. \tag{1.16}$$

The magnetic moment $\mu(j)$ of a single-particle in orbital $j = l \pm 1/2$ is uniquely defined by the quantum numbers l and s occupying the single-particle orbit [9]:

$$\mu(j) = \left[g_l \pm \frac{g_s - g_l}{2l+1} \right] j. \tag{1.17}$$

From Eq. (1.17) it can be seen that the g factor is very sensitive to the single-particle orbitals. Magnetic moments for two- and multi-particle configurations can be calculated using the single-particle values via the additivity relation [9]. Thus, together with the lifetime, the measurement of the magnetic moment can give valuable insight into the configurations of a given state.

1.2.2 Reduced transition probabilities

The decay constant λ can be calculated via [16, 17]:

$$\lambda(\sigma L) = \frac{2(L+1)}{\hbar L[(2L+1)!!]^2}\left(\frac{\omega}{c}\right)^{2L+1}|\langle\psi_f|\hat{O}(\sigma L)|\psi_i\rangle|^2. \tag{1.18}$$

In Eq. (1.18), the energy of the photon is related to ω via $E_\gamma = \hbar\omega$. The transition probability decreases with increasing multipole order by a factor of approximately 10^{-5} [9]. The last part in Eq. (1.18) describes the overlap between initial and final wave functions after applying the transition operator $\hat{O}$. This matrix element can be linked to the so-called reduced transition probability $B(\sigma L)$ [17]:

$$B(\sigma L; J_i \to J_f) = \frac{1}{2J_i+1}|\langle\psi_f||\hat{O}(\sigma L)||\psi_i\rangle|^2. \tag{1.19}$$

$B(\sigma L)$ is given in units of $e^2\text{fm}^{2L}$ for electric and $\mu_N^2\text{fm}^{2L-2}$ for magnetic transitions. At this point it is noted that the matrix element in Eq. (1.19) is a reduced matrix element (indicated by the double vertical lines). It is related to the matrix element in Eq. (1.18) by summing over all possible magnetic substates m and applying the Wigner-Eckart theorem [18]. For an $E2$ transition, Eq. (1.19) can be simplified to [9]

$$B(E2 : J_i \to J_f) = \frac{816}{E_\gamma^5\tau_p}\, e^2\text{fm}^4\text{MeV}^5\text{ps}, \tag{1.20}$$

where τ_p is the partial mean lifetime of the excited state [9]. Electric transitions are always more likely to occur compared to magnetic ones of the same multipole order. For example, $E2$ and $M1$ transitions can have similar probabilities and mixing of both types can occur. The purity of a such a transition is quantified by the multipole mixing ratio δ [19]. It is defined as the ratio of probabilities for $E2$ and $M1$ transitions, i.e., [19]

$$\delta = \frac{\langle\psi_f||\hat{O}(E2)||\psi_i\rangle}{\langle\psi_f||\hat{O}(M1)||\psi_i\rangle}. \tag{1.21}$$

Weisskopf estimate

The reduced transition strengths can be linked to single-particle behavior by introducing the Weisskopf estimate [17]. It expresses transitions in terms of the motion of a single nucleon, for example a proton. It is based on the assumption that the radial parts of the nuclear wave functions ψ_i and ψ_f are constant up to the nuclear radius

R and vanish for $r > R$. Then, the radial part of the transition probability is given by [9]:

$$\frac{\int_0^R r^2 r^L dr}{\int_0^R r^2 dr} = \frac{3}{L+3} R^L, \tag{1.22}$$

where the integral in the denominator arises from normalization and r^2 is due to its dependence of the volume element dr. By including this factor in the matrix element and replacing the angular integrals by 4π, the transition probabilities can be estimated by [9]:

$$\lambda(EL) \approxeq \frac{8\pi(L+1)}{L[(2L+1)!!]^2} \frac{e^2}{4\pi\epsilon_0 \hbar c} \left(\frac{E}{\hbar c}\right)^{2L+1} \left(\frac{3}{L+3}\right)^2 cR^{2L} \tag{1.23}$$

for electric and

$$\lambda(ML) \approxeq \frac{8\pi(L+1)}{L[(2L+1)!!]^2} \frac{e^2}{4\pi\epsilon_0 \hbar c} \left(\frac{E}{\hbar c}\right)^{2L+1} \left(\mu_p - \frac{1}{L+1}\right)^2 \left(\frac{\hbar}{m_p c}\right)^2 \left(\frac{3}{L+2}\right)^2 cR^{2L-2} \tag{1.24}$$

for magnetic transitions. The proton mass is denoted as m_p, μ_p is the magnetic moment of a single proton and $e^2/(4\pi\epsilon_0\hbar c) \approx 1/137$ is a dimensionless factor known as the fine structure constant. The final simplification comes from the assumption that the nuclear radius is related to the mass of a nucleus A according to $R = R_0 A^{1/3}$. Thus, Weisskopf Units (W.u.) for a given transition can be calculated using A and E_γ. One W.u. corresponds to the equivalent of the strength of a single nucleon being involved in that transition. This formalisim indicates whether or not a transition is collective ($B(E2) \gtrapprox 10$ W.u.) or of single-particle nature ($B(E2) \lessapprox 2$ W.u.). $B(E2)$ values are small near closed shells and can reach very high values of more than 10^2 W.u. in mid-shell regions. The evolution of collectivity with increasing neutron number and the determination of the onset of collectivity above a closed shell is of particular interest in current nuclear structure research.

1.3 Nuclear structure far from stability: production of rare isotopes

Large effort has been put into the development of experimental techniques to explore the unknowns of the nuclear landscape known as ‘terra incognita’. New production mechanisms that produce a wide range of exotic nuclei like spallation, fragmentation and fission had to be considered. The downside of these reactions is the production of a large variety of products due to the high number of reaction channels. Therefore, new procedures had to be developed to study their properties. This led to the radioactive ion beam (RIB) physics which is one of the main fields of interest in nuclear structure physics today. In general, two major types of production facilities can be distinguished and will be introduced in the following: the isotope separation on line (ISOL) method and

the complementary in-flight separation of projectile fragments [20].

A schematic overview of both methods is shown in Fig. 1.3. Time and energy scales for those production mechanisms depend on the apparatus and beam lines but typical values are given in Fig. 1.3.

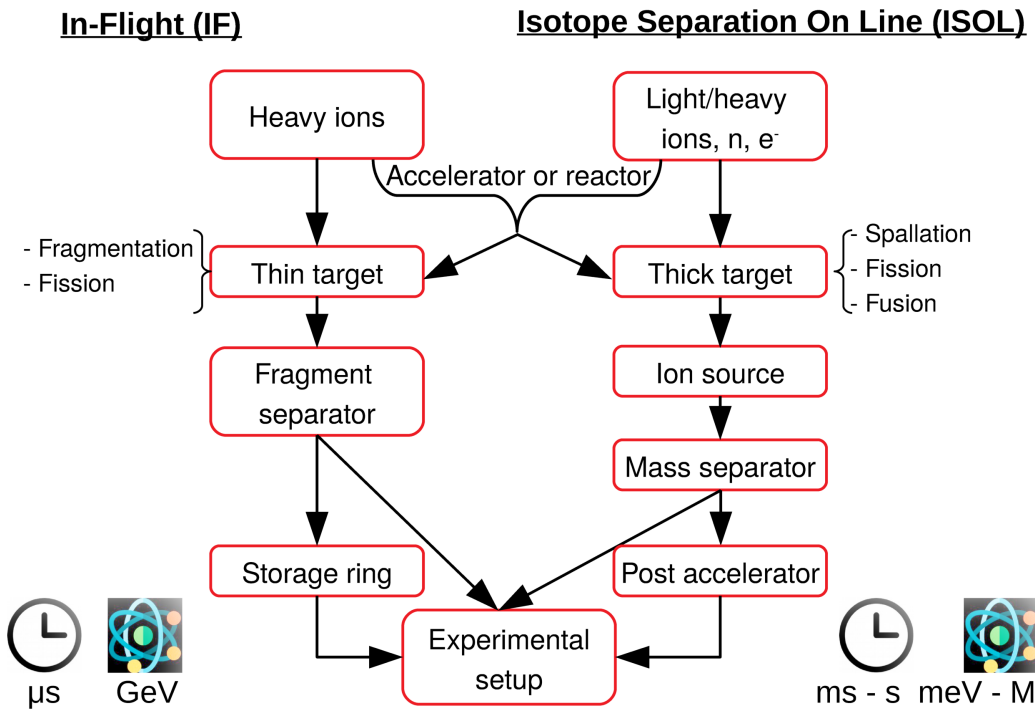

Figure 1.3: Schematic representation of the in-flight (left) and ISOL (right) technique for the production of radioactive ion beams. Typical time and energy scales are also given for comparison. Adapted from Ref. [20].

The ISOL technique is based on the production of radioactive isotopes through (usually) light particles on sufficiently thick targets to stop the beam and subsequent extraction out of target. After the extraction, the atoms are ionized, mass separated and can be transported to the experimental setup. All these steps take time, therefore the ISOL technique is limited to exotic nuclei with lifetimes in the millisecond range and above. For more details the reader is referred to Refs. [20, 21].

In contrast to the ISOL technique, the in-flight method generally uses highly energetic, heavy primary beams impinging on thin, lighter targets. One major advantage is the short time span between production and delivery of radioactive species to the experimental setup. This provides the opportunity to study most exotic nuclei with extremely short nuclear lifetimes restricted by the flight time which is typically below 1 μs. In contrast to the ISOL method, the in-flight technique is insensitive to chemical properties. The method takes advantage of the fact that the kinematics of certain nuclear reactions at high incident energies show a clear forward focusing. This enables experimenters to separate the desired products in mass-over-charge (A/Q) by means of combinations

of several magnetic (and electric) fields. An additional selection in atomic number is achieved through profiled degraders which add a selectivity through the Z dependence of the energy-loss process inside the degrader matter.

The in-flight facilities commonly use two production mechanisms, projectile fission or projectile fragmentation [22]. The latter one was first investigated in reactions of heavy ions with kinetic energies of 200 MeV/u or more [23]. The process involves a peripheral interaction of the projectile with a target nucleus where some nucleons are removed and the excited residue undergoes a de-excitation. The reaction is well described by the abrasion-ablation model [24]. It is a semi-microscopic description of the reaction where the collision of target and projectile is described by a geometrical macroscopic model and the following evaporation via statistical de-excitation [25]. While some light neutron-rich nuclei can be produced by projectile fragmentation it is mainly the source of neutron-deficient nuclei.

For the production of heavier, neutron-rich nuclei, nuclear fission has been an extremely useful method. By utilizing an inverse kinematics (i.e., heavy beam and light target), the momenta of the fragments are focused towards the beam direction. Furthermore, the resulting fragments are fully stripped of electrons and the charge states are equal to the atomic number. Projectile fission was first investigated in Ref. [26] which demonstrated the capabilities of producing neutron-rich isotopes with cross section as low as a few μb [22]. Other fission reactions such as neutron-induced or spontaneous fission are other methods for the production of neutron-rich isotopes (e.g., Ref. [27]).

1.4 Shell evolution in the region around ^{132}Sn

The tin isotopic chain with $Z = 50$ has the most stable and two doubly magic isotopes, the neutron-deficient $^{100}\mathrm{Sn}$ and the neutron-rich $^{132}\mathrm{Sn}$.

Figure 1.4 shows a section of the nuclear chart around $^{132}\mathrm{Sn}$ between $Z = 50$ (Sn) and $Z = 54$ (Xe) together with the active orbitals above $^{132}\mathrm{Sn}$. With the advances in experimental techniques and detection processing, these exotic nuclei become accessible to study the magicity and evolution of nuclear shells far away from stability. The robustness of the $^{132}\mathrm{Sn}$ core was confirmed by the investigation of single-particle states in $^{133}\mathrm{Sn}$ [28]. The purity of single-neutron excitations in $^{133}\mathrm{Sn}$ studied in a $^{132}\mathrm{Sn}$(d,p) reaction shows signatures of the magic nature of $^{132}\mathrm{Sn}$ [29]. Further evidence for the doubly magic nature of $^{132}\mathrm{Sn}$ was provided through the measurement of transition probabilities in $^{132}\mathrm{Sn}$ [30], various spectroscopy experiments around $^{132}\mathrm{Sn}$ [31, 32, 33, 34, 35], mass measurements [36] or the determination of charge radii from laser spectroscopy

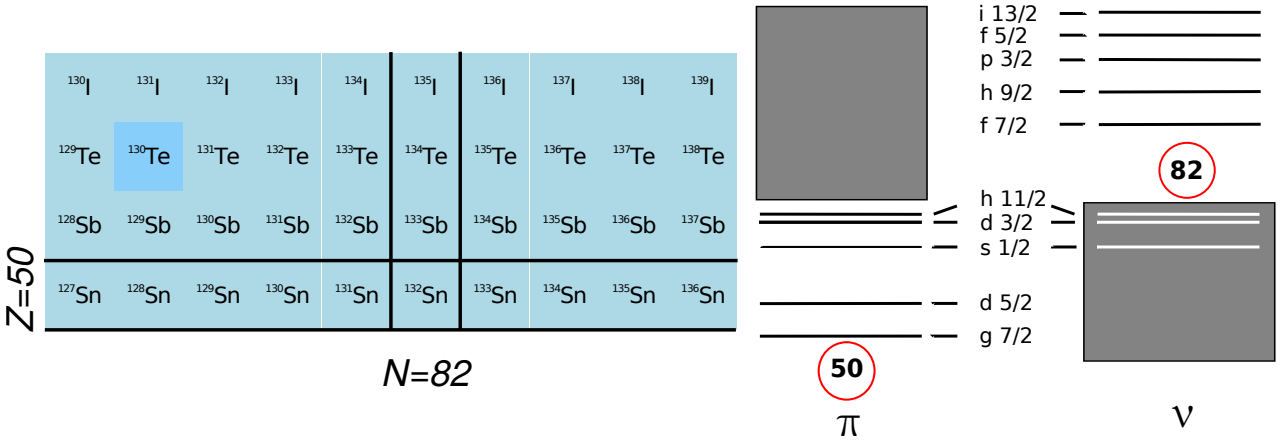

Figure 1.4: Section of the nuclear chart around the doubly magic ^{132}Sn. Proton and neutron magic numbers are labeled in black. The relevant shells around ^{132}Sn are also shown.

experiments [37].

For nuclei near closed shells, the interplay between single-particle behavior and collective motion results in coexisting nuclear shapes and exotic excitations. Some experimental signatures of collectivity in even-even nuclei will be presented in the following, taken from Ref. [8]. Collective states result from many interactions of simpler entities (e.g., single particle, two quasi-particle). Indications for an increased collectivity arise from a drop in the excitation energy of the first excited 2^+ state, $E_x(2_1^+)$. A low excitation energy of the 2_1^+ state corresponds to a highly collective state. On the other hand, excitation energies of the 2_1^+ state are particularly high for closed-shell nuclei. In ^{132}Sn, the first excited state is a 2^+ state at an excitation energy of about 4 MeV. Further information on the shape of the nucleus and degree of collectivity can be obtained when looking at the quotient of $E_x(4_1^+)/E_x(2_1^+)$ known as $R_{4/2}$ ratio. Nuclei near closed shells have typical values of $R_{4/2} < 2$. When moving further away from the magic numbers, the value increases from about $R_{4/2} = 2$ to 3.33 for mid-shell nuclei. These limits correspond to nuclear shapes coherently behaving in a macroscopic way. $R_{4/2} = 2$ describes a spherical vibrator and $R_{4/2} = 3.33$ is the ratio for an axially symmetric rotor [38], see Fig. 1.2. Another more sensitive probe of collectivity are transition probabilities because they are indirectly linked to the wave functions, more precisely the overlap of wave functions of initial and final states.

The increase of collectivity with increasing number of valence nucleons is well established for most regions close to stability but less data is available for exotic nuclei due to experimental challenges. The excitation energy of the 2_1^+ state and the reduced transition probability of the $2_1^+ \rightarrow 0_1^+$ transition in even-even nuclei around ^{132}Sn are shown in Fig. 1.5. In panel (a), the excitation energy of the 2_1^+ state is plotted as a function of neutron number. The energy reaches its maximum at $N = 82$ and decreases when moving away from the $N = 82$ shell

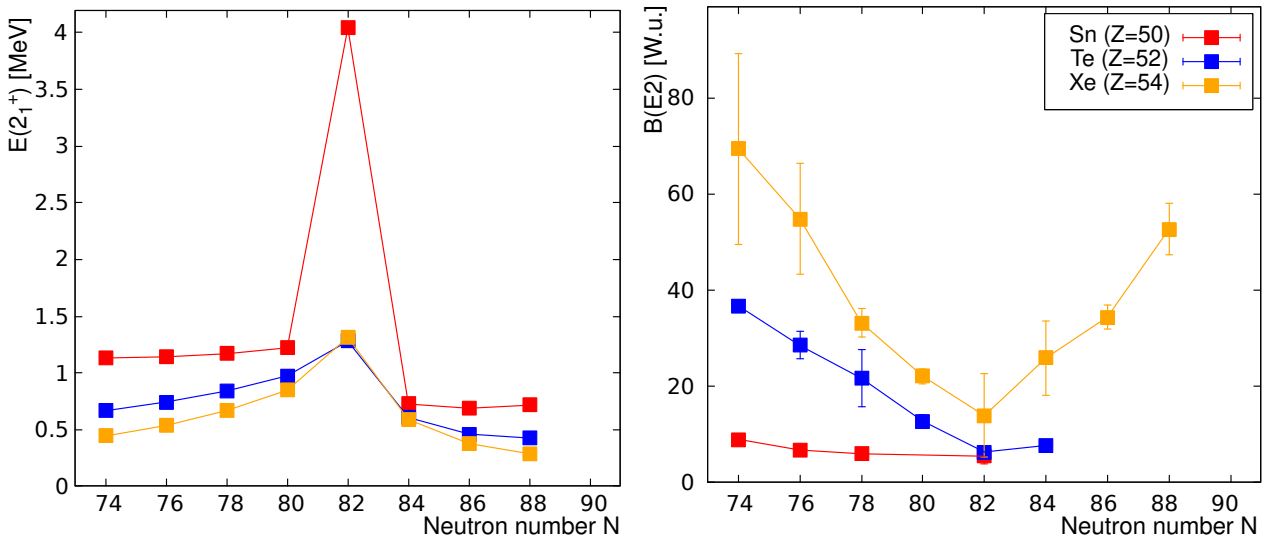

Figure 1.5: Evolution of collectivity for nuclei between $50 \leq Z \leq 54$ and $74 \leq N \leq 90$ expressed in terms of (a) $E(2_1^+)$ excitation energy and (b) $B(E2) = B(E2; 2_1^+ \rightarrow 0_1^+)$ transition strength. Data taken from Ref. [39] and from Ref. [40] for ^{126}Sn.

closure. For spherical magic nuclei, a $R_{4/2}$ ratio much lower than 2 is expected which is the case for ^{132}Sn with $R_{4/2} = 1.1$ [41]. In a similar way, the $B(E2; 2_1^+ \rightarrow 0_1^+)$ strength is lowest at $N = 82$, see Fig. 1.5(b). Thus, the development of collectivity can be traced by looking at these experimentally accessible quantities and is one of the major goals of this work.

While the behavior of proton and neutron shells is well understood for nuclei near the valley of stability, they tend to behave differently for exotic nuclei and may form new magic numbers [43]. The evolution of nuclear shells for exotic systems has been understood through extensive theoretical studies by Otsuka and colleagues and a recent review can be found in Ref. [44] and references therein. The effect that single-particle energies shift when different orbits are occupied by protons and neutrons is due to the monopole effect of the tensor force and an analytic expression is given in Ref. [45]. The monopole component of an interaction V can be computed from its diagonal matrix elements [46].

The single-particle energies corrected for the monopole shift according to the occupation of orbitals are called effective single-particle energies (ESPE) [47]. An example for such a shift as a function of neutron or proton number is shown for $Z > 50, N > 82$ in Fig. 1.6 calculated using a $V_{low\text{-}k}$ realistic interaction provided in Ref. [42]. The calculations are performed for one-valence proton ($Z = 51$) and neutron ($N = 83$) nuclei. In this example, a lowering of all single-particle energies can be observed when pairs of nucleons are added. However, the decrease is not the same for all levels, leading to a variation of single-particle gaps and, consequently, single-particle spectra that differ substantially from the one valence nuclei. Another important key ingredient

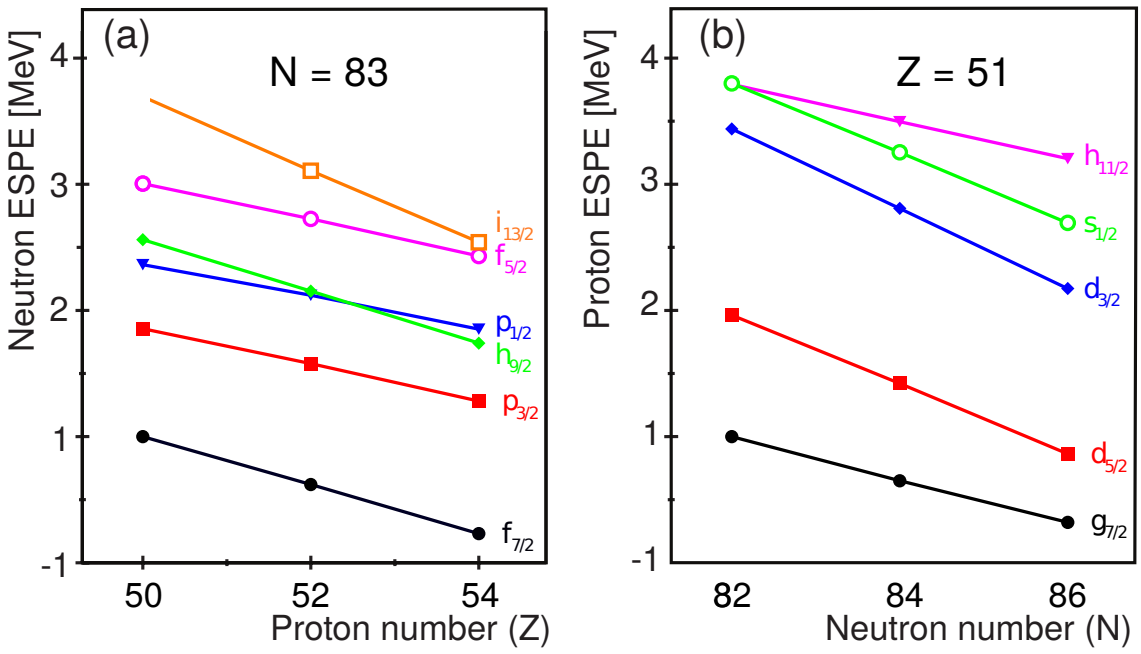

Figure 1.6: Example of the evolution of single-particle energies beyond ^{132}Sn for (a) neutrons and (b) protons as expected from theoretical calculations given in Ref. [42]. Figure taken and adapted from Ref. [42].

in understanding the evolution of shells far off stability is the tensor force. This force is, on average, attractive between $j_<$ and $j'_>$ and repulsive between $j_>$ and $j'_>$ for two nucleons in orbits j and j'. The subscript $<$ or $>$ defines the relation between the orbital angular momentum l and the spin j, i.e., $j_> = l + 1/2$ and $j_< = l - 1/2$. This effect manifests itself in a high sensitivity of evolution of states with increasing N to the proton shell occupation, for example in ^{139}Sb which shows an indication for the $\pi\,(d_{5/2}) - \pi\,(g_{7/2})$ orbital inversion, resulting in a long-lived isomer in ^{140}Sb [48]. Hence, investigating states with single-particle character above $Z = 50, N = 82$ is of major importance for the understanding and mapping of the shell evolution beyond ^{132}Sn.

The nuclei 'north-west' of ^{132}Sn (i.e., $Z > 50$, $N < 82$) are under investigation since many decades. The relevant neutron shells for $N < 82$ are indicated in the schematic in Fig. 1.4. The active valence space contains the major single-particle orbitals $0g_{7/2}, 1d_{5/2}, 2s_{1/2}, 1d_{3/2}$ and $0h_{11/2}$ for both, protons and neutrons. The unique parity $0h_{11/2}$ neutron hole orbital lies close to the Fermi surface and leads to high-spin seniority isomers below ^{132}Sn see, for example, Refs. [49, 50, 51]. The existence of these seniority isomers extends down to the middle of the neutron shell for the semimagic tin isotopes but vanishes rather quickly for the higher Z nuclei.

The objective of this thesis is to contribute and extend the knowledge of nuclear structure around the doubly magic ^{132}Sn through state-of-the-art experiments and improving the theoretical description of nuclei in this region. Two experiments at different facilities and with different goals were performed in the scope of this work

which yield complementary information. In chapter 2, an experiment is presented that was performed to determine lifetimes of excited states in the sub-ns/ns range using a hybrid array of fast scintillation detectors and high-purity germanium (HPGe) detectors. The second experiment is presented in chapter 3 and was conducted to investigate isomeric states and gain insights into the precise configurations of such long-lived states. Both measurements utilized different fission mechanisms and provide crucial insights from a nuclear reaction point-of-view. Each chapter starts with a motivation before explaining the experimental details and data analysis procedures. Results will be presented and compared to theoretical calculations. A summary of both experiments and a conclusion of the importance of this work for the understanding of the nuclear structure around $^{132}\mathrm{Sn}$ will be given in chapter 4.

Chapter 2

Lifetime measurements beyond ^{132}Sn with the ν-ball array

During 2017 and 2018, the ν-ball campaign took place at the ALTO facility of the IJCLab in Orsay, France. The experiments presented and analyzed in the following chapter, N-SI-109 and N-SI-103, were dedicated to the spectroscopy of neutron-induced reactions with fast neutrons. This was achieved by coupling the ν-ball array to the LICORNE [52] neutron source which provides fast neutrons via the inverse p(^{7}Li,n)^{7}Be reaction. One of the goals of this experiment is the determination of lifetimes and the spectroscopy of neutron-rich isotopes in the $A \sim 140$ mass region beyond the $N = 82$ shell closure. The chapter starts with a short motivation of this study followed by a description of the experimental setup. The data analysis and the experimental techniques will be described in detail. Finally, the results will be presented and discussed within theoretical frameworks.

2.1 Motivation of the experiment

The study of fission fragments has been of long-standing interest in nuclear structure physics due to the large neutron excess of the fission products. With the advancement of new generation large volume HPGe arrays such as Gammasphere [53] or Eurogam [54], a lot of spectroscopic information on neutron-rich nuclei has been gained using spontaneous fission sources such as ^{252}Cf or ^{248}Cm. Thermal neutron-induced fission can be studied extensively at, for example, the Institute Laue-Langevin in Grenoble, France; a hybrid spectrometer to study the prompt γ-ray emission of products after neutron-induced fission was first employed in the EXILL&FATIMA campaign [55]. Recently, $LaBr_3$(Ce) detectors were coupled to the high-performance Gammas-

phere array to measure sub-ns lifetimes of excited states from fission fragments [56, 57]. Because of the fission targets, certain regions on the nuclear chart were not accessible during these experiments. These limitations are visualized in Fig. 2.1, where the average N/Z ratio of fission fragments is plotted for different fission targets. The average N/Z ratio is around 1.54 for thermal neutron-induced fission on $^{235}\mathrm{U}$ and $^{241}\mathrm{Pu}$ which was studied in the EXILL campaign [27]. The spontaneous fission sources end up with fission fragments that have $N/Z \approx 1.3$ and $N/Z \approx 1.5$ for $^{252}\mathrm{Cf}$ and $^{248}\mathrm{Cm}$, respectively. At energies provided by the fast neutrons from the LICORNE neutron source, $^{238}\mathrm{U}$ and $^{232}\mathrm{Th}$ are fissile. This provides the possibility to produce more exotic, neutron-rich nuclei due to the higher average N/Z of the fission fragments around 1.57. Additionally, the investigation of the fast neutron-induced fission is of major interest in nuclear energy and reactor research [58, 59].

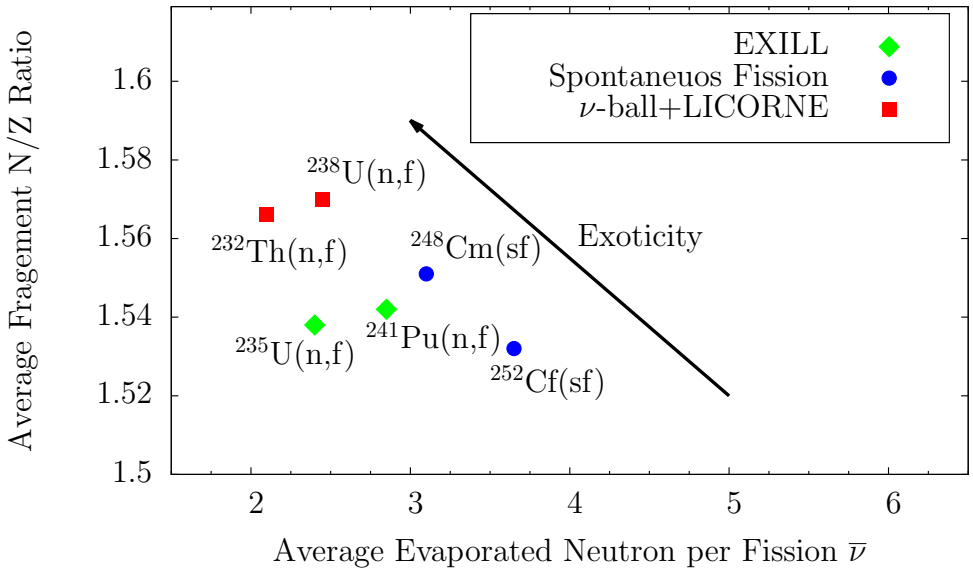

Figure 2.1: Average N/Z ratio of the fission fragments for different fission targets. Figure adapted from the proposal of N-SI-109.

The nuclei of interest in this experiment are the neutron-rich isotopes beyond the doubly magic nucleus $^{132}\mathrm{Sn}$ with a special emphasize on tellurium and iodine isotopes. The examination of nuclei around shell closures plays a key role in our understanding of the nuclear structure. Experimental information on these nuclei helps to improve theoretical models and to develop and test two-body matrix elements, in particular of the proton-neutron residual interaction. By studying neutron-rich nuclei, the evolution of shell structure with large N/Z ratios and the development of collectivity can be investigated.

Having only two valence protons outside the closed $Z = 50$ shell, the tellurium isotopes around $^{132}\mathrm{Sn}$ are expected to have coexisting collective and single-particle excitations, resulting in sub-ns lifetimes that prevail

the vibrational band structure of these isotopes at intermediate and higher spins due to the highly-mixed wave-functions [60, 61, 62]. The increasing fragmentation of wave functions can be seen, for example, in the $\pi\,(0g_{7/2}^2)$ excitations of the tellurium isotopic chain. The pure wave functions of these states in $^{134}\mathrm{Te}$ already show contributions of other orbitals in the 6^+ state of $^{136}\mathrm{Te}$ [60, 61]. Extending these measurements up to $^{138}\mathrm{Te}$ and $^{140}\mathrm{Te}$ was the aim of the experiment which would give valuable information on the orbital evolution beyond $N = 82$.

In addition to the nuclear structure and shell evolution, nuclei around $^{132}\mathrm{Sn}$ have an important role in the astrophysical r-process [63, 64]. The rapid neutron capture process is one of the building blocks of the nucleosynthesis to explain the formation of neutron-rich isotopes heavier than iron. The goal is to model the solar abundances of isotopes which requires the knowledge of nuclear structure properties for nuclei far off the valley of stability. Due to the shell structure of atomic nuclei, the abundance of isotopes in the solar system as a function of mass has several peaks, one of them around $^{132}\mathrm{Sn}$. The experimental data on these nuclei thus provides a direct use for the modeling in nucleosynthesis network calculations.

Table 2.1: Production cross sections for even-even tin and tellurium nuclei with $N \geq 82$. $^{238}\mathrm{U}$ data are taken from Ref. [65] and $^{232}\mathrm{Th}$ data from Ref. [66].

Z	A	Cross section [%]		Z	A	Cross section [%]	
		$^{238}\mathrm{U}$	$^{232}\mathrm{Th}$			$^{238}\mathrm{U}$	$^{232}\mathrm{Th}$
50	132	0.08	1.54	52	134	4.18	3.11
	134	-	0.139		136	3.32	3.44
	136	-	0.000948		138	0.92	0.755
					140	0.09	0.0195

Table 2.1 summarizes the production yields for even-even nuclei in the region of interest deduced from the LICORNE+MINIBALL experiment [65] and Ref. [66]. The cross sections for the odd-mass nuclei are interpolated from that data. Well-populated nuclei like $^{134}\mathrm{Te}$ were studied extensively in the past (see for example Refs. [67, 68]) and can be used as benchmark cases. Recently, lifetime measurements on $^{135,136}\mathrm{I}$ from the EXILL&FATIMA campaign were published in Refs. [69, 70]. The results of these nuclei will be important to test and validate the performance of ν-ball campaign in comparison with other fission campaigns.

2.2 Experimental setup

During the campaign, the ν-ball detector array was located at one of the beam lines of the Orsay 13 MV Tandem accelerator [71]. A schematic diagram of the experimental setup is shown in Fig. 2.2(a). The $^{7}\mathrm{Li}$ beam from the Tandem accelerator is focused onto a hydrogen gas cell to produce neutrons in inverse kinematics. The collimated neutron beam is guided onto the target (either $^{238}\mathrm{U}$ or $^{232}\mathrm{Th}$) to induce fission reactions. The de-excitation of fission products via the emission of γ rays was detected with the ν-ball array [72]. In the following, the production of fast neutrons with the LICORNE neutron source will be described followed by a characterization of the detector array and its data acquisition (DAQ) system.

2.2.1 The LICORNE neutron source

Neutron sources are widely used in nuclear physics and related areas. They can be categorized in four classes [9]: reactor sources, neutrons from spontaneous fission, photo-neutron sources and neutrons produced in nuclear reactions (e.g., $^{9}\mathrm{Be}(^{4}\mathrm{He},\mathrm{n})^{12}\mathrm{C}$). The LICORNE neutron source is part of the last type and emits neutrons through inverse kinematics, i.e., with a heavy ion projectile bombarding a light target [52]. As mentioned earlier, a $^{7}\mathrm{Li}$ beam provided by the 13 MV Tandem accelerator is used to produce neutrons via the $\mathrm{p}(^{7}\mathrm{Li},\mathrm{n})^{7}\mathrm{Be}$ reaction. The advantage of using a nuclear reaction is the focused, quasi-mono-energetic neutron beam which is important to study properties of nuclear fission. The natural collimation of the neutrons is achieved by choosing a heavy projectile instead of more conventional projectiles as deuterons or protons. This enhances the effective neutron flux by up to two orders of magnitude [52]. Additional focus is achieved through guidance via a lead collimator which produces a narrow neutron cone.

The $\mathrm{p}(^{7}\mathrm{Li},\mathrm{n})^{7}\mathrm{Be}$ reaction in direct kinematics has different reaction channels with various threshold energies competing with each other, if the beam energy is high enough. The energy range for the primary beam where the outgoing neutrons can easily be predicted is between 13.098 and 16.513 MeV. This beam energy results in a neutron energy between 1 and 4 MeV. Figure 2.3 shows the prediction of kinematic curves in the laboratory frame calculated in a relativistic two-body calculation. Two distinct energy peaks arise from forward and backward emission of neutrons in the center of mass frame. Due to the finite beam spot size ($\sim$ 0.8 cm) and energy straggling of $^{7}\mathrm{Li}$ in the target, deviations from the calculation are experimentally observed.

In designing the LICORNE neutron source, two solid targets were considered [52]. The first choice was polypropylene which has a large hydrogen density and the second choice was a covalent titanium hydride (TiH_2) target. The target thickness has to be optimized according to energy loss (low thickness) and reaction rate (large

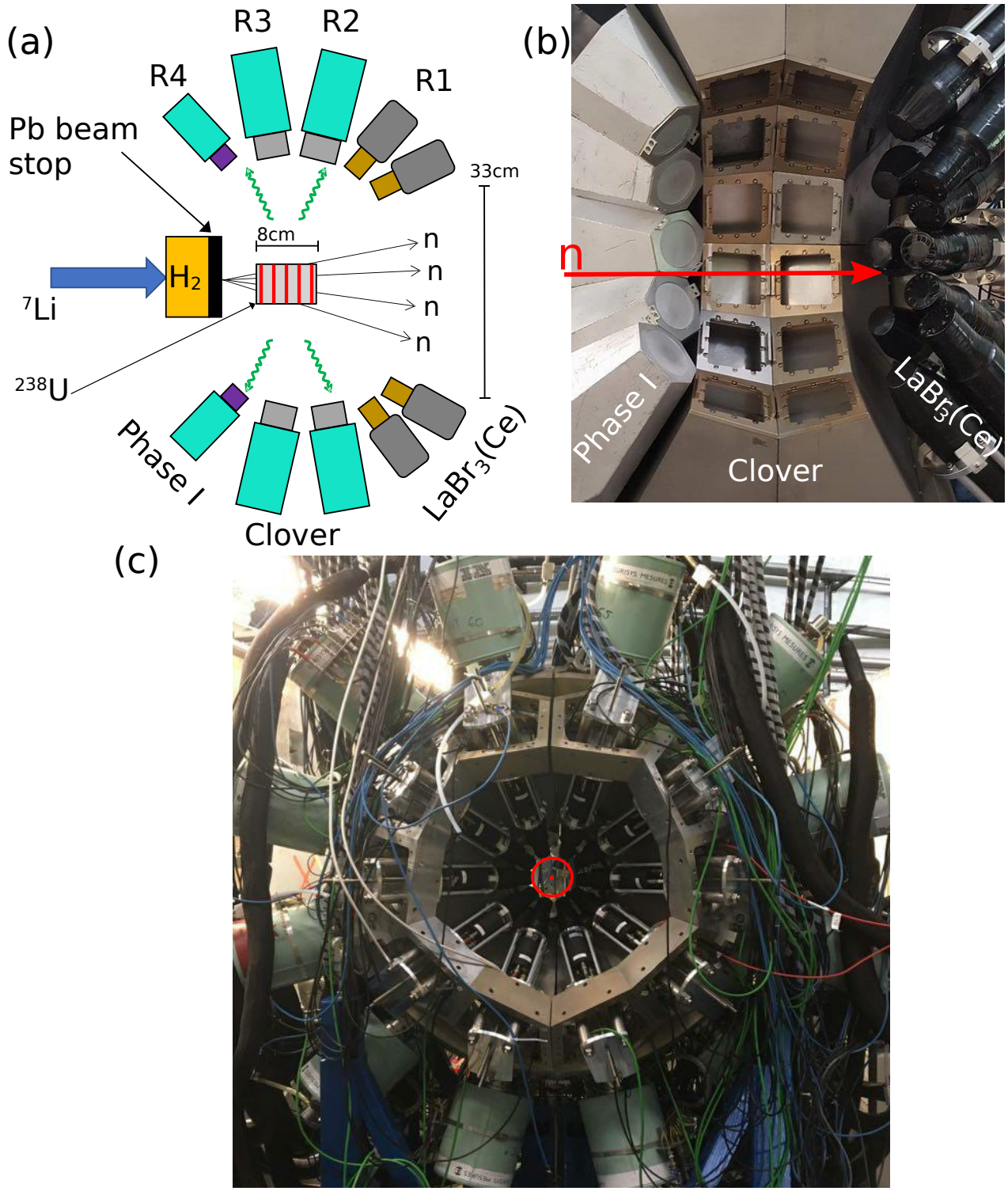

Figure 2.2: (a) Schematic overview of the experimental setup coupling the ν-ball array to the LICORNE neutron source. The $^{7}\mathrm{Li}$ beam is coming from the Tandem accelerator and the neutrons are hitting the $^{238}\mathrm{U}$ target (red) which is surrounded by the detectors from the ν-ball array. (b) Photograph of the inside of one hemisphere of the ν-ball array showing the ring structure of the detectors. (c) Picture of the ν-ball array from the back. The beam comes out of the page and the target is positioned at the center (red circle).

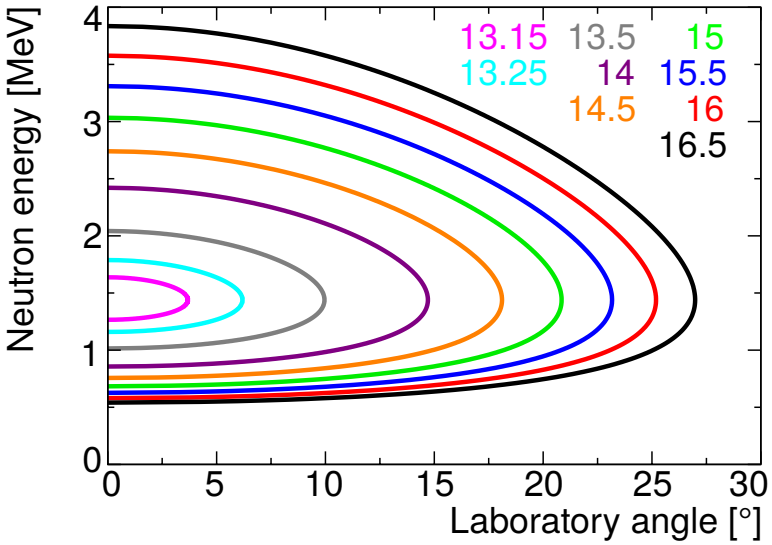

Figure 2.3: Neutron energy as a function of emission angle in the laboratory frame for different $^{7}\mathrm{Li}$ bombarding energies calculated using two-body relativistic kinematics. The energies are given in MeV. Taken from Ref. [73].

thickness). The hydrogen cell is cylindrical in shape and kept under high pressure to avoid contamination from air molecules leaking into the cell via diffusion. In order to provide a pressure barrier towards the beam line, which is kept in vacuum, a thin tantalum foil of a few μm is placed at the front of the cell.

With a beam intensity of 10^{11} pps approximately 10^{7} neutrons/s can cause 10^{5} fissions per second. The cross section for fission induced by fast neutrons is several orders of magnitude lower as for thermal neutrons. Therefore, the detectors should be moved as close to the target as possible. The necessity for shielding the detectors from bombarding neutrons is reduced by having a directional neutron source. To detect neutrons, a cylindrical EDEN detector module [74] filled with NE213 liquid scintillator was placed 3 m behind the target. Neutrons can be identified by using both time-of-flight and n/γ pulse shape discrimination [75].

2.2.2 The ν-ball array

The ν-ball array is a hybrid spectrometer consisting of HPGe and $LaBr_3$(Ce) scintillation detectors and pictures are shown in Figs. 2.2(b,c). This combination of detectors allows for high-resolution and high-efficiency γ-ray spectroscopy as well as lifetime measurements employing the fast-timing technique [76]. The detectors are aligned in four rings around the target position as can be seen in Fig. 2.2(b). Two types of HPGe detectors are used, namely Clover type and coaxial type detectors. Additionally, bismuth germanate (BGO) shields are used for Compton suppression (CS) to improve the peak-to-total ratio. In total, the following detectors were used:

- 20 $LaBr_3$(Ce) scintillators aligned in two sub-rings of 10 cylindrically shaped followed by 10 conical crystals placed around 40°. All detectors are connected to R9779 Hamamatsu photo-multiplier tubes (PMTs) without passive shielding against cross-talk. These make up ring 1 (20 channels).
- 24 HPGe Clover detector, each with two BGO channels and four germanium channels (144 channels). These form rings 2 and 3 placed around 90°.
- Ten EUROGAM Phase I coaxial HPGe detectors surrounded by ten BGO Compton shields placed in ring 4 at a backward angle of 133.5° (20 channels).
- EDEN neutron detector for monitoring the neutron flux (3 channels).

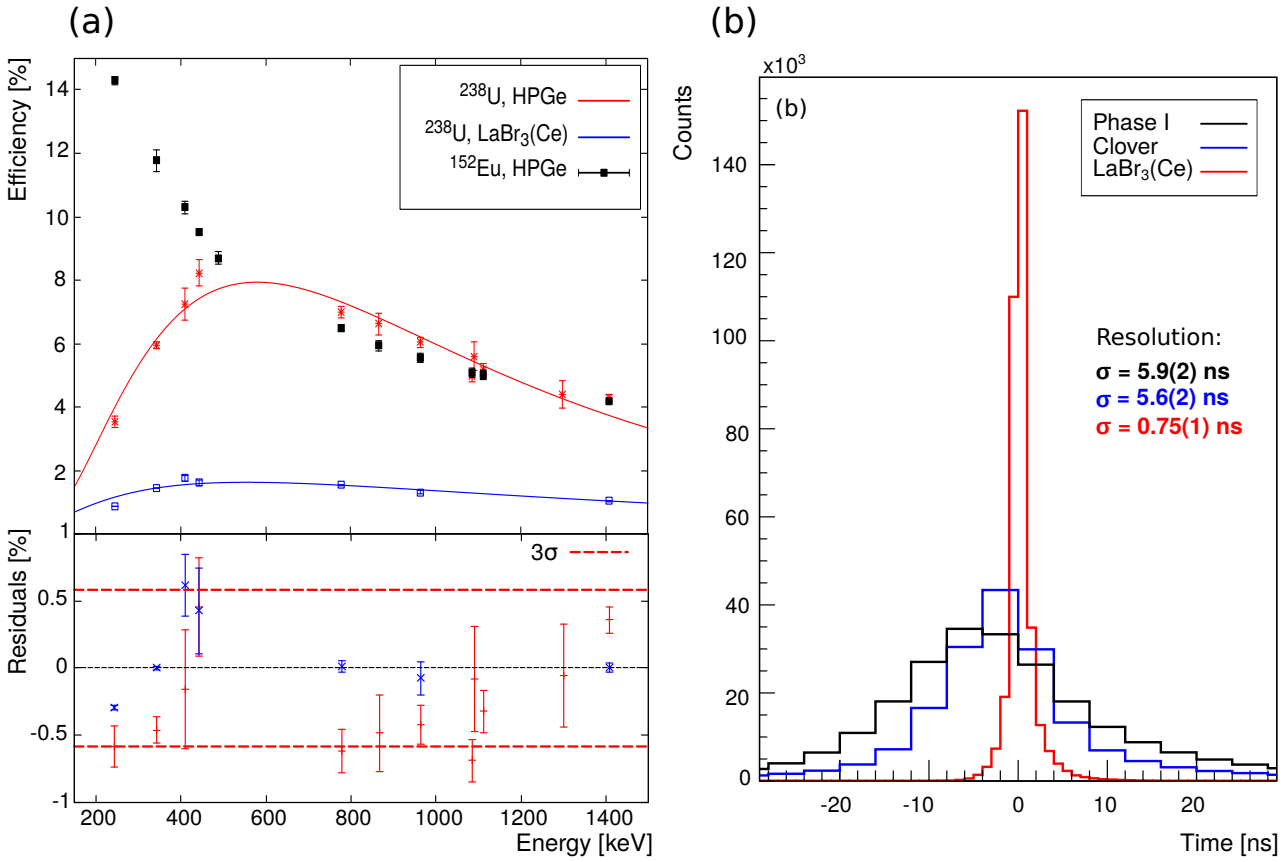

Figure 2.4: (a) Full-energy peak efficiency of the ν-ball HPGe (red) and $LaBr_3$(Ce) (blue) detectors with the ^{238}U target. ^{152}Eu source measurement data (black) are also shown for comparison. The bottom panel shows the fit residuals. (b) Time spectrum showing the time difference ΔT measured with a ^{60}Co source and the $LaBr_3$(Ce) and different HPGe detectors.

The energy resolution, measured as full-width at half maximum (FWHM) with a ^{60}Co source, amounts to 2.5 keV for all summed HPGe and 32 keV for all summed $LaBr_3$(Ce) detectors at 1.3 MeV. The time resolution

is determined by measuring the time difference of both transitions in $^{60}\mathrm{Ni}$ from the decay of $^{60}\mathrm{Co}$ (1173 and 1332 keV, respectively). The intrinsic time resolution for the $LaBr_3$(Ce) scintillators amounts to about 500 ps FWHM and is far superior to the resolution measured with HPGe detectors (in the order of 15-20 ns effective resolution for the sum of detectors in this setup) [72]. Time resolution spectra for arbitrary single detector crystals are shown in Fig. 2.4(b). The $LaBr_3$(Ce) time difference spectrum is far narrower compared to the HPGe time spectra. Note that numbers given in Fig. 2.4(b) are slightly higher compared to the quoted numbers because no energy gate was applied. It can also be seen that the Clover type HPGe crystals have a slightly better time resolution under these conditions compared to the coaxial type HPGe detectors.

The detection efficiency of the HPGe and $LaBr_3$(Ce) detectors from the ν-ball array was measured using a standard $^{152}\mathrm{Eu}$ source and the measurement is shown as black points in Fig. 2.4(a). Due to the thick actinide targets, effects such as self-absorption can strongly influence the absolute γ-ray efficiency, especially at low energies. A GEANT4 simulation [77] of a point-like $^{152}\mathrm{Eu}$ source encapsulated in the respective target is performed to obtain a relative measure for the self-absorption effects. These simulated intensities are scaled to match the intensity of the source measurement at energies above 600 keV where absorption inside the target is negligible. The curve for the first N-SI-109 measurement is shown in Fig. 2.4(a) and was fitted with an empirical function [78]. The efficiency peaks at about 400-500 keV and amounts to 4.1(2) % at 1.3 MeV for the HPGe detectors and 0.7(1) % at 1.3 MeV for the $LaBr_3$(Ce) detectors. While the data points at higher energies are comparable to the measured values from the $^{152}\mathrm{Eu}$ data, the efficiency drops rapidly at energies below 400 keV compared to the source measurement. In addition, the fit residuals are presented and the 3σ range is indicated as an error estimation which amounts to 0.6% relative uncertainty. For the N-SI-103 ^{238}U(n,f) experiment, the same target and therefore the same procedure is used to determine the absolute γ-ray efficiency. From calibration data, a value of 3.2 % at 1.4 MeV is obtained. For the $^{252}\mathrm{Cf}$ source measurement, the values directly obtained from the $^{152}\mathrm{Eu}$ data without scaling to the simulation were used. In the case of the $^{232}\mathrm{Th}$ experiment, the absolute γ-ray efficiency was determined from the intrinsic activity of the target itself and, thus, the self-absorption is already included. Details on the $^{232}\mathrm{Th}$ measurement can be found in Ref. [79].

The data were read out using the digital acquisition system FASTER (Fast Acquisition SysTem for nuclEar Research) which was developed at LPC Caen, France [80]. Two different types of digitizers were used: 125 MHz, 14-bit analog-to-digital converters (ADCs) for the HPGe and the BGO detectors and 500 MHz, 12-bit quad digital channel time-to-digital converters (QDC-TDC) for the $LaBr_3$(Ce) scintillators. For the present experiments, the data were taken in a timestamped triggerless mode, i.e., the signals are recorded each time any detector fired. Combined with the large number ($\approx$ 200) of electronic channels, this leads to a massive data rate in the order

of tens of MB per second which had to be handled during and after the experiment. Timing signals for HPGe and BGO detectors are measured with leading-edge triggering whereas a constant-fraction triggering was used for the $LaBr_3$(Ce) scintillators. Furthermore, the acquisition utilizes an internal pulse-shape analysis algorithm to achieve an even more precise timing measurement from the $LaBr_3$(Ce) signals down to 7.8 ps per channel in the digitizers [80].

2.2.3 Experimental details

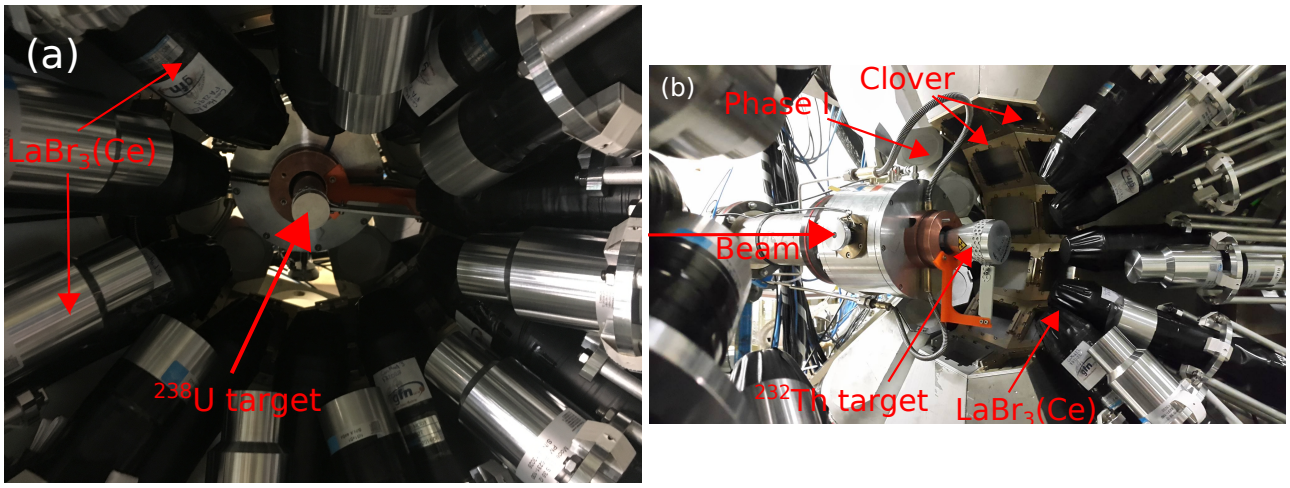

Figure 2.5: Picture of the targets used during the N-SI-109 experiment. (a) ^{238}U and (b) ^{232}Th target mounted inside the array. Different detectors are labeled accordingly.

Table 2.2: Overview of experimental details of the ν-ball fission experiments.

Experiment	Target	m_{Target} [g]	E_{Li} [MeV]	E_{Neutron} [MeV]	I_{av} [enA]	Raw data [Tb]	N_{Fissions}
N-SI-109	^{238}U	81	16.4	1.7	20	12.5	7.2×10^9
N-SI-103	^{238}U	81	18.5	3.4	80	25	6.8×10^9
N-SI-109	^{232}Th	106	16.75	1.7	100	88	4.2×10^{10}

The experiment N-SI-109 was divided into two parts which took place in February and April 2018. In total, five weeks (two weeks with ^{238}U and three weeks with ^{232}Th target) of beam time were dedicated to the study of fast neutron-induced fission. Furthermore, six days of measurement for the experiment N-SI-103 resulted in additional data for the study of fission fragments [81]. Table 2.2 gives a summary of basic information concerning the different experiments. Pictures of the targets mounted inside the array can be seen in Fig. 2.5. The fissile material was arranged in thin disks over a distance of 8-10 cm to allow low energy γ rays to escape the target. In the following, more details on the realization of experiment N-SI-109 will be provided.

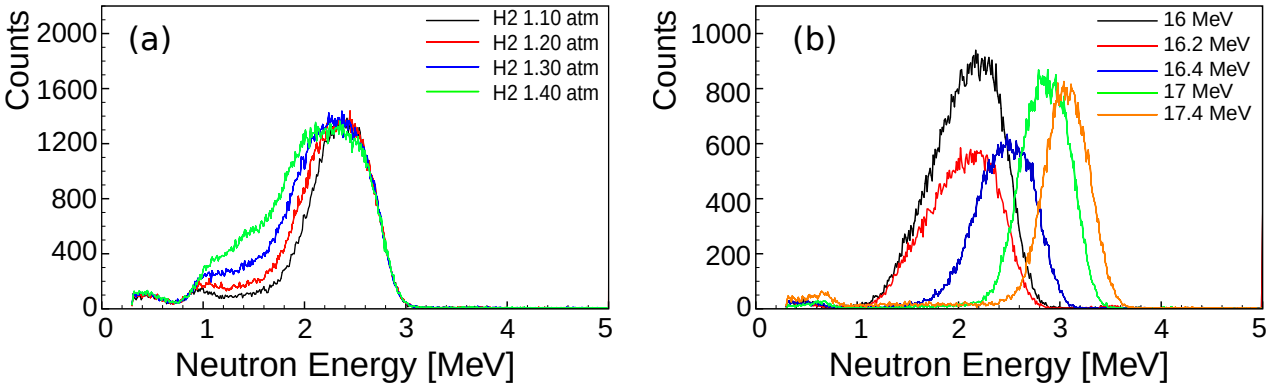

Figure 2.6: Neutron energy spectra for different (a) pressure values in the hydrogen cell and (b) different $^{7}\mathrm{Li}$ primary beam energies. Data from recorded during the online beam tuning and taken from the e-log.

One important experimental task was the tuning of the LICORNE neutron source to be optimized for the reaction cross sections and fission yields. Figure 2.6 shows neutron energy spectra as a function of (a) gas cell pressure and (b) beam energy. In Fig. 2.6(a), a dip around 1.7 MeV can be seen that increases with increasing pressure. This value is limited at 1.5 atm for all experiments because the thin (few tens of μm) tantalum foil which is located at the entrance of the hydrogen gas chamber breaks. Figure 2.6(b) illustrates the tuning of neutron energy by choosing different primary beam energies. These spectra were obtained with a gas cell pressure of 1.1 atm. The final parameters for the first $^{238}\mathrm{U}$ run were 16.4 MeV beam energy with a cell pressure of 1.45 atm such that the tantalum foil can withstand the pressure. Due to the energy loss in the cell, the $^{7}\mathrm{Li}$ beam enters the cell at 14.6 MeV resulting in an opening angle for the neutron cone of 18.7° (see Fig. 2.3). Despite the same behavior of the neutron energy in the $^{232}\mathrm{Th}$ experiment, the beam energy was chosen to be 16.75 MeV due to the higher fission cross section. In all experiments, a pulsed $^{7}\mathrm{Li}$ beam with a 2.5 MHz pulsation and a pulse width of 2 ns was used.

During the experiment, technical problems led to losses of detector channels, resulting in a reduced γ-ray detection efficiency. Furthermore, neutrons hitting the HPGe detectors cause a change in the charge collection properties within the crystal. As a result, the detector performance is reduced and the energy resolution is deteriorated, see Fig. 2.7. The average rate of the HPGe detectors were in the order of 5-7 kHz. In Fig. 2.7, the energy resolution given as FWHM is plotted against the square root of the energy for each HPGe crystal type. Two clear conclusions can be drawn from this. Firstly, the performance of the Clover type detectors is generally superior with respect to the coaxial type Phase I detectors. The energy resolution of the Clover detectors is about 0.3-0.5 keV better with respect to the Phase I detectors. Secondly, the resolution of HPGe detectors at the end of the experiment is worse. For γ rays at an energy of 1.3 MeV, the resolution increases from about

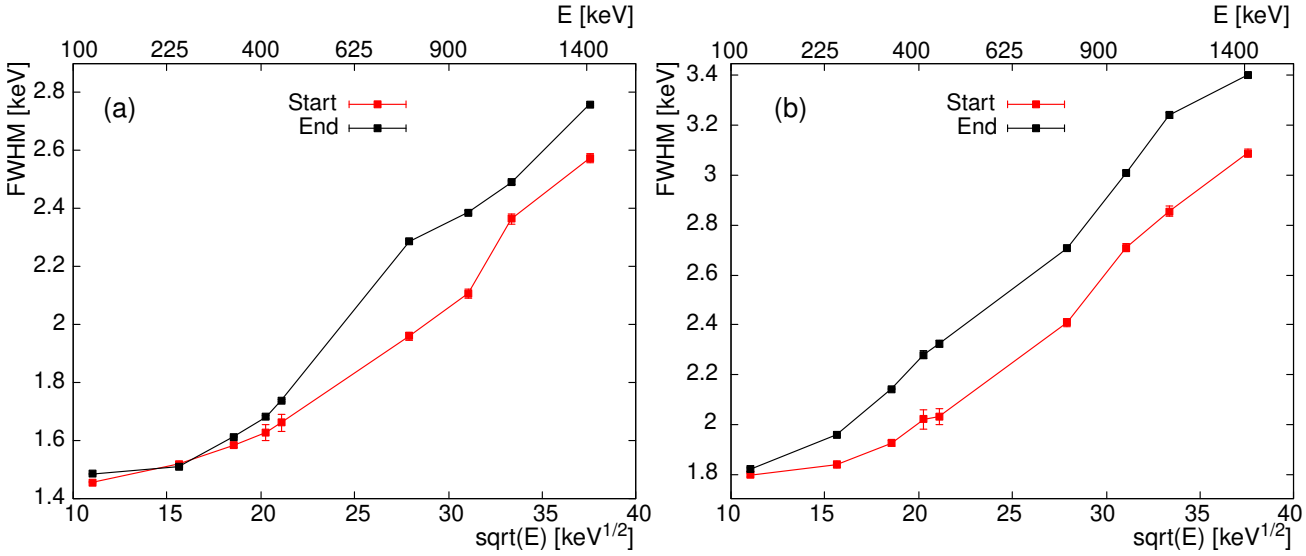

Figure 2.7: Energy resolution of the ν-ball HPGe detectors, plotted as a function of FWHM vs. $\sqrt{(E)}$ for a single (a) Clover crystal and (b) Phase I coaxial detector at the start of the experiment (red) and end of the experiment (black). The drawn line are to guide the eye and the uncertainties are mostly too small to be seen in this scale.

2.4 keV to 2.6 keV for the Clover (see Fig. 2.7(a)) and from 2.9 keV to 3.3 keV for the coaxial detectors (see Fig. 2.7(b)).

2.3 Data analysis

Figure 2.8 shows a simplified flow chart with the different stages of the raw data treatment. Each step compresses the data significantly and the compression factors are indicated in Fig. 2.8.

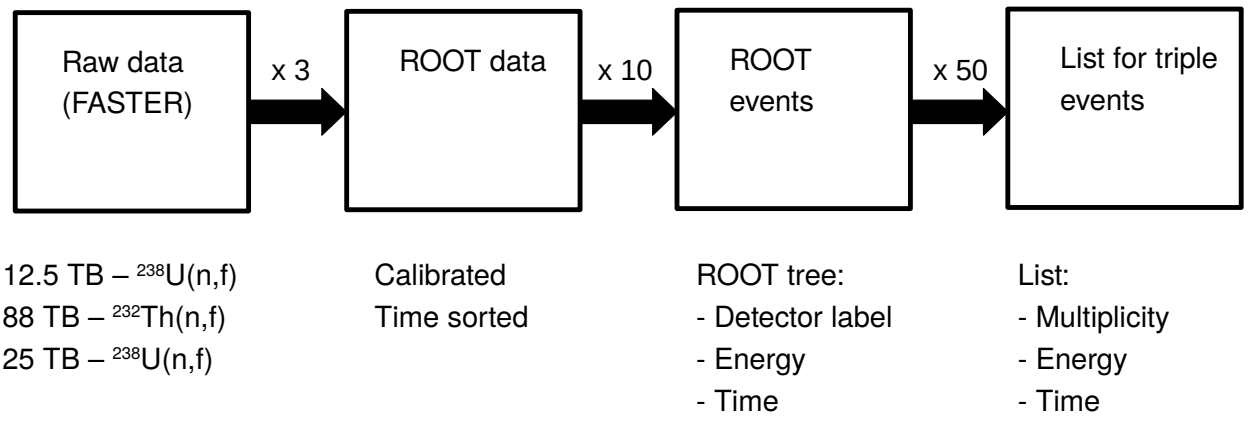

Figure 2.8: Flow chart of the different stages to treat the data. Each arrow is labeled with the respective data compression factor.

The analysis was performed using the program ROOT [82] which is a C++ based framework developed at CERN for nuclear and particle physics application. In the first step the FASTER raw data is converted into ROOT files. This conversion compresses the data by about a factor of 3-4. Subsequently, the triggerless ROOT files have to be further sorted and events built by implementing a trigger condition, e.g., when two HPGe detectors or two $LaBr_3$(Ce) detectors acquire a signal. The third step reduces the amount of usable data by approximately an order of magnitude. For the ^{238}U(n,f) experiment N-SI-109, 4×10^9 triple coincidence events were estimated. Over the whole experiment which covered seven weeks of beam time, a total of 125 TB raw data were acquired. The number of fission events estimated in each data set can be found in the last column of Tab. 2.2. In this work, steps 2-4 were accomplished for the ^{238}U(n,f) experiment while the transformation of the FASTER raw data were done by members of the collaboration during the campaign.

2.3.1 Calibrations

An energy calibration of HPGe and $LaBr_3$(Ce) detectors was performed using a ^{152}Eu source and peaks from the intrinsic activity of the targets. Over the course of the experiment, a gain drift - especially in the $LaBr_3$(Ce) scintillators - is observed. In order to correct this shift and to obtain the best possible energy resolution, a correction has to be applied. This is done using the approach from the code SOCOv2 [83]. The basic idea is to take

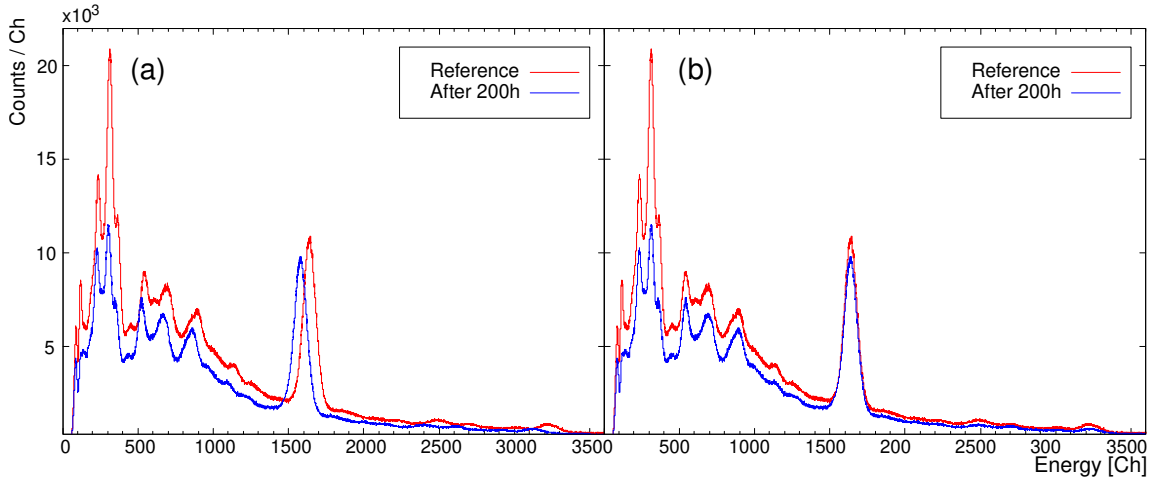

Figure 2.9: Example illustrating the effect of the gain shift correction for a $LaBr_3$(Ce) detector. (a) before applying the correction (b) after applying the correction. The spectra are taken at the beginning of the experiment (Reference) and at the end (After 200 h).

the numerical derivative of the raw singles spectra and identify peaks by the zero-crossings in the differential. The differentiated spectra exhibit a high level of noise which makes it impossible to reliably determine the peak positions based on this approach. Therefore, the spectra are first smoothed by a triangular weight function. Then, the automatic peak finder from SOCOv2 can be applied in order to track the positions of individual peaks. For more details the reader is referred to Ref. [83]. After successfully tracking the peaks, correction coefficients $\{a_i\}$ are obtained by numerical regression (either linear for HPGe or quadratic for $LaBr_3$(Ce)) and stored for each run. The corrected energy E_{corr} is then obtained by applying the coefficients to the calibrated spectra, i.e.:

$$E_{corr} = \sum_i a_i E^i. \tag{2.1}$$

An example of such a correction applied to the energy spectra is shown in Fig. 2.9 for an uncalibrated $LaBr_3$(Ce) spectrum. Before the correction (Fig. 2.9(a)), a clear shift is visible after approximately 200 h of measurement time with respect to a reference time. After applying Eq. (2.1), the corrected spectrum in Fig. 2.9(b) is properly aligned with its reference spectrum. This correction is applied for every run which lasts approximately 1 h each. The overall $LaBr_3$(Ce) energy resolution for a sum of all detectors is improved by almost 50 % at about 500 keV.

Moreover, the detectors have to be aligned in time in order to properly correlate events and construct coincidences. The time calibration is done using the prompt peaks from a ^{60}Co source. Absolute time offset values are determined for each channel relative to the beam pulse (channel 251). The time differences before and after

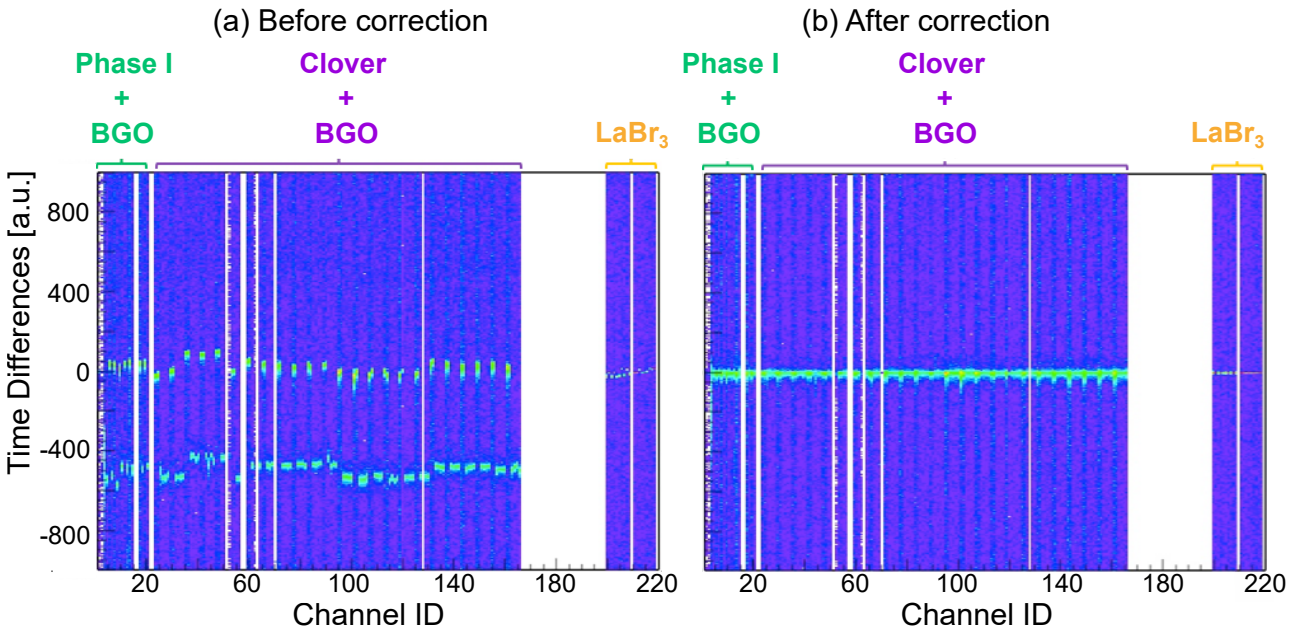

Figure 2.10: Time alignment illustrated by showing the time difference (a) before and (b) after applying the time offsets. Adapted from Ref. [72].

applying the correction is presented in Fig. 2.10. Note the superior time resolution of the $LaBr_3$(Ce) detectors shown by the smaller width around $t = 0$ compared to the HPGe and BGO detectors. After aligning all the detectors to a reference detector, a run-by-run adjustment of a chosen detector to the beam as reference value is performed.

Furthermore, a correction for the time walk has to be applied for the HPGe detectors. The time walk describes the energy dependence of the zero time response and is corrected via [84, 85]:

$$t_{cor} = t - \left(a_0 + \frac{a_1}{E_\gamma^{a_2}} \right), \tag{2.2}$$

where t_{cor} is the corrected time t and a_{0-2} are parameters obtained from fits to the data in 2D time-energy matrices. This function was chosen to correct the effects of the digitizers and the constant fraction discriminator (CFD) modules attached to the QDCs [72]. An example of the 2D correction applied to the data is shown in Fig. 2.11 before and after applying Eq. (2.2). As can be seen from Fig. 2.11, the walk correction improves the time resolution especially at lower energies. Thus, isomeric lines (expressed as horizontal lines in the energy-time matrix) are better visible.

To increase the detection efficiency alongside the peak-to-background ratio, the addback procedure was applied for the Clover detectors and Compton suppression (CS) for all HPGe detectors using the BGO scintillators.

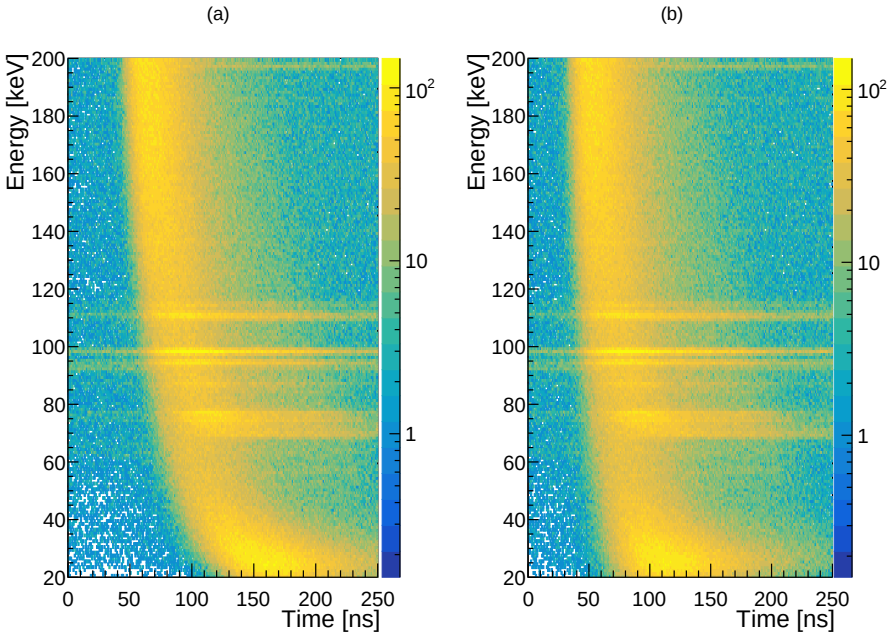

Figure 2.11: Energy versus time matrix of a single Clover HPGe detector (a) before and (b) after applying the walk correction.

If two crystals of the same Clover detector fire within one event, it is likely that both signals originate from the same γ ray and the energies are added up to one single hit. On the other hand, if a HPGe module (either Clover or Phase I) and its respective BGO shield fired within one event, the event is rejected. In the analysis, the labeling notation of HPGe detectors as modules ranging from 1 to 34 is exploited to generalize this procedure independently of the HPGe detector type. After looping over each event, the HPGe (hitGe) and BGO (hitBGO) hit pattern as well as the summed HPGe energy is recorded for each module. If the condition hitGe > 0 and hitBGO $= 0$ is fulfilled, the energy sum is extracted and used in the further analysis. The HPGe data after addback and CS in the following sections will be denoted as clean HPGe.

Figure 2.12(a) shows a HPGe spectrum before and after addback and CS. The reduction of γ rays from the Compton continuum is of the order of three to four while the number of counts in the full energy peaks either remain or increase due to the addback. The right panel of Fig. 2.12 quantifies this by showing the (b) addback factor and (c) the peak-to-background ratio improvement for the energy range of interest up to approximately 3 MeV. The addback factor is defined as ratio of number of counts in a full energy peak after and before applying the addback procedure. The peak-to-background ratio is measured by normalizing the number of counts in a full energy peak with the background underneath that is interpolated from data points around the peak. The improvement R is quantified as ratio of (P/B) with and without applying the addback and CS. The addback

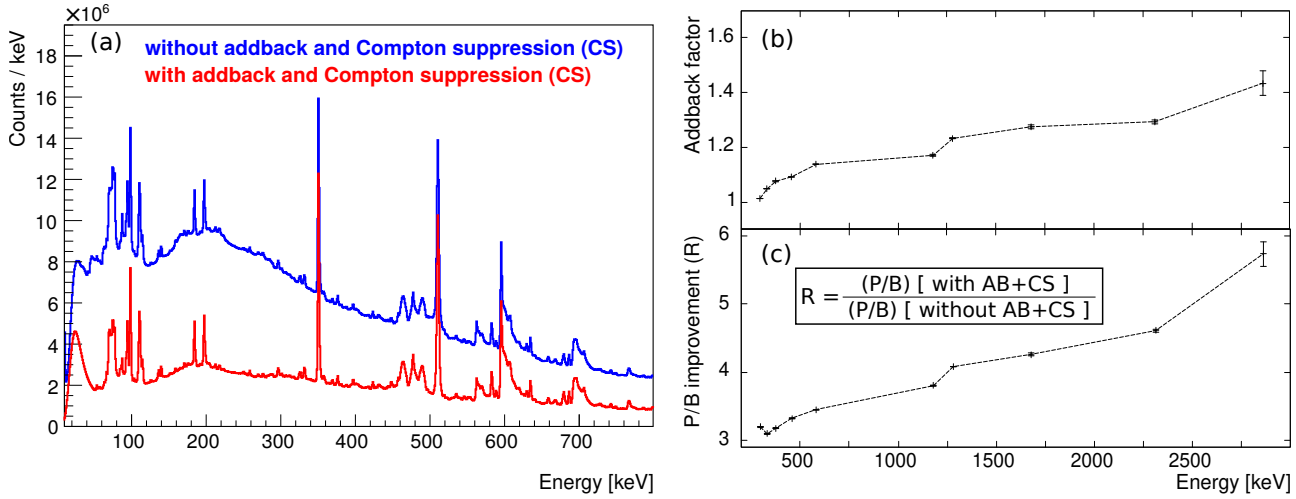

Figure 2.12: (a) HPGe γ-ray spectrum without and with addback and Compton suppression. (b) Addback factor and (c) peak-to-background improvement ratio R as a function of γ-ray energy.

factor is between 1.0 and 1.2 for energies below 1.5 MeV and increases up to 1.4 for a γ-ray energy of about 3 MeV. This is due to the higher probability of scattering and escape peaks with increasing energy. The peak-to-background ratio improves by a factor of three to four for low energies up to almost six for 3 MeV γ rays. The large number of nuclei produced in these types of experiment require the use of addback and CS to improve the peak-to-total ratio in order to identify isotopes from their characteristic γ rays.

2.3.2 Event structure and calorimetry

Event building

The last step in treating the raw data is to build events from the triggerless data. In order to perform γ-ray spectroscopy, an event is constructed if two clean HPGe detectors acquired a signal. For lifetime measurements, it is required to include $LaBr_3$(Ce) detectors in the trigger condition. Besides different trigger conditions, it is important to distinguish fission events from decay events. This is achieved by selecting a high γ-ray hit multiplicity which is characteristic for prompt fission events. Finally, a distinction between prompt events occurring within a single beam pulse and delayed events spanning several beam pulses has to be made.

In order to achieve a clean selection of fission events, a two-step trigger is used. First, a coarse hit multiplicity condition is applied, allowing only events where at least two clean HPGe detectors or two $LaBr_3$(Ce) detectors fired. The prompt time window for the $LaBr_3$(Ce) scintillators ranges from 35 to 50 ns while for the HPGe detectors the full 400 ns pulse is accepted. Further constraints to improve the fission-to-background ratio can

be done via the total γ-ray hit multiplicity. Additionally, delayed γ hits can be used in the case of known isomeric transitions to improve the peak-to-background.

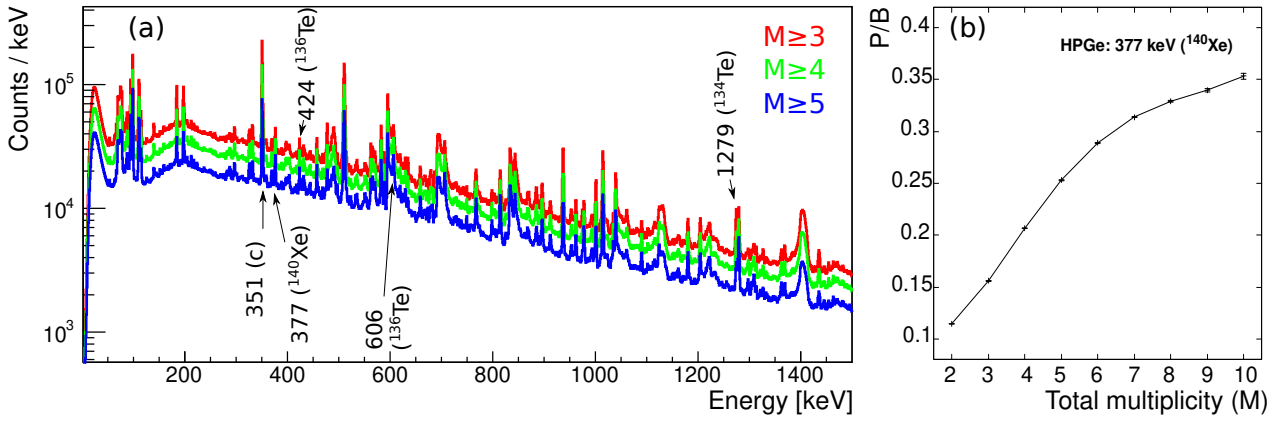

Figure 2.13: (a) HPGe γ-ray spectra as a function of minimum required total multiplicity in the offline analysis. The highlighted peaks belong to ^{21}Ne (351 keV) and ^{140}Xe (377 keV) and are representative for background and fission events, respectively. Other transitions of interest are also labeled with their respective energy. (b) Peak-to-background ratio (P/B) of the 377 keV transition as a function of minimum total multiplicity.

The effect of the total hit multiplicity for the intensity of different transitions is shown in Fig. 2.13(a) where HPGe energy spectra are plotted as a function of minimum total hit multiplicity required in the events. A strong background peak, namely 351 keV from the fusion-evaporation product $^{21}\mathrm{Ne}$, is compared to the 377 keV $2_1^+ \rightarrow 0_1^+$ transition in one of the best produced fission fragments $^{140}\mathrm{Xe}$. The energies are almost the same and, therefore, efficiency and conversion effects are negligible. Furthermore, both transitions are prompt which allows for a sound comparison.

At low hit multiplicities, the background peak dominates the overall spectrum and the peak from the fission fragment is barely visible in the full projection. The relative height of the 377 keV peak compared to the 351 keV background transition increases, with increasing minimum required multiplicity. Around hit multiplicities $M = 6, 7$ this ratio becomes significantly better which shows that high multiplicity events are favorable for selecting the fission reaction. Furthermore, the peak-to-background and peak-to-total ratios of the 377 keV transition increase significantly when only higher hit multiplicities are allowed, see Fig. 2.13(b). Note that the overall statistics is reduced by roughly an order of magnitude every three hit multiplicities and statistics is lost. Thus, the improvement in peak-to-background ratio comes at a price of loss of counts. A minimum total multiplicity condition of $M \geq 3$ is used and for well-populated nuclei $M \geq 5$ has been proven to work well in order to improve the peak-to-background ratio while not losing too much statistics. For example, the peak-to-background ratio of the 1279 keV $2_1^+ \rightarrow 0_1^+$ transition improves from 0.75(1) for $M \geq 3$ to 0.89(1) for $M \geq 5$ while reducing the

statistics by approximately a factor two.

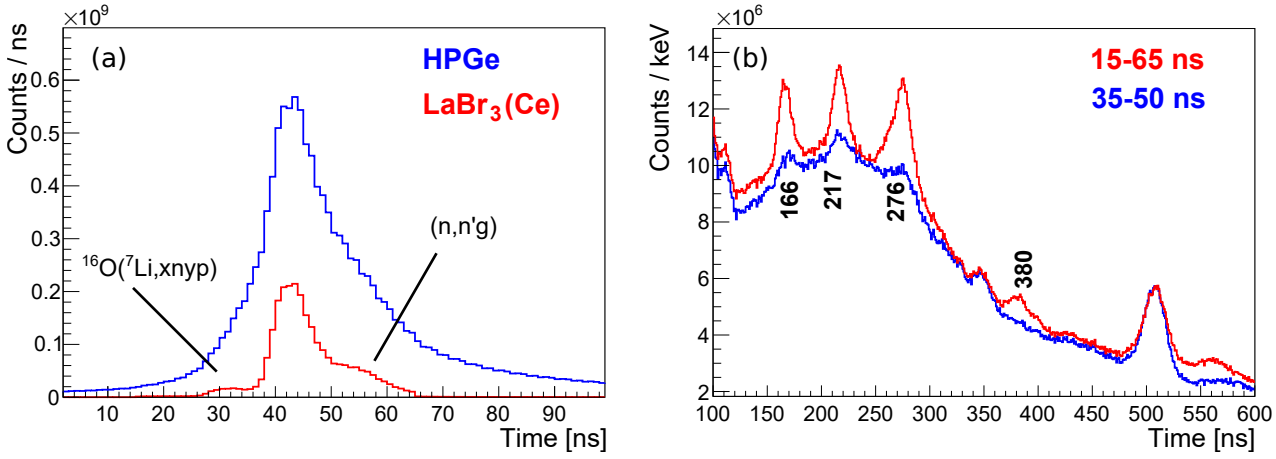

Figure 2.14: (a) Prompt time distribution of all HPGe (blue) and $LaBr_3$(Ce) (red) detectors. (b) $LaBr_3$(Ce) energy projection for different time windows. The labeled transitions belong to contaminants from inelastic neutron scattering or fusion evaporation reactions.

The detector time in a single event with respect to the beam pulse around the prompt peak is shown in Fig. 2.14(a) for HPGe and $LaBr_3$(Ce) detectors. While the time resolution of HPGe detectors is not good enough to resolve different peaks, two additional peaks are visible next to the prompt peak in the $LaBr_3$(Ce) spectrum at $t \approx 43$ ns. The γ rays from fusion-evaporation reactions of the primary beam with surrounding material from the collimator (mainly $^{7}\mathrm{Li}$ on $^{16}\mathrm{O}$) are detected before the prompt fission events because these γ rays are produced at the entrance of the LICORNE gas cell and are immediately detected before the neutrons hit the target. The peak after the prompt position arises from inelastic neutron scattering and the delay corresponds to the time-of-flight from the target to the detectors which is of the order of 10-15 ns. Utilizing the superior time resolution of the $LaBr_3$(Ce) detectors, the background lines can significantly be reduced, as shown in Fig. 2.14(b). The lines at 166, 217 and 276 keV come from inelastic scattering of neutrons on $^{139}\mathrm{La}$, $^{79}\mathrm{Br}$ or $^{81}\mathrm{Br}$, respectively. The bump around 380 keV comes from the fusion-evaporation residues. All of these contaminants can be significantly reduced when restricting the prompt $LaBr_3$(Ce) time window from 35 to 50 ns.

This $LaBr_3$(Ce) time window plays a key role in the number of events involving $LaBr_3$(Ce) coincidences. When optimizing the events for fast-timing measurements, it is essential to improve the number of $LaBr_3$(Ce)-$LaBr_3$(Ce)-HPGe (= L2C1) coincidence events. Different trigger conditions combining clean HPGe ('C') and $LaBr_3$(Ce) ('L') coincidences were investigated with the goal to increase the number of L2C1 coincidence events. Table 2.3 shows the contribution of clean HPGe detector and $LaBr_3$(Ce) scintillator coincidence events to the total trigger as a function of the $LaBr_3$(Ce) trigger window. Before comparing the different windows, it has to

Table 2.3: Trigger types for various $LaBr_3$(Ce) trigger windows. The total number of triggers is given for an arbitrary run. Clean HPGe coincidences are denoted as 'C' and $LaBr_3$(Ce) coincidence events are denoted as 'L'.

	$LaBr_3$(Ce) trigger window		
	35 - 50 ns	15 - 65 ns	15 - 100 ns
Total Triggers	$627.77 \cdot 10^3$	$661.94 \cdot 10^3$	$667.59 \cdot 10^3$
C2 [%]	85.1	80.5	79.9
L2 [%]	1.31	6.26	6.95
C3 [%]	13.1	12.3	12.2
L1C2 [%]	0.36	0.76	0.83
L2C1 [%]	0.012	0.059	0.067

be noted that the majority of events pass through the C2 and C3 trigger which reflects the higher efficiency of the HPGe detectors with respect to the $LaBr_3$(Ce) scintillators. When increasing the $LaBr_3$(Ce) trigger window, the total number of triggers, here shown for an arbitrary run, increases by a factor of 1.05 and 1.06 for the 15-65 ns and 15-100 ns time windows, respectively. A significant increase in $LaBr_3$(Ce) coincidence events by a factor of six for L2 and L2C1 events should be highlighted as these are relevant for fast-timing measurements. This can be explained by looking at the $LaBr_3$(Ce) time structure in Fig. 2.14. Despite the large increase in L2C1 coincidence events, the majority of it stems from background contributions as shown in the right panel of Fig. 2.14 and, thus, the narrow 35-50 ns trigger window was used for prompt $LaBr_3$(Ce) events. However, in order to investigate delayed $LaBr_3$(Ce) spectra above 100 ns, a delayed trigger of 65-400 ns is applied and will be used in a later section.

From the event-built data all events can be read and sorted into histograms depending on certain requirements. Despite all the compression factors, this process takes several hours up to days and is not very practical. Thus, the data is further treated and written into lists that can be sorted in the matter of minutes. This additional step after the event building is depicted in Fig. 2.8. The events are selected from certain trigger conditions such as the ones listed in Tab. 2.3. Time and energy information as well as the multiplicities are stored in a list. To further increase the compression, the lists were written in a binary format. Note that for each type of triple coincidence events a new list has to be generated. This takes about the same time as reading all events but once the list is generated the creation of new histograms can be done in a few minutes.

In summary, the available $LaBr_3$(Ce) events to be used for the fast-timing analysis are rather small (see Tab. 2.3) and events are lost due to the necessity of having narrower trigger windows. Those small time windows are required due to the background events before and after the prompt pulse, see Fig. 2.14(a). Fusion-evaporation reactions occur at the entrance window of the LICORNE neutron source and delayed γ rays from in-

elastic neutron scattering appear 10-15 ns after the prompt fission γ rays. In order to avoid having the $LaBr_3$(Ce) detectors in the neutron cone of the LICORNE source, the detectors had to be moved back, relative to the target. This lead to a drop in $LaBr_3$(Ce) efficiency compared to the expected one, resulting in a strong difference in statistics between HPGe and $LaBr_3$(Ce) detectors. This imbalance reduces the available L2C1 coincidence events for lifetime measurements drastically. The low statistics results in very large error bars as can be seen in Sec. 2.4. Thus, the experimental goal to go to more neutron-rich tellurium isotopes could not be reached.

Calorimetry

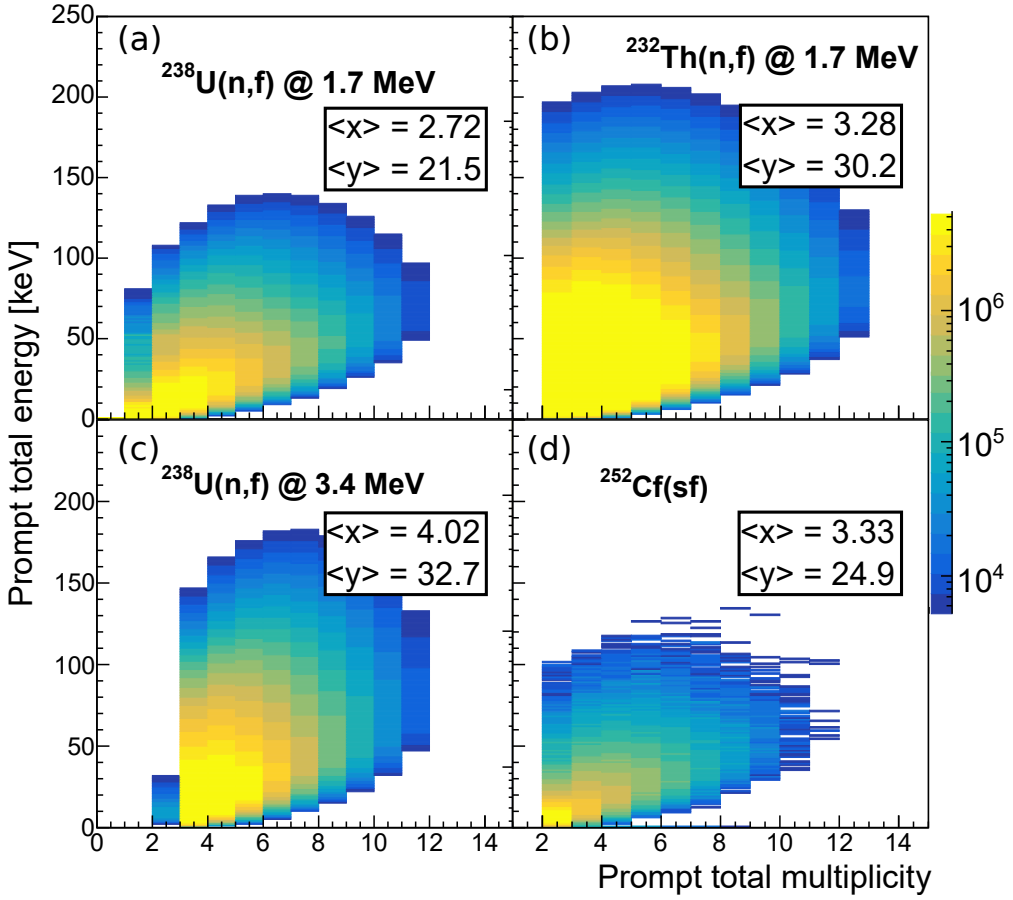

Figure 2.15: HK matrices for different fission reactions recorded with the ν-ball array. Each matrix is normalized to the same number of entries. The average values on x (hit multiplicity) and y (total energy) axes are denoted in each panel. Note that the hit multiplicity does not begin at $M_{tot} = 0$ due to the minimum trigger condition in the event-building process.

The full digitization of the ν-ball array and the capacity to process very high count rates in the detectors with no significant dead time opens the possibility of performing reaction calorimetry studies. The array operates

in a mode where measurements of γ-ray hit multiplicity (referred as 'K') and total energy deposit (referred as 'H') are possible for each event. This is a powerful tool to distinguish between different reaction channels as demonstrated in Fig. 2.15. HK matrices of the reactions used in the N-SI-109 and N-SI-103 experiments are shown in addition to the well-known $^{252}\mathrm{Cf}$ spontaneous fission reaction. It is evident that the neutron-induced fission exhibits more high multiplicity events with $K > 10$ due to interactions of the primary beam and the neutrons with surrounding material. It is also clear when comparing the different targets that the intrinsic activity of $^{232}\mathrm{Th}$ enhances low multiplicity, high energy events due to a 2.6 MeV transition of the decay of one of its decay products ($^{208}\mathrm{Tl}$). Furthermore, the HK matrices of the $^{238}\mathrm{U}$(n,f) reactions at different neutron entrance energies can be compared. The average multiplicity of $\overline{K} = 2.7$ at 1.7 MeV neutron energy increases to $\overline{K} = 4.0$ when doubling the neutron energy but, on average, the total energy only increases from $\overline{E}_{tot} = 2.1$ MeV to $\overline{E}_{tot} = 2.5$ MeV. This reflects the nature of the different reactions because of the increased probability of inelastic neutron scattering before losing enough energy to be captured. From the kinematics calculations, it is evident that the neutron cone at 3.4 MeV is significantly larger and opens up for more neutron-induced reactions with surrounding materials. These reactions strongly contribute to the total multiplicity but rather insignificantly to the detected γ-ray energy.

Additionally, the HK matrix can be used to distinguish between different fission fragments. By using the information of both prompt and delayed events, this gives rise to several degrees of freedom to improve the peak-to-background ratio. An example of this selection tool from this work is published in Ref. [86]. A comparison between $^{134}\mathrm{Te}$ and $^{137}\mathrm{I}$ in the prompt HK matrix shows that the average hit multiplicity is higher in $^{137}\mathrm{I}$ while its average total energy is slightly lower. This reflects the higher level density of the odd-even nucleus $^{137}\mathrm{I}$ compared to the even-even $^{134}\mathrm{Te}$ isotope. The high energy transitions in $^{134}\mathrm{Te}$ result in a higher average total energy despite the lower multiplicity compared to the $^{137}\mathrm{I}$ nucleus. For the identification of isomeric states, a restriction on the total delayed energy sum can be used according to the excitation energy of the isomer of interest.

2.3.3 Identification of fission fragments

Fission fragments are identified using single and multiple γ-ray coincidences. With the excellent energy resolution of the HPGe detectors and a proper background subtraction, nuclei of interest can be selected cleanly using characteristic γ-ray energies. Additionally, γ rays from its fission binary partner can be taken into account. Due to the large variety of nuclei analyzed in the present work, only selected examples are shown.

To enhance the cleanliness of identification, delayed transitions outside of the prompt peak can be used to

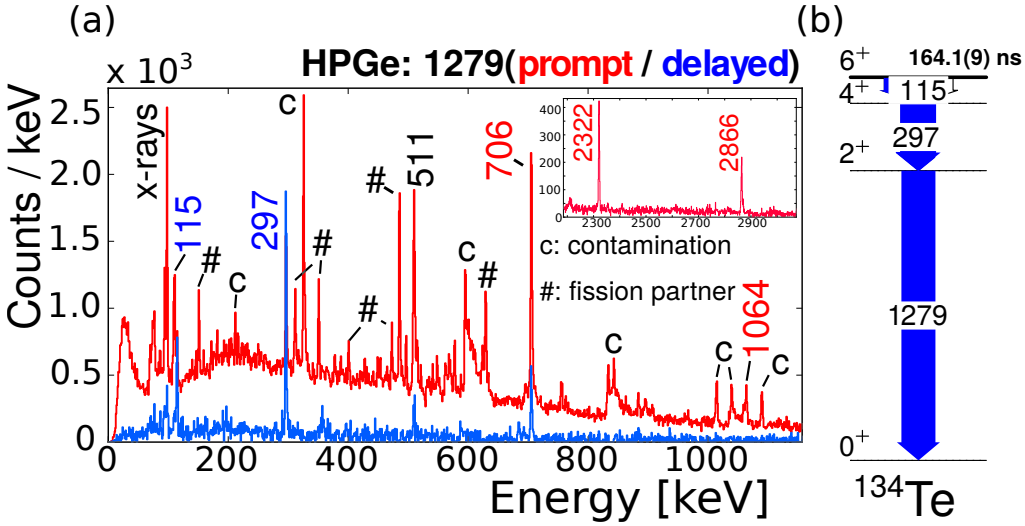

Figure 2.16: (a) Prompt (red) and delayed (blue) γ-ray spectrum after gating on the 1279 keV, $2_1^+ \rightarrow 0_1^+$ transition in ^{134}Te. (b) Level scheme of ^{134}Te below the 6_1^+ isomer [87].

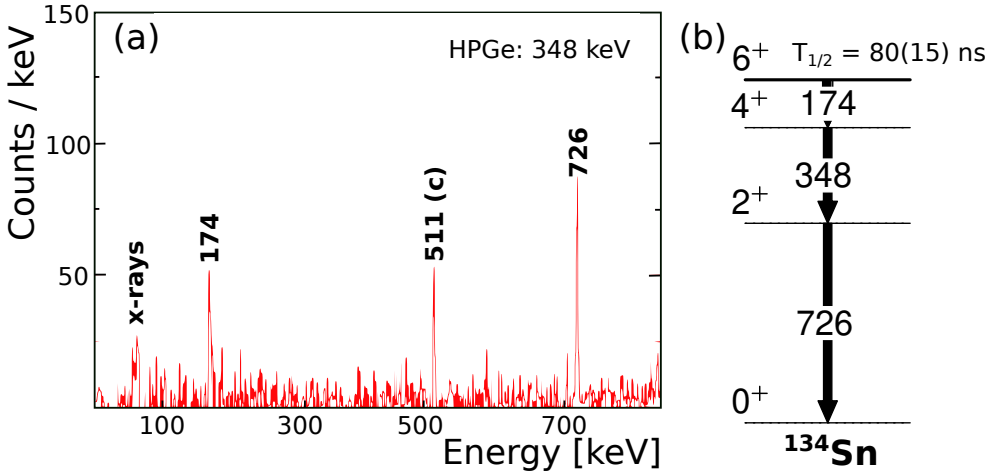

Figure 2.17: (a) Delayed γ-ray spectrum gated on the 348 keV $4_1^+ \rightarrow 2_1^+$ transition in ^{134}Sn. (b) Level scheme of the isomer decay in ^{134}Sn [87].

select an isomer. An example from the well-populated $^{134}\mathrm{Te}$ is discussed in the following. In Fig. 2.16, prompt and delayed energy projections can be seen after applying a gate on the $2_1^+ \rightarrow 0_1^+$ transition in $^{134}\mathrm{Te}$ (1279 keV). While the prompt γ-ray spectrum has a very high background, the delayed γ-ray spectrum is extremely clean. Besides 511 keV and $(n, n'\gamma)$ contaminants, only the 115 and 297 keV transitions remain in the spectrum, emphasizing the benefit of having a pulsed beam. Due to the 400 ns repetition period of the primary beam, this selection is optimal for isomeric half-lives in the range of tens of ns up to a few hundreds of ns.

The visibility and cleanliness of isotopes can be further improved by using the multi-dimensional parameters provided by measuring the full calorimetry in the array. Different parameters such as hit multiplicity or total energy deposit can be used to further enhance the peak-to-total ratio of γ rays from certain isotopes. This has to be done individually for each case and will be shown for the example of $^{134}\mathrm{Te}$ and the weaker populated $^{134}\mathrm{Sn}$.

$^{134}\mathrm{Sn}$ has a 6^+ isomer with a half-life of 80(15) ns [87] that decays via the following γ rays: 174, 348 and 726 keV. Figure 2.17 shows the delayed HPGe energy spectrum gated on the 348 keV $4_1^+ \rightarrow 2_1^+$ transition in $^{134}\mathrm{Sn}$ with background subtraction. Both remaining transitions below the isomer are visible alongside the 511 keV contaminant.

In order to quantify the cleanliness of the identification of nuclei, a figure of merit (FoM) was defined. After applying a delayed gate on the $2_1^+ \rightarrow 0_1^+$ transition (1279 keV for $^{134}\mathrm{Te}$ and 726 keV for $^{134}\mathrm{Sn}$), the FoM is:

$$\mathrm{FoM} = \frac{N_\gamma(4_1^+ \rightarrow 2_1^+)^2}{N_\gamma(351\ keV)}, \tag{2.3}$$

where $N_\gamma(4_1^+ \rightarrow 2_1^+), N_\gamma(351)$ are the number of counts of the respective $4_1^+ \rightarrow 2_1^+$ transitions and the 351 keV background peak, respectively. The latter one hereby arises from $^{21}\mathrm{Ne}$ produced in the fusion-evaporation as already discussed in Fig. 2.13. The formula is a result of a measure for the peak-to-background ratio ($P/B = N_\gamma(4_1^+ \rightarrow 2_1^+)/N_\gamma(351)$) scaled with the number of counts in the peak ($N_\gamma(4_1^+ \rightarrow 2_1^+)$). This multiplication is done to not only optimize for the peak-to-background ratio but also find the balance to the overall statistics inside the peaks of interest as mentioned in the previous section.

The analysis is presented in Fig. 2.18 showing the FoM plots as a function of different parameters for $^{134}\mathrm{Sn}$ and $^{134}\mathrm{Te}$. The prompt multiplicity shows a clear peak around $M_\gamma = 5$ or 6 and the delayed multiplicity around $M_\gamma = 3 - 4$. The flattening of the curve in Fig. 2.18(b) shows that delayed multiplicities above 4 are not relevant and do not contribute significantly to the spectrum. The relevance of the delayed summed energy is shown in Fig. 2.18(c) which has several structures, the strongest peak being at 1800 keV. While the value seems unrelated to $^{134}\mathrm{Sn}$, it can be understood by looking at it as the excitation energy of the isomer (1247 keV) plus a constant

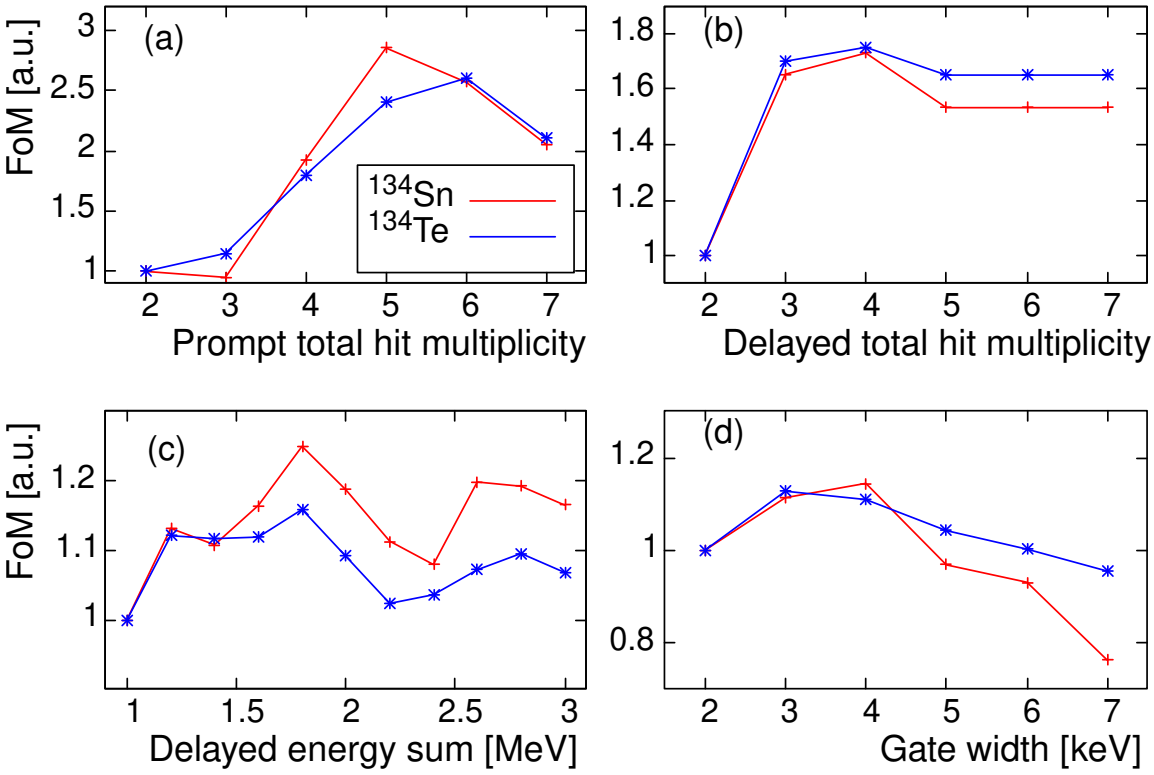

Figure 2.18: Figure of merit (FoM) plots for the identification of $^{134}\mathrm{Sn}$ (red) and $^{134}\mathrm{Te}$ (blue) as a function of (a) prompt total multiplicity, (b) delayed total multiplicity, (c) delayed summed energy and (d) gate width.

background contribution from, for example, the 511 keV peak. This adds up to about 1750 keV and, because of the 200 keV binning, ends up in a peak at 1800 keV. In $^{134}\mathrm{Te}$, the excitation of the isomer is 1691 keV and result in the same binning, thus, also peaking at 1800 keV. A second minor peak in $^{134}\mathrm{Te}$ is visible after adding 511 keV from the constant background together. It is less visible than the 1800 keV maximum in $^{134}\mathrm{Sn}$ which can be explained by the differences in peak-to-background ratio since the background is less pronounced relative to the well-populated $^{134}\mathrm{Te}$. The plot in Fig. 2.18(d) shows the FoM as a function of gate width of the respective $2_1^+ \rightarrow 0_1^+$ gates. It can be seen that a gate width of 4 keV is most appropriate for the identification of the isomer in $^{134}\mathrm{Sn}$ while a gate width of 3 keV is enough for the isomer in $^{134}\mathrm{Te}$. This analysis is used in cases of low statistics to identify the isotopes but is omitted when statistics is essential in the analysis (e.g., coincidence or lifetime measurements).

2.3.4 Experimental method: the fast-timing technique

In this work, lifetimes of excited nuclear states are determined via the fast-timing technique. This method relies on measuring the time difference between two electronic signals. In the following, a simple decay scheme is assumed, where a single γ ray is feeding an excited state with lifetime τ. The decaying transition is delayed by τ and the difference between the timing signal of both γ rays can be used to determine the lifetime. A hybrid setup of HPGe and $LaBr_3$(Ce) detectors is used which combines the good energy resolution of HPGe and the excellent time resolution of $LaBr_3$(Ce) detectors. Triple coincidence events are required where three γ rays occur in a small time window correlated to the same event. The energy measured by the HPGe detector is used to select a particular decay path within the nucleus of interest. The $LaBr_3$(Ce) energy information is used to obtain the time difference between feeding and depopulating transition. In the analysis, the data is stored in HPGe gated E_γ-E_γ-ΔT cubes for the $LaBr_3$(Ce) data. $LaBr_3$(Ce) gates on feeding and decaying transitions of the state of interest are applied to project out time difference spectra.

The intrinsic time resolution of the detectors (c.f. Sec. 2.3.6) is characterized by the FWHM of the Gaussian prompt time distribution, called prompt response function (PRF). Depending on the lifetime with respect to the FWHM of the PRF, different techniques are used to extract the lifetime. If $\tau \gtrsim$ FWHM, the slope or convolution fit method can be applied [88, 89]. The centroid shift method is used if $\tau \lesssim$ FWHM [90]. The delayed time spectrum $D(t)$ is described by the convolution of the PRF and an exponential decay function [76, 91]:

$$D(t) = n_0 \lambda \int_{-\infty}^{t} \mathrm{PRF}(t' - t_0) \cdot e^{-\lambda(t-t')} dt'. \tag{2.4}$$

In Eq. (2.4), n_0 is a normalization factor which stems from the number of counts in the time spectrum. PRF is the function that describes the prompt response of the detection system and can be assumed as Gaussian centered around the position t_0.

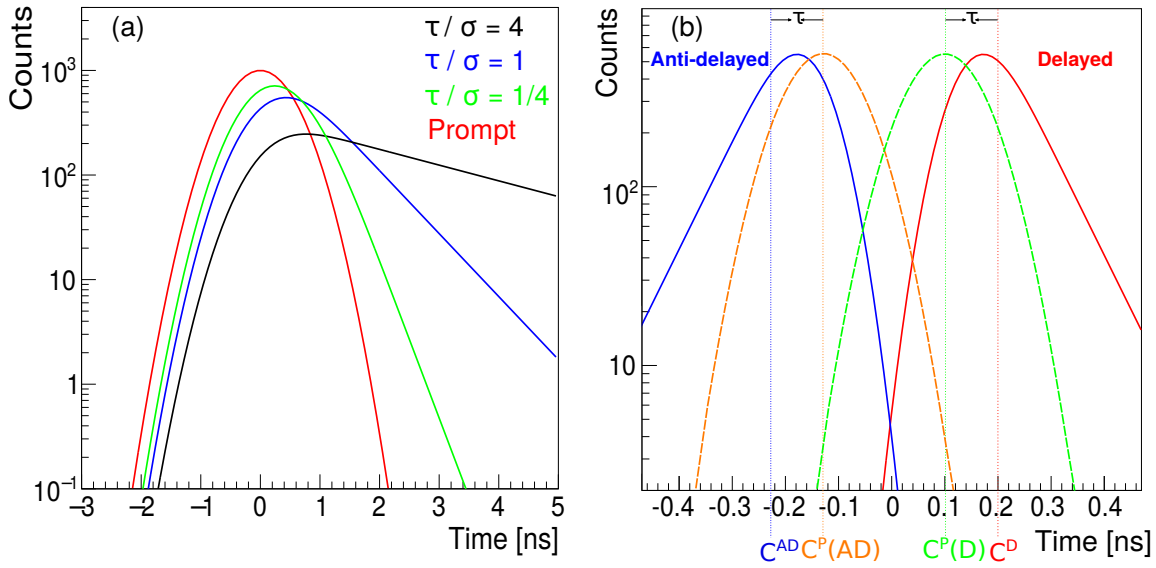

Figure 2.19: (a) Simulation of the slope method for the determination of lifetimes. The prompt distribution with $\sigma = 0.5$ ns (red) is shown together with different delayed time distributions for various lifetimes. (b) Example of the centroid difference method with delayed (red) and anti-delayed (blue) time distributions. The centroids of the respective spectra are highlighted and labeled accordingly.

The time difference distribution is asymmetric if the lifetime is longer than the FWHM of the PRF. Due to the exponential decay associated with the lifetime, the time spectrum shows a visible tail, see Fig. 2.19(a). By fitting an exponential decay to the slope of the time distribution, the decay constant and, consequently, the lifetime can be deduced.

The anti-delayed time distribution is obtained by interchanging start and stop detector and an example can be seen in Fig. 2.19(b). When the lifetimes are smaller than the time resolution, the centroid shift (or centroid difference) method has to be applied. The centroid C^P of the delayed time spectrum is defined as the first moment of the time distribution [76]:

$$C^D = \langle t \rangle = \frac{\int_{-\infty}^{\infty} tD(t)dt}{\int_{-\infty}^{\infty} D(t)dt}. \tag{2.5}$$

The lifetime can be extracted based on the fact that the centroid C^D of the delayed time distribution is shifted

with respect to that of a corresponding prompt time distribution $C^P(D)$ by the mean lifetime [90]:

$$\tau = C^D - C^P(D). \tag{2.6}$$

In the case of the anti-delayed (AD) time distribution, the lifetime is obtained by a shift from the prompt distribution to the left, i.e., $\tau = C^P(AD) - C^{AD}$ (see Fig. 2.19(b)). The centroids are indicated in Fig. 2.19(b) by dashed vertical lines. Note that due to the energy dependence of the centroid, $C^P(D)$ and $C^P(AD)$ are different. Both equations are used in a more refined version of the centroid shift method, the centroid difference method which was introduced in Ref. [76] to measure lifetimes with reduced systematic uncertainties. In short, the centroid difference ΔC between delayed and anti-delayed time distribution is measured and the lifetime is obtained by correcting this centroid difference according to the centroid difference of both prompt distributions. Due to the fact that each distribution (delayed and anti-delayed) is shifted by τ, the corrected centroid difference amounts to twice the mean lifetime [76]:

$$\Delta C = C^D - C^{AD} = C^P(D) - C^P(AD) + 2\tau = PRD + 2\tau. \tag{2.7}$$

The last step in Eq. (2.7) introduces the so-called prompt response difference formed by the combined γ-γ time walk characteristics of the system. It is given by the difference in prompt centroids of the delayed and anti-delayed time distribution, i.e., $PRD = C^P(D) - C^P(AD)$. The generalization for a system of N detectors is known as the generalized centroid difference (GCD) method [92].

Equation (2.7) holds under the assumption of no background contributions to full energy peak (FEP) events. In an experiment, background is unavoidable and the main contribution results from Compton scattered γ rays. The measured centroid has to be corrected for the time response of the background. The measured time difference of the feeder-decay coincidence is composed of four components: the true peak-peak (pp) coincidence, the coincidences of one peak contribution with the background from the other peak (pb/bp) and the background-background (bb) coincidences. Thus, the measured centroid has to be corrected for all those components according to the formula given in Ref. [57]:

$$C^t_{pp} = \frac{n_{pp}C_{pp} - n_{pb}C_{pb} - n_{bp}C_{bp} + n_{bb}C_{bb}}{n_{pp} - n_{pb} - n_{bp} + n_{bb}}. \tag{2.8}$$

Here, C^t_{pp} is the true position of the centroid after correcting the measured centroid C_{pp} for the background time distributions: C_{pb}, C_{bp} and C_{bb}. The correction has to be weighted according to the number of counts n in each component. For more details the reader is referred to Ref. [57]. Note that the time response of the

background cannot be measured at the FEP and, therefore, has to be interpolated by measuring it before and after the FEP.

2.3.5 Optimization of $LaBr_3$(Ce) timing

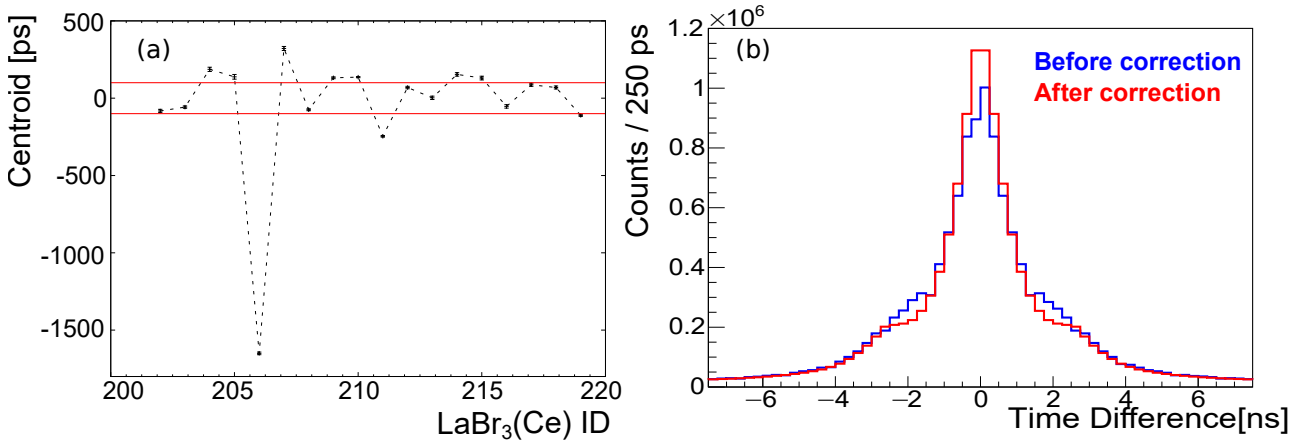

Figure 2.20: Fine time-shift correction for the $LaBr_3$(Ce) detectors. (a) Centroid position of the $LaBr_3$(Ce) prompt peak after applying a gate on the 1279 keV, $2_1^+ \rightarrow 0_1^+$ transition in ^{134}Te. The dashed black line is to guide the eye and the solid red denotes the $\pm 100\ ps$ range. (b) Time difference spectrum before and applying the fine time-shift correction.

As shown in Tab. 2.3, the fraction of $LaBr_3$(Ce)-$LaBr_3$(Ce)-HPGe coincidences is rather low and, thus, an optimization of the usable $LaBr_3$(Ce) data is essential. The time alignment of detectors as shown in Fig. 2.10 is the first step. In order to improve the resolution, additional in-beam data is used to measure the centroid of the $LaBr_3$(Ce)-$LaBr_3$(Ce) time difference distribution after gating on the 1279 keV transition belonging to the isomer in ^{134}Te. The centroids for each detector crystal are shown in Fig. 2.20(a). While most values are below or around the 100 ps limit (solid red line), one detector has a significantly shifted centroid. After implementing a correction for all the detectors, the time distribution is improved as can be seen in Fig. 2.20(b). The tail in that spectrum due to the delayed inelastic neutron scattering still remains but a substantial part of the shoulder is shifted back into the main peak, thus, improving the overall resolution and increasing the usable data.

Two different $LaBr_3$(Ce) rings were used one of which comprised cylindrical and the second one conical scintillator crystals. By looking at the time resolution of each crystal individually, it could be noted that the second ring has a much narrower time resolution. This is shown in Fig. 2.21 where the time distribution of the first ring is compared to the second ring. These spectra were again obtained by selecting clean events in coincidence with the 1279 keV transition in ^{134}Te. For the analysis with enough statistics and where a good time resolution is needed, the detectors belonging to the first ring were omitted. Note that in the case of $LaBr_3$(Ce)

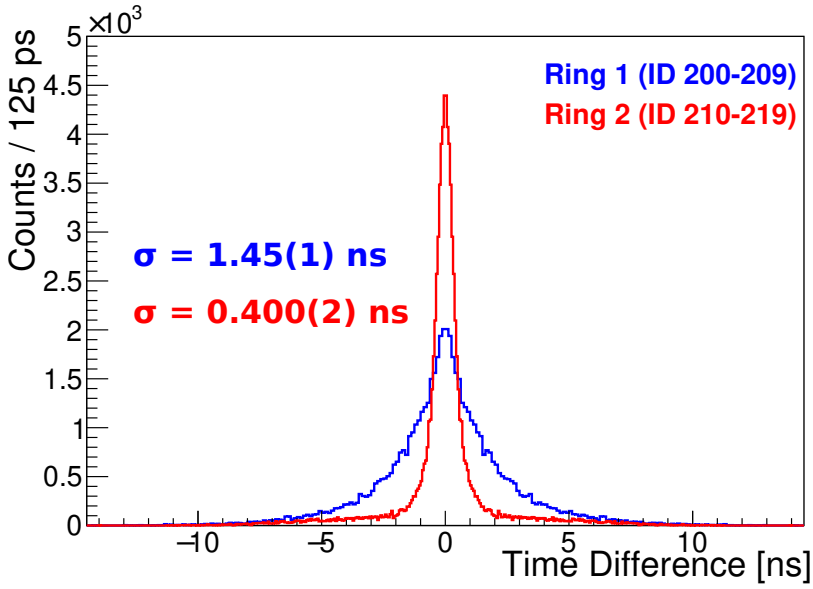

Figure 2.21: Time resolution of the different $LaBr_3(Ce)$ rings after gating on the 1279 keV transition in ^{134}Te.

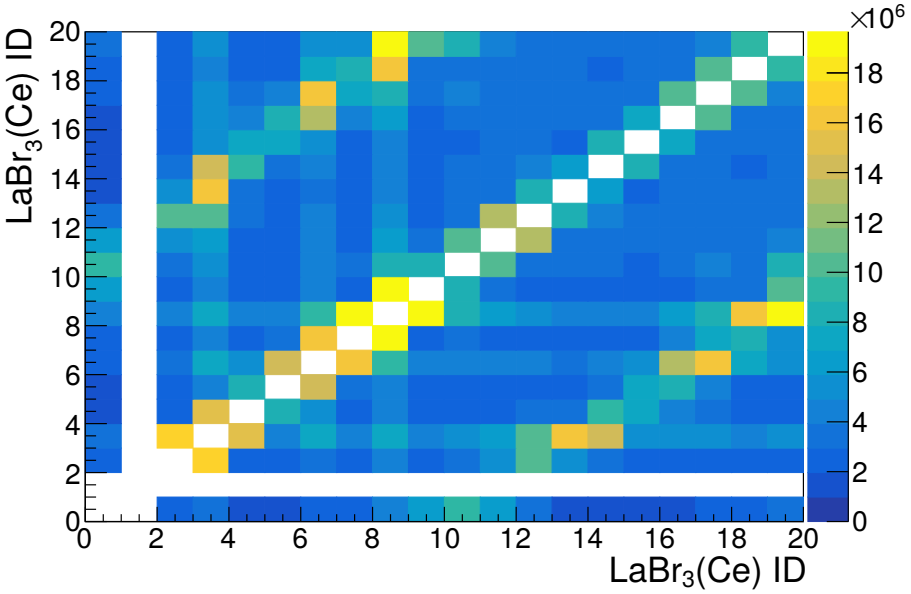

Figure 2.22: $LaBr_3(Ce)$ ID vs $LaBr_3(Ce)$ ID matrix showing the cross-talk between neighboring detectors. Each crystal has three direct neighbors (two within one ring and one between the two rings).

timing with respect to the beam pulse this is not necessary as the intrinsic resolution due to the beam pulse itself is an order of magnitude worse (see Sec. 2.3.6).

Scattering of γ rays between $LaBr_3$(Ce) detectors leads to cross-talk between neighboring detectors. This can be visualized in a matrix plotting the counts of each $LaBr_3$(Ce) coincidence with respect to one another as presented in Fig. 2.22. The detector with the ID 2 was not working and is therefore excluded in this matrix. Several diagonals with enhanced statistics can be identified. The IDs plus or minus one are always enhanced as well as the ID plus ten. This corresponds to the fact that each $LaBr_3$(Ce) detector has three direct neighbors: two within one sub-ring and one between the two rings, as shown in Fig. 2.2(b). For example, $LaBr_3$(Ce) detector number 9 has the direct neighbors 8,10 and 19. A nearest neighbor suppression is consequently applied to avoid cross-talk.

2.3.6 Lifetime measurements applied to the data and selected results

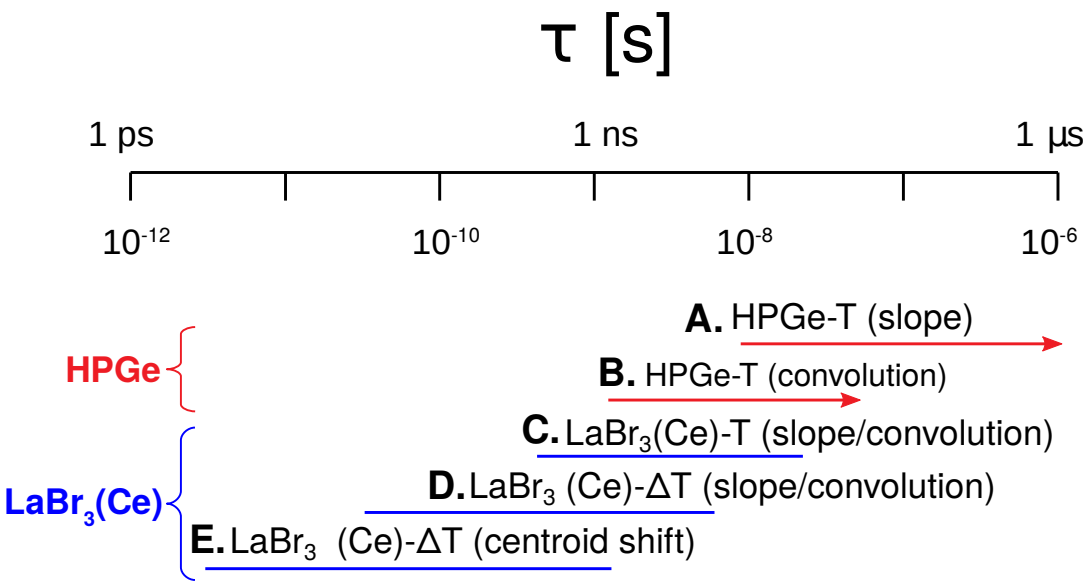

Figure 2.23: Range for the lifetime measurements used in this work for different detectors and methods. The label 'T' refers to the timing measurement with respect to the beam pulse and the method 'ΔT' to time difference measurement for a given detector pair.

In the presented experiment, lifetimes from several hundreds of ns down to tens of ps can be measured by utilizing different detector types and analysis methods. Figure 2.23 shows a schematic overview of the accessible lifetime ranges for each analysis technique. For lifetimes above tens of ns, HPGe timing with respect

to the beam pulse is sufficient and the slope method can be applied. When going down to about 1 ns, the lifetime sensitivity of the HPGe detectors can be increased by utilizing information from the prompt Gaussian and applying the convolution method. For similar and lower lifetimes, the $LaBr_3$(Ce)-beam timing is suitable. The intrinsic width of the beam pulse of about 2 ns FWHM restricts the lifetime measurement to approximately 0.5 ns. It is important to note that when measuring lifetimes with respect to the beam pulse, the result is an effective lifetime of the sum of lifetimes feeding that particular state. If these contributions are negligible, for example in the cases of long-lived isomers, the lifetime of a particular state can be given precisely. For lifetimes in the sub-ns range, $LaBr_3$(Ce)-$LaBr_3$(Ce) time differences have to be considered. The accessible range depends on the sensitivity of the chosen method (see Sec. 2.3.4). The slope method is suitable for lifetimes around or above 1 ns. The convolution method increases the sensitivity down to about 50-100 ps. In this case, the time distribution is fitted using a convolution of a prompt Gaussian with an exponential decay:

$$\begin{aligned} f(x) &= \left(e^{-\lambda x'}\right) * \left(N e^{-x'^2/2\sigma^2}\right) + c \\ &= N \int_0^\infty e^{-\lambda x'} e^{(x-x')^2/2\sigma^2} dx' + c \\ &= \frac{N}{2} e^{-\lambda\left(x-(\sigma^2\lambda)/2\right)} \left[1 + \text{erf}\left(\frac{x-\sigma^2\lambda}{\sqrt{2}\sigma}\right)\right] + c. \end{aligned} \tag{2.9}$$

The free parameters to be extracted from the fit to the data are the decay constant λ, the normalization N, the width σ and the constant background c. erf(x) is the so-called error function and describes the area under the Gaussian curve between $-x$ and x [93]. Note that Eq. (2.9) describes the convolution of a Gaussian centered around zero. In order to apply it to an arbitrary position x_0, the integral variable needs to be shifted accordingly, i.e., $x' \rightarrow (x' - x_0)$. This results in a total of five free parameters. In this work, the variation of fit parameters from the convolution method are shown as error bands. This uncertainty includes statistical fluctuations from varying the fit region, background component and prompt width.

The prompt width σ is the most sensitive fit parameter in Eq. (2.9) and has to be investigated before fitting the time distribution curves. The energy dependence of σ is given in Fig. 2.24 for different detector and lifetime methods mentioned in Fig. 2.23. These curves can be used to limit the parameter σ in the lifetime analysis. The prompt width was obtained by fitting the time distributions after gating on transitions with negligible lifetime contributions. For HPGe-beam timing, this includes lifetimes of states below 1 ns and the resulting curve is shown in Fig. 2.24(a). The data points are fitted using an exponential decay curve and a prompt width of about 6 ns is obtained for energies around 1 MeV (corresponding to FWHM$\approx$14 ns). A sharp increase in σ can be obtained for energies below 500 keV which reflects the poor time resolution for low γ-ray energies.

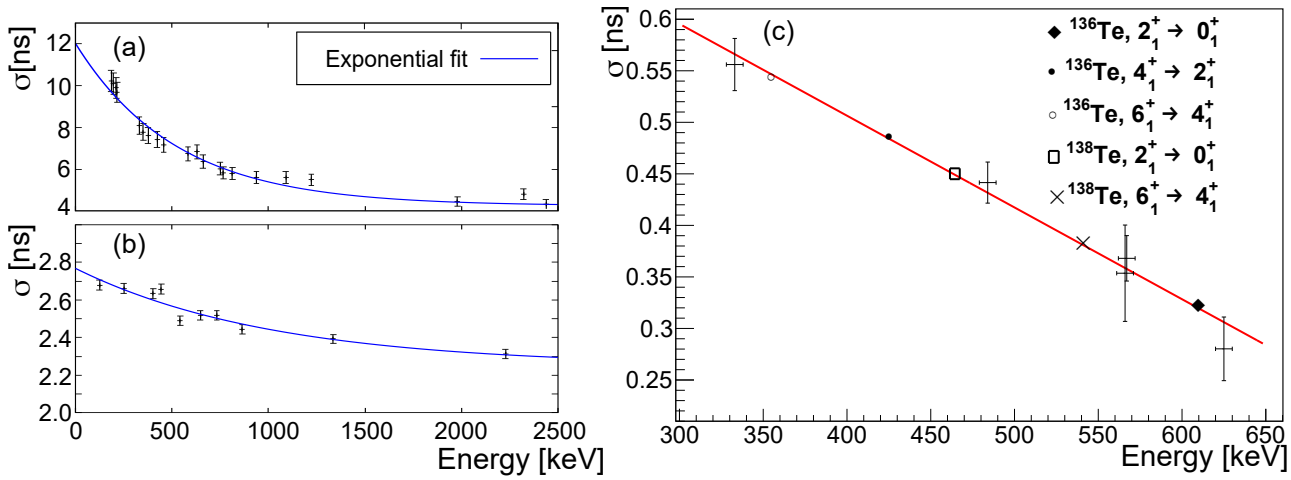

Figure 2.24: Prompt width σ as a function of energy for (a) HPGe-beam timing, (b) $LaBr_3$(Ce)-beam timing and (c) $LaBr_3$(Ce)-$LaBr_3$(Ce)-ΔT measurements. The data is interpolated using different functions. See text for details.

Figure 2.24(b) shows the energy dependence in the case of $LaBr_3$(Ce)-T measurements. The sharp increase of σ at lower energies is not as pronounced as for the HPGe detectors. This is due to the (almost) energy-independent beam profile which has an intrinsic width of about 2 ns. This width is much higher compared to the intrinsic one of the $LaBr_3$(Ce) detectors and, therefore, dominates the dependency.

The energy dependence of the prompt widths for $LaBr_3$(Ce)-$LaBr_3$(Ce)-ΔT measurements is shown in Fig. 2.23(c) and has already been used in Refs. [94, 95] to measure lifetimes in the sub-ns range. The values of σ are 0.6 ns for energies around 300 keV and drop to below 0.3 ns for energies above 600 keV. The data points in Fig. 2.24(c) are obtained by fitting prompt distributions of well-populated fission fragments from the in-beam data. Prompt means lifetimes below or around 15 ps. An example is shown in Fig. 1 of Ref. [94] for the 6_1^+ state in ^{140}Xe with a half-life of $\tau < 8.6$ ps [96]. The spectrum is fitted with a Gaussian function and the σ parameter is extracted. This was done for several transitions of well-known fission fragments and resulted in the energy dependence shown in Fig. 2.24(c). It has to be noted that all three curves in Fig. 2.24 are reference points and the interpolated values for the lifetime fits have uncertainties that have to be taken into account in the result.

To determine the uncertainty from the fit function in Eq. (2.9), a variation of fit region, prompt width and background contribution is used to introduce systematic uncertainties. The resulting error is obtained by adding these contributions in quadrature according to:

$$\Delta\tau = \sqrt{\Delta\tau_{Fit}^2 + \Delta\tau_{Region}^2 + \Delta\tau_{BG}^2 + \Delta\tau_{Prompt}^2}. \tag{2.10}$$

The individual uncertainties in Eq. (2.10) have different contributions to the overall uncertainty $\Delta\tau$ and mainly arise from the low statistics which is reflected in the large error bars (see results in Sec. 2.4). The uncertainty from the variation of the fit region and the background component are comparably small. The variation of the prompt width results in big fluctuations of the resulting lifetime but can be controlled through the functions in Fig. 2.24. Thus, the largest contribution comes from the fit itself which is rather large due to the low statistics.

For lifetimes lower than accessible through the convolution method, the centroid shift method can be used which is applicable for lifetimes down to tens of ps, see Fig. 2.23. However, this method was not applicable to the $LaBr_3$(Ce) data in this work due to the lack of calibration data recorded during the experiment. In the following, examples of timing measurements in the different lifetime regimes will be presented using selected results.

Isomers from HPGe-beam timing

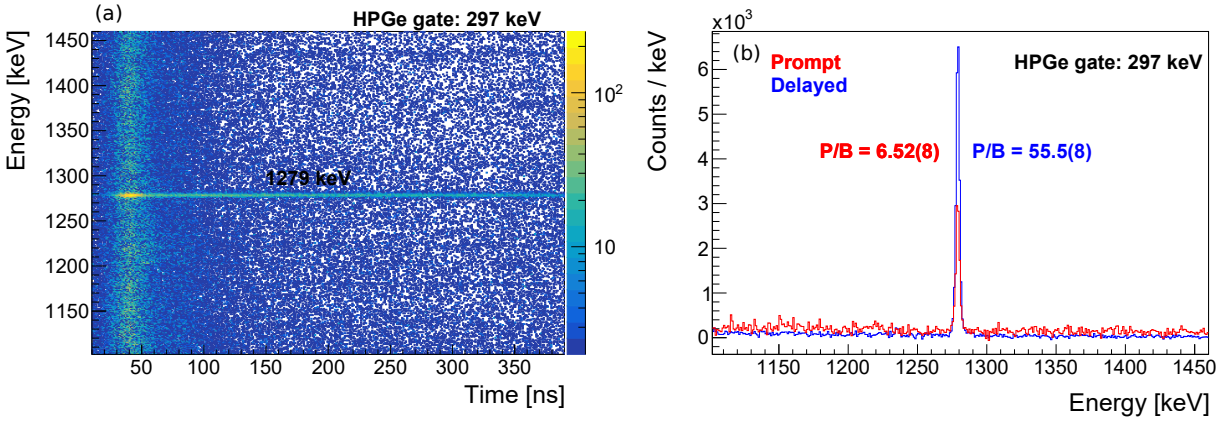

Figure 2.25: (a) Energy vs. time matrix after applying a gate on the 297 keV $4_1^+ \rightarrow 2_1^+$ transition in ^{134}Te. The energy axis is zoomed around the 1279 keV $2_1^+ \rightarrow 0_1^+$ transition in ^{134}Te. (b) Energy projection of the matrix for prompt ($t < 60$ ns) and delayed ($t > 60$ ns) events. The spectra are labeled with their respective peak-to-background (P/B) ratio.

The procedure of measuring half-lives of long-lived isomeric states is shown for the 6_1^+ isomer in ^{134}Te. The identification of γ rays has already been shown in Fig. 2.16. In order to verify the isomeric character of the 1279 keV γ ray, a HPGe gate on the 297 keV $4_1^+ \rightarrow 2_1^+$ transition is applied. The resulting time-energy matrix zoomed around 1279 keV is shown in Fig. 2.25(a). The time is limited to one beam pulse time window, i.e., 400 ns. While most background events are located around the prompt position at 45 ns, the 1279 keV peak of interest is spread over the full 400 ns time window. This indicates that the transition is below an isomer with a half-life in the order of hundreds of ns. The half-life can be measured by a projection of the time axis after applying an energy cut on 1279 keV. The resulting time spectrum and half-life is provided in Sec. 2.4.

The advantage of having a pulsed primary beam for the determination of isomers is visualized in Fig. 2.25(b). The projection of the γ-ray energy is shown for two time slices; prompt events have $t < 60$ ns and delayed γ rays have $t > 60$ ns. The number of counts for the delayed cut is higher by about a factor of two which can be explained by the longer time window. In fact, the number of counts normalized to a 100 ns time window is about a factor 2.5 higher in the prompt cut. However, the peak-to-background ratio increases significantly from 6.52(8) in the prompt window to 55.5(8) in the delayed one.

A limiting aspect in determining accurate half-lives is the number of counts in the time spectra. In order to have a reasonable amount of counts in the useful part of the time spectrum (up to five $T_{1/2}$), about 10^3 counts are necessary. This sets a limiting condition on the accessible isomers depending on the yield, γ-ray energy and isomeric ratio. In the example of ^{134}Te, around $4 \cdot 10^4$ counts are present in the peak of interest which corresponds to a yield of 4.18 % (see Tab. 2.1). Neglecting changes in efficiencies and isomeric ratios, isomers of isotopes with yields down to 0.1 % should be accessible.

LaBr$_3$(Ce)-beam timing

The application of lifetime measurements using the LaBr$_3$(Ce) timing information with respect to the beam pulse will be presented for the lifetime of the $(15/2^+_1)$ state in ^{135}I which was previously measured to be 2.51(12) ns [69].

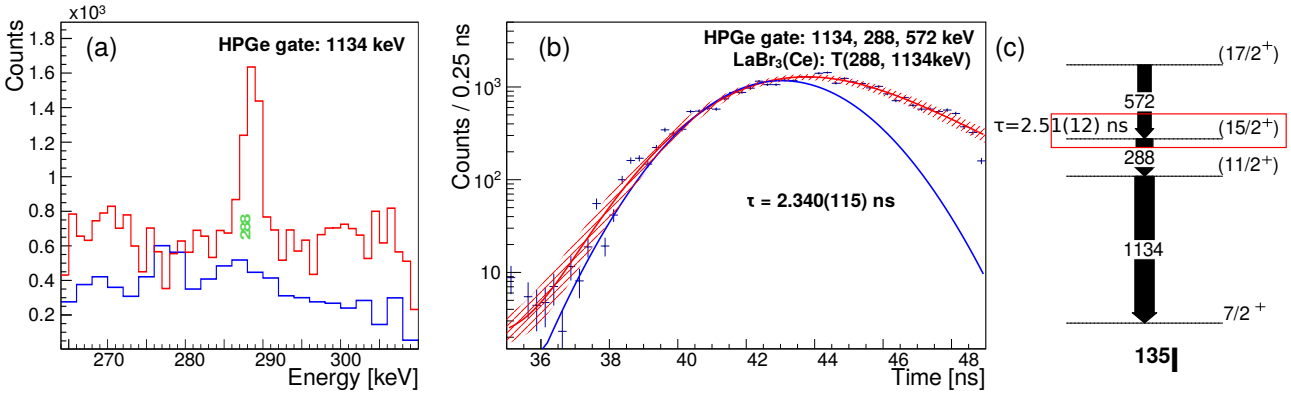

Figure 2.26: Lifetime measurement of the $(15/2^+)$ state in ^{135}I. (a) HPGe (red) and LaBr$_3$(Ce) (blue) energy spectra gated on the 1134 keV $(11/2^+) \rightarrow 7/2^+$ transition. (b) Background-subtracted LaBr$_3$(Ce) time distribution for the sumup of the 288 keV and 1134 keV transitions. Taken from Ref. [95]. (c) Relevant part of the level scheme in ^{135}I and the lifetime of the state of interest taken from Ref. [97].

Figure 2.26(a) shows the energy spectrum after applying a gate on the $(11/2^+_1) \rightarrow 7/2^+_1$ transition in ^{135}I. The spectrum is zoomed around the 288 keV $(15/2^+_1) \rightarrow (11/2^+_1)$ transition which is visible in both HPGe and LaBr$_3$(Ce) detectors. The lifetime of the $(11/2^+_1)$ state is much smaller than the τ of the $(15/2^+_1)$ state (upper

limit determined in this work, see Sec. 2.4) and, both 1134 keV and 288 keV time distributions can be added for a precise measurement of the $(15/2_1^+)$ state. This background-subtracted summed-up time distribution is shown in Fig. 2.26(b). According to the description in Sec. 2.3, a fit value of $\tau = 2.340(115)$ ns is obtained. Note that the fit extends only to about 50 ns to avoid contributions from time-delayed inelastic neutron scattering, that occur 10-15 ns after the prompt γ rays, as shown in Fig. 2.14. The shaded areas in Fig. 2.26(b) represent the uncertainty of the fit parameters and the variation of fit regions. Within the uncertainty, the result is consistent with the previous measurement. In Ref. [69], the value was calculated from a weighted average of four different values obtained from different gate combinations: 2.61(26) ns, 2.67(20) ns, 2.40(2) ns and 2.38(20) ns. The result obtained in this work is consistent with two of those values and adds an independent measurement to reduce the relative uncertainty for the lifetime of this state.

Comparison of HPGe- and $LaBr_3$(Ce)-beam timing

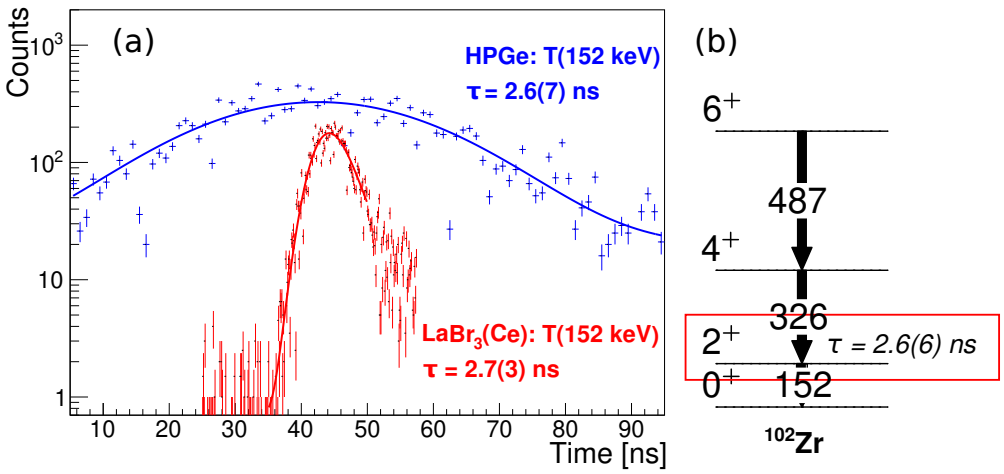

Figure 2.27: (a) Background subtracted time spectra of the 152 keV γ ray measured with the HPGe detectors (blue histogram) and $LaBr_3$(Ce) scintillators (red points). The data are fitted according to Eq. (2.9). (b) Partial level scheme of ^{102}Zr with data taken from Ref. [98].

As discussed in the beginning of this section, the convolution method can be used for lifetimes in the ns range either with the HPGe or the $LaBr_3$(Ce) detectors. In the following, an example of the well-populated ^{102}Zr isotope will be discussed using both, HPGe-beam timing and $LaBr_3$(Ce)-beam timing. First, a clean HPGe gate on either the 487 keV $6_1^+ \rightarrow 4_1^+$ or the 326 keV $4_1^+ \rightarrow 2_1^+$ transition is applied to select the nucleus of interest. Then, to measure the lifetime of the 2_1^+ state, the timing information of the 152 keV γ ray with respect to the beam pulse is projected. According to the lifetime $\tau = 2.6(6)$ ns [98], $LaBr_3$(Ce)-beam and HPGe-beam timing

are suitable, see Fig. 2.23.

Figure 2.27(a) shows the HPGe and $LaBr_3$(Ce) time distributions of the 152 keV γ ray in ^{102}Zr. The relevant part of the level scheme is shown in Fig. 2.27(b). The superior time resolution of the $LaBr_3$(Ce) detectors compared to the HPGe detectors is emphasized by the narrower prompt distribution. This enhances the slope on the right side of the prompt distribution which is barely seen in the HPGe detectors. The time distributions are fitted as described before with the convolution method. The width of the prompt function amounts to about 11 ns for the HPGe and 2.4 ns for $LaBr_3$(Ce) detectors, in accordance with the prompt widths determined in Fig. 2.24. The resulting half-lives are 2.6(7) ns and 2.7(3) ns for HPGe and $LaBr_3$(Ce) detectors, respectively. The adopted value amounts to 2.68(27) ns and matches the value from evaluated nuclear data base [98]. The consistent results from both detector measurements support the result and emphasizes the capabilities of the lifetime ranges presented in Fig. 2.23. Note that the $LaBr_3$(Ce) was only fitted up to about 50 ns due to the time structure around 55 ns from inelastic neutrons scattering reactions with the detectors, see Fig. 2.14.

Sub-ns lifetime measurement

In this section, the ns/sub-ns lifetime measurement with a known and an unknown case is discussed in more detail. The procedure for $LaBr_3$(Ce)-$LaBr_3$(Ce)-ΔT measurements is always the same and has been explained in Sec. 2.3.4. The time difference spectra are fitted using Eq. (2.9). To validate the cleanliness of the $LaBr_3$(Ce) gates, HPGe spectra after one of the $LaBr_3$(Ce) gates are projected and checked for contaminants using the superior energy resolution of the HPGe detectors.

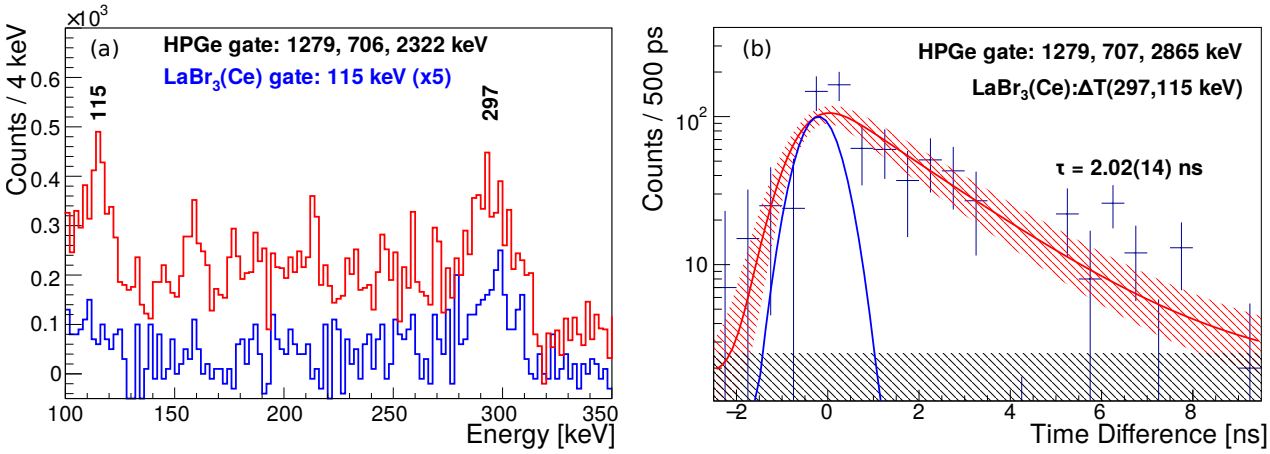

Figure 2.28: (a) Delayed $LaBr_3$(Ce) energy projection after applying a HPGe gate on several transitions in ^{134}Te (red) and an additional $LaBr_3$(Ce) gate on 115 keV (blue). (b) Time distribution of the 4_1^+ state in ^{134}Te [94, 99].

The 4_1^+ state in ^{134}Te is known to have a lifetime of $\tau = 1.96(16)$ ns [87]. Feeding and decaying transition

energies are 115 keV and 297 keV, respectively (see Fig. 2.16). Figure 2.28(a) shows delayed $LaBr_3$(Ce) energy projections after selecting ^{134}Te using a sum of HPGe gates. Both transitions below the isomer are clearly visible in the red spectrum. After applying an additional $LaBr_3$(Ce) gate on the 115 keV feeding transition, the 297 keV peak-to-background ratio is enhanced. To support the correct assignment to the ^{134}Te nucleus, coincidences with the HPGe detectors were used. The time difference spectrum after the second $LaBr_3$(Ce) gate on the decaying 297 keV transition is shown in Fig. 2.28(b). The distribution was fitted using a convolution of a prompt Gaussian and an exponential decay. The width of the prompt function is limited by the function given in Fig. 2.24(c). The resulting lifetime of $\tau = 2.02(14)$ ns is consistent with the previous measurements while slightly reducing its uncertainty. The error takes into account the variation of the fit region, background and prompt width and its effect is visualized by the shaded area in Fig. 2.28(b). Measuring the slope of the exponential tail without the convolution results in a value of 1.9(4) ns, see Ref. [99]. A cross check with HPGe-HPGe-ΔT data results in a limit of $\tau < 2.5$ ns which is consistent with the other measurements. This demonstrates the capability to measure lifetimes in the ns/sub-ns range using $LaBr_3$(Ce)-$LaBr_3$(Ce) time difference measurements and confirms the previous results. It is also shown that both, slope and convolution method, yield consistent results with HPGe and $LaBr_3$(Ce) detectors.

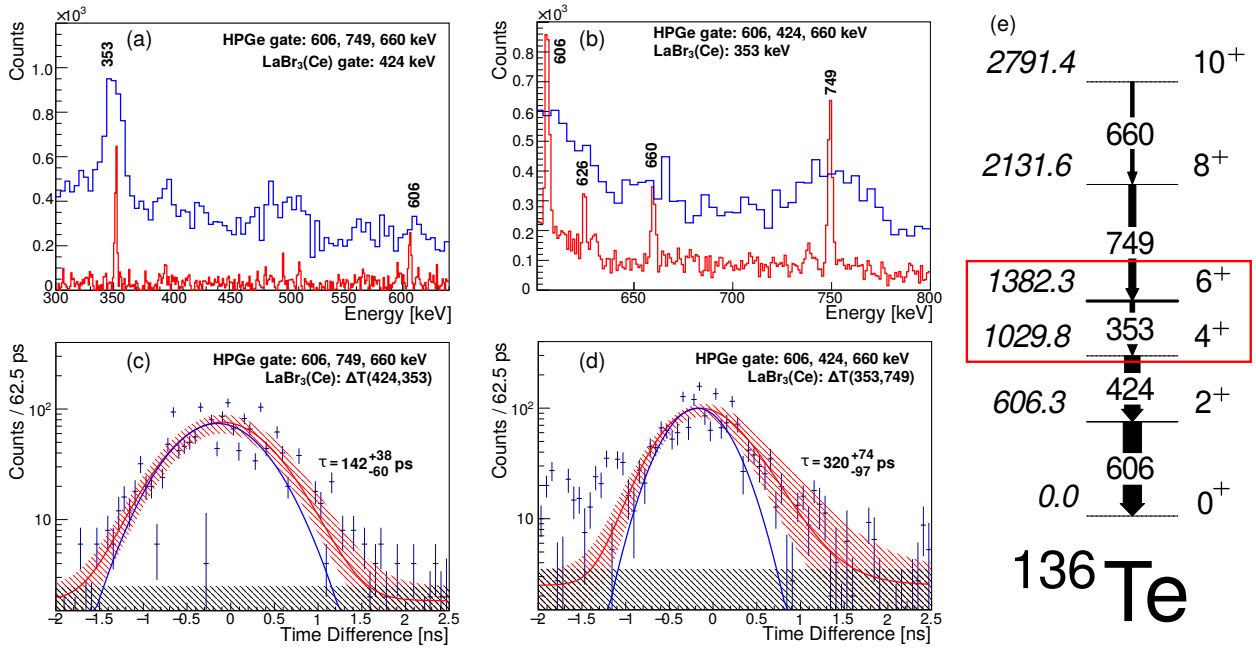

Figure 2.29: Energy projections for $LaBr_3$(Ce) (blue) and HPGe (red) after applying a first HPGe sum gate to select the ^{136}Te nucleus and a $LaBr_3$(Ce) gate on the de-exciting 424 or 353 keV transitions for the (a) 4^+ and (b) 6^+ states, respectively. Time-difference distributions to determine the lifetimes of the (c) 4_1^+ and (d) 6_1^+ states. (e) Relevant part of the level scheme in ^{136}Te with energies given keV [94].

Next, the method will be applied to excited states in $^{136}\mathrm{Te}$. The relevant yrast sequence for the lifetime analysis is shown in the level scheme of Fig. 2.29. The 4_1^+ state has a lifetime known from Coulomb excitation measurement which amounts to 100(14)ps [100]. Energy projections for $LaBr_3$(Ce) and HPGe detectors after the HPGe sum gate and an additional $LaBr_3$(Ce) gate on the 424 keV $4_1^+ \rightarrow 2_1^+$ decaying transition is shown in Fig. 2.29(a). In this spectrum, the 353 keV transition feeding the 4_1^+ state is nicely visible and no contaminants are around the peak of interest. The time difference between the 353 keV (feeder) and 424 keV (decay) transitions i.e., $\Delta T(424, 353)$, is used to measure the lifetime of the 4_1^+ state and is depicted in Fig. 2.29(c). The resulting lifetime τ of 142^{+38}_{-60} ps takes all previously described uncertainties into account, see Eq. (2.10). This value is consistent with the result from a Coulomb excitation experiment and confirms the sensitivity of the convolution method for sub-ns lifetime measurements.

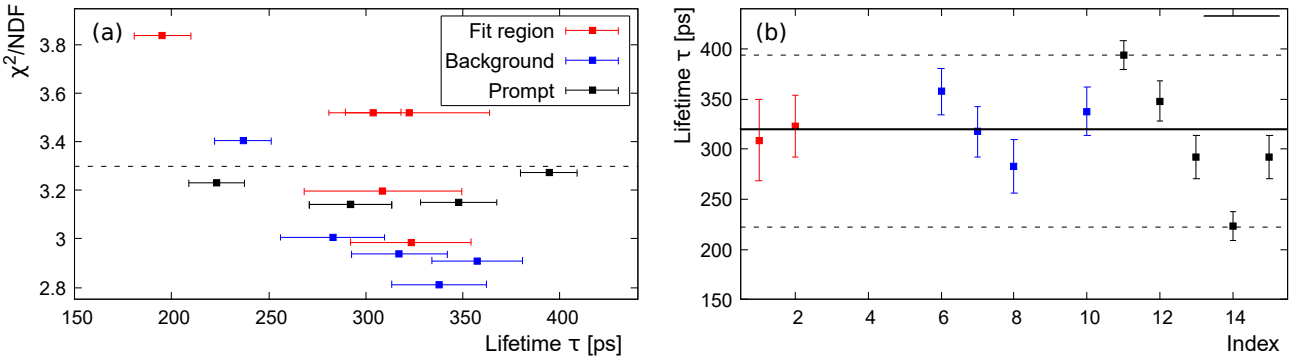

Figure 2.30: Determination of the lifetime error of the 6_1^+ state in $^{136}\mathrm{Te}$ using a χ^2 analysis. (a) χ^2/NDF as a function of lifetime value for the variation of the fit region (red) the background component (blue) and the width of the prompt Gaussian (black). (b) Fluctuation of lifetime results from different fits. The solid black line represents the mean lifetime and the dashed lines are asymmetric upper and lower error.

The previously unknown 6_1^+ lifetime is determined by measuring the $\Delta T(353, 749)$ time difference. As for the 4_1^+ state, energy projections and time difference spectra are shown in Fig. 2.29(b) and (d), respectively. After a $LaBr_3$(Ce) gate on the decaying 353 keV transition, the 749 keV peak appears rather cleanly. The obtained $\Delta T(353, 749)$ spectrum (see Fig. 2.29(d)) was fitted in the same way using the information on the prompt-time distribution from Fig. 2.24 and results in a lifetime of $\tau = 320^{+74}_{-97}$ ps.

The uncertainties are evaluated using a χ^2 analysis. From the variation of each contributing parameter in Eq. (2.10), a weighted average is obtained. Then, each residual from the weighted mean is calculated to find upper and lower limits for the lifetime value. This results in an asymmetric uncertainty and reflects the sensitivity range of the analysis technique. Fits with unreasonably high χ^2 values are excluded from this procedure. An example is shown in Fig. 2.30 for the lifetime of the 6_1^+ state in $^{136}\mathrm{Te}$. In Fig. 2.30(a), the χ^2/NDF values

are plotted for all the different fits. Values above a certain threshold (shown as dashed line) are excluded in the uncertainty analysis. This threshold is case dependent and for the 6_1^+ state in $^{136}\mathrm{Te}$ everything above $\chi^2/\mathrm{NDF} = 3.3$ is excluded, which corresponds to a 20 % increase with respect to the minimum χ^2/NDF value from all the applied fits. In Fig. 2.30(a) it can be seen that the fluctuation of the result is rather small for the variation of fit region and background component. On the other hand, the lifetime is very sensitive to the variation of the prompt region. In Fig. 2.30(b), the resulting mean lifetime from all the accepted fits is shown together with the fluctuation around that value indicated by dashed lines.

2.4 Results

2.4.1 Population and spectroscopy of fission fragments

Fission yields

The measurement of fission yields is essential not only for the population of neutron-rich nuclei but also the fission process itself and its application to nuclear energy. Fission yields of the ^{238}U(n,f) reaction were measured in Ref. [65] in a similar setup using the MINIBALL spectrometer [101]. The average neutron energy produced by the LICORNE neutron source was $E_n \approx 1.97$ MeV in Ref. [65] with respect to $E_n \approx 1.7$ MeV used in the present work.

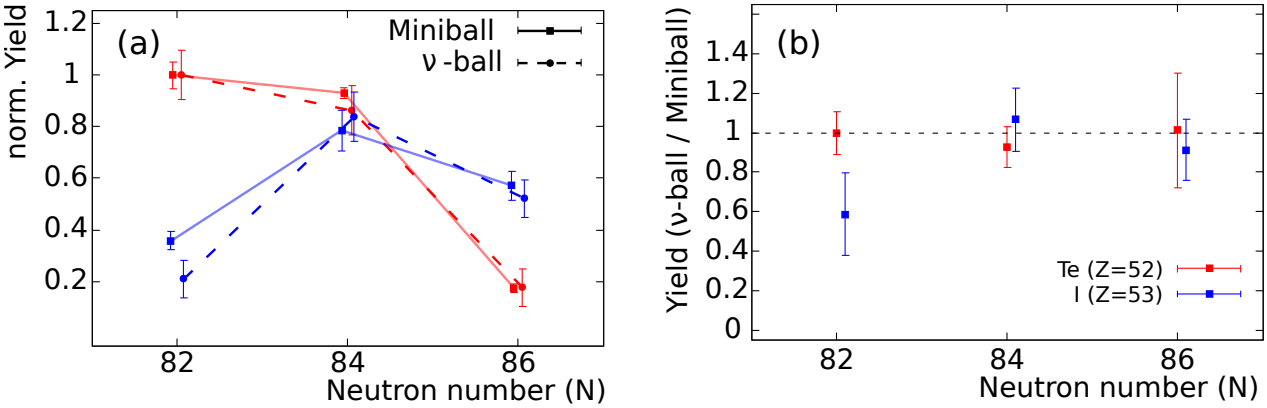

Figure 2.31: (a) ^{238}U(n,f) fission yields measured with the MINIBALL spectrometer (Ref. [65]) and the ν-ball array (this work) as a function of neutron number for the isotopes of interest. The yields are normalized to ^{134}Te. (b) Ratio of yields deduced from the present work and from the MINIBALL measurement as a function of neutron number.

For the even-even nuclei, the yields are deduced by gating on the $2_1^+ \rightarrow 0_1^+$ transition and summing up all intensities feeding the 2_1^+ state. Corrections for isomeric states and other direct ground state transitions are applied. Unobserved isomeric decays due to the limited time window from the beam pulse are accounted for according to the probability to decay within one beam pulse which is governed by the isomeric half-life. Furthermore, ground state transitions that have not been observed are also considered and their intensities estimated from previous fission studies. For odd-even nuclei, the intensities of all transitions feeding the first excited states are summed up. Estimations of unobserved ground state transitions based on previously reported data from spontaneous fission experiments are also included and result in a larger systematic uncertainty. Figure 2.31 shows the fission yields measured in this work compared with the ones from Ref. [65] as a function of neutron number. Figure 2.31(a) shows the yields for tellurium and iodine isotopes, normalized to the ^{134}Te

yield (which itself amounts to 4.18 %, see Tab. 2.1). The MINIBALL yields for the odd-Z iodine isotopes are estimated from the even-even measurement and their relative uncertainty was assumed to be 10 %. For all even-even nuclei, the measured yields match the previously reported values within the error margins. For the interpolated iodine isotopes, the value at $N = 82$ (^{135}I) is much smaller compared to the estimation based on the MINIBALL data. This discrepancy is further visualized by the plot in Fig. 2.31(b) where the ratio of the two measurements is plotted. All data points are around unity except the value of ^{135}I which is placed at about 0.6.

The technique to measure fission yields by γ-ray spectroscopy has some disadvantages for odd-even (and odd-odd) nuclei. Due to their increased level density, some intensities feeding the ground state may not be accounted for. However, in the cases of ^{135,137,139}I, a maximum of two ground state transitions were observed in this experiment (see next section about intensities and level schemes). For ^{135}I, the only ground state transition that was observed is the $(11/2^+_1) \rightarrow (7/2^+_1)$ transition. A possible $(9/2^+_1) \rightarrow (7/2^+_1)$ was not observed in the present data and has also not been reported in previous fission experiments [102, 103]. Thus, if at all, only a small contribution can be added due to the unobserved $(9/2^+_1) \rightarrow (7/2^+_1)$ transition and cannot account for the discrepancy of almost a factor two. It is important to note the semimagic nature of ^{135}I and its importance in nuclear reactor application as the precursors of the reactor poisoning ^{135}Xe [104].

Neutron evaporation channels

During the fission of a fissile system into two fragments, several neutrons are emitted. This number amounts to typically 2-3 neutrons per fission. The average neutron evaporation as a function of incident neutron energy is a well-known quantity and amounts to 2.7 for ^{238}U(n,f) fission at a neutron energy of 1.7 MeV [105].

However, little is known about the distribution of emitted neutrons for a given nucleus. Given the fact that only integer numbers of neutrons can be evaporated, a certain distribution of neutrons has to account for the averaged value. In this work, contributions from one to five evaporated neutrons are assumed to account for 100 % of the emission probability. Figure 2.32 shows the distribution of evaporated neutrons as a function of mass number for the tellurium isotopic chain. The average neutron emission per isotope $\bar{\nu}$ is consequently calculated by the first moment of the neutron distribution, i.e., $\bar{\nu} = \sum_{i=1}^{5} i \cdot p_i$. Here, p_i is the emission probability for a given number of neutrons emitted i and can be found in the respective cell of the matrix in Fig. 2.32. In the following, the approach will explained in more detail using the example of ^{134}Te.

The binary fission partner of ^{134}Te are, depending on the number of evaporated neutrons, $^{100-104}$Zr. The probability for a given neutron channel corresponds to the relative intensity of this particular partner nucleus with respect to the sum of all possible channels after gating on a transition in ^{134}Te. The intensities for even-even

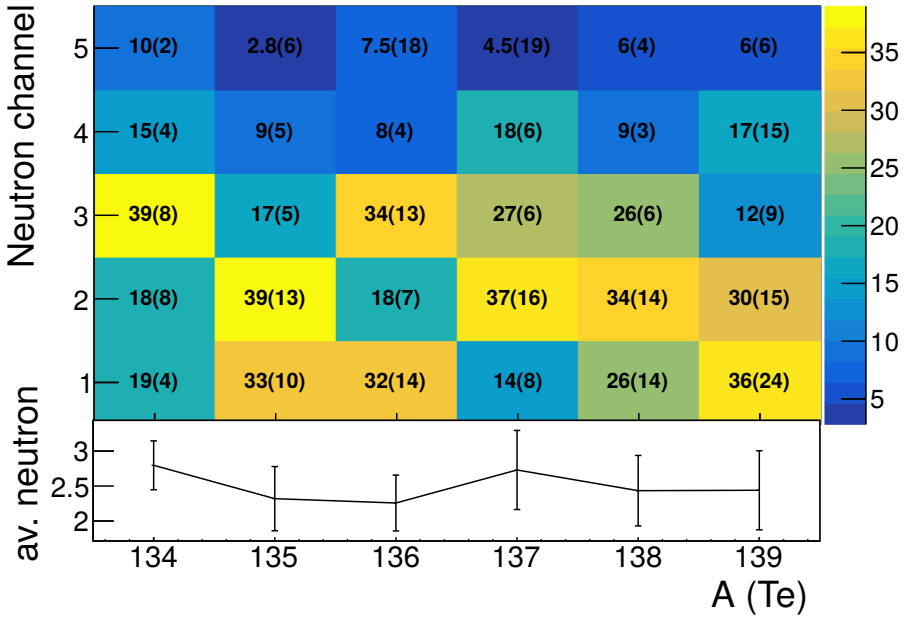

Figure 2.32: Evaporated neutrons per fission fragment (top) and average neutron distribution (bottom) against mass of the tellurium isotopes populated in the ^{238}U(n,f) reaction at an average neutron energy of 1.7 MeV. The numbers are given as relative number in % (assuming 100 % for up to five neutrons).

partner fragments were deduced by measuring the intensity of the corresponding $2_1^+ \rightarrow 0_1^+$ transition. For the odd-A cases, the unknown intensity was estimated based on known values from Refs. [106, 107]. In ^{103}Zr, for example, the unknown feeding is deduced relative to the 147 keV $(9/2_1^-) \rightarrow (7/2_1^-)$ transition and, therefore, $I(^{103}\mathrm{Zr}) = I_{109} + I_{256} + I_{unobserved} = 1.96 \cdot I_{147}$. The intensities from ^{103}Zr are taken from Ref. [106]. The contribution from the two unobserved ground-state transitions, also previously unobserved in fission, is assumed to be of the order of 5 % which takes into account the observation limit of the corresponding γ rays. This example of ^{103}Zr was used for the ^{134}Te (2n channel) and ^{135}Te (1n channel). The procedure was applied for all tellurium isotopes up to mass 138. As it is not possible to apply a clean gate on the 271 keV ground state transition in ^{139}Te from the full projection data, a relative measurement based on ^{138}Te is proposed. Inverse gates on the shared binary fission partners $^{96-99}$Zr are applied. The relative intensity of the 271 keV $(9/2_1^-) \rightarrow (7/2_1^-)$ to the $(2_1^+) \rightarrow (0_1^+)$ transition in ^{138}Te is used to determine the neutron channels relative to ^{138}Te. For the five neutron evaporation channel ^{95}Zr, a value of < 6 % is assumed, based on comparison with the other tellurium isotopes.

The average number of evaporated neutrons is shown in the bottom panel of Fig. 2.32 and is between 2.5 and 2.7 which is expected for this type of reaction. More than 50 % is concentrated in the two and three neutron evaporation channel with a small contribution from one and four neutrons of around 20 %. The evaporation of five neutrons is less significant with lower than 10 %, but not negligible and more probable as in thermal induced

fission (see, for example, Ref. [108]). An important observation can be made from Fig. 2.32 with respect to odd-even effects. The neutron emission peaks at $3n$ for the even fragments $^{134,136,138}\mathrm{Te}$ and at $2n$ for the odd fragments $^{135,137,139}\mathrm{Te}$. This means that the strongest binary partner for an even A fragment is the same as for the $A+1$ fragment and their intensities are close or the same. Hence, the strongest fission partner is always an even fragment which may present evidence for odd-even effects in the neutron evaporation probability of fast neutron-induced fission. This is the first time such an investigation has been performed and yields valuable insights into the mechanisms of nuclear fission. It will be interesting to compare this to other types of fission reactions which is outside the scope of this work.

γ-ray intensities and level schemes for the nuclei of interest

The production of neutron-rich fission fragments yields valuable information on general fission properties and is important for the design of next generation radioactive beam facilities. The population of states in a given fragment gives insights into the generation of angular momentum in nuclear fission, see Ref. [111]. Furthermore, correlations between different observables are of particular importance to gain insights into the fission mechanism itself. In this section, the population of neutron-rich isotopes beyond $^{132}\mathrm{Sn}$ will be discussed from the different measurements with the ν-ball array. This is done by looking at the γ-ray intensities detected using the HPGe detectors from the ν-ball array. Single- or double-gated HPGe spectra are used to measure the number of counts in each peak and, after correction for efficiency, are normalized to the strongest transition. The efficiency curve for the $^{238}\mathrm{U}$(n,f) reaction at 1.7 MeV average neutron energy is shown in Fig. 2.4. The efficiency for the second $^{238}\mathrm{U}$(n,f) experiment was slightly lower. No self-absorption effects were present in the $^{252}\mathrm{Cf}$ source run. The results of the transitions observed in the first $^{238}\mathrm{U}$ run are shown in Fig. 2.33 for the tellurium isotopes and Fig. 2.35 for the iodine isotopes. Details on the intensities in addition to the ones from the other experiments can be found in the appendix A. Because of the limited measurement time for the $^{252}\mathrm{Cf}$ and the second $^{238}\mathrm{U}$ experiment, only strong γ rays are listed for those reactions. The excitation energies are always determined from the first $^{238}\mathrm{U}$ measurement.

From the production cross section in Tab. 2.1 it is evident, that of all investigated nuclei $^{134}\mathrm{Te}$ is the strongest produced in the $^{238}\mathrm{U}$(n,f) reaction. This explains the abundance of levels observed for this nucleus with respect to the others. Spins up to $J = 15\ \hbar$ in $^{134}\mathrm{Te}$ or $J = 33/2\ \hbar$ in $^{137}\mathrm{I}$ were observed, comparable to measurements with data obtained from spontaneous fission of $^{248}\mathrm{Cm}$ [102] but higher than observed in thermal neutron-induced fission on $^{235}\mathrm{U}$ [112]. The population in fast neutron-induced fission provides valuable input on the population of angular momentum and excitation energy of fission fragments [111].

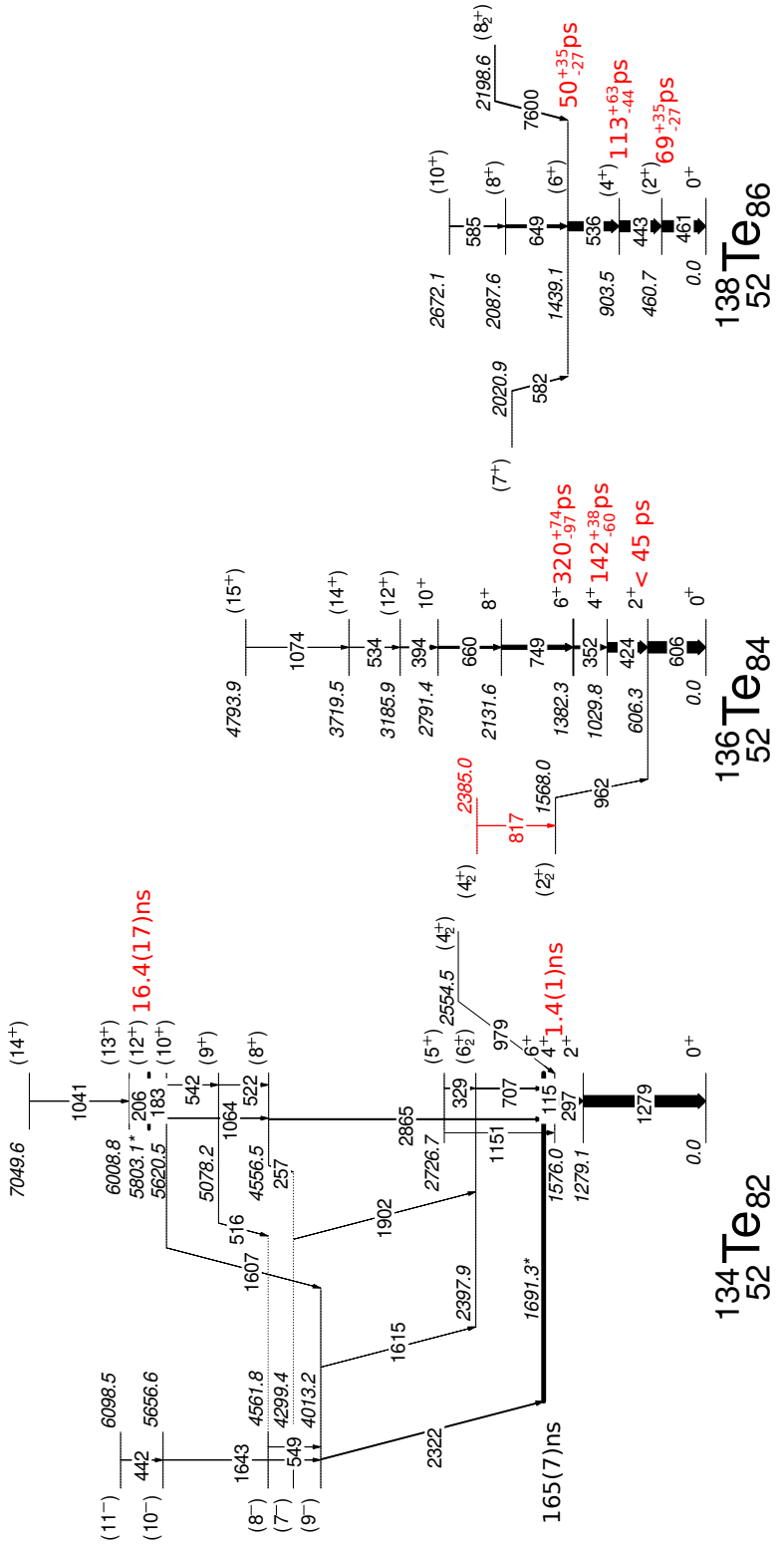

Figure 2.33: Experimental level schemes for ^{134,136,138}Te isotopes observed in the ^{238}U(n,f) reaction [94]. The intensities are normalized to the $2_1^+ \rightarrow 0_1^+$ transition. Half-lives (lifetimes) of excited states are given in ns (ps). New information is highlighted in red. Spin and parity assignments and literature values are taken from the respective evaluated data sheets [87, 109, 110].

In the following, the population of different nuclei will be compared with a focus on the first $^{238}\mathrm{U}$ measurement. Fig. 2.33 shows the level schemes of $^{134,136,138}\mathrm{Te}$ and Fig. 2.35 the ones of $^{135,137,139}\mathrm{I}$ isotopes as observed in this work. When looking at the even-even nuclei, the $6_1^+ \rightarrow 4_1^+ \rightarrow 2_1^+ \rightarrow 0_1^+$ cascade is observed with similar intensities (see Tabs. A.1, A.2 and A.3). A notable difference in the yrast sequence is present for the $8_1^+ \rightarrow 6_1^+$ transition. It evolves from 9.9(11) % in $^{134}\mathrm{Te}$, to 39(4) % and 25(3) % in $^{136}\mathrm{Te}$ and $^{138}\mathrm{Te}$, respectively. This change from the semimagic $^{134}\mathrm{Te}$ to $^{136}\mathrm{Te}$ can be further underlined by the high excitation energy of the 8_1^+ state in $^{134}\mathrm{Te}$ due to its core breaking nature.

Another interesting difference lies in the non-yrast states which are significantly stronger observed in $^{134}\mathrm{Te}$ compared to $^{136,138}\mathrm{Te}$. In $^{134}\mathrm{Te}$, such transitions have significant contributions (e.g., 5.9(6) % for the $(6_2)^+ \rightarrow 6_1^+$ transition) with respect to the low intensity in $^{136}\mathrm{Te}$ (< 0.5 %) and the non-observation in $^{138}\mathrm{Te}$. Additionally, no negative parity states in $^{136,138}\mathrm{Te}$ are observed as in $^{134}\mathrm{Te}$. This can be explained by the nature of the negative parity states requiring the breaking of a neutron pair and the involvement of orbitals with different parity. While for $^{134}\mathrm{Te}$, this results in a core breaking configuration, it is less likely to have such states when moving away from the closed shell. Inside the model space, negative parity states would have to involve the $\nu(0h_{9/2})$ or $\pi(0h_{11/2})$ orbitals which are both very high in energy (see Fig. 1.6). A similar observation of non-yrast and negative parity states in the $N = 82$ isotone $^{135}\mathrm{I}$ compared to the non-observation in the $^{137,139}\mathrm{I}$ isotopes can be stated (see Tabs. A.4, A.5 and A.6). This will be addressed in Sec. 2.5.

As can be seen in Fig. 2.33, new information on a transition feeding the non-yrast (2_2^+) was obtained within this work. The energy was already determined to be 810(15) keV with a large uncertainty [113]. In order to measure this transition more accurately, the good energy resolution of the HPGe detectors present in this experiment is utilized. Figure 2.34 shows three γ-ray spectra with different gates involving the 606 keV, $2_1^+ \rightarrow 0_1^+$ transition in the region where the $(4_2^+) \rightarrow (2_2^+)$ transition is expected. In the 606-962 keV gate combination (red), a strong peak at 817 keV is visible which is consistent with the previous findings. A small contribution from a 814 keV transition is present, originating from contamination of $^{140}\mathrm{Xe}$ which has a much higher production yield than $^{136}\mathrm{Te}$. In addition, a gate on the 606 keV transition together with several zirconium partner nuclei is shown (blue). A clear double peak structure of 814 and 817 keV is emerging. Note that the background contribution is much higher and, thus, the 814 keV line is stronger. To confirm that this peak is the transition of interest and it is correctly placed in the $^{136}\mathrm{Te}$ level scheme, a spectrum gated on 606 - 424 keV γ rays is provided (black), where, as expected, no such peak can be seen. In coincidence relations with the partner nuclei and the 2_2^+ transition of 962 keV, the 817 keV transition can still be seen, proving its position in the level scheme. The energy of this transition including systematic and statistical uncertainties can be fixed to 817(1) keV which results in a new

excitation energy of 2385.0(13) keV for this state.

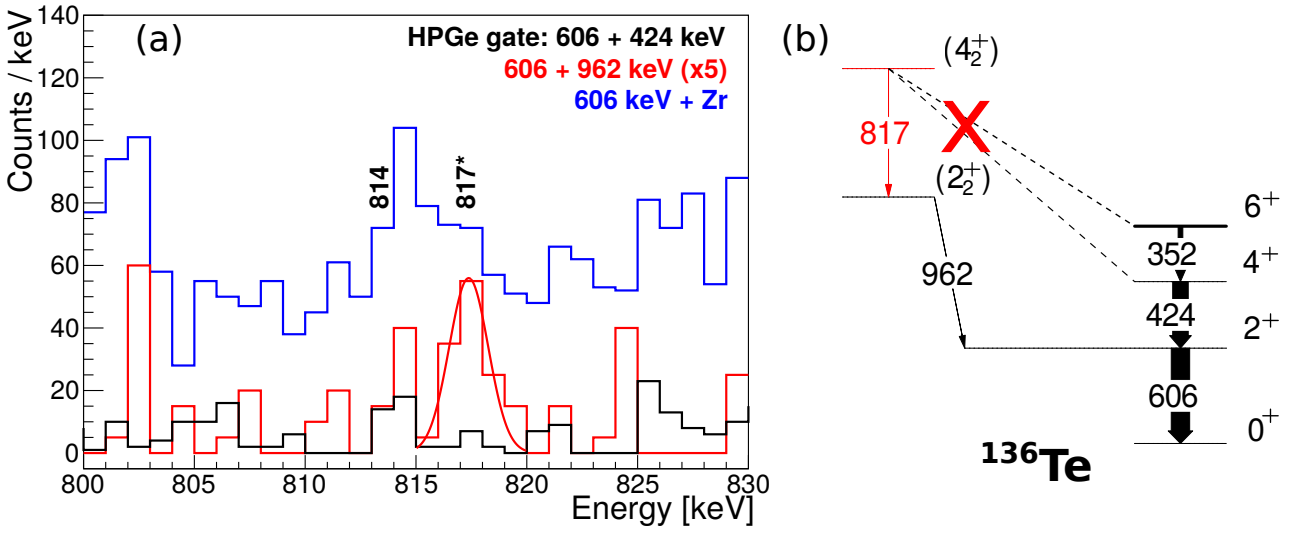

Figure 2.34: Prompt HPGe spectrum gated on the 606 keV, $2_1^+ \rightarrow 0_1^+$ transition in ^{136}Te and (1): the 424 keV, $4_1^+ \rightarrow 2_1^+$ transition (black), (2): the 962 keV $(2_2^+) \rightarrow 2_1^+$ transition (red) and (3): zirconium partner gates (blue). Transitions are labeled with their respective energy and the newly assigned transition in ^{136}Te is highlighted with an asterisk. Adapted from Ref. [94].

In this data, no direct branch to the ground state is observed which suggests a spin difference of $\Delta J \leq 2$. From the preferred multipolarity (either $M1$, $E2$ or mixed $M1/E2$) of such a transition, the spin can be fixed to either $(3^+, 4^+)$ for the 2385.0 keV state. Because of the close energy of these states predicted from shell-model calculations at 2277.4 keV for the 4_3^+ state and 2308.1 keV for $J^\pi = 3^+$ [94], both candidates are supported by the shell model. As no distinction between multipolarities is possible, a spin of (4^+) was assumed in this work [94]. An upper limit for the intensity of this $(4_2^+) \rightarrow (2_2^+)$ transition relative to the $2_1^+ \rightarrow 0_1^+$ intensity is deduced to be $< 0.25\%$, see Tab. A.2.

The reconstructed level schemes from transitions observed in the odd-Z iodine isotopes are shown in Fig. 2.35. The ground states in these nuclei are dominated by the unpaired proton in the $\pi(0g_{7/2})$ shell, resulting in a $(7/2^+)$ ground state. The intensities are more fragmented for those odd-A isotopes compared to the even-A tellurium isotones, but the overall systematic decrease in intensity when moving up the yrast sequence is still present. The increase of collectivity as a function of neutron number N can be clearly seen in the drop of excitation energy of the $(11/2_1^+)$ state from 1134 keV in the semimagic ^{135}I isotope down to 620 keV and 435 keV for ^{137,139}I, respectively. Another difference is the emergence of two bands build on top of the $(11/2_1^+)$ and $(9/2_1^+)$ states when moving away from the closed shell at $N = 84, 86$. This leads to a large number of inter-band transitions. In ^{137}I, these inter-band transitions are sometimes stronger than the intra-band transitions

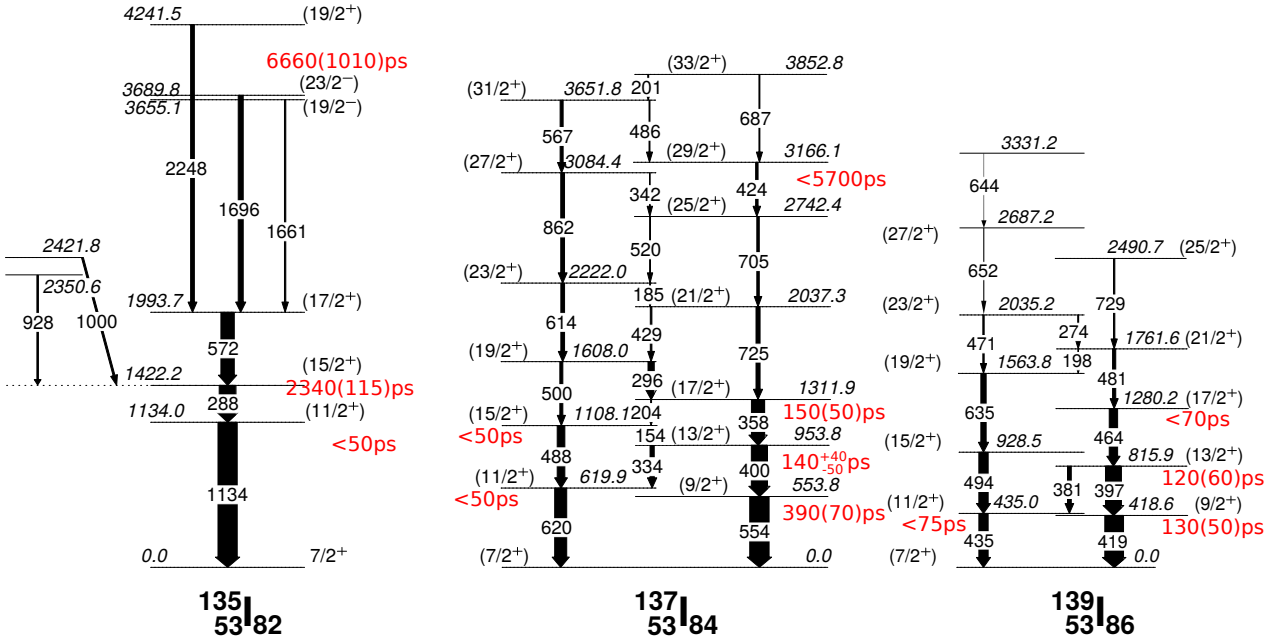

Figure 2.35: Same as Fig. 2.33 but for ^{135,137,139}I [95].

within a single band.

The level structure of the semimagic ^{135}I resembles the one of ^{134}Te and transitions decaying from states of similar origins were observed. Similar to the observation of the higher $6^+_1 \rightarrow 4^+_1$ intensity of the even-A tellurium isotopes measured in this work compared to ^{248}Cm spontaneous fission data was made for the iodine isotopes. The $(17/2^+_1) \rightarrow (15/2^+_1)$ yrast transition is observed with an intensity of 72(9) % compared to 34(7) % from the ^{248}Cm(sf) reaction (see Tab. A.4). Likewise, the 500 keV $(19/2^+_1) \rightarrow (15/2^+_1)$ transition in ^{137}I is about a factor three stronger in this experiment compared to the ^{248}Cm data given in Tab. A.5. Another difference when comparing the γ-ray intensities in ^{135}I is the stronger population of non-yrast states in the present ^{238}U(n,f) experiment compared to the ^{248}Cm(sf) measurement. For ^{139}I, the intensities are more comparable to the previous data [114] with the exception of the intensities of the transitions de-exciting the first excited $(11/2^+_1)$ and $(9/2^+_1)$ states (see Tab. A.6). In the present measurement, the 419 keV $(9/2^+_1) \rightarrow (7/2^+_1)$ ground state transition is seen strongest and in Ref. [114] the $(11/2^+_1) \rightarrow (7/2^+_1)$ transition is seen strongest.

2.4.2 Isomers above ^{132}Sn

Isomeric states such as seniority isomers or energy traps near closed shells are particularly interesting because they possess relatively pure wave functions. If the half-life is long enough compared to the time resolution of the HPGe detectors (see Fig. 2.4), it can be measured by projecting the time distribution of a particular γ ray with

respect to the beam pulse. The beam pulsation of 400 ns allows for a clean separation of prompt and delayed γ rays and is well-suited for isomers in the half-life range of several tens of ns to hundreds of ns.

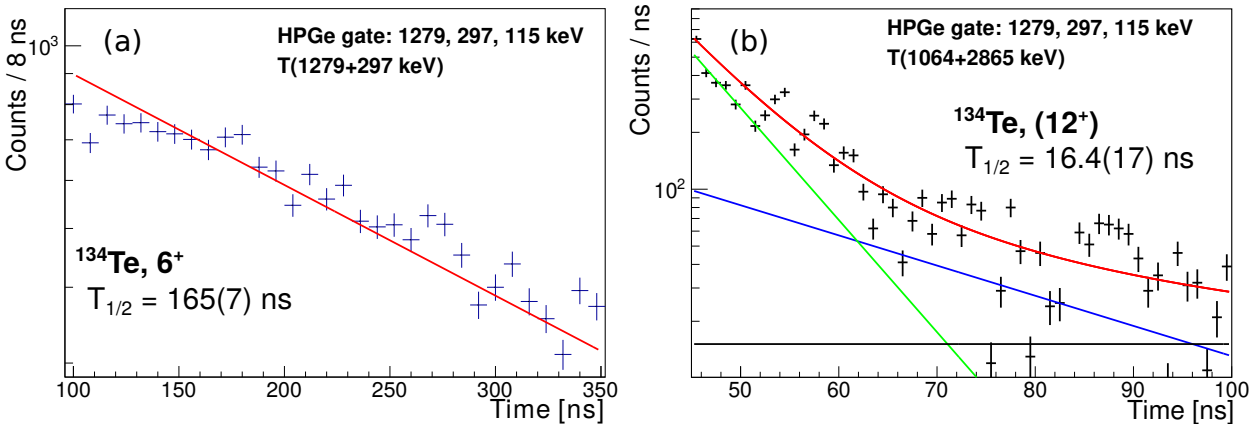

Figure 2.36: Time distributions of the (a) 6_1^+ isomer and the (b) (12_1^+) isomer in ^{134}Te. The time distribution is fitted with (a) a single exponential decay or (b) an exponential decay curve (green) with time-dependent (blue) and constant (black) background (b). Each figure is labeled with its state, gates and the resulting half-life. Taken from Refs. [86, 94].

In ^{134}Te, a 6_1^+ isomer based on a pure proton $\pi(0g_{7/2}^2)$ configuration is known with $T_{1/2} = 164.1(9)$ ns [87]. This half-life value allows for the measurement of it via HPGe timing with respect to the beam pulse (method A in Fig. 2.23). It decays via transitions of 115, 297 and 1279 keV to the ground state. The background subtracted time distribution is shown in Fig. 2.36(a) and from an exponential fit, a half-life of 165(7) ns can is obtained.

The time distribution to measure the $T_{1/2}$ of the (12_1^+) state in ^{134}Te is shown in Fig. 2.36(b). First, a delayed HPGe sum of single gates on transitions below the 6^+ isomer is applied to tag the nucleus. In a second step, the summed time distribution of the 1064 and 2865 keV transitions is projected and fitted with an exponential decay and a time-dependent background. The background contribution is obtained for gates on both sides of each energy peak and is included in the fit as a fixed parameter. Note that the 183 keV transition is not used due to the low yield and the moderate time resolution at lower energies. From the fit, a value of $T_{1/2} = 16.4(17)$ ns is obtained, consistent with the only previous measurement of $18(2)$ ns [103]. This isomer is due to a core breaking of the closed neutron shell, see Tab. 2.4.

In addition to the half-lives measured in ^{134}Te, the half-live of the 6_1^+ isomer in ^{132}Te was remeasured. A value of $T_{1/2} = 142(9)$ ns was obtained, in accordance with the previously reported value of $T_{1/2} = 145(8)$ ns [41]. The half-lives measured in this work are summarized in Tab. 2.4. Furthermore, the isomeric decay schemes of ^{134}Sn and ^{135}Sb were confirmed by identifying the γ rays belonging to those decays. Note that while the level scheme of ^{134}Sn could be reproduced, it was expected to be stronger populated in the ^{238}U(n,f) reaction.

Table 2.4: Summary of isomer half-lives measured in this work. The gates to determine the half-live are also listed. Main configurations are based on shell-model calculations discussed in Sec. 2.5.

Nucleus	J^π	Main Config.	$T_{1/2}$ [ns]		Gates [keV]
			This work	Literature	
^{132}Te	6_1^+	$\pi(0g_{7/2}^2)$	142(9)	145(8) [41]	974, 697
^{134}Te	6_1^+	$\pi(0g_{7/2}^2)$	165(7)	164.1(9) [87]	297, 1279
	(12_1^+)	$\pi(0g_{7/2}^2)\nu(0h_{11/2}^{-1}1f_{7/2}^1)$	16.4(17)	18(2) [87]	1064, 2865
^{135}I	$(23/2_1^-)$	$\pi(0g_{7/2}^2\,0h_{11/2}^1)$	4.6(7)	≈ 5 [102]	1696
^{137}I	$(29/2_1^+)$	$\nu(1f_{7/2}^2)\pi(0g_{7/2}^2\,1d_{5/2}^1)$	< 4	≈ 4 [115]	424

2.4.3 Sub-ns lifetime measurements

Lifetimes of low-lying excited states are important to probe the evolution of nuclear collectivity and benchmark theoretical calculations due to its sensitivity in the matrix elements. In the following, results of lifetime measurements in neutron-rich tellurium and iodine isotopes beyond ^{132}Sn are presented. The procedure was explained in detail in Sec. 2.3 and is the same for all excited states. Because of the lifetime range, the $LaBr_3$(Ce)-$LaBr_3$(Ce)-ΔT data were used to measure the lifetimes (see method D in Fig. 2.23). HPGe sum gates are used in all cases to select the nucleus of interest and construct $LaBr_3$(Ce) energy-energy-ΔT cubes.

The case of ^{138}Te

The production yield of the ^{138}Te isotope is approximately a factor five lower than for the ^{136}Te isotope (see Tab. 2.1) and, hence, lower statistics is expected compared to the spectra of ^{136}Te shown in Fig. 2.29. In ^{138}Te, lifetimes of the yrast states up to the (6_1^+) state were measured for the first time.

Figure 2.37(a) shows the HPGe and $LaBr_3$(Ce) energy projection after gating on the 649 keV $(8_1^+) \rightarrow (6_1^+)$ transition in ^{138}Te and the 1222 keV $2_1^+ \rightarrow 0_1^+$ transition in the strongest partner nucleus ^{98}Zr. All the transitions below the (6_1^+) states are visible in the spectrum which can be used for the lifetime analysis. In Fig. 2.37(b) the partial level scheme of ^{138}Te is shown with all the relevant feeder-decay combinations used in the analysis.

For the 2_1^+ state, the nucleus of interest is selected via a HPGe sum gate on the 536 keV and 649 keV transitions in ^{138}Te and an additional HPGe gate on the 1222 keV, $2_1^+ \rightarrow 0_1^+$ transition in ^{98}Zr. Then, the $LaBr_3$(Ce) $\Delta T(461, 443)$ time difference is used to gain information on the lifetime of the (2_1^+) state in ^{138}Te. A comparison to the HPGe data after applying the $LaBr_3$(Ce) gate is done to check for the cleanliness of the $LaBr_3$(Ce) gates. The resulting time distribution is shown in Fig. 2.38(a) with a representative fit result. For the

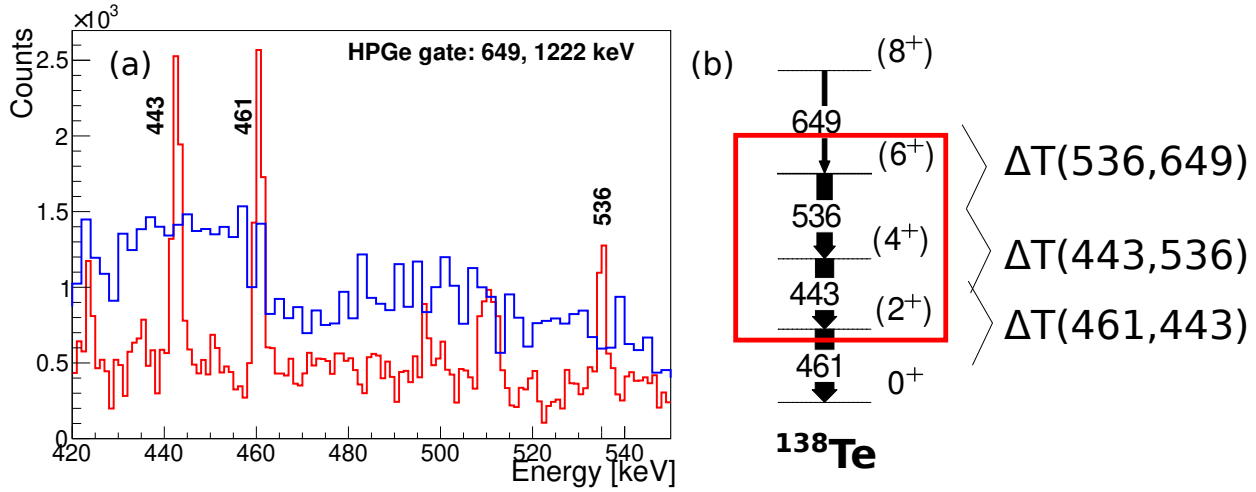

Figure 2.37: (a) HPGe (red) and $LaBr_3$(Ce) energy spectra showing transitions belonging to ^{138}Te relevant for the lifetime analysis. (b) Partial level scheme of ^{138}Te highlighting the important feeder-decay combinations for the lifetime analysis of the $(2_1^+), (4_1^+), (6_1^+)$ states.

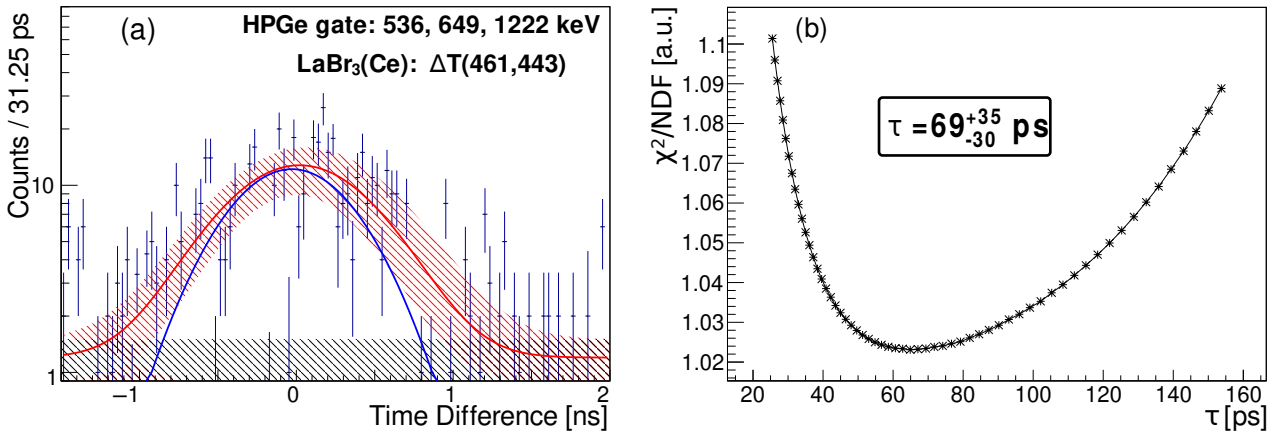

Figure 2.38: (a) Time distribution and fit for the lifetime determination of the (2_1^+) in ^{138}Te. (b) χ^2/NDF as a function of lifetime deduced from the fit [94].

convolution fit, the prompt width was varied in the range determined in Fig. 2.24(c) for that respective energy combination. Due to the limited data and the small energy difference of feeding and decaying transition, a careful χ^2/NDF analysis was performed. From different fits on the time distribution, the χ^2/NDF was extracted for a given value of the (2_1^+) lifetime. This dependency is plotted in Fig. 2.38(b) and a minimum around 70 ps is visible. A lifetime of 69^{+35}_{-30} ps was obtained for the lifetime of the (2_1^+) state in $^{138}\mathrm{Te}$.

The lifetime of the 4_1^+ state was measured by using the $\Delta T(443, 536)$ feeder-decay combination (see Fig. 2.37). After applying a HPGe sum gate, $LaBr_3$(Ce) gates on feeder and decay are applied. The time distribution is shown in Fig. B.1 of the appendix B. A resulting lifetime of $\tau = 113^{+63}_{-44}$ ps was obtained [94]. The large uncertainty comprises all contributions mentioned in Eq. (2.10). The error is dominated by the low statistics and the fluctuations due to the variation of prompt width.

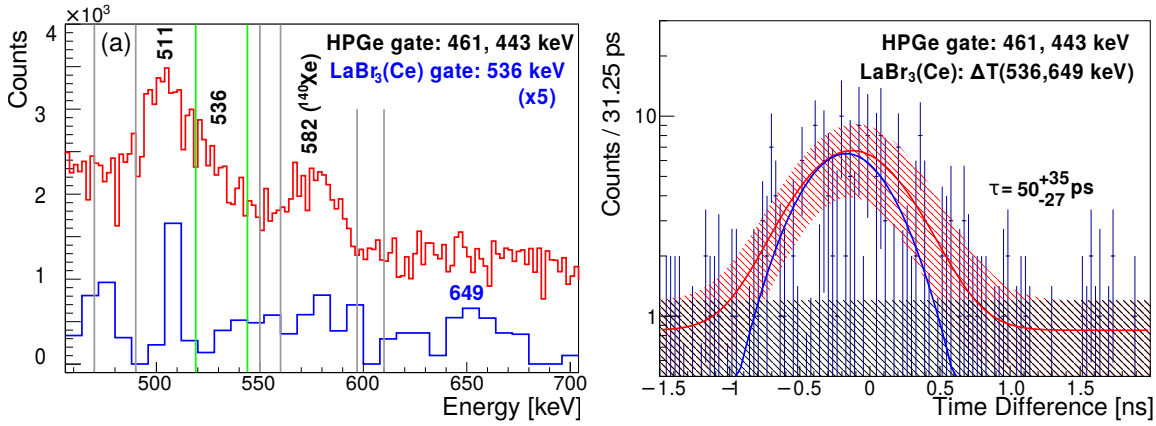

Figure 2.39: Lifetime measurement of the 6_1^+ state in the $^{138}\mathrm{Te}$. (a) $LaBr_3$(Ce) energy projection with a selection gate on HPGe detectors (red) and an additional $LaBr_3$(Ce) decay gate (blue). The $LaBr_3$(Ce) gate is indicated by vertical lines (green) with various background regions (gray lines). (b) Time difference spectrum between the 536 - 649 keV transitions. Taken from Ref. [94].

The lifetime determination of the (6_1^+) state in $^{138}\mathrm{Te}$ is shown in Fig. 2.39. To select the cascade of interest, HPGe gates on the 461 keV $(2_1^+) \rightarrow 0_1^+$ transition and the 443 keV $(4_1^+) \rightarrow (2_1^+)$ transition are used. $LaBr_3$(Ce) energy projections after that HPGe sum gate (red) and an additional $LaBr_3$(Ce) gate (blue) in $^{138}\mathrm{Te}$ are shown in Fig. 2.39(a). A peak at 582 keV mainly originating from $^{140}\mathrm{Xe}$ dominates the spectrum but a structure around $530-540$ keV is also visible. Gating on this structure (indicated by green lines in Fig. 2.39) and subtracting background in the highlighted regions results in the spectrum shown in blue. A small peak around 650 keV belonging to the 649 keV, $(8_1^+) \rightarrow (6_1^+)$ transition can be seen. The $\Delta T(536, 649)$ time difference spectrum to extract the lifetime of the (6_1^+) state is presented in Fig. 2.39(b). From the convolution fit, a lifetime of $\tau = 50^{+35}_{-27}$ ps is deduced. As this value is at the limit of the sensitivity, it cautiously takes into consideration all the

uncertainty factors from Eq. (2.10). In this case, the largest contribution to the uncertainty comes not only from the statistical fluctuation when varying the fit region but also the systematic uncertainty when varying the background component of the fit. Despite the large uncertainties in all these lifetimes, reflected by the low isotopic population in this reaction and the low detection efficiency, this measurement presents the first lifetime information on excited states in $^{138}\mathrm{Te}$.

Lifetimes in ^{137,139}I

In the following, the lifetime measurements in the iodine isotopes will be discussed in detail for the $(9/2_1^+)$ states in $^{137,139}\mathrm{I}$ according to the procedure explained in Sec. 2.3. The relevant parts of the level schemes are shown in Fig. 2.40(a) for $^{137}\mathrm{I}$ and (b) for $^{139}\mathrm{I}$.

For the $^{137}\mathrm{I}$ nucleus, the lifetime of the $(9/2_1^+)$ state can be obtained by measuring the $\Delta T(554, 400)$ time difference. To tag the nucleus and the cascade of interest, a HPGe gate on 358 keV or 725 keV above the $(13/2_1^+)$ state is used. Afterwards, a $LaBr_3$(Ce) gate on the decaying 554 keV transition is applied. The resulting energy projections are shown in Fig. 2.40(b) for $LaBr_3$(Ce) (blue) and HPGe (red) detectors. The $LaBr_3$(Ce) spectrum was generated from HPGe-$LaBr_3$(Ce)-$LaBr_3$(Ce) triple coincidences and the HPGe spectrum from HPGe-$LaBr_3$(Ce)-HPGe events. The 400 keV feeding transition is clearly visible in both spectra (in Fig. 2.40(a)) as a result of the applied gates. A relatively high peak-to-background ratio of around $P/B = 3.0(3)$ was obtained in this case. This value was obtained using a total multiplicity condition $M \geq 3$ in order to maximize statistics. A minimum total multiplicity of $M \geq 5$ as mentioned in Sec. 2.3 would correspond to a value of $P/B = 4.5(2)$. Due to the investigation of the spectra using the better energy resolution of the HPGe detectors, the selection is chosen appropriately to contain clean γ rays of interest.

In a last step, a second $LaBr_3$(Ce) gate is applied on the feeding transition to generate the time difference spectrum shown in Fig. 2.40(c). The gate includes a background subtraction of regions around the peak of interest. Due to the low statistics, this may result in statistical fluctuations and over subtraction of individual bins. These fluctuations were considered by applying a full minimization procedure when determining the lifetime result as shown for $^{136}\mathrm{Te}$ in Sec. 2.3.6. The time distribution is fitted according to Eq. (2.9). The range that was used for the prompt width is in accordance with the investigation of the prompt widths at these energies, see Fig. 2.24(c) in Sec. 2.3. A lifetime result of $\tau = 390(70)$ ps is obtained. For this result, the dominating error contribution stems from the variation of the prompt width and the statistical fluctuation was rather small.

To measure the lifetime of the $(9/2_1^+)$ state in the $^{139}\mathrm{I}$ isotope, the $\Delta T(419, 397)$ time distribution is considered. To tag the $^{139}\mathrm{I}$ nucleus, a HPGe gate on the 464 keV $(17/2_1^+) \rightarrow (13/2_1^+)$ transition is used. Then, a

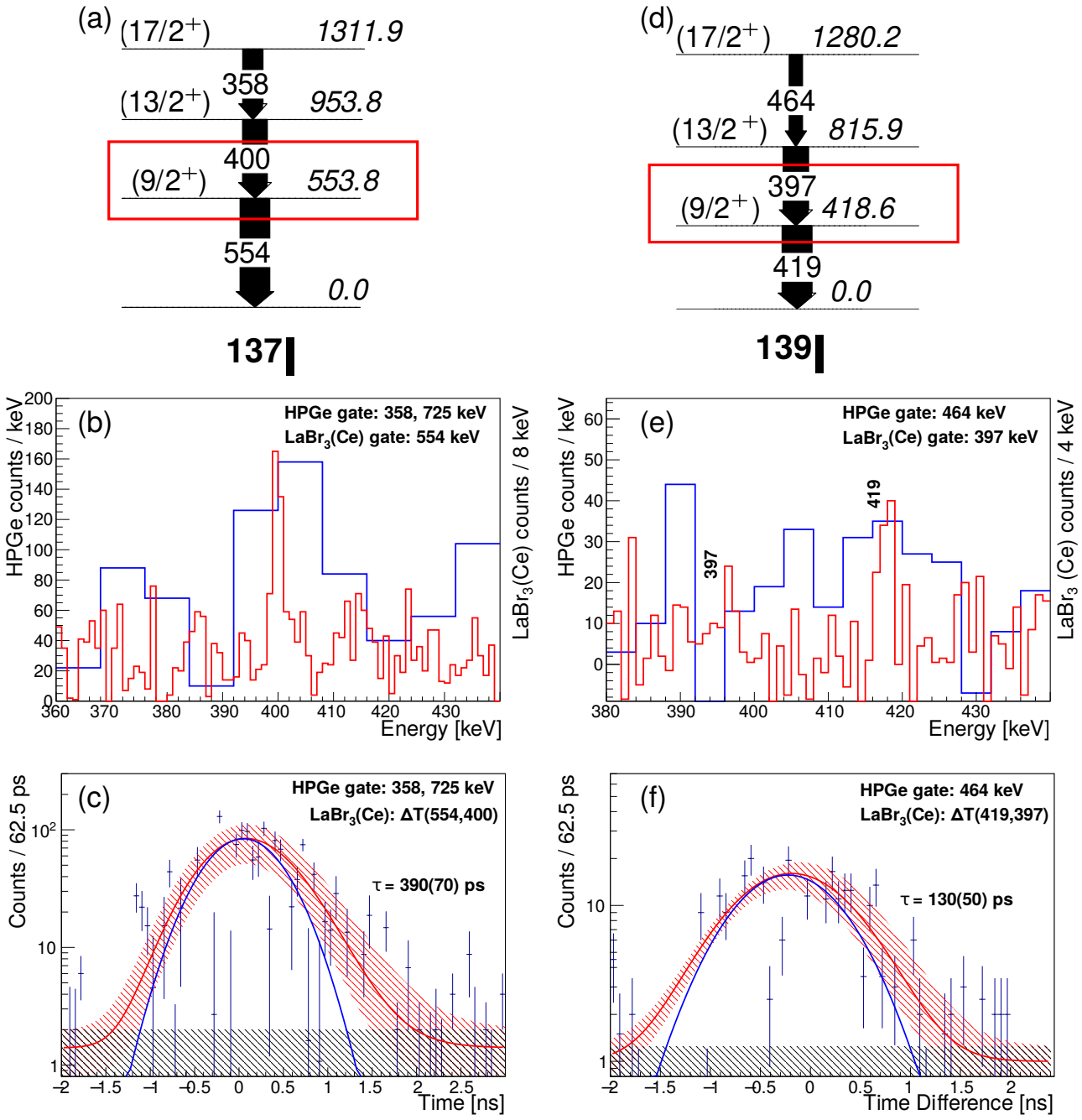

Figure 2.40: Lifetime measurements for the $(9/2_1^+)$ states in (a-c) ^{137}I and (d-f) ^{139}I. Each column shows the relevant part of the level scheme (a,d), energy projections (b,e) and time difference spectra (c,f). Adapted from Ref. [95].

$LaBr_3$(Ce) gate on 397 keV is applied, resulting in the spectra of Fig. 2.40(e). Despite the higher background level compared to the ^{137}I case and the reduced statistics due to the lower population of ^{139}I, a clear identification of the 419 keV transition decaying from the $(9/2_1^+)$ state is possible. With a peak-to-background ratio of $P/B = 1.7(3)$ it is about a factor of two lower than for the less exotic ^{137}I. The time difference spectrum after applying the additional 419 keV gate is presented in Fig. 2.40(f). The different slope on the right side of the distribution when compared to ^{137}I already indicates a shorter lifetime of the state in ^{139}I. This is confirmed by the result of the applied convolution fit, emerging in a value of $\tau = 130(50)$ ps. As expected because of the lower population, the statistical uncertainty is larger compared to ^{137}I and dominates the lifetime result in ^{139}I.

In addition to the $(9/2_1^+)$ states, the lifetimes of the $(13/2_1^+)$ and $(17/2_1^+)$ states in the ^{137,139}I isotopes are measured in the same way [95] and details are given in the appendix B. Furthermore, upper limits of the lifetimes of the $(11/2_1^+)$ states in all $^{135-139}$I isotopes were determined in this work. These lifetimes are too short to be measured with the convolution method. In the case of the ^{135}I isotope, the fact that the $(11/2_1^+)$ state is much shorter-lived than the $(15/2_1^+)$ state is consistent with the previous observation [69]. A summary of all lifetime values and limits deduced in this work using the $LaBr_3$(Ce) scintillators is given in Tab. 2.5.

Reduced transition probabilities calculated from the measured lifetimes are listed in Tab. 2.5 and compared to the ones from theory. For non-mixed $E2$ transitions, the $B(E2)$ values are calculated taking into account the respective conversion coefficients calculated using the code BrIcc [118]. In the cases where $J_f - J_i = 1$ and the mixing ratio is known, the mixed $B(M1)$ strength is given. For the $(17/2^+) \rightarrow (15/2^+)$ transition in ^{137}I, no mixing ratio is known and the mixed $B(M1)$ value can be taken as an upper limit. For the $B(M1; (9/2^+) \rightarrow (7/2^+))$ value in ^{139}I, a mean mixing ratio of $\delta = 1.0$ is assumed, based on the conversion coefficient $\alpha = 0.0151(9)$ from Refs. [114, 117]. To estimate the uncertainty in this case, the limits assuming an unmixed $M1$ transition are used while the $B(E2)$ value in the pure $E2$ limit is provided as well [117, 118].

Table 2.5: Lifetimes and reduced transition probabilities measured in this work with $B(E2)$ transition strengths given in e^2fm^4 and $B(M1)$ values in $10^{-3}\mu_N^2$. Shell-model values are calculated in the $r4h-r5i$ model space ranging from $Z=50$, $N=82$ to $Z=82$, $N=126$ using the N3LOP effective interaction (SM-I) and Kuo-Herling (SM-II) interaction (see Sec. 2.5). Spectroscopic information is taken from the evaluated nuclear data sheets [87, 97, 109, 110, 116, 117]. See Refs. [94, 95] for a comparison with previously measured values´.

Nucleus	J_i^π	τ [ps]	J_f^π	$\sigma\lambda$	δ	$B(\sigma\lambda)$			
						This Exp.	SM-I	SM-IIa	SM-IIb
^{134}Te	4_1^+	2020(140)	2_1^+	$E2$		168(12)	184	126	144
^{136}Te	2_1^+	<45	0_1^+	$E2$		>220	414	266	323
	4_1^+	142^{+38}_{-60}	2_1^+	$E2$		420^{+300}_{-90}	579	169	204
	6_1^+	320^{+74}_{-97}	4_1^+	$E2$		460^{+200}_{-90}	487	72	87
^{138}Te	2_1^+	69^{+35}_{-30}	0_1^+	$E2$		565^{+363}_{-190}	631	401	500
	4_1^+	113^{+63}_{-44}	2_1^+	$E2$		420^{+270}_{-150}	901	377	469
	6_1^+	50^{+35}_{-27}	4_1^+	$E2$		370^{+430}_{-150}	895	225	280
^{135}I	$(11/2_1^+)$	<50	$(7/2_1^+)$	$E2$		>7	195	97	110
	$(15/2_1^+)$	2340(115)	$(11/2_1^+)$	$E2$		168(9)	157	131	149
^{137}I	$(9/2_1^+)$	390(70)	$(7/2_1^+)$	$(M1/E2)$	+1.1(6)	0.38(6)	0.5	0.1	0.00031
	$(11/2_1^+)$	<50	$(7/2_1^+)$	$E2$		>177	508	299	360
	$(13/2_1^+)$	140^{+40}_{-50}	$(9/2_1^+)$	$E2$		473^{+263}_{-105}	756	295	352
		145(60)	$(11/2_1^+)$	$(M1/E2)$	+0.08(3)	1.6(8)	5.8	4.5	2.7
	$(15/2_1^+)$	<50	$(11/2_1^+)$	$E2$		>520	589	240	288
	$(17/2_1^+)$	150(50)	$(13/2_1^+)$	$E2$		840(280)	601	280	343
			$(15/2_1^+)$	$(M1)$		$2.7(9)$	8.2	2.7	5.7
^{139}I	$(9/2_1^+)$	130(50)	$(7/2_1^+)$	$(M1/E2)$	+1.0	2.9(11)	4.5	6.2	2.2
	$(11/2_1^+)$	<75	$(7/2_1^+)$	$E2$		>690	1035	207	661
	$(13/2_1^+)$	120(60)	$(9/2_1^+)$	$E2$		573^{+574}_{-191}	1361	676	832
			$(11/2_1^+)$	$(M1)$		$1.3(7)$	1.4	7.4	1.9
	$(17/2_1^+)$	<70	$(13/2_1^+)$	$E2$		>535	1253	677	845

2.5 Discussion

In the following, the results from the spectroscopy and the lifetime measurements are discussed with respect to the systematic evolution beyond $^{132}\mathrm{Sn}$ and compared to theoretical calculations. In order to compare the new experimental data on spectroscopic measurements of neutron-rich tellurium and iodine isotopes to theoretical predictions, large-scale shell-model calculations (SM) are used as a theoretical reference. The calculations for the present work are performed using the N3LOP effective interaction used in Refs. [48, 70, 94, 95, 119], including the model space $r4h - r5i$, spanned by the $1f_{7/2}, 0h_{9/2}, 1f_{5/2}, 2p_{3/2}, 2p_{1/2}, 0i_{13/2}$ orbitals for neutrons and the $0g_{7/2}, 1d_{5/2}, 1d_{3/2}, 2s_{1/2}, 0h_{11/2}$ orbitals for protons, taken above the closed ^{132}Sn core. The corresponding single-particle energies for neutrons and protons are input parameters taken from the experimental data on ^{133}Sn and ^{133}Sb [120]. The $0i_{13/2}$ neutron and $2s_{1/2}$ proton orbital energies are empirical values taken from Refs. [121, 122], respectively.

The N3LOP effective interaction was successfully used before in describing the spectroscopic properties and collectivity of even-even chains of nuclei [119, 123] and for odd-even and even-odd mass nuclei [124] in the vicinity of ^{132}Sn. The diagonalization of the considered systems has been achieved using the Antoine shell-model code [125, 126]. The results from the calculations are presented in the following sections. According to these results, a very good agreement is achieved with respect to the experimental data. Several points are discussed further in details.

For comparison, standard shell-model calculations using the NuShellX code [127] were performed additionally within this thesis. The calculations were done in the same model space using the Kuo-Herling (KH) interaction [128, 129]. The single-particle energies are taken from experimental spectra of $A = 207$ nuclei [129] with a single hole to the doubly magic $^{208}\mathrm{Pb}$ nucleus. The two-body matrix elements are modified according to fits on level energies of $^{206}\mathrm{Pb}$, $^{206}\mathrm{Tl}$ and $^{206}\mathrm{Hg}$ isotopes below $^{208}\mathrm{Pb}$ [130]. The interaction has been widely used to successfully describe experimental data on nuclei 'south-east' of $^{208}\mathrm{Pb}$ (e.g., Refs. [131, 132]) as well as data on $N = 84$ isotones [60] and neutron-rich antimony isotopes [133].

In the following, unless explicitly stated otherwise, the results from the shell-model calculation will refer to the N3LOP interaction.

2.5.1 Level schemes and configurations

In the level schemes of the semimagic nuclei $^{134}\mathrm{Te}$ and $^{135}\mathrm{I}$, both single-particle and collective structures coexist [102, 134]. As can be seen in Figs. 2.33 and 2.35, the level sequence is rather different compared to the

$N = 84, 86$ neighbors with visibly compressed excitation energy levels. The first excited states are above 1 MeV in the $N = 82$ semimagic isotones and drop below or around 600 keV when moving to $N = 84$, reflecting the nature of the closed neutron shell at $N = 82$. Apart from the yrast structures that include ns isomers in ^{134}Te, negative parity bands with interconnecting transitions are also populated.

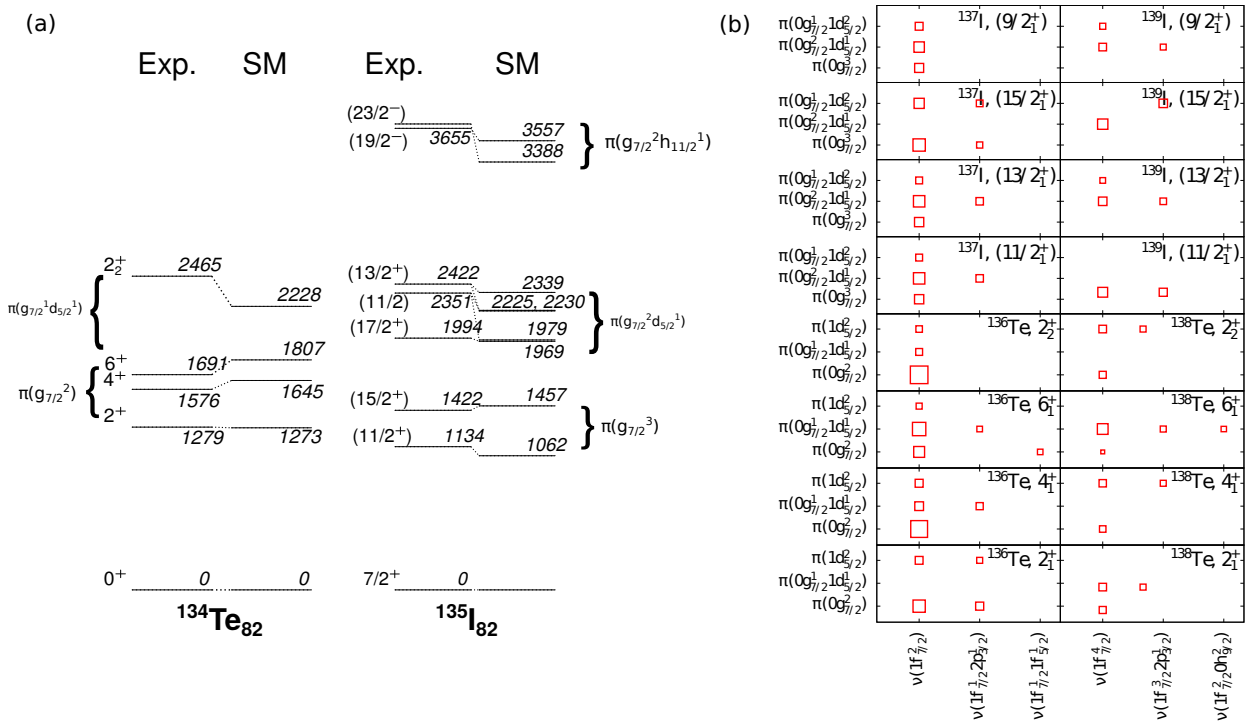

Figure 2.41: (a) Comparison of experimentally observed and theoretically calculated level schemes for ^{134}Te and ^{135}I. (b) Shell-model configurations for the $N = 84, 86$ isotones. Each panel is labeled with its respective nucleus and state. The size of each box corresponds to the proportion of the configuration in the wave function.

A comparison of excited states in the ^{134}Te and ^{135}I isotones with the SM results is shown in Fig. 2.41(a) together with the most dominant shell-model configurations. In ^{134}Te, the $2^+_1, 4^+_1$ and 2^+_2 states are mainly composed of a single configuration with about 95 % amplitude. According to the calculations, the first yrast states in the semimagic ^{134}Te and ^{135}I isotones are built on $\pi(0g^n_{7/2})$ ($n = 2$ or 3) configurations while higher-lying yrast states involve the excitation of a proton from the $\pi(0g_{7/2})$ orbital to the $\pi(1d_{5/2})$ orbital. The negative-parity states include the proton $\pi(0h_{11/2})$ shell with a large energy difference between the $\pi(0d_{5/2})$ and $\pi(0h_{11/2})$ states. Furthermore, neutron core breaking configurations of type $\nu(1d^{-1}_{3/2}1f^1_{7/2})$ in ^{134}Te and $\nu(0h^{-1}_{11/2}1f^1_{7/2})$ in ^{135}I were observed above 4 MeV excitation energy. This very well relates the behavior of ^{135}I to its semimagic neighbor ^{134}Te as the large shell gap is present for both two- and three-valence proton isotones. Note that these states are not calculated and shown in Fig. 2.41 because of the restricted model space. In addition to these

distinct single-particle type structures and neutron-core breaking configurations, $E3$ transition branches have been observed in these isotones [94, 95]. This suggests the presence of octupole collectivity in the $N = 82$ $^{134}\mathrm{Te}$ and $^{135}\mathrm{I}$ despite only having few valence particles outside the doubly magic $^{132}\mathrm{Sn}$ [134].

The excitation level schemes of the $N = 84, 86$ isotones $^{136,138}\mathrm{Te}$ and $^{137,139}\mathrm{I}$ observed in this work are more compressed and states become more fragmented as one would expect with the increase in mass number and valence particles. In these nuclei, the strongest role is played by the protons with reasonably small neutron excitations despite the clear neutron dominance and large N/Z ratio. Figure 2.41(b) shows the dominant configurations for low-lying excited states in these nuclei as predicted by the shell-model calculation. This also shows that the most prominent excitations are those between the proton $\pi(0g_{7/2})$ and $\pi(1d_{5/2})$ orbital. Furthermore, the fragmentation becomes visible with strongest contributions to the wave functions dropping from values around 20 % for $N = 84$ to values below 10 % for $N = 86$.

From a comparison of level schemes as shown in Refs. [94, 95], a perfect matching for the low-lying yrast states in all nuclei can be noted with the exception of the inversion of the $(11/2_1^+)$ and $(9/2_1^+)$ states in $^{139}\mathrm{I}$ due to their close excitation energy. The ground state configurations of these nuclei are rather fragmented where the strongest contribution comes from the $\nu(1f_{7/2}^n)$ ($n = 2, 4$) neutron configuration and the protons occupying either the $\pi(0g_{7/2})$ orbital or the $\pi(1d_{5/2})$ orbital. Those configurations continue to be dominating the low-lying structures in both isotopic chains (see Fig. 2.41(b)). In the 6_1^+ states of the $^{136,138}\mathrm{Te}$ nuclei, the $\pi(1d_{5/2})$ orbital becomes more dominant and a competition between the $\nu(1f_{7/2}^2)\pi(0g_{7/2}^1 1d_{5/2}^1)$ and the $\nu(1f_{7/2}^2)\pi(1d_{5/2}^2)$ configurations is almost continuously present in the low-lying excited states.

For the three-valence proton nuclei, the low-lying excited states can be described by coupling an additional proton in the $\pi(0g_{7/2})$ orbital to the excited states in the $A - 1$ tellurium isotones. For example, the excited yrast states up to the $(15/2_1^+)$ state are determined by a $\pi(0g_{7/2}^3)$ proton configuration and the excitation of one proton to the $\pi(1d_{5/2})$ orbital becomes relevant for the higher-spin states. The purity of these proton configurations drops with increasing number of (valence) neutrons and the yrast states become more fragmented in $^{139}\mathrm{I}$ (with about 10 % contribution) compared to the almost pure (about 90 % contribution) wave functions in $^{135}\mathrm{I}$.

When moving away from the closed $N = 82$ neutron shell, the iodine isotopes exhibit two band-like structures based on the $(11/2_1^+)$ and $(9/2_1^+)$ states. The drop in excitation energy of these states with increasing neutron number shows the increase in collectivity as more neutrons are added. In contrast to the dominant $\pi(0g_{7/2}^3)$ configuration in the $(11/2_1^+)$ states, the $(9/2_1^+)$ states originate from the excitation of a proton to the $\pi(1d_{5/2})$ orbital for $N > 82$. The structure of the $(9/2_1^+)$ state in the $N = 82$ $^{135}\mathrm{I}$ is different which also explains its non-observation. According to the calculations, the $(5/2_1^+)$ states have even stronger $\pi(0g_{7/2}^2 1d_{5/2}^1)$ components

in the wave functions but those states have not been observed in this work.

2.5.2 Transition rates and evolution of collectivity

The shell-model calculations using the effective N3LOP (SM-I) interaction uses effective charges $e_\pi = 1.6e, e_\nu = 0.6e$ to calculate reduced $E2$ transition probabilities. For comparison, calculations with the KH interaction and two sets of effective charges $(1.5e, 0.5e)$ (SM-IIa) and $(1.6e, 0.6e)$ (SM-IIb) were performed and are listed in the last two columns of Tab. 2.5. For the calculations of the $B(M1)$ strengths, a quenched spin and orbital g factor was used for SM-I [119], a quenching of $g = 0.6g_{free}$ for SM-IIa and $g = 0.7g_{free}$ for SM-IIb. The richness of results for even-Z and odd-Z isotopes beyond $^{132}\mathrm{Sn}$ as a function of neutron number allows for the investigation of both proton and neutron collectivity with increasing valence particles outside the closed shell. To discuss the evolution of collectivity based on the newly deduced transition rates, Fig. 1.5 is recalled at this point. The energies of the first excited 2^+ states already indicate some development of collectivity when moving away from the $N = 82$ closed neutron shell.

$E2$ transition probabilities

The lifetimes of the 4_1^+ state in $^{134}\mathrm{Te}$ and the $(15/2_1^+)$ state in $^{135}\mathrm{I}$ were remeasured and are consistent with previous measurements [69, 87]. The experimental $B(E2)$ values provided in Tab. 2.5 match the theoretical ones. The reduced transition probabilities amount to $B(E2) = 168(12)\ e^2\mathrm{fm}^4$ (corresponding to 4.1(3) W.u.) and $B(E2) = 168(9)\ e^2\mathrm{fm}^4$ (corresponding to 4.1(2) W.u.) for $^{134}\mathrm{Te}$ and $^{135}\mathrm{I}$, respectively. As introduced in Sec. 1.4, those values are typical for low collectivity, semimagic nuclei. The $(15/2_1^+) \rightarrow (11/2_1^+)$ transition rate in $^{135}\mathrm{I}$ is successfully reproduced in a seniority single-j approach based on the $\pi(0g_{7/2}^3)$ configuration and the $B(E2)$ value of the $4_1^+ \rightarrow 2_1^+$ transition in $^{134}\mathrm{Te}$ [69].

In Fig. 2.42(a) the $B(E2)$ transition rates for the tellurium isotopes measured in this work are appended to those known previously [39] and compared to shell-model values (shown with empty symbols and dashed lines). The new experimental values for $^{136}\mathrm{Te}$ and $^{138}\mathrm{Te}$ are presented in comparison to previous measurements in Fig. 2.42(b). Despite the large uncertainties in the present data, the systematics can be extended to higher spins and mass numbers. The experimental values for the 2_1^+ states follow a small systematic increase, while the $B(E2)$ values for the $4_1^+, 6_1^+$ states may indicate a slowed down collectivity for $A = 138$. Such a trend is indicated also in the shell-model results by mixtures in the composition of the two wave functions, see Fig. 2.41(b). The collective nature is indeed evident from the large fragmentation of strengths, despite being somewhat overestimated. Comparable to the experimentally detected ones (within the experimental un-

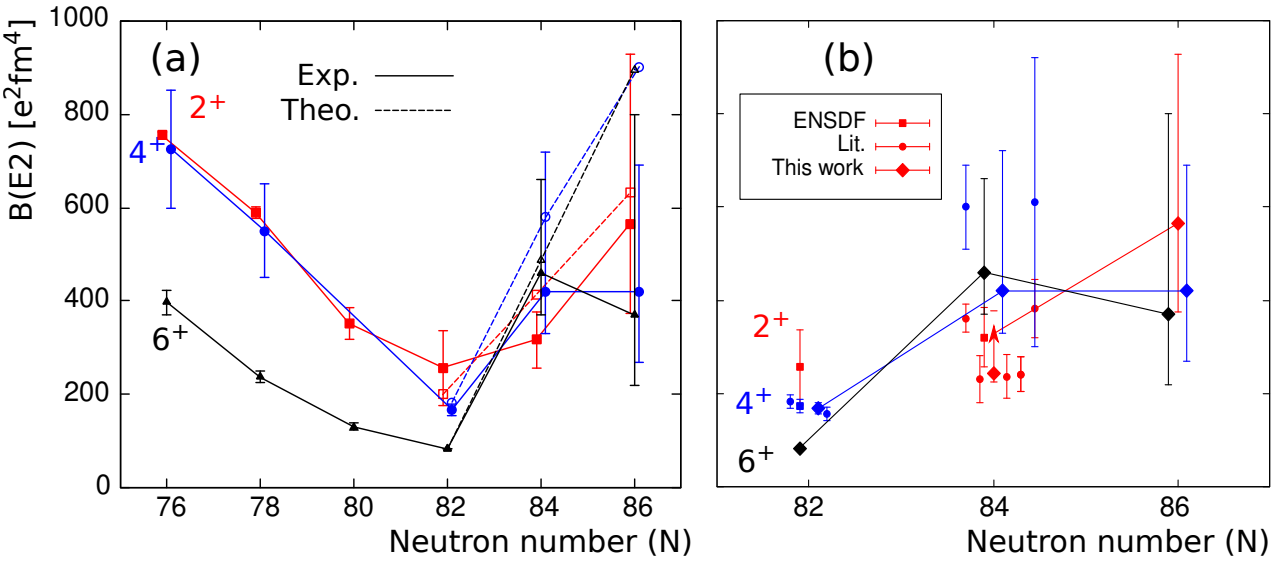

Figure 2.42: (a) Evolution of $B(E2)$ transition rates for the first excited 2^+, 4^+, 6^+ states whenever known from literature [39] and this work for even-even tellurium isotopes around the semimagic N=82. Shell-model results for the $^{134-138}$Te isotopes are shown with empty symbols and dashed lines for discussion (see SM-I in Tab. 2.5). Adapted from Ref. [94]. (b) Comparison of experimental $B(E2)$ values in neutron-rich tellurium isotopes beyond $N = 82$ from this work, the evaluated nuclear data sheets [39] and other literature values Refs. [67, 100, 113, 134, 135, 136, 137]. Solid lines are drawn to connect the values measured in this work.

certainty), the theoretical $B(E2; 2_1^+ \rightarrow 0_1^+)$ transition rates present steep increases for both ^{136,138}Te nuclei [94]. From these results, some conclusions on the moderately collective character of ^{138}Te can be drawn, such as: the relatively low $B(E2; 2_1^+ \rightarrow 0_1^+)$ value, the excitation energy ratio $R_{4/2} \leq 2$ and the transition ratio $B_{4/2}$=$B(E2; 4_1^+ \rightarrow 2_1^+)/B(E2; 2_1^+ \rightarrow 0^+) \leq 1.5$, providing critical information on the nuclear structure.

The $B(E2)$ values in the tellurium nuclei can be related to the ones in the $A + 1$ iodine isotones. A graphical comparison of all $B(E2)$ transition rates obtained in this work is shown in Fig. 2.43(a). Despite providing only upper limits for the lifetimes of the $(11/2_1^+)$ states, the lower limits for these transition probabilities show an indication for an increased collectivity with increasing valence nucleon number. Such a moderate change from $N = 82$ (^{135}I) toward $N = 86$ (^{139}I) is visible in Fig. 2.43(a) and indicates a similar development of collectivity as for the tellurium nuclei.

Several other excited states could be investigated in the iodine isotopes such as the $(13/2_1^+)$ and the $(17/2_1^+)$ states, providing the opportunity to discuss the evolution of collectivity in terms of $E2$ transition strength with increasing neutron number as shown in Fig. 2.43(a). The similarities in $B(E2)$ strengths of each $N = 82, 84, 86$ tellurium and iodine isotone can be related to the similarities in fragmentation of wave functions, see Fig. 2.41.

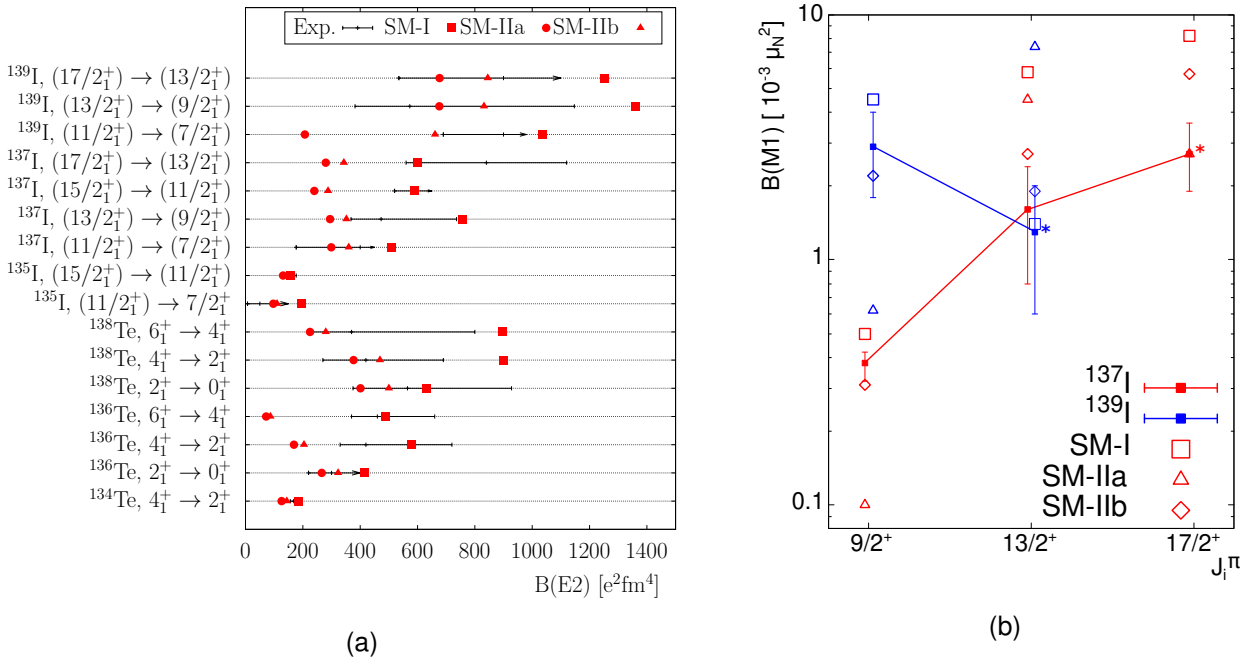

Figure 2.43: Reduced (a) $E2$ and (b) $M1$ transition probabilities for transitions in neutron-rich tellurium and iodine isotopes. $M1$ transition correspond to $\Delta J = 1$ transitions. $B(M1)$ values calculated within their respective limits are highlighted with asterisks. The shell-model label refers to the values given in Tab. 2.5. From Ref. [95].)

$M1$ transition probabilities

The experimental $B(M1)$ transition strengths are listed in comparison to theory in Tab. 2.5 and shown in Fig. 2.43(b). The $B(M1)$ value of the $(9/2_1^+) \rightarrow (7/2_1^+)$ transition in ^{139}I is almost an order of magnitude higher than for its neighboring isotope with the difference of only two neutrons. As expected, this indicates an increase in collectivity when moving away from the closed shell. Although the main component of the $(9/2_1^+)$ wave function is the same in both isotopes, the mixtures dominate the wave function in ^{139}I much more severely than in the other excited states with only about 5% of the main $\pi(g_{7/2}^2 d_{5/2})\nu(f_{7/2}^4)$ configuration.

Concerning the $(13/2_1^+)$ states, no multipole mixing ratio for the mixed $(M1 + E2)$ $(13/2_1^+) \rightarrow (11/2_1^+)$ transition is known for ^{139}I and, thus, only a lower limit is given for the $B(M1)$ value. In ^{137}I, a strong increase in $B(M1)$ strength from $J^\pi = 9/2^+$ to $J^\pi = 13/2^+$ by almost an order of magnitude is observed. Such a trend does not seem likely or as strongly pronounced for ^{139}I although no firm conclusions can be drawn from the lower $B(M1)$ limit. Even for the known case, as the mixing is not severe, the $M1$ strength is the dominating one and it is clearly showing the evolution and its collective behavior. The sensitivity of the effective g factors used in the theoretical calculations shows the necessity for an improvement in experimental uncertainties.

2.5.3 Comparison of shell-model calculations

The shell-model interaction used in the previous discussion was tuned based on the newly obtained results from this work. In this section, a comparison between experimental results and different effective interactions in the $r4h-r5i$ model space will be presented. The N3LOP and KH interactions are introduced in the previous section and a comparison based on the example of $^{136}\mathrm{Te}$ will be presented.

Figure 2.44 shows the experimentally deduced and the theoretically calculated level schemes for $^{136}\mathrm{Te}$ up to $J = 8\ \hbar$. The energies calculated with the N3LOP match the experimental ones far better. To further shed light on these differences, the occupation numbers for the main orbitals are plotted for both interactions in Fig. 2.45 up to spin $J = 14\ \hbar$.

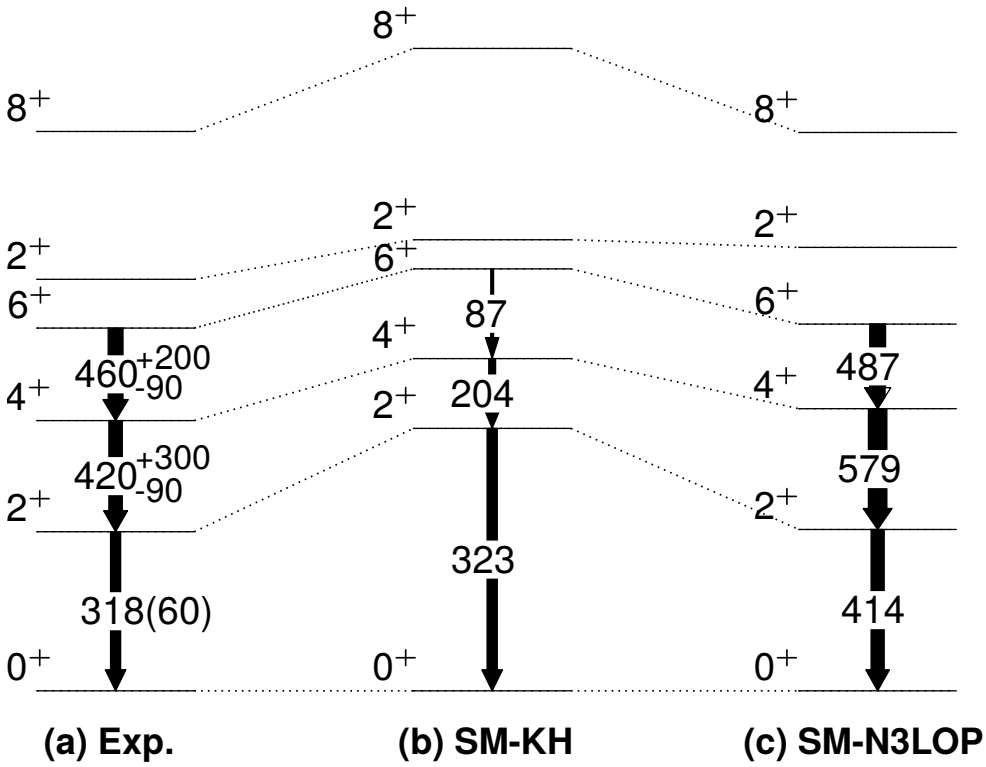

Figure 2.44: Level scheme of $^{136}\mathrm{Te}$ deduced (a) in this experiment calculated from (b) the Kuo-Herling (KH) interaction and (c) the N3LOP interaction. The transitions are labeled with their respective $B(E2)$ strengths in e^2fm^4.

In general, the occupation numbers obtained from the N3LOP interaction follow a smooth trend as a function of spin. This is not the case in the KH interaction where sudden jumps occur from one spin to the next. For the proton orbitals, no sizable component in the $\pi(1d_{5/2})$ shell is present in the wave function of the yrast states calculated with the KH interaction. For the neutron orbitals, the contributions of the $\nu(1f_{7/2})$ shell are significantly

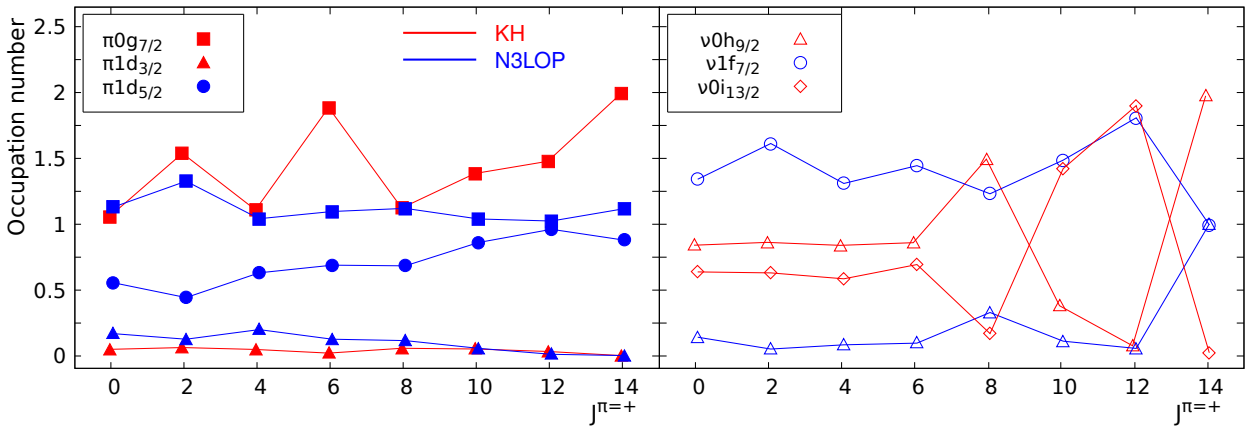

Figure 2.45: Occupation number of yrast states for protons (left) and neutrons (right) calculated using the Kuo-Herling interaction (red) and N3LOP interaction (blue) for ^{136}Te. The lines are drawn to guide the eye.

underestimated and the most important role is played by the $\nu(0h_{9/2})$ orbital. Also the $B(E2)$ values which are shown in Fig. 2.44 are much better reproduced with the N3LOP interaction.

To quantify the accuracy of both shell-model interactions, a weighted root mean square (rms) is calculated according to:

$$rms = \sqrt{\frac{1}{N} \cdot \sum_i \frac{\left(E_x^{\text{Exp.}}(J_i) - E_x^{\text{Theo.}}(J_i)\right)^2}{(2J_i+1)}}, \tag{2.11}$$

where the sum is over all states i. The sum is weighted by the spin to enhance the importance of the description of states with lower spin. Finally, the result is normalized by the number of states included in the sum, N. This quantification leads to a rms value of $rms^{\text{KH}} = 81.3$ keV for the KH interaction and $rms^{\text{N3LOP}} = 35.2$ keV for the N3LOP interaction. An improvement by more than a factor of two is achieved for the excitation energies calculated using the N3LOP interaction compared to the KH interaction. It has to be noted that the different shell-model interactions are tuned to different sets of experimental data which emphasizes the need for more experimental input and highlights the improvement of the shell-model interaction due to the input from experimental data deduced in this work.

Chapter 3

Isomers around ^{132}Sn

3.1 Motivation of the experiment

The region 'north-west' of ^{132}Sn

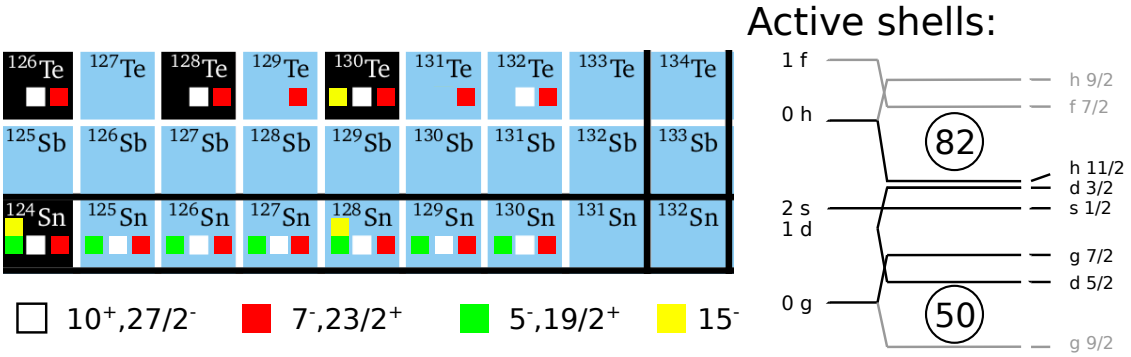

Figure 3.1: Part of the nuclear chart 'north-west' of ^{132}Sn and active orbitals relevant for the isotopes in this region. Known isomers in the tin and tellurium nuclei are highlighted by color-coded squares and the data is taken from Refs. [50, 51, 138, 139, 140, 141, 142, 143, 144, 145, 146].

The region below $N = 82$ shown in Fig. 3.1 is abundant in isomeric states typically formed by yrast spin traps. The unique parity $\nu(0h_{11/2})$ orbital is responsible for seniority isomers in isotopes with a few neutron holes away from ^{132}Sn. This results in a series of 10^+ isomers in the even-even tin and tellurium isotopes with seniority $\nu = 2$ [41, 87, 109, 147, 148, 149]. This isomer systematic persists over the entire $Z = 50$ isotopic chain while it is less pronounced in the nuclei with $Z > 50$ due to the influence of the proton configurations. The

isomer systematic was also extended to odd masses up to $^{129}\mathrm{Sn}$ through relativistic fission of $^{238}\mathrm{U}$ [51]. The transition probabilities of the 10^+ isomers was related to the $(27/2^-)$ seniority $\nu = 3$ isomers in the odd-A tin isotopes and its systematic understood in terms of a delayed filling of the $\nu(0h_{11/2})$ orbital [51].

Other neutron orbitals which are relevant in the formation of isomers in that region are the $2s_{1/2}$ and the $1d_{3/2}$ shell. Isomers with $J^\pi = 7^-$ are formed with a dominant $\nu(1d_{3/2}^{-1}0h_{11/2}^{-1})$ configuration (see, for example, Ref. [139]). In the odd-A tin isotopes, this leads to $(23/2^+)$ isomeric states which are formed by coupling a neutron hole in the $0h_{11/2}$ to the 7^- isomer in its even neighbor [49, 150, 151]. The coupling of a neutron hole in the $2s_{1/2}$ and the $0h_{11/2}$ results in 5^- isomeric states in the even-even tin isotopes [39]. With the additional coupling of a neutron hole in the $\nu(0h_{11/2})$ orbital, this results in the existence of $(19/2^+)$ excited states of isomeric character in the odd-A tin isotopes [152]. In $^{127}\mathrm{Sn}$, the g factor of the $(19/2^+)$ state revealed a non-negligible contribution of the $\nu(1d_{3/2}^{-1}0h_{11/2}^{-1})$ configuration in its wave function [153]. In $^{126}\mathrm{Sn}$, the magnetic moment of the (7^-) isomer was measured and confirmed the suggested dominant $\nu(1d_{3/2}^{-1}0h_{11/2}^{-1})$ configuration [154]. Moreover, (15^-) seniority $\nu = 4$ isomers based on a $\nu(1d_{3/2}^{1}0h_{11/2}^{\pm 3})$ configuration were observed in the even tin isotopes between $A = 120$ and $A = 128$ with the exception of $^{126}\mathrm{Sn}$ [144, 145, 146].

A summary of the observation of isomers for the tin and tellurium isotopes is shown by a color code in Fig. 3.1. From that it is clear that the abundance in low seniority isomers is much lower for the tellurium isotopes. This motivates further studies to understand the single-particle orbital evolution below $N = 82$ and the collectivity through the additional protons above the $Z = 50$ closed shell. In previous studies, most of the low energy isomeric transitions were not detected, thus, emphasizing the importance of the detection of low energy γ rays in the isomer measurement.

3.2 Experimental setup

The experiment was carried out in December 2019 at Radioactive Isotope Beam Factory (RIBF) of the RIKEN Nishina Center for Accelerator-Based Science in Saitama, Japan. It is an accelerator complex consisting of several heavy-ion accelerators coupled together to deliver high intensity and high energy beams to different experimental sites. The exotic nuclei at the RIBF are produced via fission or fragmentation reactions and separated with the in-flight separator BigRIPS [155], delivering separated secondary beams for further studies.

3.2.1 BigRIPS fragment separator

In this experiment, the primary $^{238}\mathrm{U}$ beam was accelerated to an energy of 345 MeV/u and impinged on a 0.1 mm thick tungsten target at the first focal point of the BigRIPS separator. The average intensity of the primary beam was about 80 pnA, corresponding to $5 \cdot 10^{11}$ particles/s. This reaction produces a large variety of secondary ions at high energies, often referred to as 'cocktail beam'. The process of separation and identification requires several stages and will be discussed in the following.

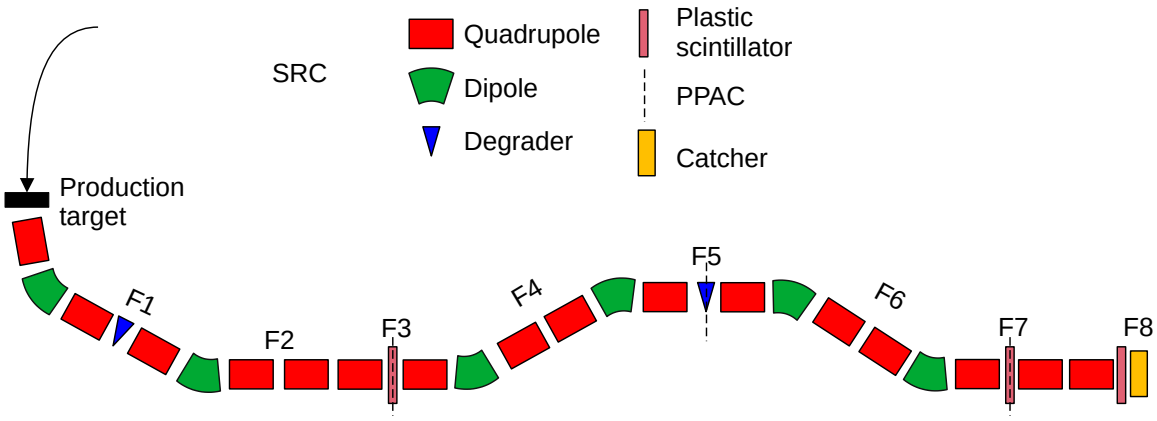

Figure 3.2: Schematic layout of the BigRIPS separator adapted from Ref. [155]. The beam line consists of superconducting quadrupole triplets (red) and dipole magnets (green). Different focal points F1-F8 are present where degraders (blue) or various tracking detectors can be placed. The beam in this experiment is stopped at F8.

BigRIPS is a two-stage radioactive ion beam separator which makes use of multiple separation steps to

enhance the resolution of the particle identification (PID). The first stage is used to produce and separate the secondary beam while the second stage is used for identification and further separation. A schematic layout is presented in Fig. 3.2. The BigRIPS fragment separator consists of six room-temperature dipole magnets with a 30° bending angle and 16 superconducting quadrupole triplets. Separation can be achieved in a large acceptance mode for high particle collection efficiency or a high-resolution mode to further improve the separation capability. There are eight focal planes (F0-F7) arranged along the BigRIPS beam line including the target position F0. The BigRIPS separator is followed by the focal point F8 where the beam can be stopped or secondary reactions can take place and their outgoing reaction products identified by the ZeroDegree Spectrometer [156]. In this experiment, the secondary beam was stopped at F8 and implanted into a copper catcher.

The transmission through the separator and the estimations of implantation rates were simulated prior to the experiment with the code LISE++ [157]. The BigRIPS beam line was imported and modified according to the experimental requirements. After the production target, the beam dump slits have to be adjusted in order to cut away the primary beam such that the secondary ions of interest remain. Those slits are after the first dipole magnetic and by selecting a proper $B\rho$ in combination with the beam dump slits, the setting can be optimized for the ions of interest.

From that point on, the separator settings are tuned for the fragments of interest with LISE++ which are used during experiment. Slits at the dispersive foci F2 and F7 are used to cut further unwanted species and enhance the beam purity. This has to be done such that the total number of secondary ions passing through the separator is below 10^4 in order to not overload the tracking detectors.

Furthermore, it has to be checked whether or not the ions are implanted in the copper. This is done by calculating the energy of the secondary ions right before the catcher at the focal point F8. All ions of interest are fully stopped in the copper catcher which has also been confirmed experimentally by taking the measured velocity β and simulating the stopping process in LISE++.

3.2.2 Detector setup

Following the BigRIPS separator, the detection setup is located at F8. A schematic overview of the setup is shown in Fig. 3.3. Identified ions are implanted in a copper catcher. Four HPGe detectors are placed in a horizontal plane at 90° with respect to each other ($\pm 45°$ and $\pm 135°$ with respect to the beam axis). Additionally, two large volume $LaBr_3$(Ce) scintillation detectors are placed at $0°$ and $90°$ to the beam. Those detectors were installed to perform some checks and are not used in the analysis and are therefore not shown in Fig. 3.3. The measurement is started by a signal from a fast plastic scintillator at F8 as indicated in Fig. 3.3. In order to

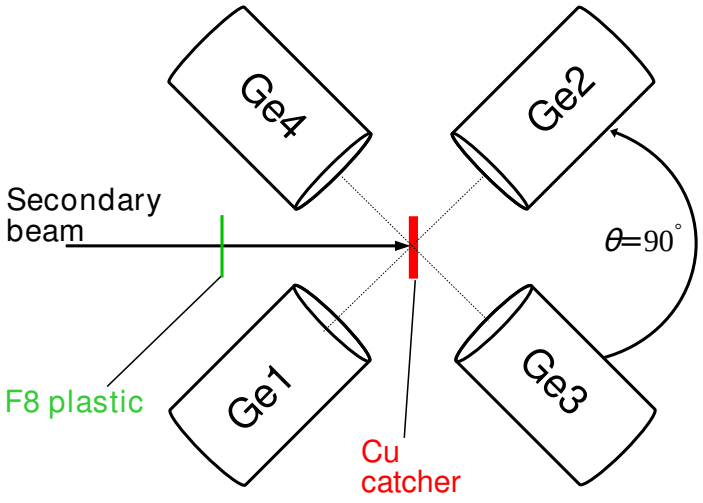

Figure 3.3: Schematic of the experimental setup viewed from the top.

verify the performance of the detectors, two detector tests were performed and the results are presented in the following.

Detector tests prior to the experiment

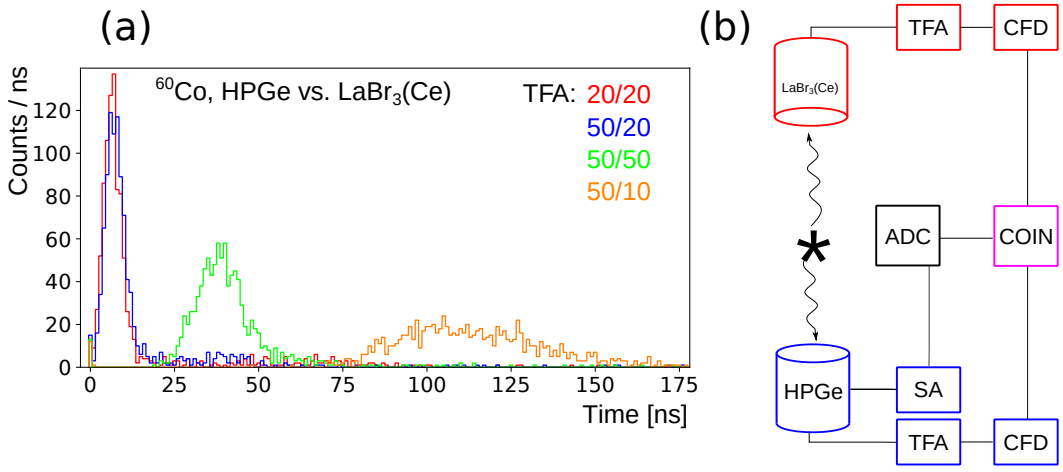

Figure 3.4: (a) Time resolution plot for one HPGe detector measured with different TFA settings in ns. (b) Simplified schematic representation of the electronics scheme for the test measurement.

HPGe detectors from ORTEC were tested for their performance in energy and time resolution. A simplified electronics scheme is shown in Fig. 3.4(b). The time resolution of the HPGe detector was measured using

coincidences with a fast $LaBr_3$(Ce) scintillator. The time signals are passed through a timing-filter amplifier (TFA), a CFD and recorded with an ADC if both detector signals arrive in a certain coincidence window. The pre-amplifier signal from the HPGe detector is processed by a shaping amplifier (SA) before it is directly fed into the ADC to record the energy information. Among the test shaping times as $\tau_{shape} = 6$ μs, typical energy resolutions of 1.7(2) keV FWHM at 1.3 MeV measured with a ^{60}Co were achieved.

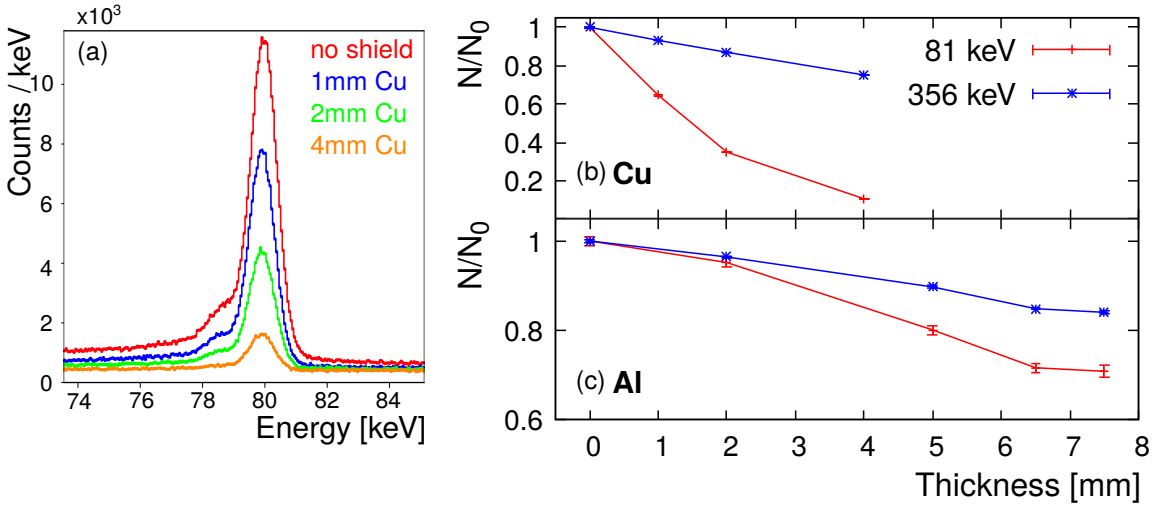

Figure 3.5: (a) HPGe spectrum zoomed around the 81 keV transition from the decay of ^{133}Ba measured with different absorbers in front of the detector. (b,c) Relative counts of the 81 keV and 356 keV transition as a function of thickness for (b) copper and (c) aluminum absorbers.

To optimize the time resolution, integration and differentiation times of the TFA were varied. Time difference plots measured with a ^{60}Co source are shown in Fig. 3.4(a) for different TFA settings. Among the tested shaping times, the best time resolution with about 9(1) ns FWHM was achieved with integration and differentiation times of 20 ns while the other resolutions are 11(1) ns (50/20), 25(2) ns (50/50) and 50(5) ns (50/10), see Fig. 3.4(a). The time resolution increases to about 20-25 ns with a ^{133}Ba source that has energies as low as 81 keV. The in-beam time resolution was determined to be similar to the source measurement.

The interest in low energy γ rays comes from the fact that many spin trap isomers decay by transitions around or below 100 keV. It is also important to shield the detectors from prompt flash events that occur when the secondary ions are implanted due to bremsstrahlung when stopping the beam. Various combinations of aluminum and copper absorbers were tested with a ^{133}Ba source. The absorption effect on the γ-ray spectrum is shown in Fig. 3.5(a). In Fig. 3.5(b,c) the relative number of counts as a function of absorber thickness for the low energy 81 keV and the 356 keV transitions are displayed. Due to the higher atomic number from copper ($Z = 29$) with respect to aluminum ($Z = 13$), it is evident that a copper shield absorbs more with respect to

an aluminum shield of the same thickness. Furthermore, lower energies are stronger absorbed due to the interaction of γ radiation with matter which scales inversely with the energy. Detectors facing the back of the catcher, labeled Ge2 and Ge3 in Fig. 3.3, will be exposed to absorption. For this case, it is important to consider the following points in order to maximize the effectiveness of the shielding and optimize the low energy efficiency. Firstly, the beam has to be stopped in the catcher which defines the minimum copper thickness for the catcher. Secondly, the prompt flash has to be reduced as much as possible while finally maximizing the full-energy peak events.

3.2.3 Data acquisition: electronics scheme

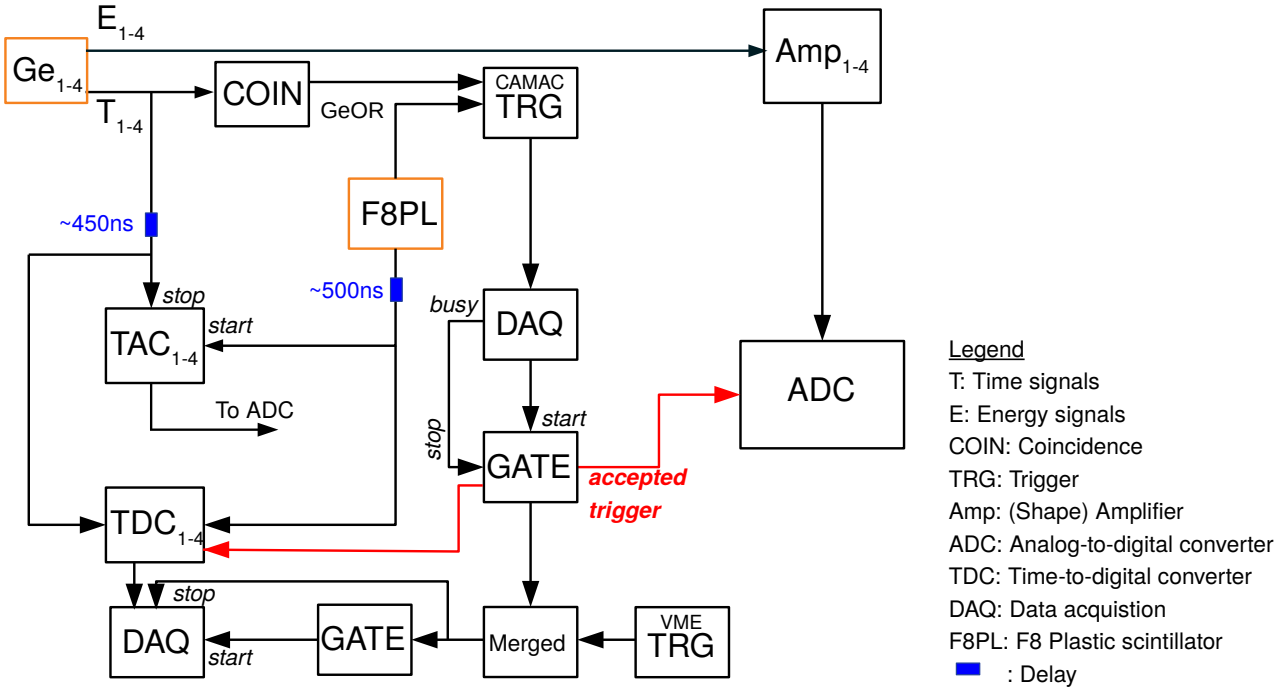

Figure 3.6: Simplified electronics scheme of the data acquisition.

A simplified electronics scheme of the setup is shown in Fig. 3.6. The energy information from the HPGe detectors (denoted as E_{1-4} in Fig. 3.6) is recorded via ADCs after amplification as shown above. The timing signals (denoted as T_{1-4} in Fig. 3.6) are either processed by time-to-amplitude converters (TACs) and fed to the ADC or converted by time-to-digital converters (TDCs).

The trigger ('CAMAC TRG') is provided by a OR condition of the HPGe timing signals and the plastic scintillator located at F8. The TAC branches are then constructed as the time difference between the plastic scintillator

and each HPGe detector. Note that different delay parameters are necessary in order to require a coincidence within a given range (= TAC range). The TDC timing is made in the same way and fed to the DAQ. Both acquisition branches are synchronized and merged via GATE modules. The accepted trigger for writing the data is constructed from the merged analog (= CAMAC) and digital (= VME) trigger and opens the DAQ for both systems.

3.3 Data analysis

The first step in analyzing the raw data is to clearly identify the particles produced in the reaction. The program ANAROOT [158], which is based on the analysis software ROOT [82], was developed at the RIBF to provide particle identification according to the procedure explained in Sec. 3.3.1. The listmode files from the raw data are unpacked, calibrations applied and information on the PID detectors, the TDCs and ADCs stored in ROOT trees which can be filled into histograms according to specific conditions.

3.3.1 Particle identification

The particles are identified in the second stage of BigRIPS based on the TOF-$B\rho$-ΔE method as explained in Ref. [159]. By measuring the time-of-flight (TOF), magnetic rigidity $B\rho$ and the energy loss ΔE, the atomic number Z and the mass-over-charge ratio A/Q can be deduced.

According to the Lorentz force, the magnetic rigidity is directly related to the mass-over-charge ratio.

$$\frac{A}{Q} = \frac{B\rho}{\gamma\beta c u} \tag{3.1}$$

In Eq. (3.1), γ is the Lorentz factor, $\beta = v/c$ the relative ion velocity, c the speed of light and u the atomic mass unit. By measuring the TOF using plastic scintillators, the velocity can be deduced from

$$\text{TOF} = \frac{L}{\beta c}, \tag{3.2}$$

where $L = 46.6\,\text{m}$ denotes the flight path length between F3 and F7 in Fig. 3.2. The plastic scintillators are read out with two photo multiplier tubes (PMT) on each side to reduce systematic uncertainties and to obtain spatial information on the ions.

Additionally, energy degraders are located at focal planes F1 and F5 to provide the possibility of further beam separation. Because of this, the particle trajectories and energies differ between F3-F5 and F5-F7. Thus, Equations (3.1) and (3.2) have to be modified accordingly:

$$\text{TOF} = \frac{L_{35}}{\beta_{35} c} + \frac{L_{57}}{\beta_{57} c}, \tag{3.3}$$

$$\left(\frac{A}{Q}\right)_{35} = \frac{B\rho_{35}}{\beta_{35}c\gamma_{35}u}, \tag{3.4}$$

$$\left(\frac{A}{Q}\right)_{57} = \frac{B\rho_{57}}{\beta_{57}c\gamma_{57}u}. \tag{3.5}$$

The indices in Eqs. (3.3-3.5) describe the flight paths between the different focal planes F3-F5 and F5-F7, respectively. For particles passing through, it is required that

$$\left(\frac{A}{Q}\right)_{35} = \left(\frac{A}{Q}\right)_{57},$$

to obtain

$$\frac{B\rho_{35}}{B\rho_{57}} = \frac{\beta_{57}\gamma_{57}}{\beta_{35}\gamma_{35}}. \tag{3.6}$$

From Eqs. (3.3) and (3.6) the mass-over-charge ratio can be reconstructed. The position information to deduce the magnetic rigidity $B\rho$ is measured using position-sensitive parallel plate avalanche counters (PPACs) [160] located at the focal planes F3,F5 and F7 to measure particle trajectories. These avalanche counters consist of two parallel electrodes separated by 3-4 mm and filled with gas. High electrical fields corresponding to a few hundreds of Volts per millimeter are applied and cause immediate electron avalanches from incident heavy ions. The position measurement in a PPAC detector is conducted using the delay-line readout method. The electrodes are connected with delay lines and positions are determined from time differences between the signals at both ends of the delay line. To further obtain information on the angle of the particle trajectory, double PPAC apertures consisting of two electrode pairs are mounted at the focal planes. From this measurement, ρ can be deduced and, together with the experimentally measured B strength from nuclear magnetic resonance probes, $B\rho$ can be obtained.

To calibrate the PID for the A/Q values, the offset for the time-of-flight measurement has to be adjusted and the optimization was performed for $^{127-129}\mathrm{Sn}$. The offset for the TOF measurement between F3-F7 was varied until a perfect matching was achieved. Figure 3.7 shows the ratio of experimental A/Q value over the theoretically predicted values assuming fully-stripped ions, e.g., A/Q$= 127/50 = 2.54$ for $^{127}\mathrm{Sn}$. The final value was chosen to be 297.25 ns.

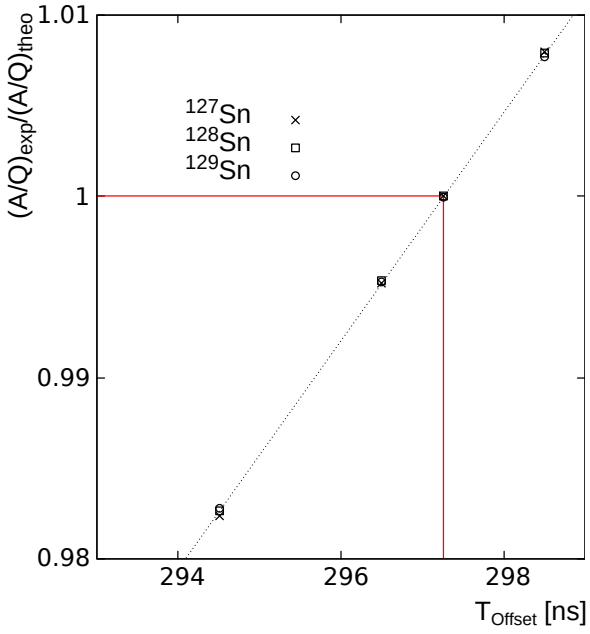

Figure 3.7: Ratio of experimental and expected (theoretical) A/Q ratio as a function of the time offset used in the BigRIPS calibration for the TOF measurement.

To achieve separation in Z, the energy loss dE/dx has to be measured. The energy loss is related to Z according to the Bethe-Bloch equation [161]:

$$\frac{dE}{dx} = \frac{4\pi \mathrm{e}^4 Z^2}{m_e v^2} nz \left[\ln \frac{2m_e v^2}{I} - \ln(1-\beta^2) - \beta^2 \right]. \tag{3.7}$$

m_e is the electron mass, e the elementary charge and Z the atomic number of the beam particle. z, n, I correspond to the material's atomic number, density and mean excitation potential, respectively. The energy loss is measured at the focal plane F7 in a multi-sampling ionization chamber (MUSIC) [162] to deduce the atomic charge number.

The energy loss is read out with multiple anodes and the geometric mean of the signals is used to determine the raw energy loss ΔE_{raw}. From Eq. (3.7) and using ΔE_{raw}, a linear relation between raw signal Z_{raw} and atomic number Z is obtained, i.e.,

$$\begin{aligned} Z &= a \cdot Z_{raw} + b, \quad \text{with} \\ Z_{raw} &= \beta \cdot \sqrt{\frac{\Delta E_{raw}}{ln(2m_e v^2/I)} - ln(1-\beta^2) - \beta^2}. \end{aligned} \tag{3.8}$$

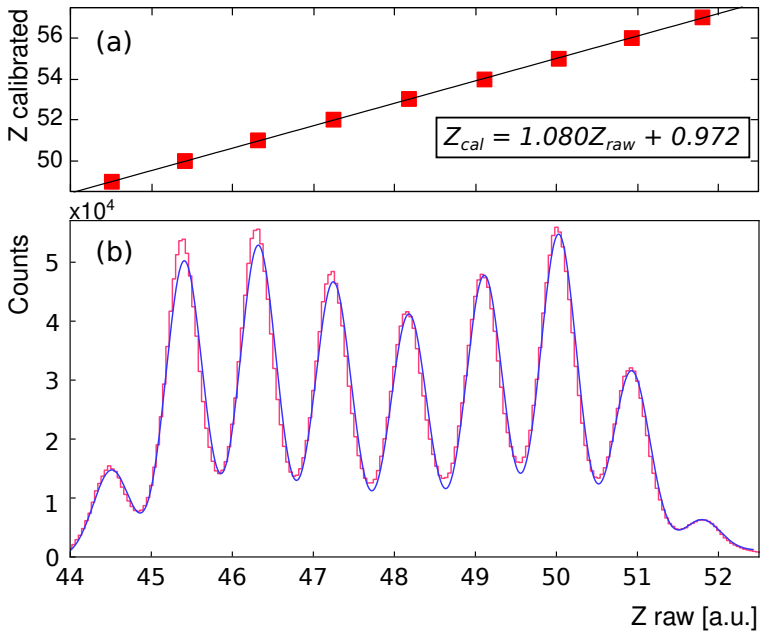

Figure 3.8: (a) Linear calibration to deduce atomic number units (Z_{cal}). (b) Z_{raw} (red) histogram and multi-Gaussian function (blue) fitted to determine the peak position.

a, b are parameters to be determined in a linear calibration. The Z_{raw} histogram is shown in Fig. 3.8(b). A multi-Gaussian function was used to fit and to obtain the centroids for a subsequent linear calibration into atomic number units. Specific atomic number values were assigned to peaks based on γ rays from known isomeric decays. A high linearity of the raw data signals is observed and little to no gain drift of the IC was observed for the entire experiment. The linear fit to determine the parameters from Eq. (3.8) is shown in Fig. 3.8(a).

The atomic charge number Z has to be independent of the velocity of the secondary ions. A dependence on the velocity would result in a slight broadening of the peaks at different Z values. The PID plot is shown in Fig. 3.11 from which no significant β dependence was observed and no correction had to be applied.

PID corrections

For a clean identification and to remove background events, several corrections and cuts using the beam-line detectors have to be applied. This procedure is adapted from Ref. [159].

Each of the plastic scintillation detectors located at F3, F7 and F8 are read out with two optically coupled PMTs. They contain position information x of an incident particle which is proportional to the natural logarithm

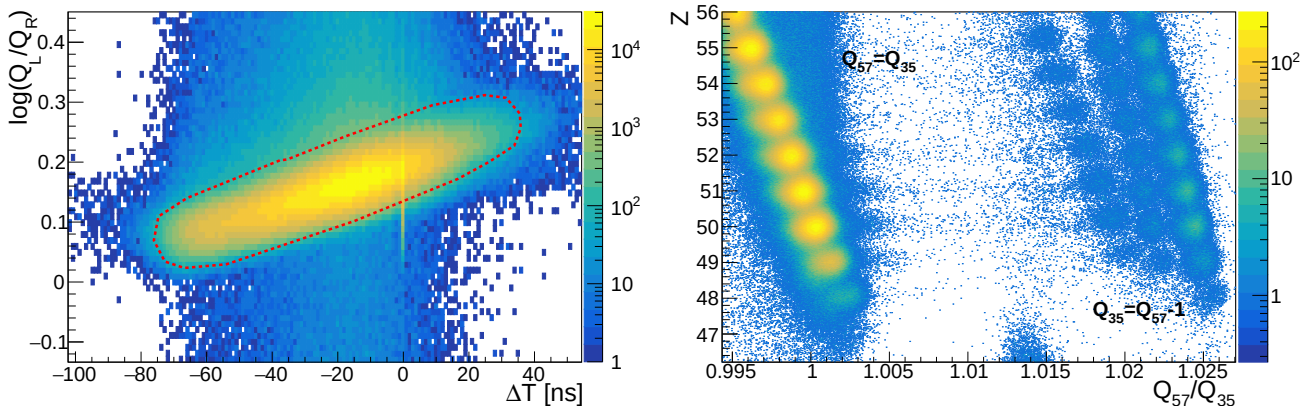

(a) (b)

Figure 3.9: (a) Example of background removal by the plastic scintillator at F7. The selection cut is indicated by a dashed red line. (b) Example of isotopes changing charge states at F5 by where the ratio of charges is determined from F3-F5 and F5-F7 A/Q measurements.

of the charge ratio Q_L/Q_R, i.e. [159]:

$$x \sim -ln\left(\frac{Q_L}{Q_R}\right). \tag{3.9}$$

Furthermore, the position information can be obtained by the time difference $\Delta T = T_R - T_L$ between the two readout signals in the same way as for the PPAC detectors. An example of such a correlation plot is shown in Fig. 3.9(a) for the F7 plastic scintillator. Inconsistent events deviate from the linear correlation and can therefore be excluded. Events which are outside the cut shown in Fig. 3.9(a) deviate from the relation that $x \sim ln(Q_L/QR) \sim \Delta T$ and have an inconsistent position determination and can therefore be removed. A second consistency cut was applied for the charges deduced from both signals of the PMTs of each plastic scintillator in a Q_L vs. Q_R plot.

When passing through the degrader at F5, electrons can be picked up and the charge state changes. In order to identify such events, the charge information before (Q_{35}) and after the degrader (Q_{57}) is measured via the timing information from the PPAC detectors. By plotting Z against the ratio Q_{57}/Q_{35}, charge exchanges can be detected and removed if necessary. This correlation plot is shown in Fig. 3.9(b).

Further inconsistent events can be removed by using the sum of the PPAC timing signals T_1 and T_2 which are obtained from either side of the delay lines. The sum of the PPAC time signals is independent of the position of the incident particle and should be a constant value [163]. Distortions from that value can occur due to multiple hit events or δ-ray generation [159]. The centroid of the T_{sum} time distributions is determined and events within

a 3σ range are accepted.

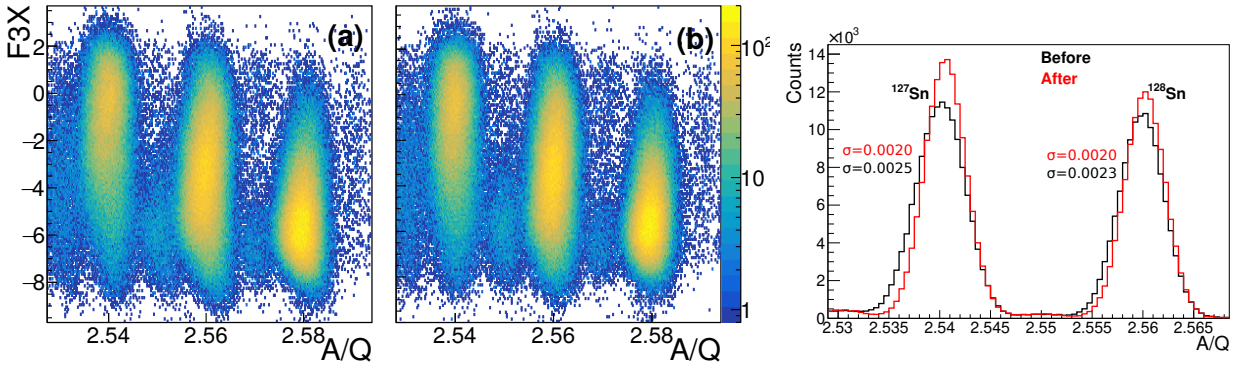

Figure 3.10: Horizontal position of the PPAC at F3 as a function of A/Q ratio for $Z = 50$ isotopes (a) before and (b) after the correction for ^{127}Sn (A/Q= 2.54). (c) A/Q projection before and after the correction. The spectra correspond to the x projections of the matrices in (a) and (b).

For the next correction, the correlation between A/Q ratio and position and angles of the PPAC detectors at the different focal planes is investigated. For a clean identification, the mass-to-charge ratio should be independent of the position or angle. An example is shown in Fig. 3.10 for the horizontal position of the PPAC detectors at F3 for tin $(Z = 50)$ isotopes. The A/Q is corrected as a function of position (and angle) with a polynomial up to third order, i.e., [159]:

$$A/Q_{cor} = A/Q + f_1(\text{F3X}) + f_2(\text{F3A}) + f_3(\text{F5X}) + f_4(\text{F5A}) + f_5(\text{F7X}) + f_6(\text{F7A}), \tag{3.10}$$

where X and A denote the horizontal position and the angle measured with the different PPAC detectors and f_{1-6} are polynomials up to the third order. Note that the correction is optimized for a specific A/Q ratio, in this example for A/Q=2.54 (^{127}Sn). The improvement in A/Q resolution is of the order of 10-20 % as can be seen in Fig. 3.10(c). After the correction, the resolution given as σ is $\sigma = 0.002$ for ^{127,128}Sn and about twice higher for the respective tellurium isotones.

The last correction applied for this experiment is concerning the ionization chamber located at F7. The final ΔE signal from the MUSIC is averaged from six individual readout lines. To exclude events that reacted inside the ionization chamber which ultimately leads to a false Z identification, a linear correlation between individual signals is required. This is guaranteed by applying cuts on all different correlation combinations and excluding events that do not follow a straight line. It has to be noted that the effect of these cuts is very small $(< 0.001\%)$ but is applied due to its importance in the Z determination. Events caused by reactions in the scintillator can be removed by comparing the charge-integrated signals from the plastic scintillator at F7 and the ΔE signal

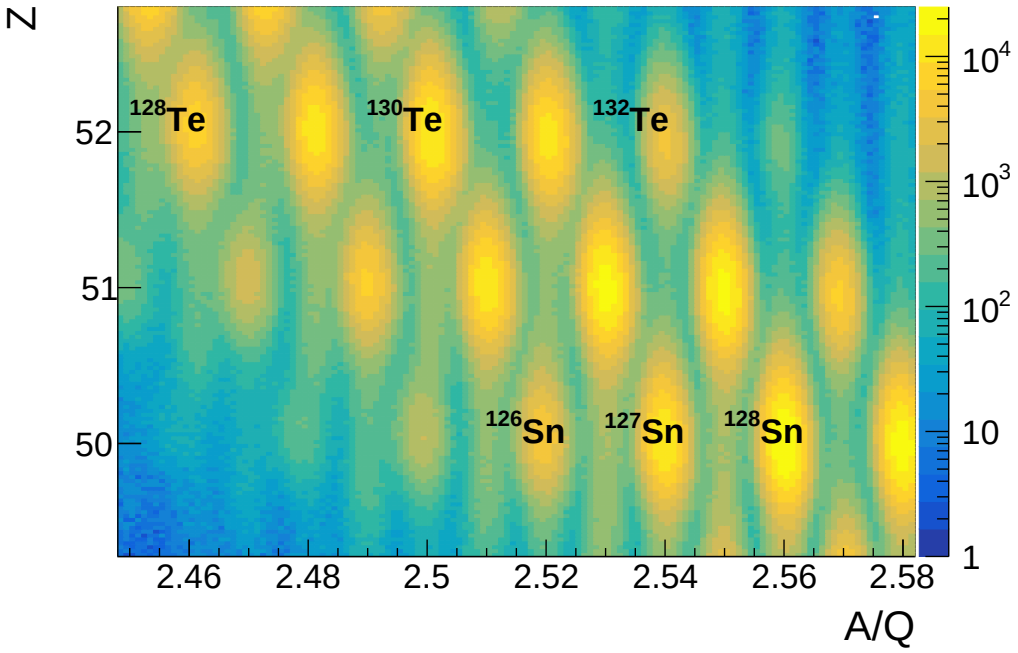

Figure 3.11: Final particle identification plot. Isotopes of interest are labeled accordingly.

from the MUSIC chamber. The Z resolution given as $\Delta Z/Z$ is 0.0092(1) for $Z = 50$ (Sn). The final particle identification plot after all corrections is shown in Fig. 3.11. In total, for the centered fragments $^{127,128}\mathrm{Sn}$ a total of $2.25 \cdot 10^6$ and $2.7 \cdot 10^6$ ions were produced and identified.

3.3.2 Detector calibration and efficiency

The energy of the HPGe detectors was calibrated using standard $^{152}\mathrm{Eu}$ and $^{60}\mathrm{Co}$ sources. Further gain matching was applied from the in-beam data to account for the energy shifts of one of the detectors. After the energy calibration, the detectors have to be calibrated and aligned in time in order to properly determine the $T_{1/2}$ of the isomeric states of interest.

Timing

The TAC modules were set to a fixed range for the entire experiment ($20\ \mu\mathrm{s}$) and calibrated using a TAC calibrator. The ADC channel to time conversion is done using a linear calibration function. Furthermore, the HPGe time signals were recorded using TDC modules with a $10\ \mu\mathrm{s}$ range. Figure 3.12 shows the TAC alignment procedure exemplary for one run and all detectors. The previously mentioned TAC calibration places the prompt position

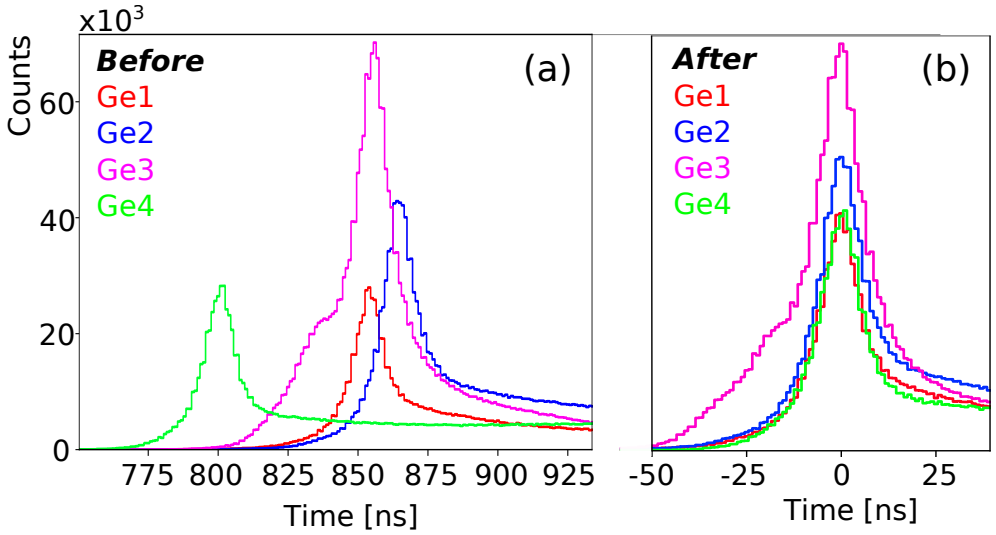

Figure 3.12: TAC spectra around the prompt peak for the different detectors (a) before and (b) after the alignment.

for each detector at an arbitrary position in the TAC spectrum (see Fig. 3.12(a)). After shifting all the centroids to zero, the detectors are perfectly aligned as shown in Fig. 3.12(b). A second check that has to be made is that the prompt position in the TAC spectra stays constant over the entire experiment and does not shift. This was confirmed by looking at the individual TAC spectra and aligning them, if necessary.

The same procedure was applied to the TDC data. In order to verify that both timing signals yield the same information, TAC and TDC values are plotted against each other. Apart from very few uncorrelated data points, a linear relation between both signals is present. Thus, both timing branches can be used to obtain the same information and to cross-check the results.

The last step is to correct the time walk according to Eq. (2.2) as discussed in Sec. 2.3. The energy dependence is obtained from similar 2D energy-time matrices for each detector individually. Overall, an improvement of the time resolution for energies below 200 keV in the order of 5 to 10 % was achieved. Higher energies are not affected by this correction.

HPGe efficiency

The HPGe efficiency was deduced with a $^{152}\mathrm{Eu}$ source that covers energy ranges between 100 and 1400 keV. The source was placed right before and right behind the implantation zone and two different efficiency curves were obtained, see Fig. 3.13. When the source is placed in the front of the catcher, the backward detectors Ge1 and Ge4 have a higher efficiency due to the fact that the γ rays reach the detectors without being shielded by

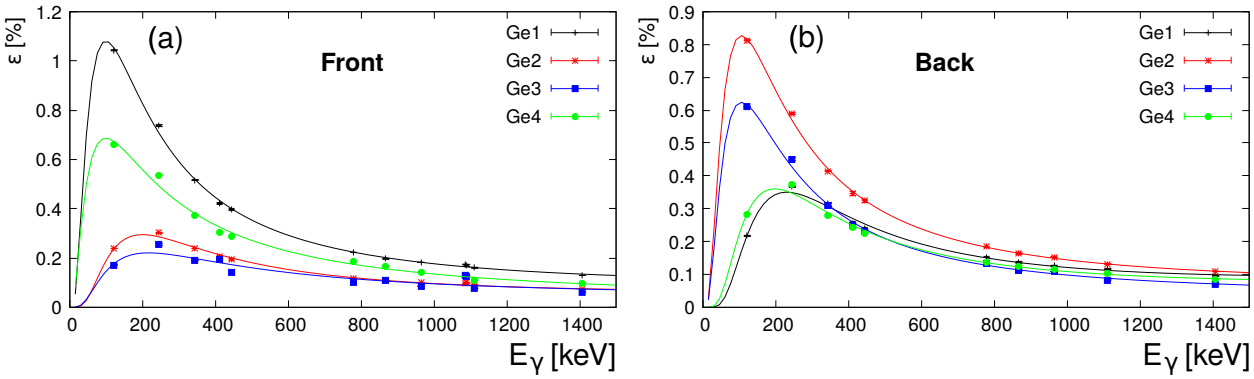

Figure 3.13: HPGe detection efficiency with the source placed in (a) in front of and (b) behind the implantation zone. Differences in efficiency arise from different electronic settings and positions of detectors from the source.

Table 3.1: Efficiency parameters for the HPGe detectors according to Eq. (3.11). The relative uncertainties of the parameters are around 10-20 %.

	Front				Back			
	a_0	a_1	a_2	a_3	a_0	a_1	a_2	a_3
Ge1	-25.2	13.6	-2.34	0.125	-79.4	38.1	-6.05	0.312
Ge2	-54.5	26.1	-4.15	0.213	-27.4	14.5	-2.47	0.131
Ge3	-40.1	18.4	-2.85	0.141	-27.2	14.2	-2.39	0.125
Ge4	-17.2	8.8	-1.45	0.071	-62.5	30.3	-4.88	0.253
sum	-40.4	21.2	-3.51	0.185	-41.1	21.6	-3.49	0.182

the copper material from the catcher. This effect was already investigated during the testing of the detectors, see Fig. 3.5. The reverse is true when the source is placed behind the catcher. For a proper estimation of the efficiency, the average efficiency values for each detector are used from both curves shown in Fig. 3.13. The data points were fitted using an empirical function [78]:

$$ln(\epsilon) = a_0 + a_1 \cdot ln(E_\gamma) + a_2 \cdot ln(E_\gamma)^2 + a_3 \cdot ln(E_\gamma)^3, \tag{3.11}$$

where $\{a_i\}$ are obtained from the fit. The parameters are given in Tab. 3.1 and their relative uncertainties are in the order of 10-20 %.

3.3.3 Isomers and half-lives

The identification of isomers can be visualized when looking at energy-time matrices. An example for ^{128}Sn is shown in Fig. 3.14 which displays such a matrix in coincidence with ^{128}Sn ions. ^{128}Sn decays via two isomers: a (15^-) isomer with $T_{1/2} = 0.22(4)$ μs and a (10^+) isomer with $T_{1/2} = 2.91(14)$ μs [148], see level scheme

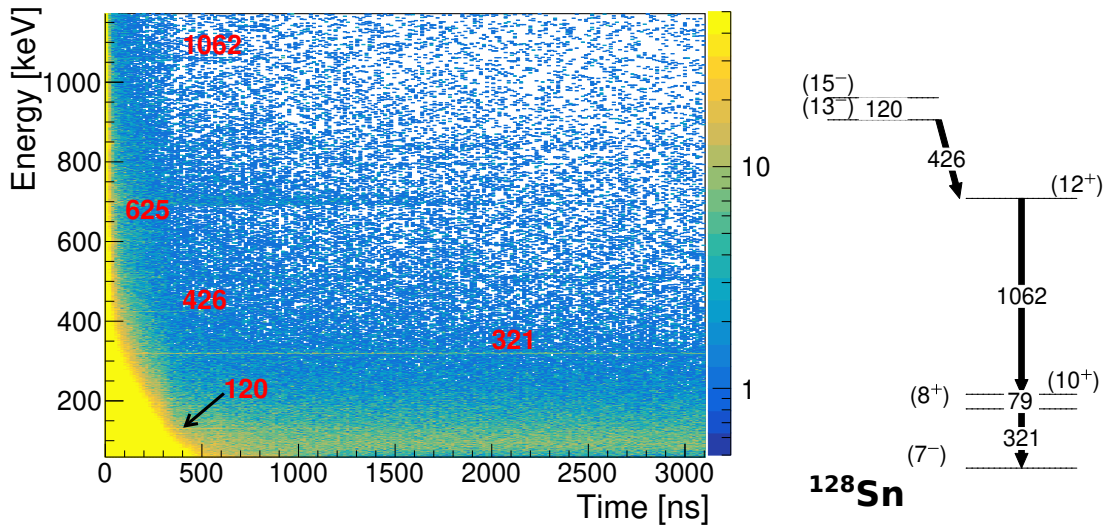

Figure 3.14: Identification of isomeric transitions in ^{128}Sn in an energy versus time matrix. The partial level scheme of the decay of the (15^-) and (10^+) isomers is shown on the right with energies in keV taken from Ref. [148].

in Fig. 3.14. All transitions below the isomers of interest are of isomeric character which can be seen by the horizontal lines in the time-energy matrix displayed in Fig. 3.14. The difference in isomeric half-life can also be seen by how far these lines extend in x direction.

The low energy transitions are not well visible in the 2D matrix. Apart from the shielding possibilities discussed in Sec. 3.2.2, low energy peaks can be enhanced by only looking at delayed γ rays away from the prompt flash. To emphasize the capabilities of choosing appropriate time cuts for the identification of low energy γ rays, two examples of ^{126}Sn and ^{132}Te are shown in Fig. 3.15. In ^{126}Sn both, 76 keV and 112 keV, transitions are visible where the former is less pronounced due to the reduced efficiency at low energies (see Fig. 3.13). The low energy $7^- \rightarrow 5^-$ transition is below the detection threshold of the HPGe detectors used in this experiment and is therefore not observed. In ^{132}Te, both low energy transitions of 104 keV and 151 keV can be well identified when selecting γ rays outside of the prompt flash. This highlights the capabilities of identifying low energy transitions in radioactive ion beam experiments thanks to optimized detection parameters of the system selected and tested prior to the experiment as explained in Sec. 3.2.2.

The time information can either be extracted from the TDC or TAC measurement. Unless denoted otherwise, the TAC data are shown while the TDCs are used for a cross-check.

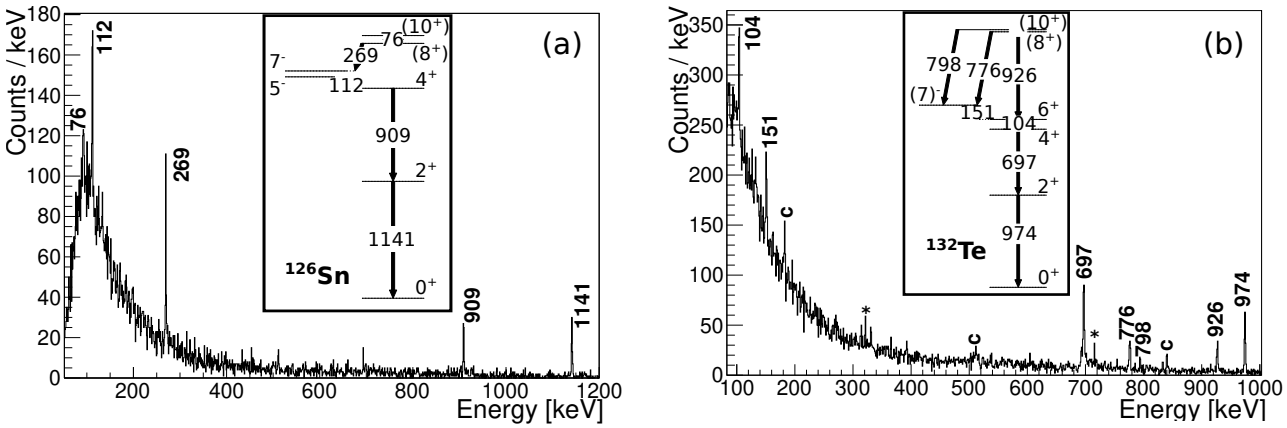

Figure 3.15: Delayed γ rays measured in coincidence with (a) $^{126}\mathrm{Sn}$ and (b) $^{132}\mathrm{Te}$ ions. Partial level schemes of the decay from the (10^+) isomers are shown in the insets. Data taken from Refs. [41, 147]. Transitions from the isomeric decays are labeled with their respective energy and contaminants are marked with 'c'. Unknown transitions are marked with asterisks.

In the cases of only one isomer decaying in a cascade, the half-life is obtained using a single exponential fit with a constant background. The statistical uncertainty includes a variation of the fit parameters. If multiple isomers decay in a cascade, the half-life of the lower isomers have to be determined using the Bateman equations [164]. For two isomers connected in a cascade, the decay curve of the lower-lying isomer $N^2(t)$ can be described via:

$$N^2(t) = N_0^1 \frac{\lambda_1}{\lambda_2 - \lambda_1} \cdot \left(e^{-\lambda_1 t} - e^{-\lambda_2 t}\right) + N_0^2 e^{-\lambda_2 t}, \tag{3.12}$$

where N_0^1, N_0^2 describe the initial population of mother (N_0^1) and daughter (N_0^2) with their respective decay constants λ_1, λ_2. The uncertainties are determined from a variation of fit regions and background components and added in a similar way as explained in Sec. 2.3.6.

3.4 Results

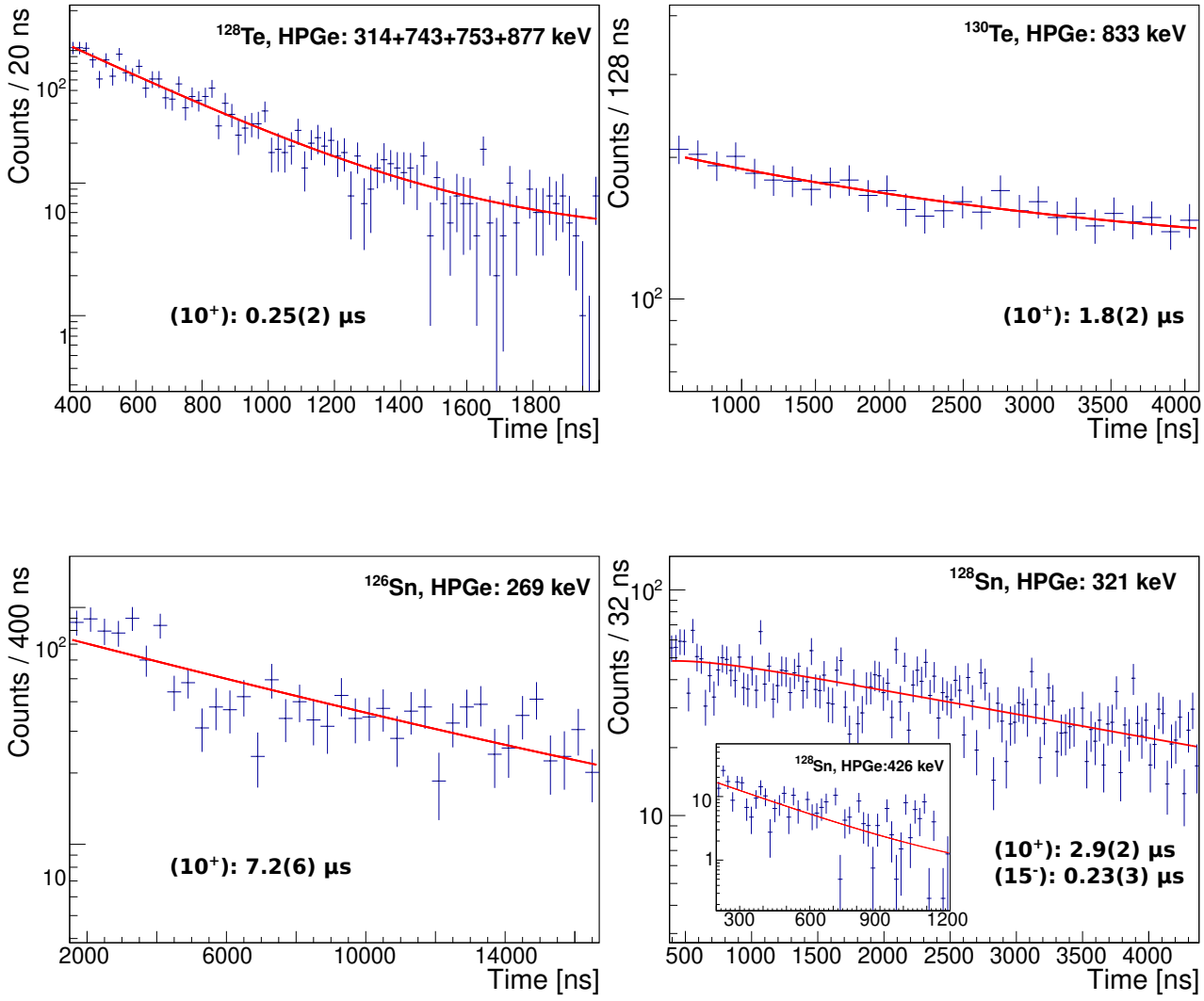

Figure 3.16: Half-life measurements for isomers of interest populated in this work. Each panel is labeled with their respective PID and HPGe gate as well as the resulting half-life.

Isomers in neutron-rich tin and tellurium isotopes were populated and identified in this work. Known (10^+) isomers in the $N = 76, 78, 80$ isotones were remeasured. In addition, the high-spin $(27/2^-), (23/2^+)$ isomers in ^{127}Sn and the (15^-) isomer in ^{128}Sn were confirmed. No higher-lying isomer (e.g., (15^-)) in ^{126}Sn was found in this nucleus. This means that either the half-life is too short ($T_{1/2} < 100$ ns) or not enough statistics was acquired. A higher-lying isomer search was also performed in ^{132}Te and potential candidates are marked in

Fig. 3.15(b) with asterisks. More data and a precise analysis would allow further information on such an isomer in $^{132}\mathrm{Te}$.

Table 3.2: Experimental results on half-lives measured in this work. Isomeric decay information is provided (excitation energy spin and parity J^π, γ-ray energy E_γ). Literature $T_{1/2}$ values are shown for comparison. Excitation energies, spins and parities and literature half-lives are taken from Refs. [39, 142]. Theoretical values are taken from Ref. [51] for the tin isotopes and Ref. [141] for the tellurium isotopes.

Nucleus	E_x	J_i^π	J_f^π	E_γ	$T_{1/2}$ [μs]		$B(E2)$ [e^2fm^4]	
	[keV]			[keV]	This exp.	Lit.	This exp.	Theo.
$^{126}\mathrm{Sn}$	2492	(10^+)	(8^+)	79	7.2(6)	7.7(5)	5.5(4)	4
$^{127}\mathrm{Sn}$	1827	$(19/2^+)$	$(15/2^+)$	715	4.5(3)	4.52(12)	42(3)	30
	1931	$(23/2^+)$	$(19/2^+)$	104	1.0(3)	1.19(13)	19(6)	22
	2552	$(27/2^-)$	$(23/2^-)$	142	0.24(3)	0.25(3)	28(5)	30
$^{128}\mathrm{Sn}$	2492	(10^+)	(8^+)	79	3.0(3)	2.91(14)	13(1)	11
	4100	(15^-)	(13^-)	426	0.23(3)	0.22(3)	54(12)	
$^{130}\mathrm{Sn}$	2435	(10^+)	(8^+)	97	1.6(2)	1.61(15)	13.1(14)	10
$^{128}\mathrm{Te}$	2791	(10^+)	(8^+)	102	0.25(2)	0.24(2)	80(6)	79
$^{130}\mathrm{Te}$	2668	(10^+)	(8^+)	833	1.8(2)	1.90(8)	90(15)	82
$^{132}\mathrm{Te}$	2723	(10^+)	(8^+)	798	3.6(5)	3.70(9)	45(6)	42

Half-lives of the isomeric states measured in this work are obtained by gating on transitions belonging to the isomer of interest. Some examples are shown in Fig. 3.16 for the $N = 76, 78$ isotones $^{126,128}\mathrm{Sn}$ and $^{128,130}\mathrm{Te}$. For $^{126}\mathrm{Sn}$, $^{128}\mathrm{Te}$ and $^{130}\mathrm{Te}$, the (10^+) isomer is the highest isomeric state and the time distributions are fitted using a single exponential decay curve and a constant background. Whenever applicable, several transitions below the isomer are added in order to increase the statistics. Each panel in Fig. 3.16 is labeled with their respective energy gates and the results are listed in Tab. 3.2. As it can be seen, in several cases the uncertainties in this work could be improved.

For $^{128}\mathrm{Sn}$, the (10^+) isomer is fed by a (15^-) isomer with a much shorter half-life. The time spectrum used to obtain the half-life of the (15^-) isomer is shown in the inset of the respective panel in Fig. 3.16. The result of $T_{1/2} = 0.23(3)$ μs is then fed into the decay curve of the (10^+) isomer according to Eq. (3.12).

In a similar way, the half-lives of the $(27/2^-)$ and $(23/2^+)$ isomers in $^{127}\mathrm{Sn}$ were obtained. The time distribution for the $(27/2^-)$ is obtained from the 480 keV $(23/2^-) \rightarrow (23/2^+)$ transition and fitted using a single exponential. The half-life of the $(23/2^+)$ was then fitted using $T_{1/2} = 0.24(3)$ μs from the previous fit to obtain the half-life of the $(23/2^+)$ state from the 104 keV transition. The time distribution is shown in Fig. 3.17 and marks

the first time of the measurement of this half-life from its direct decaying transition. The $T_{1/2}$ value amounts to 1.0(3) μs and is consistent with the previously reported results [51, 151, 165].

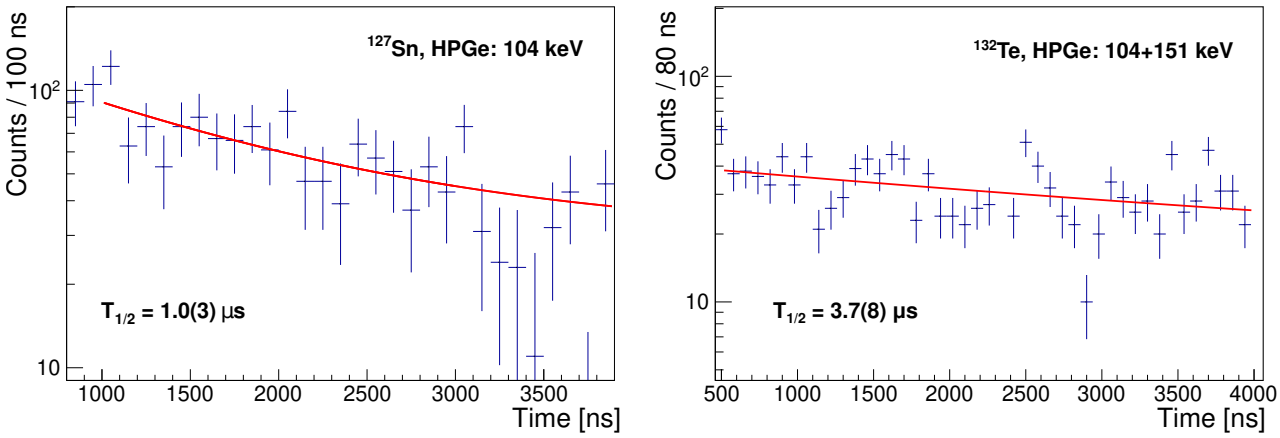

Figure 3.17: Time distribution of low energy transitions to measure the half-life of the $(23/2^+)$ isomer in ^{127}Sn and the (10^+) isomer in ^{132}Te.

The lowest isomeric state in ^{127}Sn is the $(19/2^+)$ state which is fed by both higher-lying isomers. To avoid any contributions from the $(27/2^-)$ or $(23/2^+)$ half-life, the time distribution for the $(19/2^+)$ state is fitted from 5 μs on, which corresponds to about $5 \cdot T_{1/2}[(23/2^+)]$. The result of $4.5(3)$ μs is consistent with previously reported values and is given in Tab. 3.2.

In addition, the half-lives of the (10^+) states in the $N = 80$ isotones ^{130}Sn and ^{132}Te were remeasured. For ^{130}Sn, a sum of gates on all detected transitions below the isomer was used. The resulting half-life of 1.6(2) μs confirms the previously reported value of 1.61(15) μs [149].

For ^{132}Te, the half-life was independently measured in two ways. First, a sum of transitions directly depopulating the (10^+) state and bypassing the long-lived $(7)^-$ isomer are used, i.e., 798 keV, 776 keV and 926 keV (see Fig. 3.15(b)). The result amounts to $T_{1/2} = 3.5(6)$ μs and was obtained from a single exponential fit. In addition, low energy transitions decaying from the $(7)^-$ isomer with $T_{1/2} = 28.1(15)$ μs [149] are used to measure the half-life of the (10^+) isomer by using Eq. (3.12). The corresponding fit is shown in Fig. 3.17 and further demonstrates the capabilities of measuring low energy transitions with this setup. The resulting half-life of $3.7(8)$ μs is consistent with the first fit and amounts to a weighted average of $T_{1/2} = 3.6(5)$ μs as given in Tab. 3.2.

3.5 Discussion

Figure 3.18 shows the systematic evolution of (a) excitation energy and (b) $B(E2)$ strength for the $J^\pi = 10^+$ isomers below $N = 82$. The excitation energy follows a smooth trend as a function of neutron number and is almost constant for both isotopic chains. It increases from 2565 keV in $^{126}\mathrm{Sn}$ to 2435 keV in $^{130}\mathrm{Sn}$. This is an indicator for a seniority $\nu = 2$ $\nu(0h^n_{11/2})$ configuration. When adding two protons to the system, the excitation energy slightly increases but the evolution as a function of neutron number remains almost constant. This increase in excitation energy can be attributed to the extra proton excitation which also plays a role in the wave functions of these excited states.

Reduced $E2$ transition probabilities are calculated according to Eq. (1.20) in the same way as in chapter 2. For the isotopes of interest, spectroscopic information is taken from the evaluated nuclear data sheets [41, 147, 148, 149, 165]. The transition strengths are corrected for internal conversion using the coefficients calculated with BrICC [118] and the results are presented in Tab. 3.2. To compare the experimental findings with those from theoretical predictions, results from calculations were taken from Refs. [51, 141]. The data for the tin isotopes was obtained from shell-model calculations using a $^{88}\mathrm{Sr}$ core with the $\pi(1p_{1/2}0g_{9/2})$ orbitals for the protons and the $\nu(0g_{7/2}, 1d_{5/2}, 1d_{3/2}, 2s_{1/2}, 0h_{11/2})$ orbitals for the neutrons [51]. The interaction was derived from a CD-Bonn nucleon-nucleon potential as described in Ref. [166]. Single-particle energies are adopted from Ref. [167] with additional monopole corrections as described in Ref. [51]. An effective neutron charge of $e_\nu = 0.70e$ was used to calculated reduced $E2$ transition probabilities.

The evolution of $B(E2; (10^+) \rightarrow (8^+_1))$ values in the tin isotopes can be described by the subshell fill of the $\nu(0h_{11/2})$ orbital [51]. When discussing the evolution of transition rates in the tellurium isotones, it can be assumed that the $8^+_1, 10^+_1$ states include not only pure $\nu(0h^{-2}_{11/2})$ configurations but also configurations with proton admixtures, i.e. [141]:

$$|1\rangle = \left[\nu(0h^{-2}_{11/2}) \otimes \pi(0^+)\right]_{8^+,10^+},$$

$$|2\rangle = \left[\nu(0h^{-2}_{11/2}) \otimes \pi(2^+)\right]_{8^+,10^+}.$$

The former one describes the pure neutron excitation while the latter one includes an excitation of the proton part. To calculate the transition probabilities, a two-state mixing of those configurations is assumed to describe the residual proton-neutron configuration. The mixed states are then given by a coupling of both configurations weighted with a mixing amplitude ϵ:

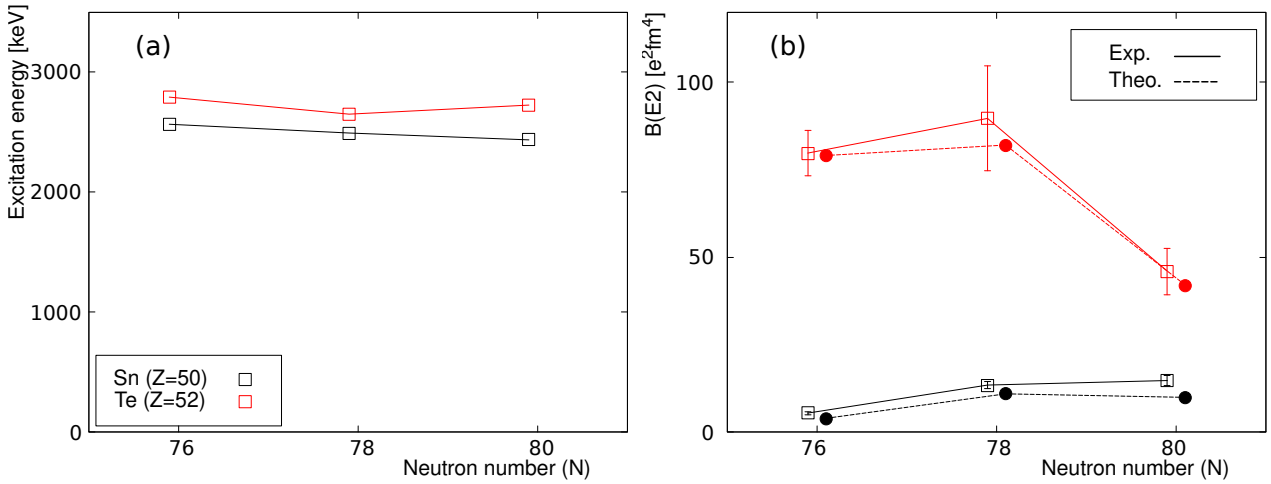

Figure 3.18: Evolution of (a) excitation energy and (b) $B(E2)$ strengths for the 10^+ isomers of neutron-rich tin and tellurium isotopes as a function of neutron number. Experimental values from this work are given as open squares and theoretical ones as filled circles. Lines are drawn to guide the eye.

$$|10^+_1\rangle = [|1\rangle + \epsilon|2\rangle]_{10^+},$$

$$|8^+_1\rangle = [|1\rangle + \epsilon|2\rangle]_{8^+}.$$

The $B(E2)$ strength of the $10^+ \rightarrow 8^+$ transition in the tellurium isotopes can then be calculated using the overlap of those mixed wave functions [141]:

$$B(E2[\text{Te}]; 10^+ \rightarrow 8^+) \sim \left(\sqrt{B(E2; \nu(10^+ \rightarrow 8^+))} + \epsilon 1.9 \cdot \sqrt{B(E2; \pi(2^+ \rightarrow 0^+))}\right)^2, \tag{3.13}$$

where the summands correspond to the $B(E2)$ strength of a pure neutron $10^+ \rightarrow 8^+$ and a pure proton $2^+ \rightarrow 0^+$ transition weighted with a factor to account for the spin difference. The $B(E2)$ values for the pure configurations are taken from the experimental transitions in the tin isotones and the tellurium isotopes. The results are listed in the last column of Tab. 3.2.

The evolution of $B(E2; (10^+_1) \rightarrow (8^+_1))$ strength is shown in Fig. 3.18(b). For the tin isotopes, the description of the calculated transition strengths matches the experimental values very well. The increase in measured $B(E2)$ values can be attributed to the filling of the $\nu(0h_{11/2})$ orbital [49, 51, 138]. Deviations between experimental and theoretical values may be assigned to the increasing influence of proton-core excitations when moving away from the closed neutron shell. In addition to the isomers in the even-even tin isotopes, the half-lives of all three isomers in ^{127}Sn were remeasured. The experimental values for the higher-lying $(27/2^-)$ and $(23/2^+)$ isomers are perfectly reproduced by the calculations. Those states are dominated by the $\nu(0h^{-3}_{11/2})$ and the $\nu(1d^{-1}_{3/2}0h^{-2}_{11/2})$ configurations, respectively. The $B(E2)$ strength of the $(19/2^+) \rightarrow (15/2^+)$ transition is slightly

underestimated by the theoretical calculation. The main components in the wave function of this state are $\nu(1d_{3/2}^{-1}0h_{11/2}^{-2})$ and $\nu(2s_{1/2}^{-1}0h_{11/2}^{-2})$, as also confirmed by a measurement of its g factor [153]. The deviation of $B(E2)$ strength shows that this mixing is insufficiently represented in the calculation and that comparison with experimental data is essential.

With the addition of two protons to the tin core, the $B(E2)$ strength increases by roughly an order of magnitude. This shows the clear increase in collectivity with the addition of only two protons. As has been shown for the tellurium isotopes beyond $N = 82$ in Sec. 2.5, despite the large N/Z ratio, those protons play a dominant role in the evolution of collectivity away from the closed neutron shell. Similar to the excitations in the tellurium isotopes with $N \geq 82$, the low-lying yrast states up to $J = 6$ are governed by the proton $\pi(0g_{7/2}^2)$ configuration. The experimental $B(E2; (10_1^+) \rightarrow (8_1^+))$ values are well reproduced by the two-state mixing model from Ref. [141]. It was shown in Ref. [141] that small mixings of a proton 2^+ excitation in the 8^+ and 10^+ states can account for the strong increase in $B(E2)$ value which could be confirmed in this work. In comparison to the previous chapter, it can be concluded that the effect of the slowing down of the collectivity is less pronounced for $N < 82$ compared to $N > 82$.

Chapter 4

Summary and outlook

4.1 Part I: Lifetime measurements around ^{132}Sn with the ν-ball array

The first part of this thesis shows results from spectroscopy and lifetime measurements of neutron-rich nuclei around $^{132}\mathrm{Sn}$ using the ν-ball hybrid spectrometer. This part of the thesis work includes a complete description of the experimental setup, data analysis and an interpretation based on state-of-the-art theoretical calculations.

The results were obtained in an experiment coupling the LICORNE neutron source to the ν-ball array at the ALTO facility of the IJCLab in Orsay, France. Nuclei of interest were populated in fast neutron-induced fission of $^{238}\mathrm{U}$ and γ rays detected with a combination of HPGe detectors and $LaBr_3$(Ce) scintillators. Lifetimes were extracted for neutron-rich tellurium ($Z = 52$) and iodine ($Z = 53$) isotopes beyond $N = 82$. From the measured lifetimes, reduced transition probabilities were deduced which provide insights into the evolution of collectivity beyond $^{132}\mathrm{Sn}$. An expected fast onset of collectivity for neutron number $N = 84$ and higher was not indicated from the present data. This was observed distinctly for both tellurium and iodine set of isotopes investigated in this work. The effect of the slowed down collectivity is seen most prominently in the $B(E2)$ strengths of the $4_1^+ \rightarrow 2_1^+$ and $6_1^+ \rightarrow 4_1^+$ transitions in $^{138}\mathrm{Te}$.

The new information on spectroscopic data and reduced transition probabilities obtained from the analysis in this work was compared to shell-model calculations using different effective interactions. Experimental excitation energies for all isotopes were reproduced using a state-of-the-art N3LOP effective interaction. Reduced transition probabilities are well described while the slowing down of the collectivity is not exactly reproduced. A comparison with different effective interactions highlights the importance of the $\pi(1d_{5/2})$ proton orbital and the $\nu(1f_{7/2})$ and $\nu(2p_{3/2})$ neutron orbitals in the successful description of the low-lying excited states in neutron-rich

tellurium and iodine isotopes.

These results yield valuable input for theoretical models and opens new questions concerning the evolution of collectivity outside the doubly magic $^{132}\mathrm{Sn}$. Future measurements to improve the uncertainty and extend lifetime information up to $N = 90$ would be of great importance to gain a more complete picture on the nuclear structure beyond $N = 82$. Therefore, the optimization of the experimental setup and the possibility to use the centroid shift method will be crucial.

4.2 Part II: Isomers around ^{132}Sn

In the second part of this thesis isomers around $^{132}\mathrm{Sn}$ were investigated after in-flight fission of $^{238}\mathrm{U}$ at the Radioactive Isotope Beam Facility (RIBF) of the RIKEN Nishina Center in Saitama, Japan. This chapter included a detailed description of the experimental setup and a preparation of the experiment. A detailed data analysis with a special emphasis on the particle identification procedure was provided. Half-lives of isomers below the doubly magic $^{132}\mathrm{Sn}$ were remeasured and compared to theoretical calculations.

The isotopes of interest were produced and identified with the particle tracking detectors of the BigRIPS fragment separator using the $B\rho$-TOF-ΔE method and implanted in a copper catcher at the F8 focal point of the ZeroDegree Spectrometer. Delayed γ rays were measured using four HPGe detectors in a compact geometry. Half-lives of isomeric transitions were remeasured to deduce reduced transition probabilities which were successfully reproduced by shell-model calculations. A special emphasis was made on low energy transitions which were, in some cases, used for the first time to extract the isomeric half-life and better precision was obtained in several cases.

By comparing the reduced transition probabilities from the tin isotopes to the respective tellurium isotones it was concluded that despite the large neutron excess the collectivity is strongly influenced by the two valence protons. This is in accordance with the results from the first part of this work. However, the slowing down of the collectivity is less significant below $N = 82$ than above the closed neutron shell.

Future studies to search for high-spin isomers in that region are of great interest to gain a deeper understanding into the role of the protons outside the $Z = 50$ closed shell. Furthermore, the study of the magnetic moments would allow to shed light on the detailed configurations.

Appendix A

Gamma-ray intensities for different fission reactions

This appendix presents the γ-ray intensities measured for neutron-rich tellurium and iodine isotopes during the ν-ball campaign as shown in Figs. 2.33 and 2.35, respectively. The main results are obtained from the ^{238}U(n,f) N-SI-109 fission experiment discussed in Sec. 2.4. In addition, a comparison to the additional ^{238}U(n,f) data, ^{252}Cf(sf) data from the commissioning run and ^{248}Cm(sf) data from the literature is given.

Table A.1: Transitions associated with ^{134}Te as observed in the current work. Spins and parities are taken from the evaluated nuclear data sheet [87].

Nucl.	$J_i^\pi \rightarrow J_f^\pi$	E_γ [keV]	I_γ [rel]			
			^{238}U	^{238}U	^{252}Cf	^{248}Cm
			1.7 MeV	3.4 MeV		[87]
^{134}Te	$2_1^+ \rightarrow 0_1^+$	1279.1(5)	100(10)	100(20)	100(20)	100(20)
	$4_1^+ \rightarrow 2_1^+$	296.9(5)	74(10)	71(4)	87(12)	88(18)
	$6_1^+ \rightarrow 4_1^+$	115.3(5)	66(9)	< 70	40(15)	20(4)
	$(6_2)^+ \rightarrow 6_1^+$	706.6(7)	5.9(6)	11(3)		9.2(18)
	$(4_2^+) \rightarrow 4_1^+$	978.5(4)	4.0(11)			6.4(13)
	$(5_1^+) \rightarrow (6_2)^+$	328.7(6)	2.1(4)	2.5(6)		3.3(6)
	$(5_1^+) \rightarrow 4_1^+$	1150.7(4)	3.3(8)			3.7(7)

Continued on next page

Table A.1 – *Continued from previous page*

Nucl.	$J_i^\pi \to J_f^\pi$	E_γ [keV]	I_γ [rel]			
			^{238}U	^{238}U	^{252}Cf	^{248}Cm
			1.7 MeV	3.4 MeV		[87]
	$(9_1^-) \to 6_1^+$	2322.0(10)	8.4(11)	4.1(14)		10(2)
	$(9_1^-) \to (6_2)^+$	1615.2(7)	0.61(14)	1.9(5)		1.8(4)
	$(7_1^-) \to (6_2)^+$	1901.5(6)	0.47(14)	0.7(2)		0.60(12)
	$(8_1^+) \to 6_1^+$	2865.2(7)	9.9(11)	18(3)		6.9(14)
	$(8_1^+) \to (7_1^-)$	257.1(7)	< 2	1.3(8)		0.20(4)
	$(8_1^-) \to 9_1^-$	548.6(8)	1.5(2)	0.8(3)		4.0(8)
	$(9_1^+) \to (8_1^+)$	521.7(9)	0.3(2)	0.7(3)		1.3(3)
	$(9_1^+) \to (8_1^-)$	516.4(5)	0.7(3)	2.4(5)		2.0(4)
	$(10_1^+) \to (8_1^+)$	1064.0(6)	1.5(2)	1.0(2)		2.4(5)
	$(10_1^+) \to (9_1^+)$	542.3(10)	< 0.8			1.5(3)
	$(10_1^+) \to (9_1^-)$	1607.3(8)	0.55(13)	1.0(3)		0.4(1)
	$(10_1^-) \to (9_1^-)$	1643.4(8)	0.37(11)	0.6(3)		1.2(2)
	$(12_1^+) \to (10_1^+)$	182.6(6)	1.3(3)	3.5(12)		1.4(3)
	$(13_1^+) \to (12_1^+)$	205.7(7)	1.0(7)	< 2		1.3(3)
	$(11_1^-) \to (10_1^-)$	441.9(8)	0.33(13)	< 0.7		0.20(4)
	$(14_1^+) \to (13_1^+)$	1040.8(7)	1.1(3)	1.6(4)		0.3(1)

Table A.2: Same as Tab. A.1 but for ^{136}Te. Spins and parities taken from Ref. [109].

Nucl.	$J_i^\pi \to J_f^\pi$	E_γ [keV]	I_γ [rel]			
			^{238}U	^{238}U	^{252}Cf	^{248}Cm
			1.7 MeV	3.4 MeV		[109]
^{136}Te	$2_1^+ \to 0_1^+$	606.3(6)	100(10)	100(10)	100(13)	100
	$4_1^+ \to 2_1^+$	423.5(5)	84(12)	85(14)	80(14)	94(10)
	$6_1^+ \to 4_1^+$	352.5(5)	69(11)[3]	61(9)	45(9)	79(2)
	$(2_2^+) \to 2_1^+$	961.7(6)	0.47(12)			
	$8_1^+ \to 6_1^+$	749.3(5)	39(4)	38(6)	33(8)	37(4)
	$(4_2^+) \to (2_2^+)$	817.0(10)*	< 0.25			
	$10_1^+ \to 8_1^+$	659.8(5)	19(2)	19(3)	20(10)	19(2)
	$(12_1^+) \to 10_1^+$	394.5(5)	8.5(16)	5.3(12)	< 10	
	$(14_1^+) \to (12_1^+)$	533.6(5)	3.9(1.2)	4.8(1.5)	< 10	
	$(15^+) \to (14_1^+)$	1074.4(6)	1.2(5)	1.5(6)		

Table A.3: Same as Tab. A.1 but for $^{138}\mathrm{Te}$. Spins and parities taken from Ref. [110]. Transitions marked with a $\times$ are not observed and their intensity is given as observation limit.

Nucl.	$J_i^\pi \to J_f^\pi$	E_γ [keV]	I_γ [rel]			
			$^{238}\mathrm{U}$	$^{238}\mathrm{U}$	$^{252}\mathrm{Cf}$	$^{248}\mathrm{Cm}$
			1.7 MeV	3.4 MeV		[110]
$^{138}\mathrm{Te}$	$(2_1^+) \to 0_1^+$	460.7(5)	100(10)	100(20)	100(20)	100(3)
	$(4_1^+) \to (2_1^+)$	442.8(6)	97(10)	87(15)	> 49	85(7)
	$(6_1^+) \to (4_1^+)$	535.6(6)	62(9)[4]	65(12)	< 28	48(5)
	$(7_1^+) \to (6_1^+)$	581.8(5)	7(3)	< 18		8.5(7)
	$(8_1^+) \to (6_1^+)$	648.5(6)	25(3)	33(11)		19.0(9)
	$(8_2^+) \to (6_1^+)$	759.5(7)	9(2)	23(6)		5.8(3)
	$(10^+) \to (8_1^+)$	584.5(6)	7(1)	< 12		8.8(7)
	$(10^+) \to (8_2^+)$	474.2(2)$^\times$	<0.8	< 1.3		1.8(3)
	$(10^+) \to (8_1^+)$	671.8(1)$^\times$	<0.5	< 1.3		2.1(4)
	$(10^+) \to (8_2^+)$	561.1(1)$^\times$	<0.9	< 1.3		3.8(3)

Table A.4: Same as Tab. A.1 but for $^{135}\mathrm{I}$. Spins and parities taken from Ref. [97].

Nucl.	$J_i^\pi \to J_f^\pi$	E_γ [keV]	I_γ [rel]			
			$^{238}\mathrm{U}$	$^{238}\mathrm{U}$	$^{252}\mathrm{Cf}$	$^{248}\mathrm{Cm}$
			1.7 MeV	3.4 MeV		[97]
$^{135}\mathrm{I}$	$(11/2^+) \to (7/2^+)$	1134.0(5)	100(10)			100(20)
	$(15/2^+) \to (11/2^+)$	288.2(5)	84(15)			87(17)
	$(17/2^+) \to (15/2^+)$	571.5(5)	72(9)			34(7)
	$(11/2) \to (15/2^+)$	928.4(10)	13(5)			0.8(2)
	$(13/2^+) \to (15/2^+)$	999.6(6)	12(6)			0.5(1)
	$(19/2^-) \to (17/2^+)$	1661.4(6)	7(2)			5(1)
	$(23/2^-) \to (17/2^+)$	1696.1(6)	27(6)			11.8(24)
	$(19/2^+) \to (17/2^+)$	2247.8(6)	< 14			3.1(6)

Table A.5: Same as Tab. A.1 but for ^{137}I. Spins and parities taken from Ref. [116].

Nucl.	$J_i^\pi \rightarrow J_f^\pi$	E_γ [keV]	I_γ [rel]			
			^{238}U	^{238}U	^{252}Cf	^{248}Cm
			1.7 MeV	3.4 MeV		[116]
^{137}I	$(9/2^+) \rightarrow (7/2^+)$	553.8(5)	100(10)			100(1)
	$(11/2^+) \rightarrow (7/2^+)$	619.9(5)	36(7)			37(2)
	$(13/2^+) \rightarrow (9/2^+)$	400.0(5)	82(9)			64(2)
	$(13/2^+) \rightarrow (11/2^+)$	333.9(5)	15(4)			17(1)
	$(15/2^+) \rightarrow (11/2^+)$	488.0(5)	18(5)			4.6(7)
	$(15/2^+) \rightarrow (13/2^+)$	154.0(10)	< 2			-
	$(17/2^+) \rightarrow (13/2^+)$	358.2(5)	59(7)			44(1)
	$(17/2^+) \rightarrow (15/2^+)$	204.0(8)	$4(2)$			-
	$(19/2^+) \rightarrow (15/2^+)$	500.0(5)	4.0(17)			1.3(4)
	$(19/2^+) \rightarrow (17/2^+)$	296.1(6)	31(9)			9(1)
	$(21/2^+) \rightarrow (17/2^+)$	725.4(5)	21(4)			11(1)
	$(21/2^+) \rightarrow (19/2^+)$	429.3(6)	8(4)			0.4(1)
	$(23/2^+) \rightarrow (19/2^+)$	614.0(5)	9(3)			7(1)
	$(23/2^+) \rightarrow (21/2^+)$	184.7(7)	< 2			< 2
	$(25/2^+) \rightarrow (21/2^+)$	705.1(7)	13(4)			2.3(1)
	$(25/2^+) \rightarrow (23/2^+)$	520.4(6)	< 2			0.7(1)
	$(27/2^+) \rightarrow (23/2^+)$	862.4(5)	5.2(18)			1.8(1)
	$(27/2^+) \rightarrow (25/2^+)$	342.0(6)	< 2.5			0.15(3)
	$(29/2^+) \rightarrow (25/2^+)$	423.7(12)	9(5)			1.5(1)
	$(31/2^+) \rightarrow (27/2^+)$	567.3(8)	5(3)			2.2(1)
	$(31/2^+) \rightarrow (29/2^+)$	485.5(10)	5(3)			-
	$(33/2^+) \rightarrow (29/2^+)$	686.7(7)	5(2)			0.30(5)
	$(33/2^+) \rightarrow (31/2^+)$	201.6(10)	< 5			0.9(1)

Table A.6: Same as Tab. A.1 but for ^{139}I. Spins and parities taken from Ref. [117].

Nucl.	$J_i^\pi \to J_f^\pi$	E_γ [keV]	I_γ [rel]			
			^{238}U	^{238}U	^{252}Cf	^{248}Cm
			1.7 MeV	3.4 MeV		[117]
^{139}I	$(9/2^+) \to (7/2^+)$	418.6(5)	100(10)			80(4)
	$(11/2^+) \to (7/2^+)$	435.0(5)	80(15)			100(5)
	$(13/2^+) \to (9/2^+)$	397.3(5)	78(11)			64(3)
	$(13/2^+) \to (11/2^+)$	380.9(5)	14(4)			7(1)
	$(15/2^+) \to (11/2^+)$	493.5(5)	67(16)			65(3)
	$(17/2^+) \to (13/2^+)$	464.3(5)	42(9)			42(2)
	$(19/2^+) \to (15/2^+)$	635.3(5)	34(5)			33(2)
	$(21/2^+) \to (17/2^+)$	481.4(6)	19(5)			25(2)
	$(21/2^+) \to (19/2^+)$	197.8(7)	16(8)			20(2)
	$(23/2^+) \to (19/2^+)$	471.4(7)	9(5)			6(1)
	$(23/2^+) \to (21/2^+)$	273.6(8)	< 10			18(2)
	$(25/2^+) \to (21/2^+)$	729.1(18)	8(3)			12(2)
	$(27/2^+) \to (23/2^+)$	652.2(10)	4(3)			5(1)
	$(31/2^+) \to (27/2^+)$	643.8(6)	2.9(15)			2(1)

Appendix B

Additional time distributions

In this appendix, more information on the time distributions for the lifetime measurements is provided. The results are given in Tab. 2.5 of Sec. 2.4.3.

^{138}Te

The 4_1^+ state in $^{138}\mathrm{Te}$ discussed in Sec. 2.4.3 is measured via the $\Delta T(443, 536)$ time difference. HPGe and $LaBr_3$(Ce) energy spectra are shown in Fig. B.1(a) to show the selection of the γ rays. The time distribution is shown in Fig. B.1(b) and the result of the lifetime amounts to $\tau = 113^{+63}_{-44}$ ps [94].

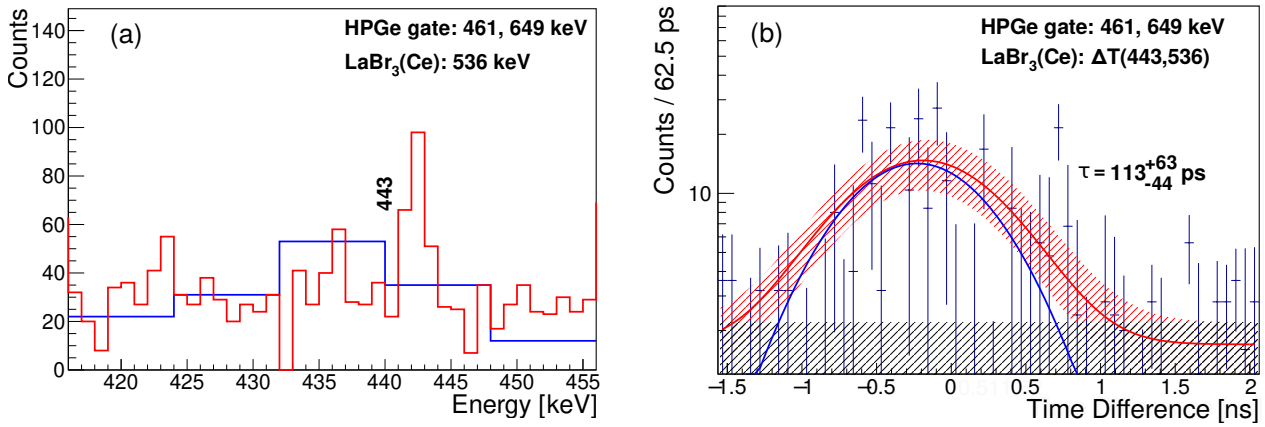

Figure B.1: (a) HPGe (red) and $LaBr_3$(Ce) energy projection after a HPGe gate to select $^{138}\mathrm{Te}$ and a $LaBr_3$(Ce) gate on the feeding 536 keV $6_1^+ \rightarrow 4_1^+$ transition. (b) Time distribution to measure the lifetime of the 4_1^+ state.

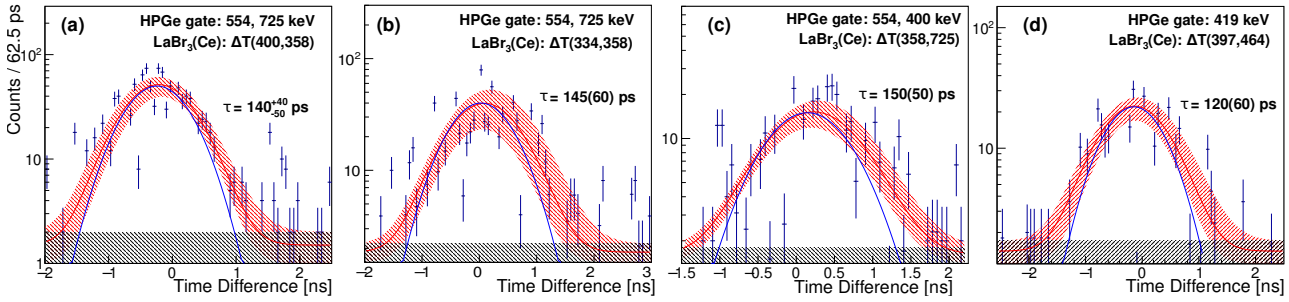

Figure B.2: Time distribution to measure the lifetime of the (a,b) $(13/2_1^+)$ state and (c) $(17/2_1^+)$ state in ^{137}I as well as the (d) $(13/2_1^+)$ state in ^{139}I. Taken from Ref. [95].

^{137}I

From the level scheme shown in Fig. 2.35 discussed in Sec. 2.4.3 it can be seen that the $(13/2_1^+)$ state in ^{137}I is either measured via the $\Delta T(334, 358)$ or the $\Delta T(400, 358)$ time difference. The $(17/2_1^+)$ state in ^{137}I is measured via the $\Delta T(358, 725)$ time difference. The respective time distributions are shown in Figs. B.2(a-c). The lifetime of the $(13/2_1^+)$ state was measured to be $\tau = 140^{+40}_{-50}$ ps from the $\Delta T(400, 358)$ distribution and $\tau = 145(60)$ ps from the $\Delta T(334, 358)$ distribution which shows consistent results. The lifetime of the $(17/2_1^+)$ state amounts to $150(50)$ ps (see Fig. B.2c).

^{139}I

The $\Delta T(397, 464)$ time distribution is used to measure the lifetime of the $(13/2_1^+)$ state in ^{139}I according to the level scheme presented in Fig. 2.35. The time spectrum is shown in Fig. B.2(d). From the fit, a lifetime of $\tau = 120(60)$ ps is obtained.

Appendix C

Résumé en francais

Motivation de la physique

Le noyau atomique est un système quantique composé de protons et de neutrons maintenus ensemble par l'interaction nucléaire forte. Il a été démontré que les noyaux dont le nombre de protons Z ou de neutrons N est égal à 2,8,20,28,50,82 ou 126 ont des configurations particulièrement stables. Ces noyaux sont appelés magiques. Le modèle en couches nucléaire introduit par Mayer et Jensen [4, 5] reproduit ces nombres magiques. Les nucléons sont supposés de se déplacer indépendamment sur différentes couches dans un potentiel moyen créé par le noyau. Les noyaux magiques correspondent à des configurations particulières de couches entièrement occupées.

L'étude des noyaux proches des couches fermées est importante en raison de leur structure relativement simple avec seulement quelques particules de valence. On sait que la structure en couches évolue en s'éloignant de la stabilité dans les noyaux présentant un grand déséquilibre proton-neutron. Ces noyaux sont appelés exotiques et avec les progrès des installations de faisceaux d'ions radioactifs, ils deviennent expérimentalement accessibles. Le ^{132}Sn est un noyau doublement magique avec 50 protons et 82 neutrons. Avec l'ajout de particules au-dessus de ^{132}Sn, les phénomènes collectifs commencent à jouer un rôle et les états excités sont régis non seulement par des configurations à particules individuelles mais aussi par des excitations collectives.

Les signatures de la collectivité dans les noyaux pairs sont, par exemple, l'énergie d'excitation du premier état 2^+ excité, le rapport d'énergie $E_x(4_1^+)/E_x(2_1^+)$ ou la probabilité de transition réduite $B(E2)$ de la transition $2_1^+ \rightarrow 0_1^+$ [8]. Les premières quantités sont directement liées à la mesure des énergies des rayons gamma et la valeur $B(E2)$ peut être extraite en mesurant la durée de vie τ d'un état excité. Un signe de haute collectivité

correspond à une basse énergie d'excitation de l'état 2_1^+ et à une valeur haute de $B(E2)$ par rapport aux noyaux voisins. Lorsque l'on s'éloigne d'une couche fermée, on s'attend à ce que la collectivité augmente. Ce développement de la collectivité autour de la couche fermée en neutrons $N = 82$ n'est pas entièrement compris, ce qui est l'objectif principal de cette thèse.

Partie I : Mesures de durée avec le système ν-ball

Dans la première partie de ce travail, les durées de vie des états excités au-delà du ^{132}Sn ont été mesurées dans le cadre de la campagne ν-ball. La campagne ν-ball a eu lieu auprès de l'installation ALTO du laboratoire IJCLab à Orsay. Des informations spectroscopiques et de durée de vie ont été obtenues pour les isotopes riches en neutrons au-delà de ^{132}Sn. Les résultats expérimentaux ont été comparés aux calculs de modèle en couches. De nouvelles perspectives sur le développement de la collectivité pour les noyaux avec $N > 82$ ont été obtenues.

Les isotopes riches en neutrons qui nous intéressent ont été peuplés dans la fission de ^{238}U induite par des neutrons rapides avec la source de neutrons LICORNE dans une réaction p(^{7}Li,n)^{7}Be [52]. Un faisceau primaire de ^{7}Li produit par l'accélérateur Tandem de l'installation ALTO a été pulsé avec un temps de répétition de 400 ns. L'énergie moyenne des neutrons a été choisie en fonction de la section efficace de fission pour être d'environ 1.7 MeV. Les neutrons ont été utilisés pour induire la fission sur une cible épaisse de 81 g ^{238}U. L'utilisation d'une cible en ^{238}U par rapport aux études de fission précédentes a été motivée par le plus grand rapport N/Z des fragments de fission résultants. Ainsi, il est attendu que des noyaux plus riches en neutrons soient accessibles dans cette réaction. Les rayons gamma venant des fragments de fission ont été détectés avec le spectromètre hybride ν-ball [72].

Celui-ci était composé de détecteurs en germanium hautement purifié (HPGe) et de scintillateurs en bromure de lanthane ($LaBr_3$). Ces détecteurs ont été choisis pour combiner l'excellente résolution énergétique des détecteurs HPGe et la bonne résolution temporelle des détecteurs $LaBr_3$, afin de mesurer les durées de vie à l'aide de la technique 'fast-timing' bien établie. Les détecteurs ont été positionnés en quatre anneaux autour de la cible. Le premier anneau était composé de dix scintillateurs $LaBr_3$ cylindriques de 1.5 pouce $\times$ 2 pouces et de dix scintillateurs coniques de 1 pouce $\times$ 1.5 pouces $\times$ 2 pouces. Les deuxième et troisième anneaux étaient chacun constitués de 12 détecteurs HPGe de type clover. En plus, un anneau de dix détecteurs HPGe coaxiaux a été utilisé. Tous les détecteurs HPGe étaient équipés de boucliers en germanate de bismuth (BGO) pour réduire le bruit de fond dû à la diffusion Compton des rayons de gamma. Nous avons mesuré que la résolution en énergie typique des détecteurs HPGe était d'environ 2.5 keV à 1.3 MeV, alors que la résolution

des détecteurs de type clover et de phase-I est de l'ordre de 1.8 keV et 2.9 keV, respectivement. La résolution temporelle des détecteurs HPGe et $LaBr_3$ mesurée avec une source ^{60}Co était respectivement d'environ 13 ns et 200 ps. L'efficacité de détection des rayons gamma a été déduite de la mesure d'une source de ^{152}Eu, corrigée de l'auto-absorption due à la géométrie de la cible. Elle s'élève à environ 4.1(2) % pour les détecteurs HPGe et 0.7(1) % pour les détecteurs $LaBr_3$.

Les données ont été accumulées en mode sans trigger à l'aide du système d'acquisition FASTER [80] qui est capable de gérer simultanément un grand nombre de canaux avec des détecteurs. Les détecteurs HPGe opéraient à des fréquences moyennes de 5 à 7 kHz. Les informations d'énergie et de temps de tous les détecteurs étaient enregistrées, permettant des études calorimétriques détaillées et une reconstruction complète de la multiplicité des événements. L'utilisation d'un faisceau pulsé a permis l'étude des coïncidences promptes et retardées. Cette méthode a été employée avec succès pour mesurer les isomères à longue durée de vie dans la période de quelques dizaines de ns à quelques centaines de ns [86, 94]. Cette réaction produit de nombreux noyaux qui se désintègrent via des schémas de désexcitation avec de nombreux rayons gamma. Cela correspond à des événements à forte multiplicité de rayons gamma. Des conditions de sélection d'évènements de multiplicité plus élevées améliorent la propreté de l'identification des événements de fission et sont donc utilisés dans l'analyse.

Les fragments de fission ont été identifiés grâce aux coïncidences double gamma et triple gamma provenant de transitions connues dans ces noyaux. Les schémas de niveaux des isotopes du tellure et de l'iode $N = 82, 84, 86$ riches en neutrons ont été construits et les intensités relatives des rayons gamma ont été extraites. Les données ont été comparées aux résultats d'études précédentes sur la fission induite par les neutrons thermiques et la fission spontanée. Les données indiquent que des spins élevés similaires étaient peuplés dans cette réaction. Dans le ^{136}Te, la transition $(3_1^+, 4_2^+) \rightarrow (2_2^+)$ a été à nouveau mesurée avec une précision bien supérieure grâce à l'excellente résolution en énergie des détecteurs HPGe. De plus, le schéma des niveaux du ^{138}Te a été révisé en termes d'ordre des niveaux excités.

Les informations temporelles des détecteurs sont extraites de différentes manières, en fonction de la durée de vie des états excités. L'information temporelle HPGe par rapport à la pulsation du faisceau est utilisée pour les mesures de durées de vie $\tau \gtrsim 5$ ns, limitées par la résolution temporelle des détecteurs HPGe. Pour $\tau \sim 1$ ns, l'information temporelle du faisceau par rapport aux détecteurs $LaBr_3$ a été utilisée. Pour $\tau < 1$ ns, la différence de temps entre deux détecteure $LaBr_3$ a été mesurée. Dans ce cas, des matrices de triple coïncidence HPGe-$LaBr_3$-$LaBr_3$ ont été construites. Une fenêtre d'énergie HPGe a été appliquée pour sélectionner un noyau d'intérêt. Ensuite, la différence de temps d'un rayon gamma peuplant et dépeuplant l'état est mesurée. Cela

mène à la construction de la distribution retardée de temps. Elle peut être décrite par une convolution d'une gaussienne prompte avec une décroissance exponentielle qui permet d'estraire les durées de vie pour $\tau > 50$ ps jusqu'à plusieurs ns.

Plusieurs durées de vie d'états de basse énergie d'excitation ont été remesurées dans des isotopes de tellurium et d'iode riches en neutrons avec $N \geq 82$ comme les durées de vie des états 4_1^+ connues dans ^{134,136}Te et la durée de vie de (15/2$_1^+$) dans ^{135}I. Ensuite, des durées de vie inconnues dans ^{136,138}Te et ^{137,139}I ont été mesurées pour les premiers états excités et certaines limites supérieures ont été proposées pour les états $(11/2_1^+)$ dans ^{135,137,139}I et $(17/2_1^+)$ dans ^{139}I. Ce travail fournit les premières mesures de durée de vie dans les noyaux ^{138}Te, ^{137}I et ^{139}I. Les durées de vie mesurées ont été utilisées pour déduire les probabilités de transition réduites.

Les résultats expérimentaux sont comparés aux prédictions théoriques issues de calculs de modèles en couches déjà utilisées pour les noyaux aux-dessus du noyau ^{132}Sn et bien connues pour cette région [48, 70, 94, 95, 119]. Un espace de valence impliquant les orbitales $1f_{7/2}, 0h_{9/2}, 1f_{5/2}, 2p_{3/2}, 2p_{1/2}, 0i_{13/2}$ pour les neutrons et $0g_{7/2}, 1d_{5/2}, 1d_{3/2}, 2s_{1/2}, 0h_{11/2}$ pour les protons est utilisé ainsi qu'une interaction effective N3LOP. Les énergies des particules individuelles pour les neutrons et les protons sont extraites des données expérimentales de ^{133}Sn et ^{133}Sb [120]. Les énergies orbitales des neutrons $0i_{13/2}$ et des protons $2s_{1/2}$ sont tirées des sources suivantes Réf. [121, 122], respectivement.

Les schémas de niveaux expérimentaux ont été relativement bien reproduits par les résultats des prédictions théoriques. Les états yrast de bas spin des isotopes du tellure peuvent être décrits par le couplage des deux protons de valence dans l'orbitale $\pi(0g_{7/2})$. Avec l'augmentation du nombre de neutrons N, ces états sont plus fragmentés. De plus, il a été démontré que les excitations des états yrast de bas spin dans les isotopes d'iode riches en neutrons résultent du couplage d'un proton avec l'orbitale $\pi(0g_{7/2})$ de son isotone de tellure respectif. Dans les isotones $N = 82$, l'isotope ^{134}Te et l'isotope ^{135}I, des excitations neutrons au travers de la couche fermée $N = 82$ ont été identifiées à une énergie d'excitation élevée, supérieure à 4 MeV, qui en conséquence, confirme le charactère magique du noyau ^{132}Sn.

Les probabilités de transition réduites montrent une tendance globale croissante en fonction du nombre de neutrons, ce qui indique une collectivité croissante de ces transitions. La systématique globale de cette évolution est reproduite par les calculs théoriques, mais elle est parfois surestimée. Il s'est avéré que le développement de la collectivité avec $N > 82$ pour les isotopes du tellure et de l'iode est ralentie par rapport aux noyaux avec $N < 82$ et par rapport aux prédictions théoriques. De plus, le rôle des protons dans les noyaux $Z = 52$ (tellure) et $Z = 53$ (iode) est dominant malgré le grand rapport N/Z dans ces noyaux.

Ce travail contribue à la compréhension de la collectivité au-delà du ^{132}Sn. Des mesures futures pour réduire les barres d'incertitude et étendre les durées de vie jusqu'à $N = 90$ seraient d'une grande importance pour obtenir une image plus complète de l'évolution des couches au-delà de $N = 82$.

Partie II : Isomères autour de ^{132}Sn

Dans la deuxième partie de cette thèse, les isomères autour du ^{132}Sn ont été étudiés après la fission coulombienne du ^{238}U. Les isomères sont des états méta-stables avec des durée de vies significativement plus longues que 1 ns [10]. Ils peuvent avoir des origines différentes, par exemple, en raison de grandes différences de spin entre l'état initial et l'état final ou en raison de formes différentes. Un autre type d'isomères est celui des isomères de séniorité, où la séniorité ν est le nombre de paires couplées à $J > 0$. Cela pourrait résulter à des transitions de faible énergie qui mènent finalement à de longues durée de vies en raison de la dépendance en $1/E_\gamma^{2L+1}$ des taux de transition de gamma [9, 10].

Dans la région inférieure à $N = 82$, différents types d'isomères apparaissent en raison de l'orbitale de parité unique $\nu(0h_{11/2})$. Par exemple, des isomères 10^+ avec séniorité $\nu = 2$ sont présents dans les isotopes pairs en dessous de $N = 82$ [147, 148, 149, 168, 169, 170]. D'autres configurations peuvent impliquer les orbitales $\nu(1d_{3/2})$ ou $2s_{1/2}$. Alors que la systématique pour les isotopes de l'étain avec $N < 82$ est bien étudiée et plutôt complète, l'abondance des isomères connus des mêmes configurations est beaucoup plus faible pour les isotopes du tellure. Ceci motive la poursuite de l'étude pour comprendre l'évolution de l'orbitale $\nu(0h_{11/2})$ et l'influence des protons de valence en dessous de $N = 82$. Dans les études précédentes, la plupart des transitions isomères de basse énergie n'ont pas été détectées, ce qui souligne l'importance de la détection des rayons gamma de basse énergie dans la mesure des isomères.

Les isotopes d'intérêt ont été produits par la fission de l'uranium au centre de faisceaux d'isotopes radioactifs (RIBF) du RIKEN Nishina Center à Saitama, au Japon. Un faisceau primaire de ^{238}U accéléré par un ensemble d'accélérateurs en cascade jusqu'à une énergie de 345 MeV/u est utilisé sur une cible primaire pour produire une grande variété d'ions secondaires différents, que l'on appelle le faisceau cocktail. Ce cocktail d'ions secondaires a été séparé et identifié à l'aide du séparateur de fragments BigRIPS [156]. Le séparateur de fragments BigRIPS est constitué d'aimants dipolaires à température ambiante et d'aimants quadripolaires supraconducteurs. L'identification a été réalisée par la méthode $B\rho$-TOF-ΔE [156, 159] à l'aide de détecteurs de suivi de particules situés à différents points focaux du séparateur de fragments. Des compteurs à avalanche à plaques parallèles, sensibles à la position et des scintillateurs plastiques rapides ont été utilisés pour mesurer la rigidité magnétique ($B\rho$) et le temps de vol (TOF). Ces informations peuvent être utilisées pour déduire le

rapport masse sur charge A/Q grâce à l'équation de Lorentz. La perte d'énergie ΔE est mesurée à l'aide d'une chambre d'ionisation à échantillonnage multiple avec laquelle le numéro de charge atomique peut être reconstruit. En outre, plusieurs corrections à la procédure d'identification des particules ont été appliquées pour optimiser l'identification des ions d'intérêt.

Les ions identifiés sont implantés dans un collecteur en cuivre au point focal F8 après le séparateur de fragments BigRIPS. Les rayons retardés gamma provenant des états isomères d'intérêt ont été mesurés à l'aide de quatre détecteurs HPGe dans une géométrie compacte. Afin de vérifier les performances des détecteurs, deux tests de détection ont été effectués avant l'expérience pour optimiser la résolution temporelle des détecteurs HPGe qui s'élève à environ 9(1) ns FWHM mesurée avec une source ^{60}Co. Les informations temporelles ont été acquises à l'aide de convertisseurs temps/amplitude (TAC) et de convertisseurs temps/numérique (TDC) qui couvraient des temps d'acquisition de 20 μs et 10 μs, respectivement.

Les isomères ont été identifiés dans les matrices énergie-temps 2D après avoir ouvert une fenêtre sur un isotope d'intérêt. Les fenêtres sur les transitions inférieures à l'isomère ont été utilisées pour mesurer les durées de vie. Toutes les transitions inférieures à un état isomérique sont retardées par sa désintégration et peuvent être utilisées dans l'analyse des données. Une attention particulière a été portée à la mesure des transitions de basse énergie qui sont communes dans les décroissances d'isomères. Certaines de ces demi-vies isomériques ont été mesurées pour la première fois par des transitions directes à basse énergie. Par exemple, la demi-vie de l'isomère $(23/2^+)$ dans ^{127}Sn a été mesurée directement par la transition $(23/2^+) \rightarrow (19/2^+)$ de 104 keV. Les demi-vies isomériques des isotopes d'étain et de tellure riches en neutrons entre $N = 76$ et $N = 80$ ont été remesurées et les résultats sont conformes aux mesures précédentes. Une recherche d'un isomère avec spin plut haut dans le ^{126}Sn n'a pas abouti et des transitions potentielles d'un tel isomère ont été observées dans le ^{132}Te.

Les probabilités de transition $E2$ réduites sont calculées pour les transitions isomériques. Les résultats expérimentaux ont été comparés aux prédictions théoriques. Les isotopes de l'étain ont été comparés à des calculs de modèles en couche en utilisant un espace modèle qui ne comprend que les orbitales de neutrons inférieures à $N = 82$, c'est-à-dire $\nu(0g_{7/2}, 1d_{5/2}, 1d_{3/2}, 2s_{1/2}, 0h_{11/2})$. Les calculs déjà utilisés pour la région de ^{132}Sn avec une interaction effective dérivée d'un potential nucléon-nucléon CD-Bonn [51, 166] reproduisent bien les résultats expérimentaux. L'évolution systématique des probabilités de $B(E2)$ dans les isotopes de l'étain peut être comprise en termes de remplissage retardé de l'orbitale neutron $\nu(0h_{11/2})$.

Les intensités des transitions dans les isotopes du tellure sont beaucoup plus élevées que celles des isotones de l'étain, ce qui démontre l'augmentation de la collectivité lorsque l'on ajoute deux protons au système.

Les taux de transition $E2$ dans les isotopes du tellure ont été comparés aux calculs utilisant un modèle de mélange à deux états déduit des excitations de neutrons à partir des valeurs $B(E2)$ de l'étain et des excitations de protons à partir des valeurs $B(E2; 2_1^+ \rightarrow 0_1^+)$ du tellure [141]. Ces calculs montrent l'effet des valeurs $B(E2)$ lors de l'ajout d'un léger mélange de configurations de protons, ce qui démontre l'importance des protons de valence dans ces systèmes. Comparé à la première partie de cette thèse, cela indique que le rôle des protons est significatif dans les noyaux avec $N > 82$ et $N < 82$ malgré le grand excès de neutrons dans ces isotopes riches en neutrons.

Bibliography

[1] G. Gamow. *Proc. R. Soc. Lond. A*, 126:632, 1930.

[2] C. F. v. Weizsäcker. *Z. Phys. A*, 96:431, 1935.

[3] K. L. G. Heyde. *The Nuclear Shell Model*. Springer-Verlag, 1994.

[4] M. G. Mayer. On closed shells in nuclei. *Physical Review*, 74:235, 1948.

[5] M. G. Mayer and H. Jensen. *Elementary Theory of Nuclear Shell Structure*. Wiley New York, 1955.

[6] A. Bohr, B. R. Mottelson. *Nuclear Structure Vol. I*. World Scientific, 1975.

[7] E. Meyer Jr. *American Journal of Physics*, 38:1202, 1970.

[8] R.F. Casten. *Nuclear Structure from a Simple Perspective*. Oxford University Press, 1990.

[9] K. S. Krane. *Introductory Nuclear Physics*. John Wiley & Sons, 1988.

[10] P. Walker and G. Dracoulis. *Nature*, 399:35, 1999.

[11] K. Jain et al. *Nucl. Phys. A*, 591:61, 1995.

[12] P. van Isacker. *J. Phys.: Conf. Ser.*, 322:012003, 2011.

[13] G. Racah. *Phys. Rev.*, 63:367, 1943.

[14] P.C. Srivastava, B. Bhoy, and M.J. Ermamatov. *Prog. Theor. Exp. Phys.*, 2019:103D01, 2019.

[15] T. Faestermann, H. Grawe, and M. Gorska. *Prog. Part. Nucl. Phys.*, 69:85, 2013.

[16] H. Morinaga and T. Yamazaki. *In-beam Gamma-Ray Spectroscopy*. North-Holland, Amsterdam, 1976.

[17] J.M. Blatt, V.F. Weisskopf. *Theoretical Nuclear Physics*. Springer-Verlag New York Inc., 1979.

[18] E. P. Wigner. *Gruppentheorie und ihre Anwendung auf die Quantenmechanik der Atomspektren*. Springer Vieweg, 1931.

[19] K.S. Krane. *Phys. Rev. C*, 8:1494, 1973.

[20] M. Huyse. *The Why and How of Radioactive-Beam Research*. Springer Berlin Heidelberg, 2004.

[21] P. van Duppen. *Isotope Separation On Line and Post Acceleration*. Springer Berlin Heidelberg, 2006.

[22] D. J. Morrissey and B. M. Sherrill. *In-Flight Separation of Projectile Fragments*. Springer Berlin Heidelberg, 2004.

[23] A. S. Goldhaber and H. H. Heckman. *Ann. Rev. Nucl. Part. Sci.*, 28:161, 1978.

[24] J.-J. Gaimard and K.-H. Schmidt. *Nucl. Phys. A*, 531:709, 1991.

[25] D. J. Morrisey et al. *Phys. Rev. Lett.*, 43:1139, 1979.

[26] M. Bernas et al. *Phys. Lett. B*, 331:19, 1994.

[27] M. Jentschel et al. *J. Instrum.*, 12:11003, 2017.

[28] K. L. Jones et al. *Nature*, 465:454, 2010.

[29] K. L. Jones et al. *Phys. Rev. C*, 84:034601, 2011.

[30] D. Rosiak et al. *Phys. Rev. Lett.*, 121:252501, 2018.

[31] M. Górska et al. *Phys. Lett. B*, 672:313, 2009.

[32] J. Taprogge et al. *Phys. Rev. Lett.*, 112:132501, 2014.

[33] R. Orlandi et al. *Physics Letters B*, 785:615, 2018.

[34] J. Benito et al. *Phys. Rev. C*, 102:014328, Jul 2020.

[35] K. Whitmore et al. *Phys. Rev. C*, 102:024327, 2020.

[36] M. Dworschak et al. *Phys. Rev. Lett.*, 100:072501, Feb 2008.

[37] C. Gorges et al. *Phys. Rev. Lett.*, 122:192502, 2019.

[38] P. Cejnar, J. Jolie, and R. F. Casten. *Rev. Mod. Phys.*, 82:2155, 2010.

[39] `http://www.nndc.bnl.gov/nudat2/`.

[40] J. M. Allmond et al. *Phys. Rev. C*, 84:061303(R), 2011.

[41] Yu. Khazhov, A. Rodionov, S. Sakharov, and B. Singh. *Nucl. Data Sheets*, 104:497, 2005.

[42] L. Coraggio, A. Covello, A. Gargano, and N. Itaco. *Phys. Rev. C*, 87:034309, 2013.

[43] O. Sorlin and M.-G. Porquet. *Prog. Part. Nucl. Phys.*, 61:602, 2008.

[44] T. Otsuka, A. Gade, O. Sorlin, T. Suzuki, and Y. Utsuno. *Rev. Mod. Phys.*, 92:015002, 2020.

[45] T. Otsuka, T. Suzuki, R. Fujimoto, H. Grawe, and Y. Akaishi. *Phys. Rev. Lett.*, 95:232502, 2005.

[46] R. K. Bansal and J. B. French. *Phys. Lett.*, 11:145, 1964.

[47] A. Umeya and K. Muto. *Phys. Rev. C*, 74:034330, 2006.

[48] R. Lozeva et al. *Phys. Rev. C*, 93:014316, 2016.

[49] R. H. Mayer et al. *Phys. Lett. B*, 336:308, 1994.

[50] C.T. Zhang et al. *Phys. Rev. C*, 62:057305, 2000.

[51] R. L. Lozeva et al. *Phys. Rev. C*, 77:064313, 2008.

[52] M. Lebois et al. *Nucl. Instrum. Meth. Phys. Res. A*, 735:145, 2014.

[53] I-Y. Lee. *Nucl. Phys A*, 520:c641, 1990.

[54] P J Nolan, F A Beck, and D B Fossan. *Annu. Rev. Nuc. Part. Sci.*, 44:561, 1994.

[55] J.-M. Regis et al. *Nucl. Instrum. Meth. Phy. Res. A*, 763:210, 2014.

[56] M. Rudigier et al. *Acta Phys. Pol. B*, 48:351, 2017.

[57] E. R. Gamba, A. M. Bruce, and M. Rudigier. *Nucl. Instrum. Meth. Phys. Res. A*, 928:93, 2019.

[58] T. Abram and S. Ion. *Energy Policy*, 36:4323, 2008.

[59] G. Locatelli, M. Mancini, and N. Todeschini. *Energy Policy*, 61:1503, 2013.

[60] A. Korgul et al. *Eur. Phys. J. A*, 7:167, 2000.

[61] W. Urban et al. *Phys. Rev. C*, 62:044315, 2000.

[62] S. H. Liu et al. *Phys. Rev. C*, 81:014316, 2010.

[63] J. J. Cowan, F.-K. Thielemann, and J. W. Truran. *Phys. Rep.*, 208:267, 1991.

[64] M. Arnould, S. Goriely, and K. Takahashi. *Phys. Rep.*, 450:97, 2007.

[65] J. N. Wilson et al. *Phys. Rev. Lett.*, 118:222501, 2017.

[66] `https://wwwndc.jaea.go.jp`.

[67] K. Kawade, G. Battistuzi, H. Lawin, K. Sistemich, and J. Blomqvist. *Z. Phys.*, A298:187, 1980.

[68] C. J. Barton et al. *Phys. Lett. B*, 551:269, 2003.

[69] P. Spagnoletti et al. *Phys. Rev. C*, 95:021302(R), 2017.

[70] R. Lozeva et al. *Phys. Rev. C*, 98:024323, 2018.

[71] M. Vergnes. *Nucl. Instrum. Meth.*, 146:81, 1977.

[72] M. Lebois et al. *Nulc. Instrum. Meth. Phys. Res. A*, 960:163580, 2020.

[73] J. N. Wilson et al. *Phys. Proc.*, 59:31, 2014.

[74] H. Laurent et al. *Nucl. Instrum. Meth. Phys. Res. B*, 326:517, 1993.

[75] M. L. Roush, M. A. Wilson, and W. F. Hornyak. *Nucl. Instrum. Meth. Phys. Res.*, 31:112, 1964.

[76] J.-M. Regis et al. *Nucl. Instrum. Meth. Phy. Res. A*, 622:83, 2010.

[77] S. Agostinelli et al. *Nucl. Instrum. Meth. Phys. Res. A*, 506:250, 2003.

[78] K. Debertin and R. G. Helmer. *Gamma and x-ray spectrometry with semiconductor detectors*. Elsevier, Amsterdam, 1988.

[79] D. Thisse et al., 2021. in preparation.

[80] `http://faster.in2p3.fr`.

[81] N. Jovancevic et al. *Acta Phys. Pol. B*, 50:297, 2019.

[82] S. Brun and F. Rademakers. *Nucl. Instrum. Meth. Phys. Res. A*, 389:81, 1997.

[83] `https://gitlab.ikp.uni-koeln.de/nima/soco-v2`.

[84] H. Spieler. *IEEE Trans. Nucl. Sci.*, NS-29/3:1142, 1982.

[85] J.-M. Regis et al. *Nucl. Instrum. Meth. Phy. Res. A*, 684:36, 2012.

[86] G. Häfner et al. *J. Phys.: Conf. Ser.*, 1643:012135, 2020.

[87] A. A. Sonzogni. *Nucl. Data Sheets*, 103:1, 2004.

[88] B. Olsen and L. Bolström. *Nucl. Instrum. Meth.*, 44:65, 1966.

[89] L. Boström, B. Olsen, W. Schneider, and E. Matthias. *Nucl. Instrum. Meth.*, 44:61, 1966.

[90] H. Mach, R. L. Gill, and M. Moszyński. *Nucl. Instrum. Meth. Phys. Res. A*, 280:49, 1989.

[91] Z. Bay. *Phys. Rev.*, 77:419, 1950.

[92] J.-M. Regis et al. *Nucl. Instrum. Meth. Phy. Res. A*, 726:191, 2013.

[93] L. C. Andrews. *Special functions of mathematics for engineers*. SPIE Press, 1998.

[94] G. Häfner et al. *Phys. Rev. C*, 103:034317, 2021.

[95] G. Häfner et al. *Phys. Rev. C*, 104:014316, 2021.

[96] A. Lindroth, B. Fogelberg, H. Mach, M. Sanchez-Vega, and J. Bielcik. *Phys. Rev. Lett.*, 82:4783, 1999.

[97] B. Singh, A. A. Rodionov, and Y. L. Khazov. *Nucl. Data Sheets*, 109:517, 2008.

[98] D. De Frenne. *Nucl. Data Sheets*, 110:1745, 2009.

[99] R. Lozeva, M. Si, and G. Häfner. *EPJ Web Conf.*, 232:04008, 2020.

[100] J. M. Allmond et al. *Phys. Rev. Lett*, 118:092503, 2017.

[101] N. Warr et al. *Eur. Phys. J. A*, 49:40, 2013.

[102] C. T. Zhang et al. *Phys. Rev. Lett.*, 77:3743, 1996.

[103] S. K. Saha et al. *Phys. Rev. C*, 65:017302, 2001.

[104] W. M. Stacey. *Nuclear Reactor Physics*. Wiley-VCH, 2007.

[105] T. Ethvignot et al. *Phys. Rev. Lett.*, 94:052701, 2005.

[106] M.A.C. Hotchkis et al. *Nucl. Phys. A*, 530:111, 1991.

[107] W. Urban et al. *Nucl. Phys. A*, 689:605, 2001.

[108] S. S. Kapoor, R. Ramanna, and P. N. Rama Rao. *Phys. Rev.*, 131:283, 1963.

[109] E. A. McCutchan. *Nucl. Data Sheets*, 152:331, 2018.

[110] J. Chen. *Nucl. Data Sheets*, 146:1, 2017.

[111] J. N. Wilson et al. *Nature*, 590:566, 2021.

[112] S. Mukhopadhyay et al. *Phys. Rev. C*, 85:064321, 2012.

[113] V. Vaquero et al. *Phys. Rev. C*, 99:034306, 2019.

[114] W. Urban et al. *Phys. Rev. C*, 65:024307, 2002.

[115] A. Korgul and others. *Phys. Rev. C*, 64:021302(R), 2001.

[116] E. Browne and J. K. Tuli. *Nucl. Data Sheets*, 108:2173, 2007.

[117] P. K. Joshi, B. Singh, S. Singh, and A. K. Jain. *Nucl. Data Sheets*, 138:1, 2016.

[118] T. Kibédi, T. W. Burrows, M. B. Trzhaskovskaya, P. M. Davidson, and C. W. Nestor Jr. *Nucl. Instrum. Meth. Phys. Res. A*, 589:202, 2008.

[119] H. Naïdja et al. *Phys. Rev. C*, 95:064303, 2017.

[120] Yu. Khazhov, A. Rodionov, and F. G. Kondev. *Nucl. Data Sheets*, 112:855, 2011.

[121] F. Andreozzi et al. *Phys. Rev. C*, 56:R16(R), 1997.

[122] W. Urban et al. *Eur. Phys. J. A*, 5:239, 1999.

[123] H. Naïdja and F. Nowacki. *EPJ Web Conf.*, 193:01005, 2018.

[124] H. Naïdja and F. Nowacki. *J. Phys.: Conf. Ser.*, 966:012061.

[125] E. Caurier, G. Martínez-Pinedo, F. Nowacki, A. Poves, and A. P. Zuker. *Rev. Mod. Phys.*, 77:427, 2005.

[126] E. Caurier and F. Nowacki. *Acta Phys. Pol. B*, 30:705, 1999.

[127] B. A. Brown and W. D. M. Rae. *Nucl. Data Sheets*, 120:115, 2014.

[128] J. B. McGrory and T. T. S. Kuo. *Nucl. Phys. A*, 247:283, 1975.

[129] E. K. Warburton and B. A. Brown. *Phys. Rev. C*, 43:602, 1991.

[130] L. Rydström, J. Blomqvist, R. J. Liotta, and C. Pomar. *Nucl. Phys. A*, 512:217, 1990.

[131] Chong Qi, L. Y. Jia, and G. J. Fu. *Phys. Rev. C*, 94:014312, 2016.

[132] N Lalović et al. *J. Phys. G: Nucl. Part. Phys.*, 45:035105, 2018.

[133] J. Shergur et al. *Phys. Rev. C*, 72:024305, 2005.

[134] J. P. Omtvedt et al. *Phys. Rev. Lett.*, 75:3090, 1995.

[135] H. Mach et al. *Proceedings of the 9th International Spring Seminar on Nuclear Physics, Vico Equense, Italy*, page 263, 2008.

[136] L. M. Fraile et al. *Nucl. Phys. A*, 805:218, 2008.

[137] M. Danchev et al. *Phys. Rev. C*, 84:061306(R), 2011.

[138] R. Broda et al. *Phys. Rev. Lett.*, 68:1671, 1992.

[139] B. Fogelberg and P. Carle. *Nucl. Phys. A*, 323:205, 1979.

[140] B. Fogelberg, K. Heye, and J. Sau. *Nucl. Phys. A*, 352:157, 1981.

[141] J. Genevey et al. *Phys. Rev. C*, 63:054315, 2001.

[142] R. Broda et al. *Eur. Phys. J. A*, 20:145, 2004.

[143] J.A. Pinston et al. *J. Phys. G: Nucl. Part. Phys.*, 30:R57, 2004.

[144] R. Lozeva et al. *AIP Conf. Proc.*, 1090:164, 2009.

[145] S. Pietri et al. *Phys. Rev. C*, 83:044328, 2011.

[146] L.W. Iskra et al. *Phys. Rev. C*, 89:044324, 2014.

[147] J. Katakura and K. Kitao. *Nucl. Data Sheets*, 97:765, 2002.

[148] Z. Elekes and J. Timar. *Nucl. Data Sheets*, 129:191, 2015.

[149] B. Singh. *Nucl. Data Sheets*, 93:33, 2001.

[150] J. Genevey et al. *Phys. Rev. C*, 65:034322, 2002.

[151] H. Gausemel et al. *Phys. Rev. C*, 69:054307, 2004.

[152] J. A. Pinston et al. *Phys. Rev. C*, 61:024312, 2000.

[153] L. Atanasova et al. *Eur. Phys. Lett.*, 91:42001, 2010.

[154] G. Ilie et al. *Phys. Lett. B*, 687:305, 2010.

[155] T. Kubo. *Nucl. Instrum. Meth. Phys. Res. B*, 204:97, 2003.

[156] T. Kubo et al. *Prog. Theo. Exp. Phys.*, 2012:03C003, 2012.

[157] O. B. Tarasov and D. Bazin. *Nucl. Instrum. Meth. Phys. Res. B*, 376:185, 2016.

[158] `https://ribf.riken.jp/RIBFDAQ/index.php?Tools/Analysis/ANAROOT`.

[159] N. Fukuda et al. *Nucl. Instrum. Meth. Phys. Res. B*, 317:323, 2013.

[160] H. Kumagai et al. *Nucl. Instrum. Meth. Phys. Res. A*, 470:562, 2001.

[161] H. Bethe. *Z. Phys.*, 76:293, 1932.

[162] K. Kimura et al. *Nucl. Instrum. Meth. Phys. Res. A*, 297:190, 1990.

[163] H. Kumagai et al. *Nucl. Instrum. Meth. Phys. Res. B*, 317:717, 2013.

[164] H. Bateman. *Proc. Cambrige Phil. Soc*, 15:423, 1910.

[165] A. Hashizume. *Nucl. Data Sheets*, 112:1647, 2011.

[166] M. Hjorth-Jensen, T.T.S. Kuo, and E. Osnes. *Phys. Rep.*, 261:125, 1995.

[167] H. Grawe, K. Langanke, and G. Martinez-Pinedo. *Rep. Pro. Phys.*, 70:1525, 2007.

[168] K. Kitao, Y. Tendow, and A. Hashizume. *Nucl. Data Sheets*, 96:241, 2002.

[169] T. Tamura. *Nucl. Data Sheets*, 108:455, 2007.

[170] J. Katakura and Z.D. Wu. *Nucl. Data Sheets*, 109:1655, 2008.

List of Figures

List of Tables

List of Publications

Publications in refereed journals

[1] A. Esmaylzadeh, L. M. Gerhard, V. Karayonchev, J.-M. Régis, J. Jolie, M. Bast, A. Blazhev, T. Braunroth, M. Danhoff, F. Dunkel, C. Fransen, G. Häfner, L. Knafla, M. Ley, C. Müller-Gatermann, K. Schomacker and N. Warr, K.-O. Zell.
Liftime determination in ^{190,192,194,196}Hg via γ-γ fast-timing spectroscopy.
Physical Review C **98**, 014313 (2018).

[2] C. M. Petrache, J.-M. Régis, C. Andreoiu, M. Spieker, C. Michelagnoli, P. E. Garret, A. Astier, E. Dupont, F. Garcia, S. Guo, G. Häfner, J. Jolie, F. Kandzia, V. Karayonchev, Y.-H. Kim, L. Knafla, U.Köster, B. F. Lv, N. Marginean, C. Mihai, P. Mutti, K. Ortner, C. Porzio, S. Prill, N. Saed-Samii, W. Urban, J. R. Vanhoy, K. Whitmore, J. Wisniewski and S. W. Yates.
Collectivity of the 2p-2h proton intruder band of ^{116}Sn.
Physical Review C **99**, 024303 (2019).

[3] G. Häfner, K. Moschner, A. Blazhev, P. Boutachkov, P. J. Davies, R. Wadsworth, F. Ameil, H. Baba, T. Bäck, M. Dewald, P. Doornenbal, T. Faestermann, A. Gengelbach, J. Gerl, R. Gernhäuser, S. Go, M. Górska, H. Grawe, E. Gregor, H. Hotaka, T. Isobe, D. G. Jenkins, J. Jolie, H. S. Jung, I. Kojouharov, N. Kurz, M. Lewitowicz, G. Lorusso, R. Lozeva, E. Merchan, F. Naqvi, H. Nishibata, D. Nishimura, S. Nishimura, N. Pietralla, H. Schaffner, P.-A. Söderström, K. Steiger, T. Sumikama, J. Taprogge, P. Thöle, H. Watanbe, N. Warr, V. Werner, Z. Y. Xu, A. Yagi, K. Yoshinaga and Y. Zhu.
Properties of γ-decaying isomers in the ^{100}Sn region populated in fragmentation of a ^{124}Xe beam.
Physical Review C **100**, 024302 (2019).

[4] A. Goldkuhle, C. Fransen, A. Dewald, K. Arnswald, M. Bast, M. Beckers, A. Blazhev, T. Braunroth, G. Hackenberg, G. Häfner, J. Litzinger, J. Jolie, C. Müller-Gatermann, F. von Spee, N. Warr, D. Werner and K. O. Zell.
Lifetime measurement of excited states in ^{46}Ti.
European Physical Journal A **55**, 53 (2019).

[5] R.L.Canavan, M.Rudigier, P.H.Regan, M.Lebois, J.N.Wilson, N.Jovancevic, P.-A.Soderstrom, S.M.Collins, D.Thisse, J.Benito, S.Bottoni, M.Brunet, N.Cieplicka-Orynczak, S.Courtin, D.T.Doherty, L.M.Fraile, K.Hadynska-Klek, G.Häfner, M.Heine, L.W.Iskra, V.Karayonchev, A.Kennington, P.Koseoglou, G.Lotay, G.Lorusso, M.Nakhostin, C.R.Nita, S.Oberstedt, Zs.Podolyak, L.Qi, J.-M.Regis, V.Sanchez-Tembleque, R.Shearman, V.Vedia and W.Witt.
Half-life measurements in ^{164,166}Dy using γ-γ fast-timing spectroscopy with the ν-Ball spectrometer.
Physical Review C **101**, 024313 (2020).

[6] L.Knafla, P.Alexa, U.K oster, G.Thiamova, J.-M.Regis, J.Jolie, A.Blanc, A.M.Bruce, A.Esmaylzadeh, L.M.Fraile, G.de France, G.Häfner, S.Ilieva, M.Jentschel, V.Karayonchev, W.Korten, T.Kroll, S.Lalkovski, S.Leoni, H.Mach, N.Marginean, P.Mutti, G.Pascovici, V.Paziy, Zs.Podolyak, P.H.Regan, O.J.Roberts, N.Saed-Samii, G.S.Simpson, J.F.Smith, T.Soldner, C.Townsley, C.A.Ur, W.Urban, A.Vancraeyenest and N.Warr.
Lifetime measurements in the odd-A nucleus ^{177}Hf.
Physical Review C **102**, 054322 (2020).

[7] L.Knafla, G.Häfner, J.Jolie, J.-M.Regis, V.Karayonchev, A.Blazhev, A.Esmaylzadeh, C.Fransen, A.Goldkuhle, S.Herb, C.Muller-Gatermann, N.Warr and K.O.Zell.
Lifetime measurements of ^{162}Er: evolution of collectivity in the rare-earth region.
Physical Review C **102**, 044310 (2020).

[8] V.Karayonchev, J.Jolie, A.Blazhev, A.Dewald, A.Esmaylzadeh, C.Fransen, G.Häfner, L.Knafla, J.Litzinger, C.Muller-Gatermann, J.-M.Regis, K.Schomacker, A.Vogt, N.Warr, A.Leviatan and N.Gavrielov.
Test of collectivity in ^{98}Zr by absolute transition rates.
Physical Review C **102**, 064314 (2020).

[9] R.-B.Gerst, A.Blazhev, N.Warr, J.N.Wilson, M.Lebois, N.Jovancevic, D.Thisse, R.Canavan, M.Rudigier, D.Etasse, E.Adamska, P.Adsley, A.Algora, M.Babo, K.Belvedere, J.Benito, G.Benzoni, A.Boso, S.Bottoni, M.Bunce, R.Chakma, N.Cieplicka-Orynczak, S.Courtin, M.L.Cortes, P.Davies, C.Delafosse, M.Fallot, B.Fornal, L.M.Fraile, D.Gjestvang, A.Gottardo, V.Guadilla, G.Häfner, K.Hauschild, M.Heine, C.Henrich, I.Homm, F.Ibrahim, L.W.Iskra, P.Ivanov, S.Jazrawi, A.Korgul, P.Koseoglou, T.Kroll, T.Kurtukian-Nieto, L.Le Meur, S.Leoni, J.Ljungvall, A.Lopez-Martens, R.Lozeva, I.Matea, K.Miernik, J.Nemer, S.Oberstedt, W.Paulsen, M.Piersa, Y.Popovitch, C.Porzio, L.Qi, D.Ralet, P.H.Regan, D.Reygadas Tello, K.Rezynkina, V.Sanchez-Tembleque, C.Schmitt, P.-A.Soderstrom, C.Surder, G.Tocabens, V.Vedia, D.Verney, B.Wasilewska, J.Wiederhold, M.Yavachova, F.Zeiser and S.Ziliani.
Prompt and delayed γ spectroscopy of neutron-rich ^{94}Kr and observation of a new isomer.
Physical Review C **102**, 064323 (2020).

[10] G.Häfner, R.Lozeva, H.Naidja, M.Lebois, N.Jovancevic, D.Thisse, D.Etasse, R.L.Canavan, M.Rudigier, J.N.Wilson, E.Adamska, P.Adsley, M.Babo, K.Belvedere, J.Benito, G.Benzoni, A.Blazhev, A.Boso, S.Bottoni, M.Bunce, R.Chakma, N.Cieplicka-Orynczak, S.M.Collins, M.L.Cortes, P.J.Davies, C.Delafosse, M.Fallot, B.Fornal, L.M.Fraile, R.-B.Gerst, D.Gjestvang, V.Guadilla, K.Hauschild, C.Henrich, I.Homm, F.Ibrahim, L.W.Iskra, S.Jazwari, J.Jolie, A.Korgul, P.Koseoglou, Th.Kroll, T.Kurtukian-Nieto, L.Le-meur, J.Ljungvall, A.Lopez-Martens, I.Matea, L.Matthieu, K.Miernik, J.Nemer, S.Oberstedt, W.Paulsen, M.Piersa, Y.Popovitch, C.Porzio, L.Qi, D.Ralet, P.H.Regan, D.Reygadas Tello, K.Rezynkina, V.Sanchez, C.Schmitt, P.-A.Soderstrom, C.Surder, G.Tocabens, V.Vedia, D.Verney, N.Warr, B.Wasilewska, J.Wiederhold, M.S.Yavahchova, F.Zeiser and S.Ziliani.
Spectroscopy and lifetime measurements in ^{134,136,138}Te isotopes and implications for the nuclear structure beyond N=82.
Physical Review C **103**, 034317 (2021).

[11] A.Esmaylzadeh, V.Karayonchev, G. Häfner, J.Jolie, M.Beckers, A.Blazhev, A.Dewald, C.Fransen, A.Goldkuhle, L.Knafla and C.Muller-Gatermann.
Triaxiality in the mid-shell nucleus ^{112}Pd.
Physical Review C **103**, 054324 (2021).

[12] J.N.Wilson, D.Thisse, M.Lebois, N.Jovancevic, D.Gjestvang, R.Canavan, M.Rudigier, D.Étasse, R-B.Gerst, L.Gaudefroy, E.Adamska, P.Adsley, A.Algora, M.Babo, K.Belvedere, J.Benito, G.Benzoni, A.Blazhev, A.Boso, S.Bottoni, M.Bunce, R.Chakma, N.Cieplicka-Orynczak, S.Courtin, M.L.Cortés, P.Davies, C.Delafosse, M.Fallot, B.Fornal, L.Fraile, A.Gottardo, V.Guadilla, G. Häfner, K.Hauschild, M.Heine, C.Henrich, I.Homm, F.Ibrahim, L.W.Iskra, P.Ivanov, S.Jazrawi, A.Korgul, P.Koseoglou, T.Kröll, T.Kurtukian-Nieto, L.Le Meur, S.Leoni, J.Ljungvall, A.Lopez-Martens, R.Lozeva, I.Matea, K.Miernik, J.Nemer, S.Oberstedt, W.Paulsen, M.Piersa, Y.Popovitch, C.Porzio, L.Qi, D.Ralet, P.H.Regan, K.Rezynkina, V.Sanchez-Tembleque, S.Siem, C.Schmitt, P.-A.Söderström, C.Surder, G.Tocabens, V.Vedia, D.Verney, N.Warr, B.Wasilewska, J.Wiederhold, M.Yavahchova, F.Zeiser and S.Ziliani.
Angular momentum generation in fission.
Nature **590**, 566 (2021).

[13] G. Häfner, A.Esmaylzadeh, J.Jolie, J.-M.Régis, C.Muller-Gatermann, A.Blazhev, C.Fransen, R.-B. Gerst, V.Karayonchev, L.Knafla, N.Saed-Samii and K.O.Zell.
Lifetime measurements in ^{182}Pt using γ-γ fast-timing.
European Physical Journal A **57**, 174 (2021).

[14] G.Häfner, R.Lozeva, H.Naidja, M.Lebois, N.Jovancevic, D.Thisse, D.Etasse, R.L.Canavan, M.Rudigier, J.N.Wilson, E.Adamska, P.Adsley, M.Babo, K.Belvedere, J.Benito, G.Benzoni, A.Blazhev, A.Boso, S.Bottoni, M.Bunce, R.Chakma, N.Cieplicka-Orynczak, S.M.Collins, M.L.Cortes, P.J.Davies, C.Delafosse, M.Fallot, B.Fornal, L.M.Fraile, R.-B.Gerst, D.Gjestvang, V.Guadilla, K.Hauschild, C.Henrich, I.Homm, F.Ibrahim, L.W.Iskra, S.Jazwari, J.Jolie, A.Korgul, P.Koseoglou, Th.Kroll, T.Kurtukian-Nieto, L.Le-meur, J.Ljungvall, A.Lopez-Martens, I.Matea, L.Matthieu, K.Miernik, J.Nemer, S.Oberstedt, W.Paulsen, M.Piersa, Y.Popovitch, C.Porzio, L.Qi, D.Ralet, P.H.Regan, D.Reygadas Tello, K.Rezynkina, V.Sanchez, C.Schmitt, P.-A.Soderstrom, C.Surder, G.Tocabens, V.Vedia, D.Verney, N.Warr, B.Wasilewska, J.Wiederhold, M.S.Yavahchova, F.Zeiser and S.Ziliani.
First lifetime investigations of N$>$82 iodine isotopes: the quest for collectivity.
Physical Review C **104**, 014316 (2021).

[15] S.Y.Jin, S.T.Wang, J.Lee, A.Corsi, K.Wimmer, F.Browne, S.Chen, M.L.Cortes, P. Doornenball, T.Koiwai, C.X.Yuan, A.Algora, D.Brugnara, J.Cederkäll, J.Gerl, M.Gorska, G.Häfner, K.Kokubun, P.Koseoglou, S.Kubono, P.Li, P.Liang, J.Liu, Z.Liu, T.Lokotko, J.Park, H.Sakurai, L.G.Sarmiento, Z.Y.Sun, R.Taniuchi, W.Xian and I.Zanon.
Spectroscopy of ^{98}Cd by two-nucleon removal from ^{100}In.
accepted in *Physical Review C* (2021).

Publications in conference proceedings

[16] G. Häfner, K. Moschner, A. Blazhev, P. Boutachkov, P. J. Davies, R. Wadsworth, F. Ameil, H. Baba, T. Bäck, M. Dewald, P. Doornenbal, T. Faestermann, A. Gengelbach, J. Gerl, R. Gernhäuser, S. Go, M. Górska, H. Grawe, E. Gregor, H. Hotaka, T. Isobe, D. G. Jenkins, J. Jolie, H. S. Jung, I. Kojouharov, N. Kurz, M. Lewitowicz, G. Lorusso,, E. Merchan, F. Naqvi, H. Nishibata, D. Nishimura, S. Nishimura, N. Pietralla, H. Schaffner, P.-A. Söderström, K. Steiger, T. Sumikama, J. Taprogge, P. Thöle, H. Watanbe, N. Warr, V. Werner, Z. Y. Xu, A. Yagi, K. Yoshinaga and Y. Zhu.
Properties of γ-decaying isomers in the ^{100}Sn region revisited.
Acta Physica Polonica B **50**, 431 (2019).

[17] N. Jovancevic, M. Lebois, J. N. Wilson, D. Thisse, L. Qi, I. Matea, F. Ibrahim, D. Verney, M. Babo, C. Delafosse, F. Adsley, G. Tocabens, A. Gottardo, Y. Popovitch, J. Nemer, R. Canavan, M. Rudigier, K. Belvedere, A. Boso, P. Regan, Zs. Podolyak, R. Shearman, M. Bunce, P. Ivanov, S. Oberstedt, A. Lopez-Martens, K. Hauschild, J. Ljungvall, R. CHakma, R. Lozeva, P.-A. Söderström, A. Oberstedt, D. Etasse, D. Ralet, A. Blazhev, R.-B. Gerst, G. Häfner, N. Cipelicka-Orynczak, L. W. Iskra, B. Fornal, G. Benzoni, S. Leoni, S. Bottoni, C. Henrich, P. Koseoglou, J. Wiederhold, I. Homm, C. Surder, T. Kroll, D. Knezevic, A. Dragic, L. Cortes, N. Warr, K. Miernik, E. Adamska, M. Piersa, K. Reynkina, L. Fraile, J. Benito Garcia, V. Sanchez, A. Algora, P. Davies, V. Guadilla-Gomez, M. Fallot, T. Kurtukian-Nieto, C. Schmitt, M. Heine, D. Reygadas Tello, M. Yavachova, M. Diakaki, F. Zeiser, W. Paulson and D. Gjestvang.
Spectroscopy of neutron induced reactions with the ν-Ball spectrometer.
Acta Physica Polonica B **50**, 297 (2019).

[18] E.Adamska, A.Korgul, A.Fijalkowska, K.Miernik, M.Piersa, R.Canavan, D.Etasse, N.Jovancevic, M.Lebois, M.Rudigier, D.Thisse, J.N.Wilson, P.Adsley, A.Algora, M.Babo, K.Belvedere, J.Benito, A.Blazhev, G.Benzoni, A.Boso, S.Bottoni, M.Bunce, R.Chakma, N.Cieplicka-Orynczak, M.Ciemala, S.Collins, L.Cortes, P.Davies, C.Delafosse, M.Fallot, B.Fornal, L.M.Fraile, R.-B.Gerst, D.Gjestvang, A.Gottardo, V.Guadilla, G.Häfner, K.Hauschild, M.Heine, C.Henrich, I.Homm, F.Ibrahim, L.W.Iskra, P.Koseoglou, T.Kroll, T.Kurtukian Nieto, L.Le-Meur, S.Leoni, J.Ljungvall, A.Lopez-Martens, R.Lozeva, I.Matea, J.Nemer, S.Oberstedt, W.Paulsen, Y.Popovitch, L.Qi, D.Ralet, P.H.Regan, D.Reygadas Tello, K.Rezynkina, V.Sanchez-Tembleque, C.Schmitt, P-A.Soderstrom, C.Surder, G.Tocabens, V.Vedia, D.Verney, N.Warr, B.Wasilewska, M.Yavahchova and F.Zeiser.
γ-ray spectroscopy of ^{85}Se produced in ^{232}Th fission.
Acta Physica Polonica B **51**, 843 (2020).

[19] R. Lozeva, M. Si and G. Häfner.
Beyond ^{132}Sn: Examples of new data on exotic neutron-rich Te isotopes from fission and β-decay
EPJ Web of Conferences **232**, 04008 (2020).

[20] G. Häfner, R.Lozeva, A.Blazhev, R.L.Canavan, D.Etasse, J.Jolie, N.Jovancevic, R.-B.Gerst, Th.Kröll, M.Lebois, P.H.Regan, M.Rudigier, D.Thisse, N.Warr, J.N.Wilson and the N-SI-109 collaboration.
Lifetime measurements around ^{132}Sn with the ν-Ball array.
Journal of Physics: Conference Series **1643**, 012135 (2020).

Eklärung zur Dissertation

Hiermit versichere ich an Eides statt, dass ich die vorliegende Dissertation selbstständig und ohne die Benutzung anderer als der angegebenen Hilfsmittel und Literatur angefertigt habe. Alle Stellen, die wörtlich oder sinngemäß aus veröffentlichten und nicht veröffentlichten Werken dem Wortlaut oder dem Sinn nach entnommen wurden, sind als solche kenntlich gemacht. Ich versichere an Eides statt, dass diese Dissertation noch keiner anderen Fakultät oder Universität zur Prüfung vorgelegen hat; dass sie - abgesehen von unten angegebenen Teilpublikationen und eingebundenen Artikeln und Manuskripten - noch nicht veröffentlicht worden ist sowie, dass ich eine Veröffentlichung der Dissertation vor Abschluss der Promotion nicht ohne Genehmigung des Promotionsausschusses vornehmen werde. Die Bestimmungen dieser Ordnung sind mir bekannt. Darüber hinaus erkläre ich hiermit, dass ich die Ordnung zur Sicherung guter wissenschaftlicher Praxis und zum Umgang mit wissenschaftlichem Fehlverhalten der Universität zu Köln gelesen und sie bei der Durchführung der Dissertation zugrundeliegenden Arbeiten und der schriftlich verfassten Dissertation beachtet habe und verpflichte mich hiermit, die dort genannten Vorgaben bei allen wissenschaftlichen Tätigkeiten zu beachten und umzusetzen. Ich versichere, dass die eingereichte elektronische Fassung der eingereichten Druckfassung vollständig entspricht.

Teilpublikationen

- G. Häfner *et al.*, Phys. Rev. C **103**, 034317 (2021).
- G. Häfner *et al.*, Phys. Rev. C **104**, 014316 (2021).

Orsay, den 27. Juli 2021

(Guillaume Häfner)

université PARIS-SACLAY

ÉCOLE DOCTORALE
Particules, hadrons, énergie et noyau: instrumentation, imagerie, cosmos et simulation (PHENIICS)

Titre: Durées de vie et structure nucléaire autour de ^{132}Sn

Mots clés: structure nucléaire, spectrométrie gamma, durée de vie, ^{132}Sn

Résumé: L'étude des noyaux riches en neutrons autour du noyau double-magique ^{132}Sn offre l'une des meilleures possibilités d'étudier les éléments de matrice à deux corps des théories de physique nucléaire loin de la stabilité. Une quantité sensible pour obtenir les informations sur les fonctions d'onde nucléaires sont les durées de vie des états excités. Pendant ce travail, two experiences ont été analysé.

La première expérience est consacrée aux mesures de durée de vie et été réalisée à l'installation ALTO à Orsay. Des noyaux riches en neutrons on été produits lors de la fission de ^{238}U à l'aide de neutrons rapides et les rayons γ on été détectés avec une combinaison de détecteurs au germanium hautement purifié (HPGe) et au bromure de lanthane ($LaBr_3$). De nouvelles informations spectroscopiques et les durées de vie des étas bas dans les isotopes de tellure et de l'iode au dessus de $N = 82$ on été mesurées. Les durées de vie des états excités de faible énergie dans les noyaux ^{134,136}Te et ^{135}I on été remesurées et l'état 6_1^+ dans le ^{136}Te a été mesuré pour la première fois. Les premiers résultats des durées de vie des états $2_1^+, 4_1^+$ et 6_1^+ dans le ^{138}Te et des états $(9/2_1^+), (13/2_1^+)$ et $(17/2_1^+)$ dans les ^{137,139}I on été obtenus et les probabilités de transition réduites on été extraites. Les données expérimentales on été comparées aux calculs théoriques du modèle en couches. Ce travail fournit de nouvelles perspectives sur l'évolution de la collectivité en dehors du double-magique ^{132}Sn et contribue à la compréhension de la structure nucléaire au dessus de $N = 82$.

La deuxième expérience est consacrée à l'étude des ètats nucléaires isomères en dessous de ^{132}Sn. L'expérience a été conduite à l'installation de faisceaux d'isotope radioactifs du centre RIKEN Nishina au Japon. Des noyaux exotiques ont été produits pars fission de ^{238}U et le faisceu cocktail résultant a été séparé en masse et identifié par le séparateur de fragments BigRIPS. Les ions d'intérêt ont été implantés dans un capteur et les rayons γ ont été détectés à l'aide de quatre détecteurs HPGe en géométrie serrée. Les durées de vie des isomères des isotope d'étain et de tellure riches en neutrons on été mesurées et les résultats on été comparés aux calculs théoriques. Les deux expériences on permis de confirmer l'importance des excitations de proton pour l'évolution de la collectivité dans les isotopes du tellure autour de $N = 82$.

université PARIS-SACLAY

ÉCOLE DOCTORALE
Particules, hadrons, énergie et noyau : instrumentation, imagerie, cosmos et simulation (PHENIICS)

Title: Lifetimes and nuclear structure around ^{132}Sn

Keywords: nuclear structure, gamma spectroscopy, lifetime, ^{132}Sn

Abstract: The investigation of neutron-rich nuclei around the doubly magic ^{132}Sn provides one of the best opportunities to test two-body matrix elements from nuclear theory far off the valley of stability. A sensitive probes to gain information into the nuclear wave functions are lifetimes of excited states. In the course of this work, data from two experiments were analyzed.
The first experiment dedicated to lifetime measurements was performed at the ALTO facility in Orsay. Neutron-rich nuclei were produced in fast neutron-induced fission of ^{238}U and γ rays detected using a combination of high-purity germanium (HPGe) and lanthanum bromid ($LaBr_3$) detectors. New spectroscopic information and lifetimes of low-lying excited states in tellurium and iodine isotopes beyond $N = 82$ were measured. Lifetimes of low-lying excited states in ^{134,136}Te and ^{135}I were remeasured and the 6_1^+ state in ^{136}Te was measured for the first time. First results on lifetimes of the $2_1^+, 4_1^+$ and 6_1^+ states in ^{138}Te and $(9/2_1^+), (13/2_1^+)$ and $(17/2_1^+)$ states in ^{137,139}I are obtained and reduced transition probabilities were extracted. The experimental data were compared to theoretical calculations in the framework of the nuclear shell model. This work provides new insights into the development of collectivity outside the doubly magic ^{132}Sn and contributes to the understanding of the nuclear structure beyond $N = 82$.
The second experiment was dedicated to the investigation of isomers below ^{132}Sn. The experiment was performed at the Radioactive Isotopes Beam Facility of the RIKEN Nishina Center in Japan. Exotic nuclei were produced through in-flight fission of ^{238}U and the resulting cocktail beam mass separated and identified using the BigRIPS fragment separator. Ions of interest were implanted in a copper catcher and γ rays detected using four HPGe detectors in close geometry. Half-lives of isomers in neutron-rich tin and tellurium isotopes were remeasured and the results compared to theoretical calculations. From both experiments, the importance of the proton excitations for the evolution of collectivity in the tellurium isotopes around $N = 82$ could be confirmed.

université PARIS-SACLAY

ÉCOLE DOCTORALE
Particules, hadrons, énergie et noyau: instrumentation, imagerie, cosmos et simulation (PHENIICS)

Titel: Lebensdauern und Kernstruktur um ^{132}Sn

Schlüsselwörter: Kernstruktur, Gammaspektroskopie, Lebensdauer, ^{132}Sn

Abstrakt: Die Untersuchung neutronenreicher Kerne um den doppelt magischen Kern ^{132}Sn bietet eine der besten Möglichkeiten um Zwei-Körper-Matrixelemente aus kernphysikalischen Theorien fernab der Stabilität zu untersuchen. Eine sensitive Größe um Informationen über die Kernwellenfunktionen zu erhalten sind Lebensdauern angeregter Zustände. Im Zuge dieser Arbeit wurden zwei Experimente ausgewertet.
Das erste Experiment ist Lebensdauermessungen gewidmet und wurde an der ALTO Einrichtung in Orsay durchgeführt. Neutronenreiche Kerne wurden in Spaltung von ^{238}U mittels schneller Neutronen produziert und Gammastrahlen mit einer Kombination aus hochreinen Germanium (HPGe) und Lanthanbromid ($LaBr_3$) Detektoren detektiert. Neue spektroskopische Informationen und Lebensdauern von angeregten Zuständen in Tellur- und Iodisotopen jenseits von N=82 wurden ermittelt. Lebensdauern von tiefliegenden angeregten Zuständen in ^{134,136}Te und ^{135}I wurden neu gemessen und der 6_1^+-Zustand in ^{136}Te wurde erstmals bestimmt. Erste Ergebnisse von Lebensdauern $2_1^+, 4_1^+$- und 6_1^+-Zustände in ^{138}Te und $(9/2_1^+), (13/2_1^+)$- und $(17/2_1^+)$-Zustände in ^{137,139}I wurden erlangt und reduzierte Übergangswahrscheinlichkeiten extrahiert. Die experimentellen Daten wurden mit theoretischen Schalenmodellrechnungen verglichen. Diese Arbeit liefert neue Erkenntnisse über die Entwicklung der Kollektivität außerhalb des doppelt magischen ^{132}Sn und trägt zum Verständnis der Kernstruktur jenseits von $N = 82$ bei.
Das zweite Experiment ist der Untersuchung isomerer Kernzustände unterhalb von ^{132}Sn gewidmet und wurde an der Einrichtung für radioaktive Isotopenstrahlen des RIKEN Nishina Zentrums in Japan durchgeführt. Exotische Kerne wurden mittels Spaltung von ^{238}U produziert und der resultierende Cocktailstrahl massenseparierte und mittels BigRIPS Fragmentseparator identifiziert. Ionen, die von Interesse sind, wurden in einer Vorrichtung implantiert und Gammastrahlen mit Hilfe von HPGe Detektoren in kompakter Geometrie detektiert. Halbwertszeiten von Isomeren in neutronenreichen Zinn- und Tellurisotopen wurden nachgemessen und die Ergbenisse mit theoretischen Rechnungen verglichen. Durch de Ergebnisse beider Experimente konnte die Relevanz der Protonenanregungen für die Evolution der Kollektivität in Tellurisotopen bestätigt werden.